ULTRA-WIDEBAND ANTENNAS AND COMPONENTS FOR WIRELESS COMMUNICATION SYSTEMS

OSAMA MOHAMED HARAZ AHMED

A THESIS

IN

THE DEPARTMENT OF

ELECTRICAL AND COMPUTER ENGINEERING

PRESENTED IN PARTIAL FULFILLMENT OF THE REQUIREMENTS

FOR THE DEGREE OF DOCTOR OF PHILOSOPHY

CONCORDIA UNIVERSITY

MONTREAL, QUEBEC, CANADA

SEPTEMBER 2011

CONCORDIA UNIVERSITY
SCHOOL OF GRADUATE STUDIES

This is to certify that the thesis prepared

By: Osama Mohamed Haraz Ahmed

Entitled: Ultra-Wideband Antennas and Components for Wireless Communication Systems

and submitted in partial fulfillment of the requirements for the degree of

DOCTOR OF PHILOSOPHY in Electrical Engineering

complies with the regulations of the University and meets the accepted standards with respect to originality and quality.

Signed by the final examining committee:

Dr. B. Desai — Chair

Dr. L. Shafai — External Examiner

Dr. M. Bertola — External to Program

Dr. A.A. Kishk — Examiner

Dr. R. Paknys — Examiner

Dr. A.R. Sebak — Thesis Supervisor

Approved by

Chair of Department or Graduate Program Director

September 1, 2011

Dean of Faculty

Abstract

Ultra-wideband Antennas and Components for Wireless Communication Systems

Osama Ahmed, P.hD.

Concordia University, September 2011

Ultra-wideband (UWB) technology is rapidly developing as a high speed, and high data rate wireless communication mode. There are many challenges in dealing with this new emerging technology. One of these challenges is how to design an antenna element that can operate effectively in the entire UWB frequency range. Another big challenge is to design UWB antenna beamforming systems including suitable UWB components such as feed networks, transitions, crossovers, hybrid couplers and phase shifters to meet the UWB requirements.

This thesis is primarily focused on designing UWB antenna elements and other microwave components for UWB wireless communications applications. The thesis starts with designing and implementing different new UWB disc monopole and hybrid antennas with discussions covering their operation, electrical behavior and performance. Antennas are developed using microstrip technology to achieve low profile and compatibility with printed circuit board (PCB) technology. Different techniques for obtaining a bandstop function in the 5.0-6.0 GHz frequency band to avoid interference with other existing wireless local area network (WLAN) systems are numerically and experimentally presented. A UWB feed network prototype based on a modified two-section Wilkinson

power divider is then developed. The designed feed network has been used in constructing two-element and four-element antenna arrays. The two-element antenna array has a total directive gain of about 5.5–8.5 dBi within the whole UWB frequency band while for the four-element antenna array, the achieved total directive gain is about 7.5–11.5 dBi.

Two different UWB slot-coupled microstrip-to-microstrip vertical transitions are also addressed. The proposed transitions utilize trapezoidal- and butterfly-shaped microstrip patches at the top and bottom layers. The broadside coupling between microstrip-coupled patches is achieved by cutting a rectangular-shaped slot in the mid-layer ground plane. The designed transitions are used to develop 3dB/90° hybrid couplers with good return loss, insertion loss, coupling and isolation characteristics across the desired frequency range. Then two different 45° phase shifters are developed to be used in building 4 × 4 Butler matrices for UWB beamforming applications.

Finally, two compact and inexpensive multiple beamforming network (M-BFN) prototypes are developed. The developed microwave components using multi-layer microstrip PCB technology are used to design 4 × 4 Butler matrices. These matrices avoid using any crossing lines or crossovers and exhibit large bandwidth for UWB applications. To validate the proposed design, experimental prototypes of the proposed 4 × 4 matrices are designed, fabricated and tested. A four patch antenna array is connected to these matrices to form multiple beamforming array systems. Simulations are carried out on these beamforming systems and the obtained radiation characteristics are also presented and discussed.

Acknowledgments

All my thanks to the God, to the successful completion of this work.

I would like also to express my most sincere gratitude to my supervisor, Professor Abdel-Razik Sebak for his support, guidance and encouragement. His vast experience and deep understanding of the subject proved to be immense help to me, and also his profound viewpoints and extraordinary motivation enlightened me in many ways.

A special acknowledgement goes to Professor Tayeb Denidni and Mr Mahmoud Niroo Jazi at institute national de la recherche scientifique (INRS) for their help in radiation patterns measurements.

I am also grateful to Mr Jules Gauthier, Mr Steve Dubé and Mr Traian Antonescu, in Poly-Grames Research Center at École Polytechnique de Montréal for all of their fabrication and technical assistance throughout my graduate program.

Many thanks are given to Dr Sadegh Farzaneh for the valuable technical and scientific discussions, feasible advices and various kinds of help.

I also would like to acknowledge the Egyptian Ministry of Higher Education and the Department of Electrical Engineering, Faculty of Engineering, Assiut University, in Egypt for their financial support.

Finally, I cannot finish without mentioning my parents and my wife, who have been offering all round support during the period of my study.

Table of Contents

List of Figures

List of Tables

List of Symbols

[A]	Square matrix
b	Electric facet flux vector
$\vec{B}$	Magnetic flux density [Wb/m^2]
[B]	Square matrix
BW	Bandwidth
BW_{notch}	Notch bandwidth
c	The speed of electromagnetic waves in vacuum (299792458 m/s) or the value of the source or excitation defined for the problem
$[C]$	Square matrix represents the discrete curl operator
$[\tilde{C}]$	Square matrix represents the discrete divergence operator
C_n	Number of crossovers in $N \times N$ Butler matrix, $C_n = 2C_{n-1} + 2^{n-2}(2^{n-2} - 1),\ C_1 = 1$
d	Magnetic facet flux vector or Length of the feed gap
dB	Decibels
$\vec{D}$	Electric flux density [C/m^2]
e	Electric grid voltage
$\vec{E}$	Electric field intensity [V/m]
f	Frequency
f_1	First or fundamental mode of the disc monopole antenna

$f_2, f_3, \ldots f_N$	Higher order modes or harmonics of the disc monopole antenna
f_c	Center frequency
f_L	Lowest resonance or lower edge frequency
f_{notch}	Notch center frequency
f_U	Upper resonance or upper edge frequency
GHz	Gigahertz, 10^9 hertz
h	Magnetic grid voltage
$\vec{H}$	Magnetic field intensity [A/m]
H_n	Number of hybrid couplers in $N \times N$ Butler matrix, $H_n = Nn/2$
k_o	Wave number in free space
L_G	Length of the finite ground plane
L	Length of the substrate
n	Order of the matrix $N = 2^n$
N	Number of antennas
p	Antenna perimeter
P_n	Number of phase shifters in $N \times N$ Butler matrix, $P_n = N(n-1)/2$
RL	Return loss positive valued for passive loads (–20 log|S11|)
R_{slot}	Radius of the circular slot
S_{11}	Reflection coefficient, expressed as an S parameter
S_{21} (=S_{12})	Transmission coefficient, expressed as an S parameter
S_{31} (=S_{31})	Transmission coefficient, expressed as an S parameter
S_{32} (=S_{23})	Isolation between port # 2 and port #3, expressed as an S parameter
$tan\delta$	Loss tangent

W_{feed}	Width of the feedline
W	Width of the substrate
x	The electric field vector
λ	Wavelength
λ_o	Wavelength in free space
ε_o	Permittivity of free space, 8.854 x 10^{-12} [F/m]
ε_r	Relative permittivity of the medium
ε	Permittivity of the medium ($\varepsilon_r\ \varepsilon_o$)
ε_{eff}	Effective permittivity of the medium
μ	Permeability of the medium
μ_o	Permeability of free space, 4π x 10^{-7} [H/m]
Φ_E	Electric scalar flux [C]
Φ_B	Magnetic scalar flux [Wb]
Δt	Maximum time step
η_o	Intrinsic impedance for free space
η	Intrinsic impedance of the medium
φ	Linear phase progression,$\varphi = (2m-1)\frac{\pi}{N}, m$ integer, $m \in [1 - N/2, N/2]$
σ	Conductivity
Ω	Ohms
θ	Elevation angle
θ_o	Steered main-beam direction, $\theta_o = sin^{-1}(\lambda\varphi/2\pi d)$
ϕ	Azimuth angle

List of Abbreviations

2D	Two-Dimensional
3D	Three-Dimensional
3G	Third-Generation
ABW	Absolute Bandwidth
BFN	Beamforming Network
BW	Bandwidth
CAD	Computer-Aided Design
CB-CPW	Conductor Backed-Coplanar Waveguide
CDMA	Code Division Multiple Access
CF	Center Frequency
CPW	Coplanar Waveguide
CST MWS	Computer Simulation Technology Microwave Studio
DGS	Defected ground structure
DR	Dielectric Resonator
DRA	Dielectric Resonator Antenna
EBG	Electromagnetic Bandgap
EIRP	Effective Isotropic Radiated Power
EM	Electromagnetic
FBW	Fractional Bandwidth
FCC	Federal Communication Commission

FDMA	Frequency Division Multiple Access
FDTD	Finite Difference Time Domain
FE	Finite Element
FIT	Finite Integration Technique
Gbps	Gega bits per seconds
HFSS	High Frequency Structure Simulator
IEEE	Institute of Electrical and Electronics Engineers
IC	Integrated Circuits
IE	Integral Equation
ISM	Industrial, Scientific, and Medical
LTCC	Low-Temperature Co-fired Ceramic
MBA	Multi-Beam Antennas
Mbps	Mega bits per seconds
M-BFN	Multiple-Beamforming Network
MEA	Multi-Element Antenna
MGE	Maxwell Grid Equations
MMW	Millimeter Wave
NB	Narrowband
PCB	Printed Circuit Board
PNA	Programmable Network Analyzer
PSD	Power Spectral Density
RL	Return loss
SBA	Switched-Beam Antenna

SDMA	Space Division Multiple Access
SICC	Substrate Integrated Circular Cavities
SIR	Signal-to-Interference Ratio
SLL	Sidelobe Level
SM	Spatial Multiplexing
SNR	Signal-to-Noise Ratio
TDMA	Time Division Multiple Access
TEM	Transverse Electromagnetic
TSA	Tapered Slot Antenna
UWB	Ultra-Wideband
VSWR	Voltage Standing Wave Ratio
Wi-Fi	Wireless Fidelity
WiMAX	Worldwide interoperability for Microwave Access
WLAN	Wireless Local Area Networks
WMAN	Wireless Metropolitan Area Networks
WPAN	Wireless Personal Area Network

Chapter 1

Introduction

1.1 Motivation for Use of UWB Technology

Currently, there is an increased interest in Ultra-wideband (UWB) technology for use in several present and future applications. UWB technology received a major boost especially in 2002 since the US Federal Communication Commission (FCC) permitted the authorization of using the unlicensed frequency band starting from 3.1 to 10.6 GHz for commercial communication applications [1]. Although existing third-generation (3G) communication technology can provide us with many wide services such as fast internet access, video telephony, enhanced video/music download as well as digital voice services, UWB –as a new technology– is very promising for many reasons. The FCC allocated an absolute bandwidth up to 7.5 GHz which is about 110% fractional bandwidth of the center frequency. This large bandwidth spectrum is available for high data rate communications as well as radar and safety applications to operate in. The UWB technology has another advantage from the power consumption point of view. Due to spreading the energy of the UWB signals over a large frequency band, the maximum power available to the antenna –as part of UWB system– will be as small as in order of 0.5mW according to the FCC spectral mask shown in Figure 1.1. This power is considered to be a small value and it is actually very close to the noise floor compared to what is currently used in different radio communication systems [2].

Figure 1.2 shows the comparison between conventional narrowband (NB) versus UWB communications in both time- and frequency-domains. The conventional NB radio systems use NB signals which are sinusoidal waveforms with a very narrow frequency spectrum in both transmission and reception. Unlike a NB system, an Ultra-wideband radio system can transmit and receive very short duration pulses. These pulses are considered UWB signals because they have a very narrow time duration with very large instantaneous bandwidth starting from 500 MHz up to 7.5 GHz [2]-[3]. According to the definition in [4], one important feature of a radar and communications transmitter is called the effective isotropic radiated power (EIRP) which can be defined as the product of its gain and input power. Figure 1.3 shows the FCC spectral mask of the indoor UWB EIRP emission level. It can be seen that the maximum signal power is limited to −41.3 dBm per MHz throughout the whole UWB frequency range from 3.1 to 10.6 GHz. All the UWB systems and devices must work within this spectral mask for legal operation in order to comply with the FCC standards and regulations.

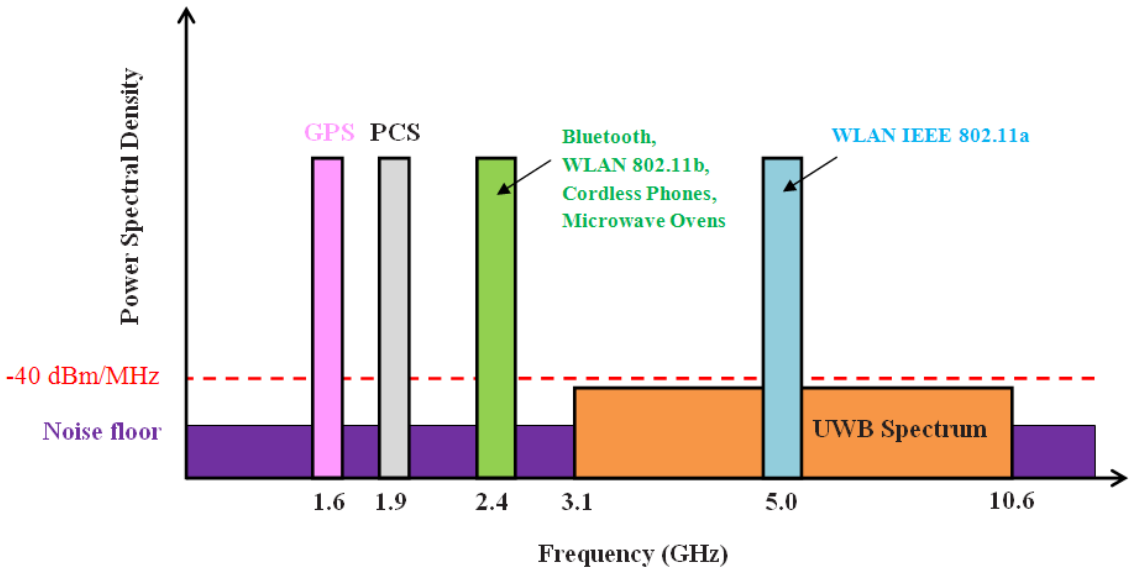

Figure 1.1 UWB versus other radio communication systems (reproduced from [5]).

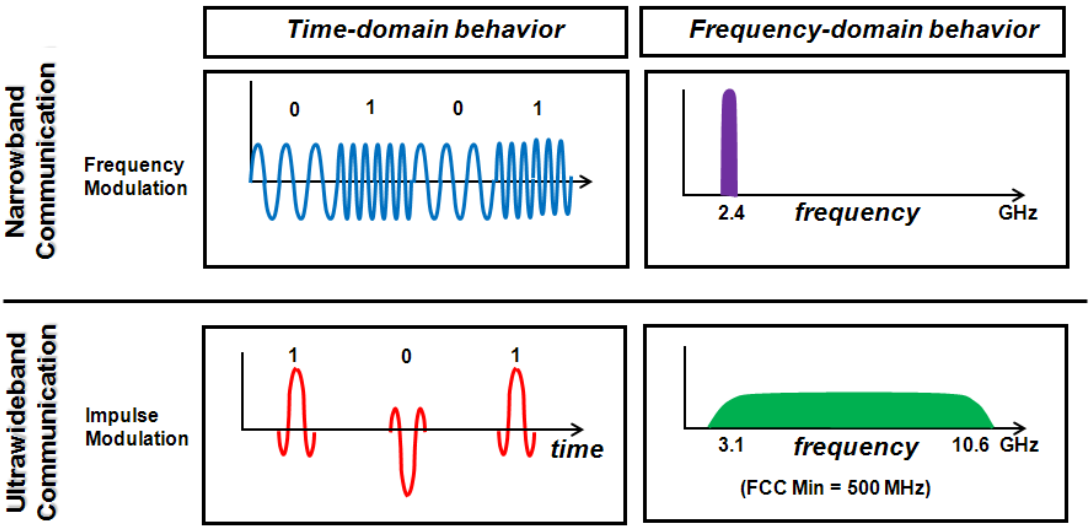

Figure 1.2 Time- and frequency-domain behaviors for conventional narrowband versus UWB communications (reproduced from [5]).

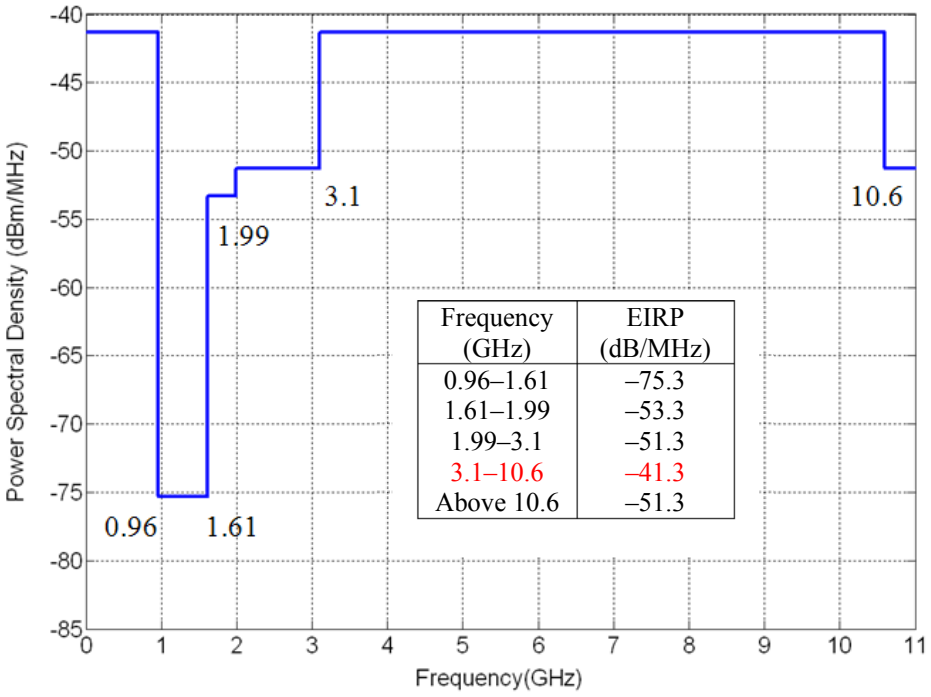

Figure 1.3 FCC spectral mask for indoor UWB systems (reproduced from [1]).

The huge bandwidth for UWB systems −compared to other conventional NB systems− can show a number of important advantages. There is an increasing demand for high speed and high data rate applications in communication systems [6]. One of those advantages is the ability of UWB system to achieve high data rates in future wireless communications which requires increasing the bandwidth of the communication system. Another advantage of UWB systems is the ability to effectively reduce fading and interference problems in different wireless propagation channel environments because of the limited transmitted power of UWB systems [7]. This is in addition to exploiting multipath or frequency diversity because of the huge bandwidth of UWB systems [8]. The signal-to-noise ratio (SNR) of the UWB system can be increased using some techniques such as antenna diversity and beamforming which in turn will provide range extension and boost the capacity of worldwide interoperability for microwave access (WiMAX) for wireless metropolitan area networks (WMAN), and wireless fidelity (Wi-Fi) for wireless local area networks (WLAN) [9].

In radar/sensor and imaging applications, when a signal is transmitted through a wireless propagation channel, both amplitude and phase of the signal will be varied instantaneously with time. These different signal multipath components may be added together constructively or destructively depending on their phase relationships. If these signal multipath components are in phase, they will be added together constructively but if they are out-of-phase, they will be added together destructively. This phenomenon is called multipath fading and is caused by interference that occurs due to reflections, diffractions or scattering from the various objects in the wireless propagation channel and it may affect the overall communication quality between transmitter and receiver [10]-[12].

The solution of this severe fading problem is achieved by using smart antenna systems which are good candidates to maximize the received signal, enhance the SNR, increase the communication range, boost the channel capacity, improve communication quality, overcome the severe multipath fading problems and hence improve the overall UWB system performance [13].

Smart antennas or multi-beam antennas (MBA) are considered very important and key elements in present and future wireless communication systems [14], [15]. These antenna systems can be generally classified into two main categories based on transmit strategy: smart adaptive antenna arrays and switched-beam antenna (SBA) systems [16]. Smart adaptive arrays are able to process signals by changing their weights adaptively according to a certain algorithm in order to direct the main beam towards the desired direction and/or to create pattern nulls in directions of undesired signals or interference. The advantage of this smart adaptive antenna array system is the remarkable increase in the signal-to-interference ratio (SIR) of the whole system and hence improves the overall performance of the system [17]. However, these antenna array systems are very complex in their physical structure and hence they are expensive to implement.

On the other hand, switched-beam antenna (SBA) systems which generate multiple fixed beams consist of antenna array elements connected to a multiple beamforming networks (M-BFN). The $N \times M$ beamforming network (BFN) has N fixed input or beam ports and M outputs connected to antenna array elements [18]. Because SBAs system is less complex in physical structure compared to the adaptive array system and hence inexpensive to implement, fabricate and test, it is considered to be more preferable by both academia and industry. There are many different M-BFN matrices have been proposed

such as the Blass matrix [19], [20], Nolen matrix [21], [22], Rotman lens [23], [24] and Butler matrix [25]-[27]. The Butler matrix is considered to be one of the most popular and widely-known networks among different switched beam networks.

1.2 Challenges of UWB Technology

UWB systems have shown a number of important advantages with great potential. To make UWB technology effective, there are several challenges to address. One of these challenges is the design of good and suitable UWB antenna as an important part of any UWB system. The antenna to be used for UWB applications must be operated over the entire 3.1-10.6 GHz FCC frequency spectrum and it must be capable of achieving high a matching impedance bandwidth of 7.5 GHz. Besides that, the behavior of both group delay and phase versus frequency is another consideration that must be taken into account when we design the antenna. This is a very important characteristic of any UWB antenna because it measures the distortion and ringing of the signal in the time domain. An UWB antenna must have also a stable radiation pattern across the whole UWB frequency range as well as an omni-directional radiation pattern to be suitable for short-range indoor wireless communication applications and mobile/portable devices [28]. The efficiency requirements such as high efficiency, stable gain design as well as the physical constrains such as a physically small, planar design to be applicable for recent mobile and portable devices are also very important [29].

Antenna array technologies are considered to be very attractive for different personal communication applications. Recently, there has been a great interest in the application of antenna arrays in wireless communications because of the increasing demand

for high speed and high data rates for wireless communications. Antenna array allows using the available spatial domain efficiently by using a multi-element antenna (MEA) array such as in space division multiple access (SDMA), besides other conventional domains such as frequency, time, and code in frequency division multiple access (FDMA), time division multiple access (TDMA), and code division multiple access (CDMA) respectively. This will increase the number of degrees of freedom and then it will improve the overall system performance. The significant improvement in data transmission reliability where the bit error rate is very low is also another advantage of using MEA technology [12], [16].

Combining both MEA and UWB technologies together with all their advantages will be an exciting application in very high data rate communications. It has been shown that the beamforming technique among these different techniques can achieve interference mitigation, SNR enhancement and range extension [30].

1.3 Objectives

The overall objective of this thesis is to design a small size and low cost suitable antenna for UWB short-range communications applications integrated with a compact and inexpensive BFN to form a beamforming antenna array system for UWB applications. There are many challenges in dealing with the new emerging technologies like UWB technology. One of these challenges is how to design an antenna element that can operate effectively in the entire UWB frequency range. In this thesis, different UWB antenna designs are investigated in order to understand their operation mechanism that leads

to the UWB characteristics. Another challenge related to the design of UWB beamforming antenna array system is the design of suitable components such as feed networks, transitions, hybrid couplers and phase shifters to meet the UWB requirements.

The design objectives for the UWB antennas and associated compact and inexpensive BFN for UWB communications applications are:

- Design, build and test different UWB antenna elements with band-rejection capabilities to avoid interference with other existing WLAN systems with good performance for UWB communications applications.
- Design, build and test UWB feed networks circuits with good performance for antenna array applications and use them to construct UWB antenna arrays by connecting the developed UWB antenna elements with the designed UWB feed network.
- Design, build and test different UWB components such as vertical transitions and hybrid couplers and phase shifters with UWB frequency bandwidth for multi-layer microwave circuits.
- Design, build and test compact and inexpensive UWB Butler matrices as BFN.

1.4 Organization of the Thesis

This thesis is organized in seven chapters as follows: Chapter 2 covers the background introduction to UWB technology with discussing the advantages, applications and standards of the UWB technology in Section 2.2. It also presents the literature review for different UWB antenna designs and the techniques used for obtaining bandstop function in Section 2.3. In addition, Section 2.4 introduces a survey on different UWB linear an-

tenna arrays designs. This is followed by a survey on UWB feed network designs and other associated microwave components in Section 2.5. Then, Section 2.6 gives the background information about different beamforming techniques for UWB applications with addressing the Butler matrix architecture. Finally, the chapter conclusions are outlined in Section 2.7.

In Chapter 3, the theoretical background and analysis are discussed. Section 3.2 presents the numerical and analytical techniques used in the analysis of all structures in this thesis. Electromagnetic (EM) numerical modeling techniques of both Ansoft High Frequency Structure Simulator (HFSS) and Computer Simulation Technology Microwave Studio (CST MWS) simulation programs used in designing these components and circuits are introduced. It is followed by discussing the design methodology and the operation principle of UWB antennas based on the investigation of their performance and characteristics in Section 3.3. Finally, the chapter is summarized in Section 3.4.

In Chapter 4, different designs for UWB planar printed circuit board (PCB) disc monopole and hybrid antennas are studied. Section 4.2 discusses the novel design for a printed circular disc monopole antenna with two steps and a circular slot and demonstrating some parametric studies to address the effect of different antenna parameters on its performance. This is followed by introducing the Ansoft HFSS and CST simulation results as well as the measured results for the fabricated antenna prototype. Then the band-notched antenna with bandstop function in 5.0-6.0 GHz frequency band is designed based on the parametric studies carried out on bandstop filter element parameters. Smaller size

maple-leaf shaped monopole antennas with two different designs for band rejection are proposed in Section 4.3. Other shapes for planar PCB disc monopole antennas are proposed in Section 4.4. In those different designs, we are trying to reduce the antenna overall dimensions to come up with the best antenna candidate for mobile and portable UWB applications or even decrease the metallic area to enhance the antenna efficiency and the gain as well. One design uses a radiating element in the shape of a butterfly while the other design uses a trapezoidal shape with a bell-shaped cut. Section 4.5 presents the compact hybrid printed monopole antenna loaded with a dielectric resonator (DR). This hybrid combination of both printed monopole and DR provides us with a very compact antenna design which is very suitable for UWB indoor communication applications. Finally, the chapter conclusions are given in Section 4.6.

In Chapter 5, a compact design for UWB feeding network, and associated microwave components such as transitions, hybrid couplers and phase shifters are demonstrated. Simulated as well as the measured results for some designed prototypes are discussed. Section 5.2 presents a compact UWB feeding network prototype based on modifying the conventional Wilkinson power divider. The designed UWB feed network is then integrated with the previously designed UWB antenna in Chapter 4 to construct two- and four-element linear antenna arrays as in Section 5.3. The performance of antenna arrays are analyzed. It is followed by the design of two different vertical transition prototypes using multi-layer microstrip PCB technology for UWB applications as in Section 5.4. One design uses butterfly-shaped patches while the other uses trapezoidal patches. Then we developed two different 90° hybrid couplers by extending the 2-port transitions to 4-port

hybrid couplers in Section 5.5. Section 5.6 demonstrates the design of two 45° phase shifters based on exploiting the broadband coupling feature of the designed transitions. A conventional microstrip transmission line is used as a reference line with the designed trapezoidal and butterfly transitions to come up with constant phase with frequency. Finally, the chapter conclusions are summarized in Section 5.7.

In Chapter 6, two different configurations for UWB 4 × 4 Butler matrices using two-layer microstrip PCB technology are designed, optimized, fabricated and measured. The simulated as well as the measured results are presented with detailed discussion and explanation is provided. Finally, Section 6.3 summarizes the chapter conclusions.

Chapter 7 presents the conclusion and contributions for the carried out research followed by suggestions for future work.

In Appendix A, we provided a detailed analysis for the modified UWB Wilkinson power dividers.

In Appendix B, a detailed analysis for two-layer microstrip-to-microstrip vertical transition as a four-port network is discussed.

Chapter 2

Background and Literature Review

2.1 Introduction

According to the Institute of Electrical and Electronics Engineers (IEEE) standard [31], the bandwidth of an antenna is defined as the frequency band within which the antenna performance and characteristics agree well with a specific standard. For Ultra-wideband (UWB) antenna design, there are two different definitions for antenna bandwidth, i.e. impedance bandwidth and radiation bandwidth. Impedance bandwidth can be defined as the frequency range where the antenna reflection coefficient (S11) or return loss (RL = –20 log|S11|) is better than 10 dB or the antenna voltage standing wave ratio (VSWR) is less than 2.0:1. The radiation bandwidth of an antenna is defined as the frequency range where the antenna radiation patterns are relatively stable at all frequencies.

The frequency bandwidth of an antenna can be expressed in terms of either the absolute bandwidth (ABW) or the fractional bandwidth (FBW). Assuming that the antenna bandwidth has a lower edge frequency of f_L, an upper edge frequency of f_U and a center frequency of f_c. The ABW is defined as the difference between the upper and the lower edge frequencies of operation while the FBW can be defined as the percentage of the ratio between the absolute bandwidth and the center frequency as given in Eq. (2.1) and Eq. (2.2), respectively:

$$\text{ABW} = (f_U - f_L) \tag{2.1}$$

$$\text{FBW} = \frac{ABW}{f_c} = \frac{(f_U - f_L)}{f_c} \times 100\% \tag{2.2}$$

where the center frequency $f_c = \frac{(f_U + f_L)}{2}$.

Another definition for the bandwidth in case of broadband antennas which is the ratio of the upper edge frequency f_U to the lower edge frequency f_L, as given in Eq. (2.3):

$$\text{BW} = \frac{f_U}{f_L} \tag{2.3}$$

In this chapter, the literature review and background information related to the design of antennas and other associated microwave components for UWB communication applications are provided. This chapter is organized as follows; Section 2.2 presents a brief introduction to the definition, standards and main advantages of ultra-wideband technology as well as its potential applications. A survey for different UWB antenna designs is investigated and presented in Section 2.3. Then, Section 2.4 introduces the background information about UWB linear antenna array and its advantages. Then, the survey for UWB feed networks and other associated microwave components such as vertical transitions, hybrid couplers and phase shifters are introduced in Section 2.5. Section 2.6 gives background information about different beamforming techniques antenna array systems followed by conclusions in Section 2.7.

2.2 Ultra-wideband (UWB) Technology

UWB technology is considered to be attractive by many researchers, scientists and engineers and a promising technology for high-speed, high data rates and short-range indoor wireless communications. This is especially true when the US FCC permitted using the frequency band from 3.1 to 10.6 GHz for UWB radio applications in 2002 [1].

Currently, there is a great interest in UWB system design and implementation in both academic research and industry areas. The concept of UWB radio was first developed several decades ago exactly in the late 1960's. The U.S. Department of Defense first founded the term 'ultra wideband' in 1989 [32]. In the beginning, UWB was mainly for military purposes such as radar applications which use wideband signals in frequency domain or very short duration pulses in the time domain to get fast, reliable and accurate information about moving targets such as missiles. Recently, the FCC defined UWB as a signal with a minimum absolute bandwidth of 500 MHz where the fractional bandwidth is about 20% of the center frequency [1]. UWB systems use a very short duration pulse to transmit data over a large absolute bandwidth of up to 7.5 GHz. The FCC allowed in 2002 using the unlicensed frequency band of 3.1-10.6 GHz with a limited transmitted power of –41.3 dBm/MHz for use in commercial wireless applications. Recently, it has shown to be of increasingly great research interest especially in the field of personal and commercial wireless communications.

There are many potential applications for the UWB new emerging technology that can be used in recent personal and commercial communication systems, vehicular radar systems, and imaging systems such as ground-penetrating radar, wall-imaging systems, medical systems, and surveillance systems. UWB systems have shown a number of noticeable features compared to other existing conventional NB systems. One of those features is less complexity of UWB systems compared to conventional NB systems. Another feature is their low cost which becomes very attractive for commercial communications applications. Because the available power level for UWB systems is very low for FCC legal operation, this enables them to work very close to the noise floor level and hence to

have a noise-like signal spectrum which makes them good at mitigating severe multipath fading environments, strong interference and jamming. Some radar applications such as positioning, geo-location, localization and tracking objects require excellent time-domain resolution and high accuracy which can be achieved by using UWB systems rather than conventional NB systems [33]. For Wireless Personal Area Networks (WPANs) environments, UWB technology is an excellent solution for the ultra high-speed data services up to 500 Mega bit per second (Mbps). These speeds can be greatly increased by using antenna arrays instead of single antenna element and different beamforming techniques.

2.3 UWB Antenna Design

UWB antennas, key components of the UWB system, have received attention and significant research in recent years [34]-[49]. With the increasing popularity of UWB systems, there have been breakthroughs in the design of UWB antennas. Implementation of a UWB system is facing many challenges and one of these challenges is to develop an appropriate antenna. This is because the antenna is an important part of the UWB system and it affects the overall performance of the system. Currently, there are many antenna designs that can achieve broad bandwidth to be used in UWB systems such as the Vivaldi antenna, bi-conical antenna, log periodic antenna and spiral antenna as shown in Figure 2.1. A Vivaldi antenna [34]-[38] is one of the candidate antennas for UWB operation. It has a directional radiation pattern and hence it is not suitable for either indoor wireless communication or mobile/portable devices which need omni-directional radiation patterns to enable easy and efficient communication between transmitters and receivers in all directions. Mono-conical and bi-conical antennas [39]-[41] have bulky structures with

large physical dimensions which limit their applications. Also, log periodic [40], [42] and spiral antennas [43]-[46] are two different UWB antennas that can operate in the 3.1-10.6 GHz frequency band but are not recommended for indoor wireless communication applications or mobile/portable devices. This is because they have large physical dimensions as well as dispersive characteristics with frequency and severe ringing effect [42]. This is why we are looking for another candidate for UWB indoor wireless communications and mobile/portable devices that can overcome all these shortcomings. This candidate is the planar or printed monopole antenna [47]-[69]. Planar monopole antennas [47]-[55] with different shapes of polygonal (rectangular, trapezoidal... etc), circular, elliptical…etc have been proposed for UWB applications as shown in Figure 2.2.

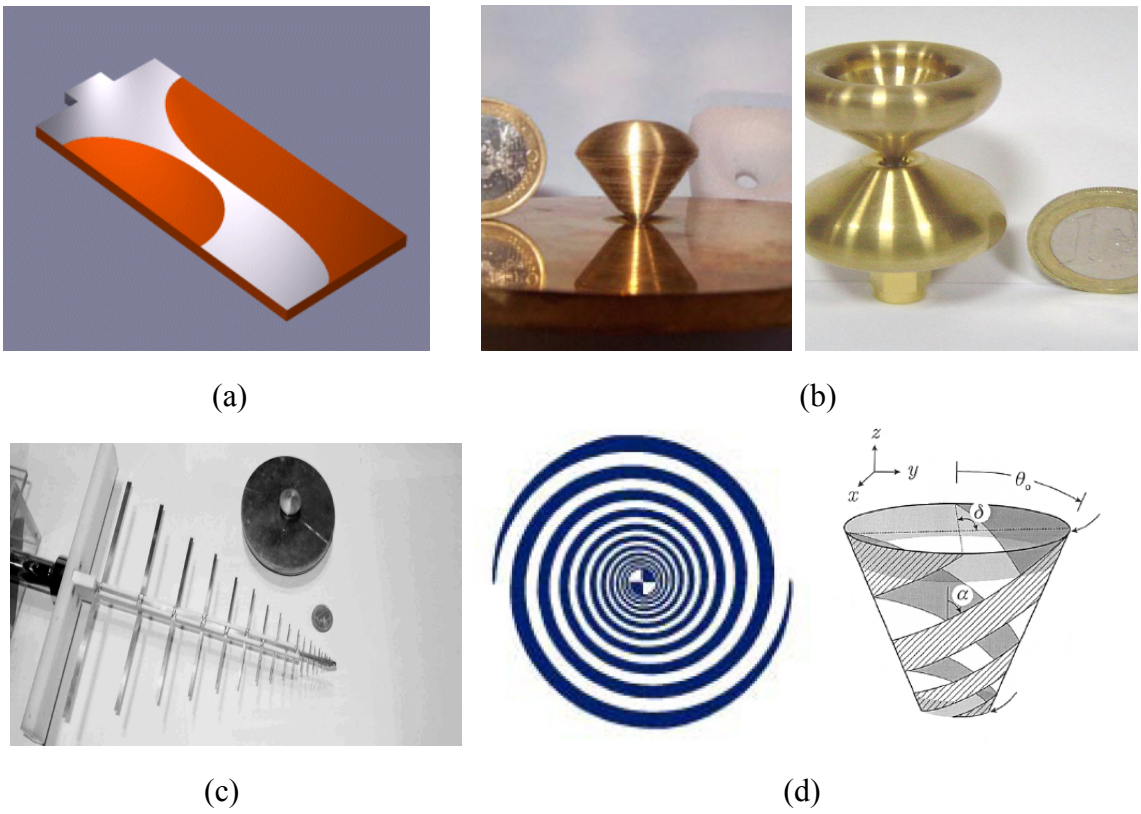

Figure 2.1 (a) Vivaldi antenna [35] (b) Mono-conical and bi-conical antenna [40] (c) Log-periodic antenna [40] and (d) Spiral and conical spiral antenna [45]

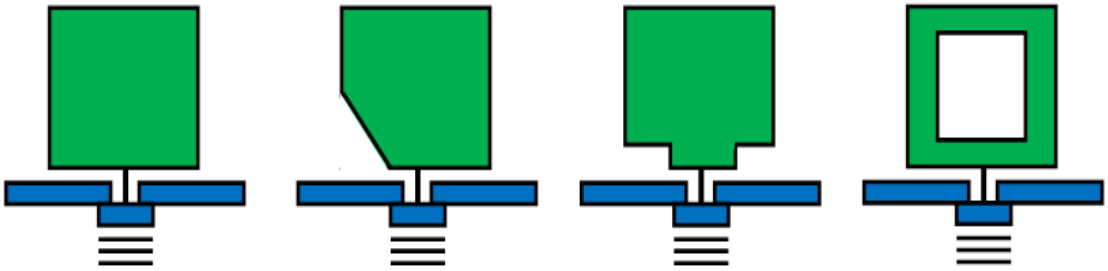

(a) Rectangular [47]-[50]

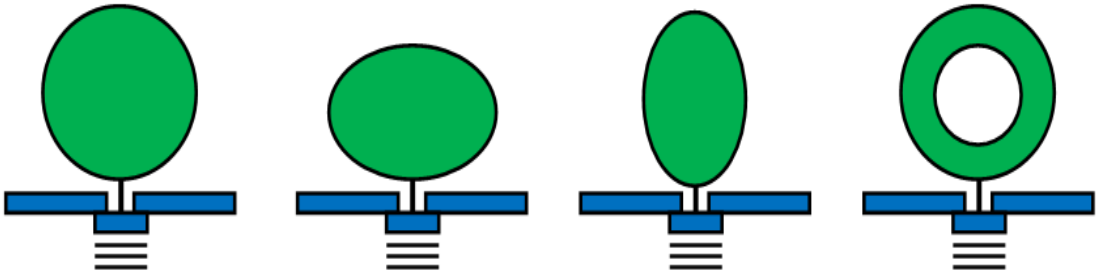

(b) Circular and elliptical [51]-[52]

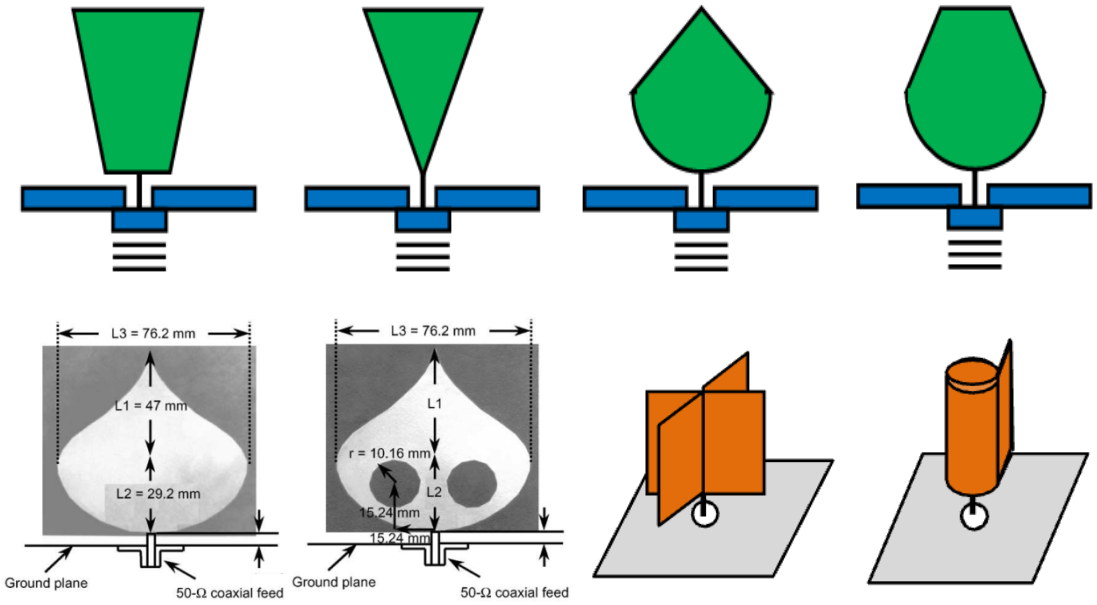

(c) Other shapes [53]-[55]

Figure 2.2 Modified shape planar antennas for UWB applications.

Due to their wide frequency impedance bandwidth, simple structure, easy fabrication on printed circuit boards (PCBs), and omni-directional radiation patterns, printed PCB versions of planar monopole antennas are considered to be promising candidates for applications in UWB communications. Recent UWB antenna designs focus on small printed antennas because of their ease of fabrication and their ability to be integrated with other components on the same PCBs [56]-[69]. Figure 2.3 illustrates several realizations of planar PCB or printed antenna deigns.

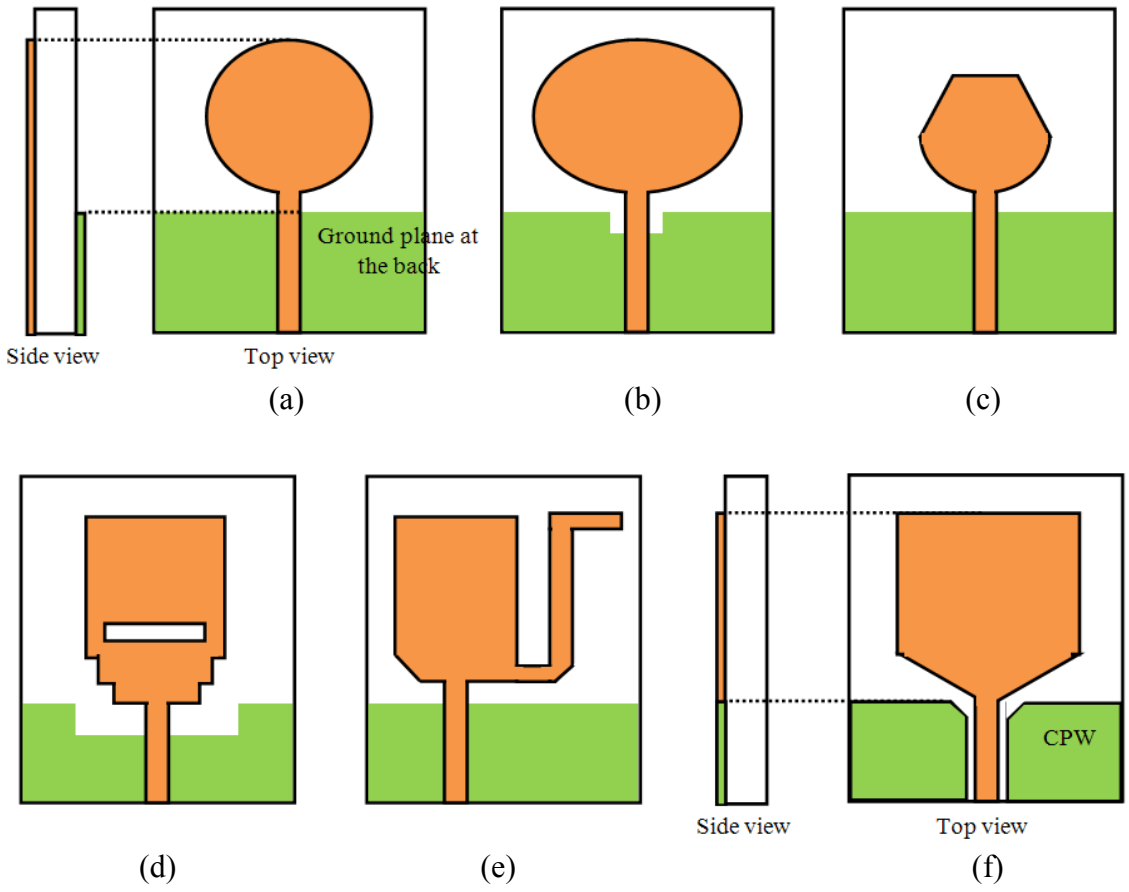

Figure 2.3 Planar PCB or printed antenna designs [64]-[69].

However, there are several existing NB communication systems operating below 10.6 GHz in the same UWB frequency band and may cause interference with the UWB systems such as IEEE 802.11a WLAN system or HIPERLAN/2 wireless system. These systems operate at 5.15–5.825 GHz which may cause interference with a UWB system. To avoid the interference with the existing wireless systems, a filter with bandstop characteristics may be integrated with UWB antennas to achieve a notch function at the interfering frequency band [70]-[81]. Figure 2.4 shows several developed bandstop antenna designs.

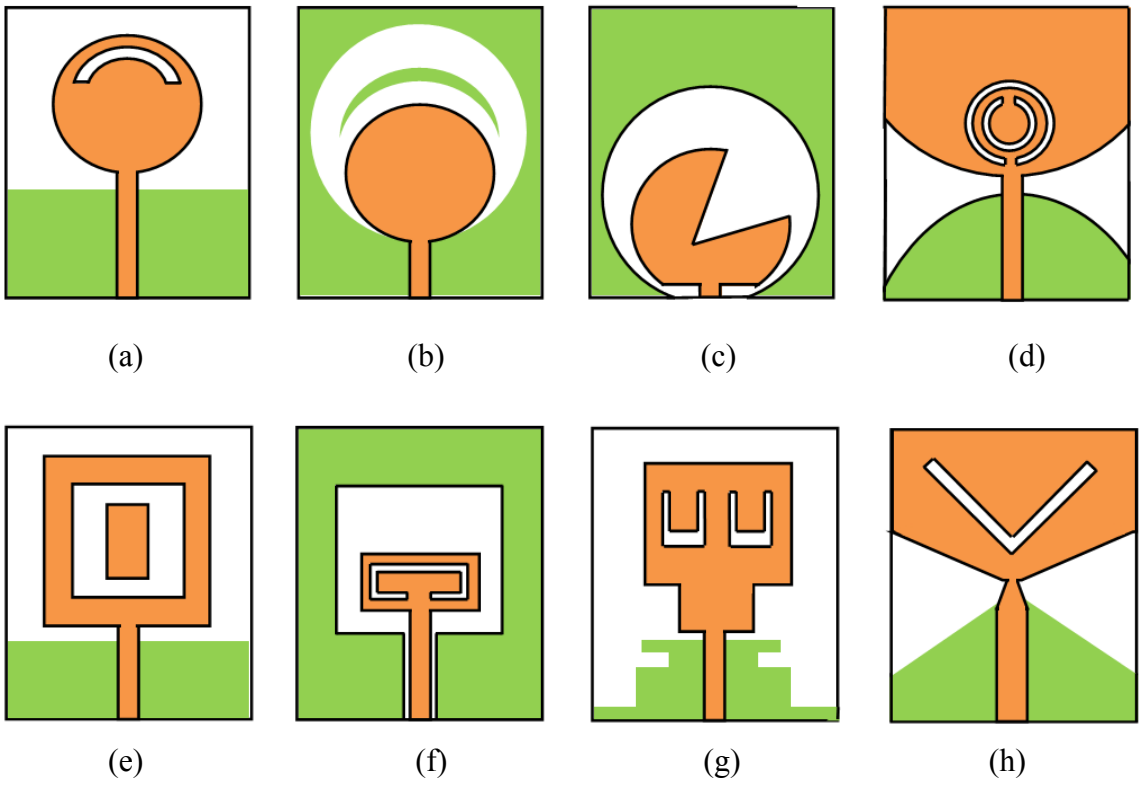

Figure 2.4 Printed antenna designs with single bandstop functions [70]-[78].

2.4 UWB Linear Antenna Arrays

A high gain antenna system is needed especially in certain applications such as microwave imaging, localization and/or radar applications. A UWB single antenna element has relatively low gain of order of 3 or 4 dBi across the frequency band of operation. This can be improved using antenna arrays instead of just a single element. One important and critical problem in designing an antenna array system is the grating lobes. They appear when the inter-element spacing among antenna elements exceeds approximately the wavelength at the operating frequency. In order to avoid grating lobes at higher frequencies, this space should be kept smaller than a half wavelength at upper UWB frequency f = 10.6 GHz. Actually, there are a few designs for antenna array for UWB applications [82]-[87]. In [82], only two-element antenna array as shown in Figure 2.5 is introduced with maximum achieved impedance bandwidth of about 83% (3.1-7.5 GHz). Both two-element and four-element antenna arrays, as illustrated in Figure 2.6, have been presented in [83]. The achieved total directive gain for the proposed two-element and four-element arrays in the UWB frequency band are 3.6-8.5 dBi (+4.9 dBi gain variation) and 6.5-10.5 dBi (+4.0 dBi gain variation), respectively. Some other UWB antennas arrays have been introduced such as leaf-shaped bowtie [84], [85] and tapered-slot-fed antenna arrays [86]. For the two- and four-element UWB leaf-shaped bowtie antenna arrays as shown in Figure 2.7, the radiation pattern is unidirectional which is not suitable for communications applications. The four-element UWB tapered-slot-fed antenna arrays as shown in Figure 2.8, is large and not planar with directional radiation patterns.

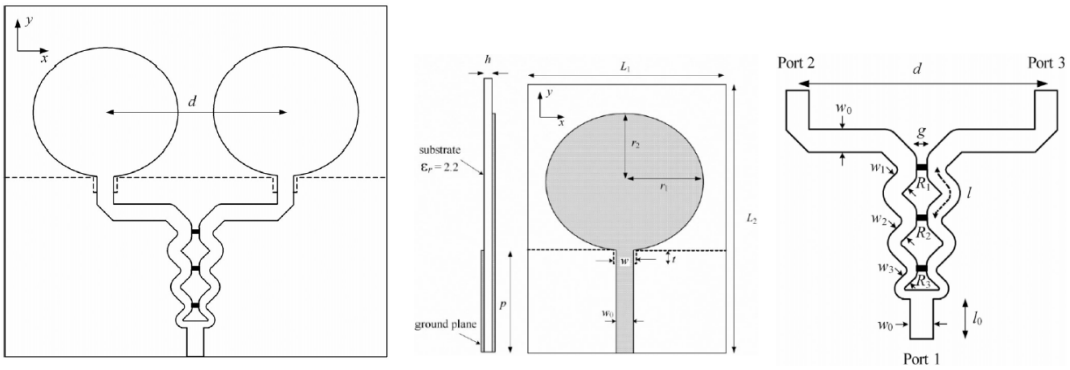

Figure 2.5 Two-element UWB antenna array [82].

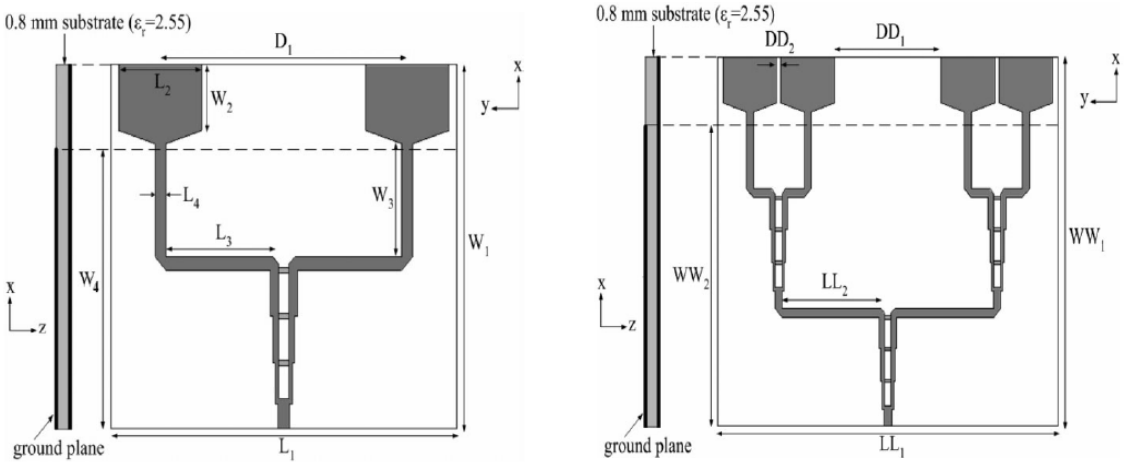

Figure 2.6 Two- and four-element UWB antenna arrays [83].

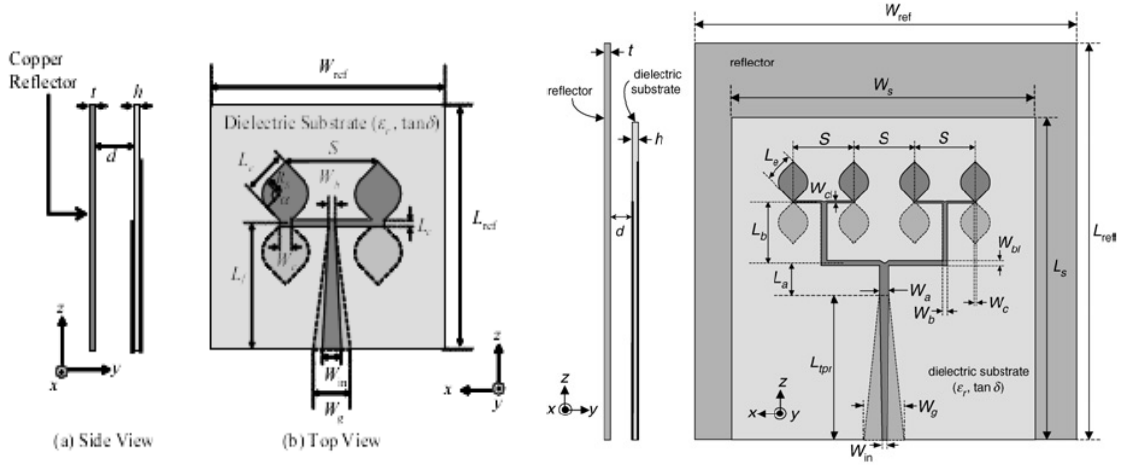

Figure 2.7 Two- and four-element UWB leaf-shaped bowtie antenna arrays [84], [85].

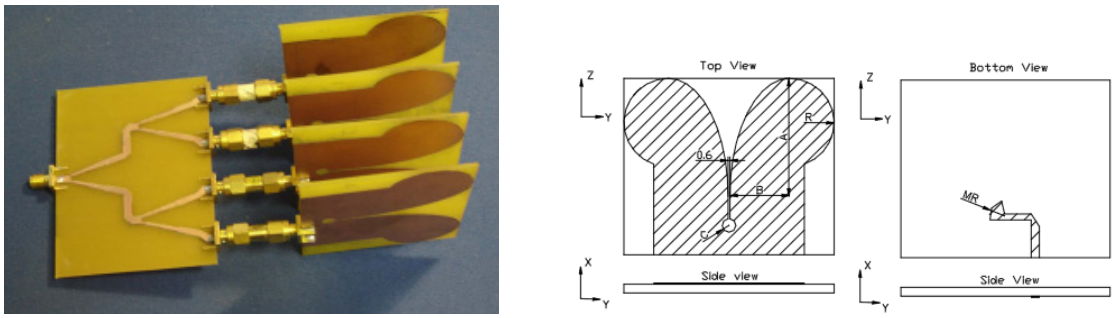

Figure 2.8 Four-element UWB tapered-slot-fed antenna array [86].

2.5 UWB Feed Networks and Associated Components

There are many different types of feed networks or power dividers/combiners that can be used in different applications. The T-junction power divider/combiner is considered to be the most popular and simplest three-port network as shown in Figure 2.9 [88]. The T-junction can be used as a 2:1 power divider if we feed it from input port # 1 to divide the power equally into two halves between output ports 2 and 3. It can be also used as a power combiner if we feed it from two input ports 2 and 3 to combine the power to output port # 1. The type and the application of the power divider can be determined according to the phase difference between the two output ports. The power divider can be in-phase, quadrature-phase or out-of-phase if the phase difference between the output ports is 0°, 90° or 180°, respectively.

Wilkinson power dividers are the most popular and widely used in various microwave circuits because of the ease and simplicity in the design, realization, implementation and testing [88]. Wilkinson power dividers have shown many advantages such as well-matched output ports with high isolation between them because of the use of an isolation resistor. Also, they are considered to be in-phase power dividers because the two

output ports have the same phase. Basically, Wilkinson power dividers are for narrow-band applications and therefore cannot be used for broadband or wideband applications such as ultra-wideband. This is why several proposed designs have been introduced to increase the operating bandwidth of the conventional Wilkinson power divider or even to reduce its size for certain applications as shown in Figure 2.10(a, b, c & d) [89]-[93]. It has been found that bandwidth enhancement can be achieved by increasing the number of divider sections, i.e. three-section Wilkinson power divider [89], [90], or by modifying the original Wilkinson divider by adding open-circuited stub matching networks which increase the operating bandwidth [91]. Another technique to obtain a broadband design is implemented by using multi-layered microstrip PCB technology to achieve a broadband in-phase power divider as shown in Figure 2.10(e) [94].

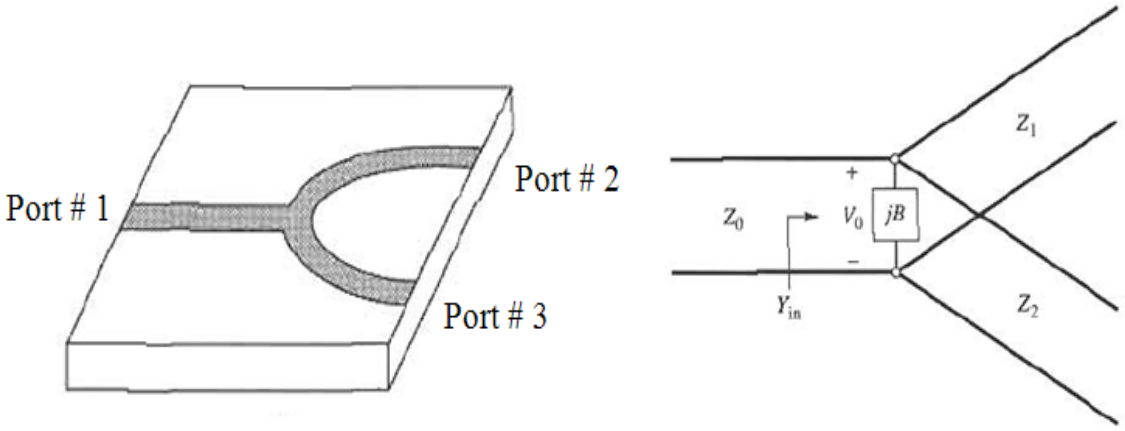

(a) (b)

Figure 2.9 (a) Microstrip T-junction [88] and (b) Transmission line model of lossless T-junction [88].

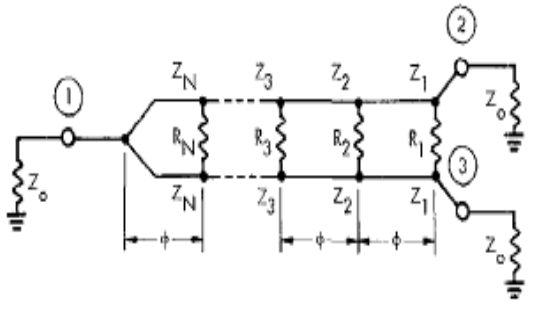

(a)

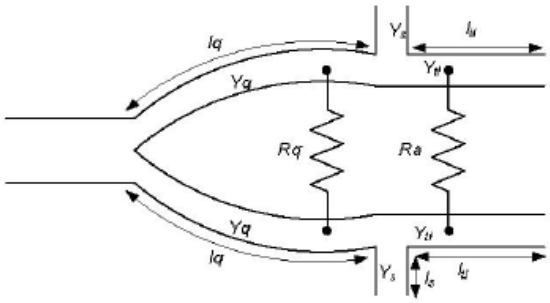

(b)

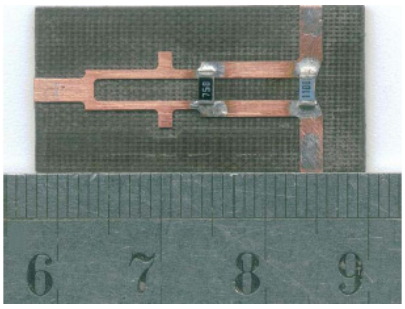

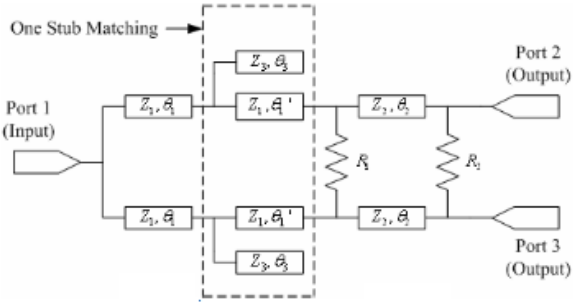

(c)

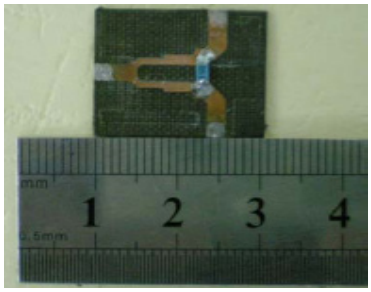

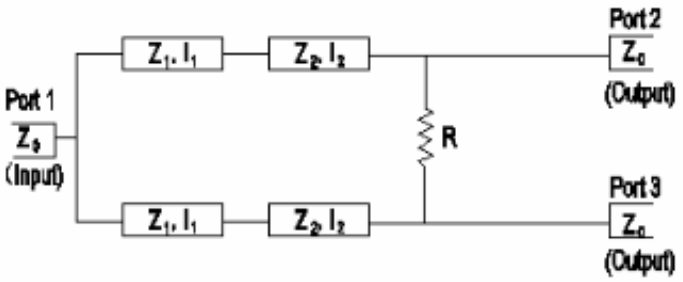

(d)

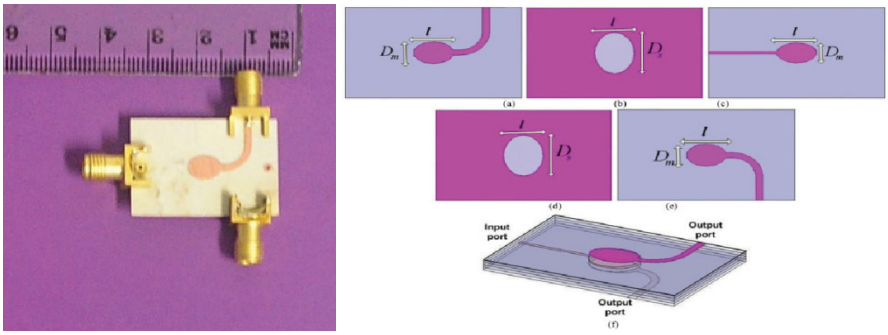

(e)

Figure 2.10 (a) Broadband multi-section feed network [89] (b) Modified single stage Wilkinson power divider [90] (c) Modified two-section Wilkinson power divider [91] (d) Compact modified two-section Wilkinson power divider [92] and (e) Multi-layer in phase power divider [94].

2.5.1 UWB Vertical Transitions

Vertical transitions are basic elements of microwave circuits and key components in multi-layered beamforming networks such as Butler matrices. They are considered to be good alternatives that avoid the crossovers, or cross lines problems such as limiting operating bandwidth and increasing radiation losses. The main goal when we design any good transition is to achieve a minimum insertion loss over a maximum possible bandwidth. Recently, different designs for the multi-layered vertical transitions have been studied for wideband applications to achieve a wide bandwidth with a reasonable insertion loss [95]-[101]. Figure 2.11 presents some designs for wideband vertical transitions using different implementation technologies. In [95], a vertical transition in a multi-layer millimeter wave (MMW) module at 30 GHz using Substrate Integrated Circular Cavities (SICC) is proposed. Another design proposed in [96] uses broadband multi-layered transition using high efficiency Low-Temperature Co-fired Ceramic (LTCC) technology. Other designs are implemented using PCB technology. It can be noticed that the coupling mechanism between the two layers can be achieved by using either an aperture (slot) or via-holes. It has been found that transitions through via-holes have complexity in structure and difficulty in fabrication that will lead to performance degradation especially at higher frequencies [97]. To overcome the deficiencies through via-holes transitions, aperture- or slot-coupled vertical transitions can be used instead as better replacement for via-hole transitions. The aperture or slot which may take different shapes such as rectangular, circular, and elliptical or any other shape is etched on the common ground plane between the two layers [98]-[100].

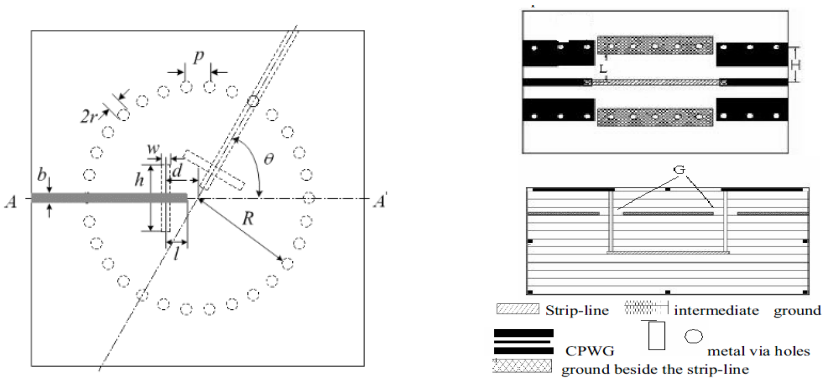

(a) (b)

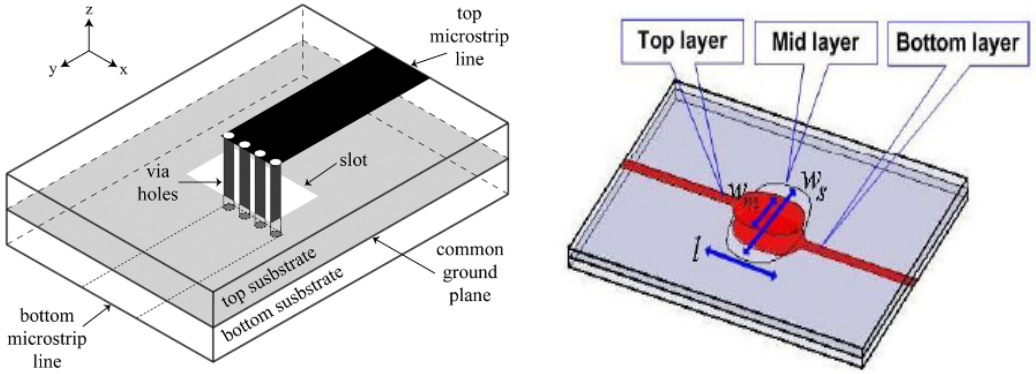

(c) (d)

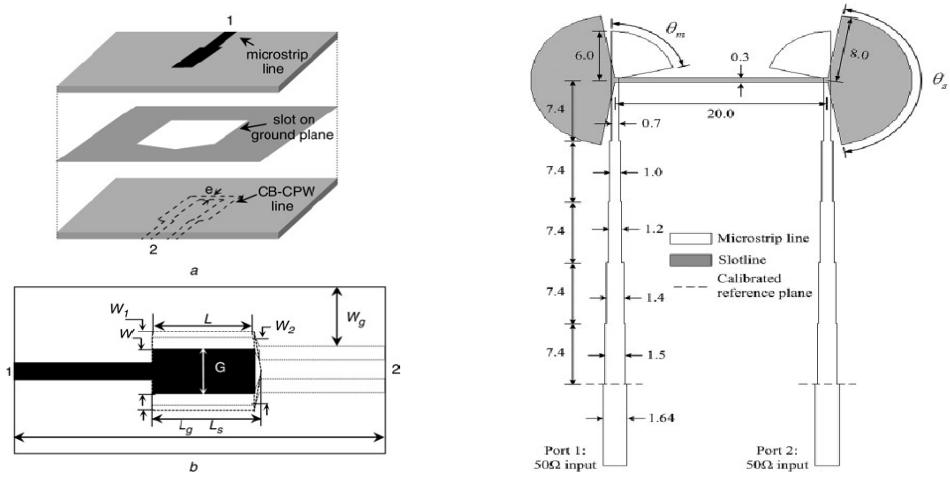

(e) (f)

Figure 2.11 (a) SICC multi-layered vertical transition at 30 GHz [95] (b) LTCC multi-layered vertical transition [96] (c) Vertical microstrip transition using via hole array vertical metallic-wall [97] (d) Aperture-coupled vertical microstrip elliptical transition [98] (e) Microstrip to conductor backed coplanar waveguide (CB-CPW) transition [99] and (f) Microstrip to slot-line transition [100].

2.5.2 UWB 90° Hybrid Couplers

Hybrid couplers are fundamental and important microwave passive devices that can be widely used in many microwave integrated circuits (IC) applications such as in balanced mixers, modulators, and beamforming networks. A hybrid coupler is defined as a four port network [88]. They can be used as a divider/combiner to divide or combine signals with the desired phase. Some traditional and well-known 90° directional couplers such as branched-line, coupled line and Lange coupler are illustrated in Figure 2.12. Those types of couplers have a narrow bandwidth operation characteristic. For broadband wireless communication applications such as UWB systems, there are certain requirements for the design of good and efficient hybrid couplers. Couplers should have high-performance, low cost and small size. There are many different techniques to design broadband directional couplers as shown in Figure 2.13. A technique introduced by [108] uses coupled lines with a slotted ground plane underneath. The spacing requirement between the lines is too small to achieve the desired coupling and hence the coupler becomes difficult to fabricate. Moreover, there are some serious constraints that affect the overall performance of these types of structures. Another approach [110] is used to improve the performance and reduce the size of the conventional branch-line coupler by using a microstrip electromagnetic bandgap (EBG) element. The broadside coupling approach is considered another technique proposed to avoid the problems of spacing restrictions between the lines in coupled line couplers [106], [107], [109]. This suggested technique uses a multi-layered structure consisting of two dielectrics substrates and three metallic layers. Two microstrip patches of any shape are installed on the top and bottom

layers while a broadside coupling slot is etched in the common ground plane (middle layer).

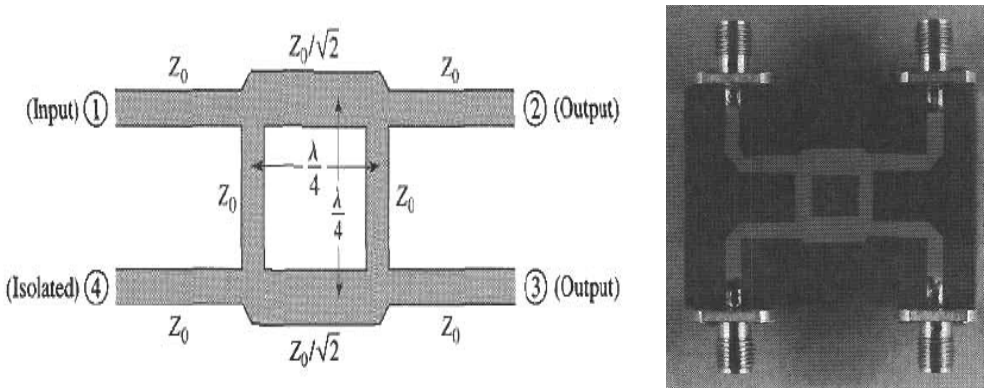

(a)

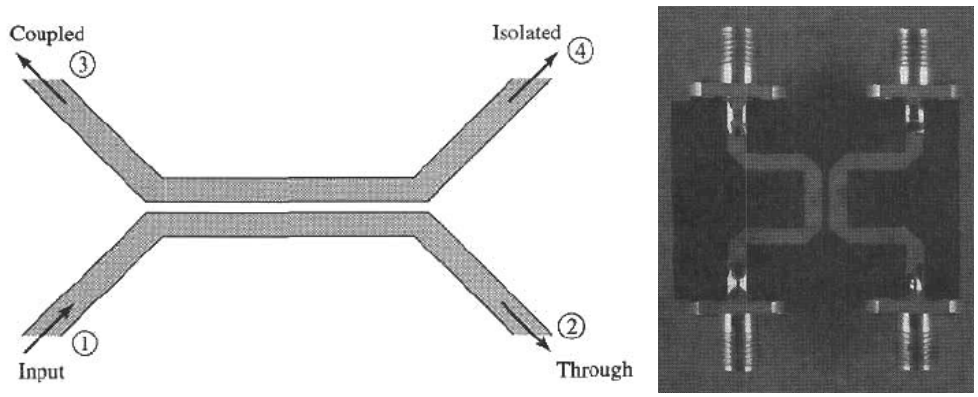

(b)

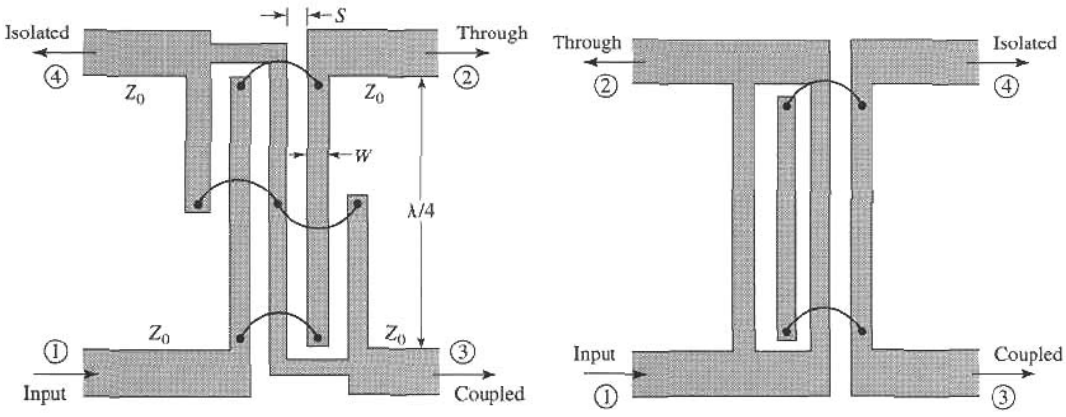

(c)

Figure 2.12 (a) Geometry and photograph of a branched-line coupler [88] (b) Geometry and photograph of a coupled line coupler [88] and (c) Microstrip Lange coupler [88].

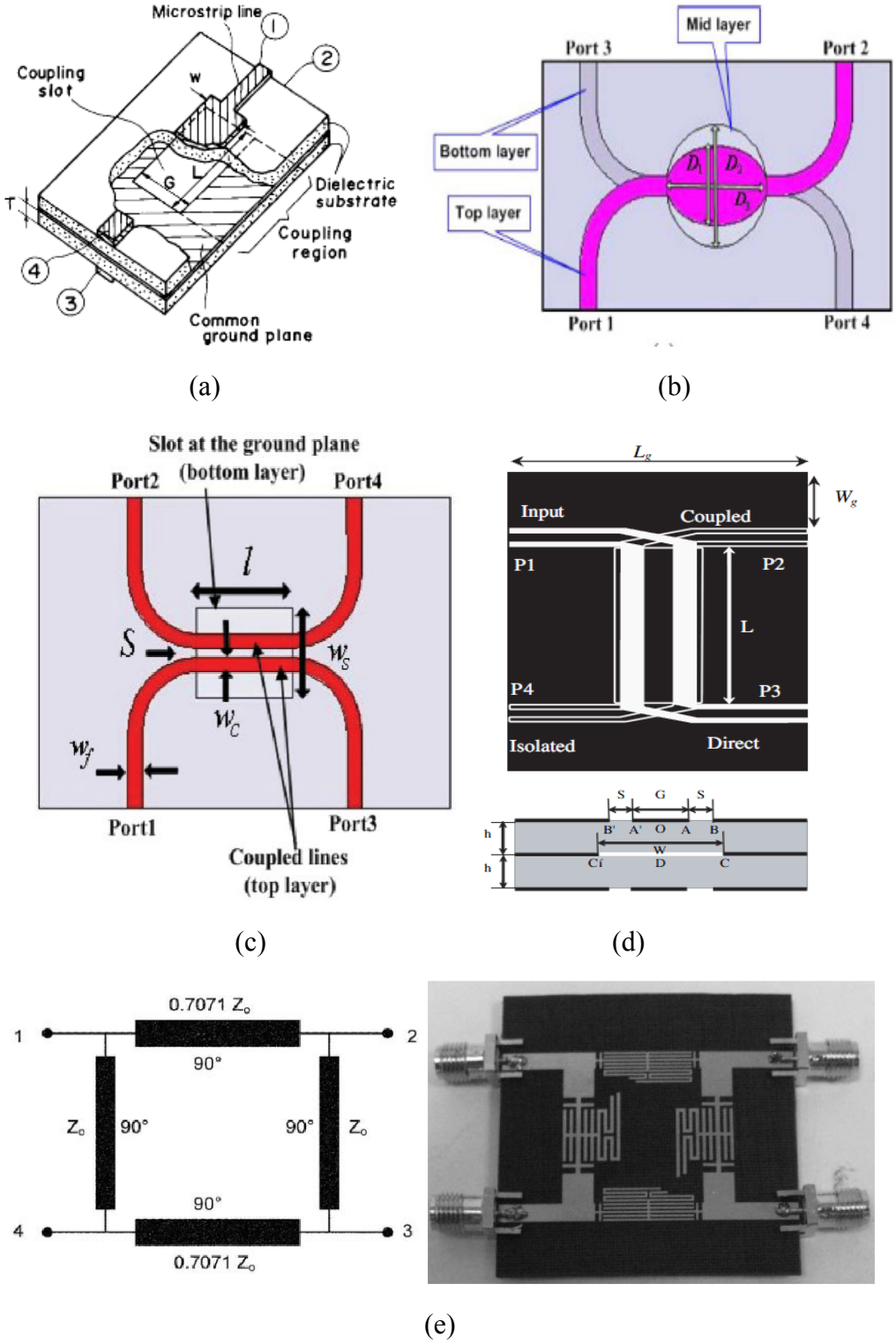

Figure 2.13 (a) Slot-coupled rectangular directional coupler [106] (b) Slot-coupled elliptical directional coupler [107] (c) Quadrature coupler with slotted ground plane [108] (d) Broadside directional slot-coupled coupler [109] and (e) Improved branch-line coupler on microstrip EBG element [110].

2.5.3 UWB Phase Shifters

There is a big need for phase shifters due to their consideration as important microwave devices widely used in various applications such as electronic beam scanning phased arrays, phase modulators… etc. Conventional phase shifters have narrowband performance where the phase changes linearly with increasing frequency. Because of the non-dispersive characteristic and broadband propagation properties of microstrip PCB technology, phase shifters should be implemented using microstrip PCB for wideband operation. Figure 2.14 shows the original Schiffman phase shifter which is considered to be one of the first designs based on using different sections of coupled-strip transmission lines operating in the transverse electromagnetic (TEM) mode and a reference transmission line [113]. By controlling the degree of coupling between coupled lines and the length of those lines, the desired constant broadband phase difference between these lines can be obtained. The problem with the original Schiffman phase shifter is that the achieved bandwidth does not cover the desired UWB frequency range. Recently, researchers have tried to improve the original Schiffman phase shifter to achieve the desired broadband phase response as shown in Figure 2.15 [114]-[117]. This can be achieved by using cascade of multiple coupled parallel transmission line sections connected to each other [116]. These designs have a large size and some limitations in PCB fabrication because of very small gaps to achieve tight coupling. Another approach is achieved by using dumb-bell-shaped phase shifter having multi-section stubs but the bandwidth achieved is not enough for UWB operation [114]. In [115], an improved wideband Schiffman phase shifter is proposed by modifying the ground plane underneath the microstrip coupled lines to form a defected ground structure (DGS) while the

achieved bandwidth is from 1 GHz to 3.5 GHz. Another approach to design a broadband phase shifter in multi-layered PCB technology is achieved by using the multi-layered vertical elliptical transition and a microstrip reference line as in [117].

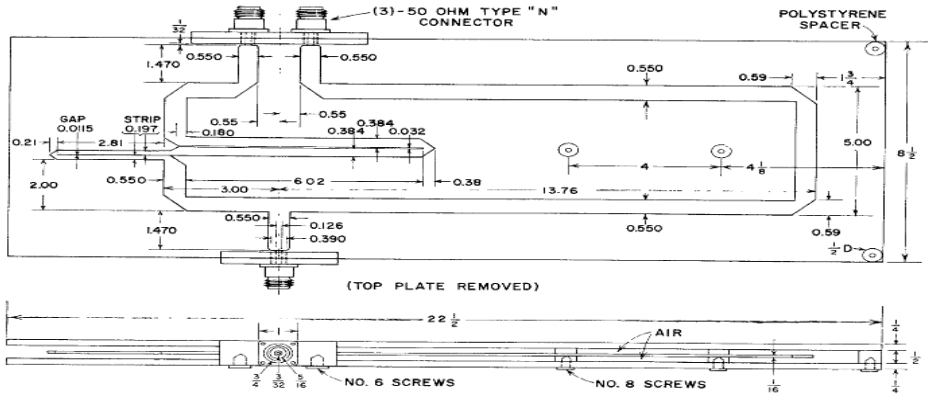

Figure 2.14 Original Schiffman phase shifter [113].

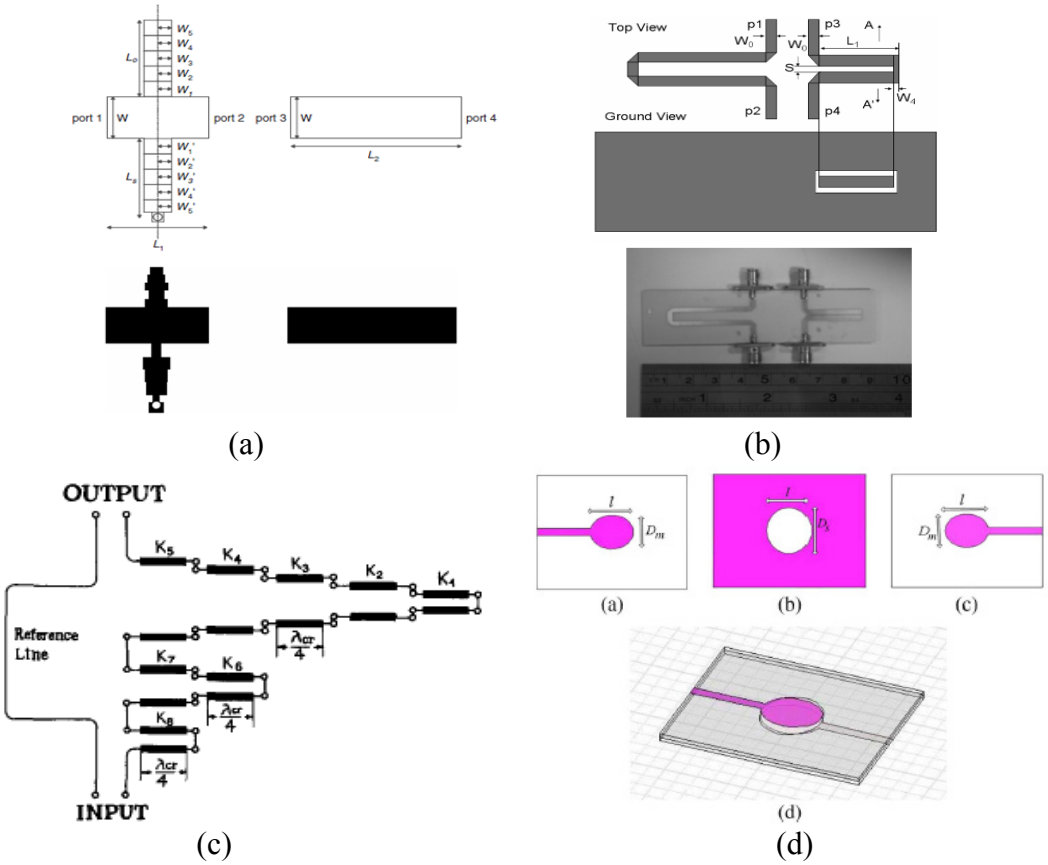

Figure 2.15 (a) Improved broadband dumb-bell-shaped phase shifter using multi-section stubs [114] (b) Improved wide-band Schiffman phase shifter [115] (c) Modified Schiffman phase shifter [116] and (d) Slot-coupled elliptical phase shifter [117].

2.6 UWB Beamforming Techniques

According to FCC regulations, the power spectral density (PSD) of UWB signal is limited for legal operation by the strict power regulations of the FCC mask. The maximum achievable coverage range will be limited by using a multi-element antenna array. This problem can be solved by using smart antenna systems. Beamforming is one of the most popular techniques that can be used to provide both coverage range extension and interference mitigation [9]. The potential of combining UWB and smart antenna systems technologies is to exploit the benefits of each. An exciting application of multi-antenna UWB techniques is in very high speed and high data-rate communications. UWB smart antenna systems have the ability to increase the data-rate of UWB systems beyond the current state of the art, i.e. 500 Mbps to several Giga bit per second (Gbps). This can be achieved by using the spatial-multiplexing benefit as well as exploiting the large gain in system capacity because of the huge bandwidth of UWB systems. This high speed and high data rates will be useful in many future applications such as multimedia communications. For those reasons we should give great attention to research in multi-element antenna array UWB communications systems.

2.6.1 Background Beamforming Techniques

Beamforming techniques can be generally classified into two main categories: conventional or fixed beamforming techniques and modern or adaptive techniques. The fixed beamforming technique is considered to be a simple technique to improve the system performance. Switched-beam antenna (SBA) systems are defined as antenna array

systems that can generate multiple fixed beams with increased performance [16]. Many different structures of multi-beam network beamformers have been proposed such as the Blass matrix [19], [20], the Nolen matrix [21], [22], the Rotman lens [23], [24], and the Butler matrix [25]-[27]. Butler matrix is considered to be the popular network among these beamformers. This is because of its simple design and ease of implementation and testing as shown in Figure 2.16. More details about the UWB Butler matrix beamformer architecture is given in the following section.

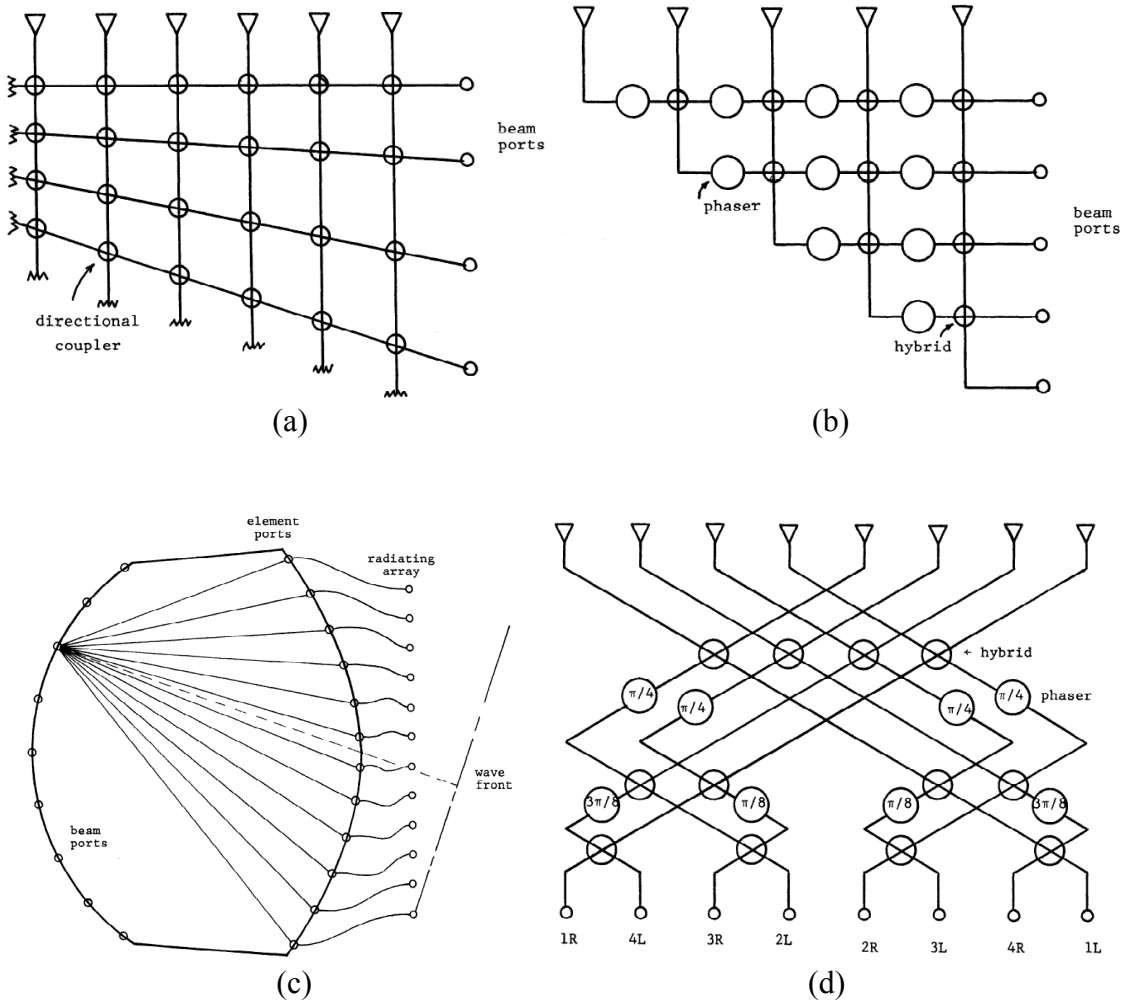

Figure 2.16 Schematic block diagram of (a) Blass matrix BFN [22] (b) Nolen matrix BFN [22] (c) Rotman lens beamformer [22] and (d) Butler matrix BFN [22].

2.6.2 Butler Matrix Architecture

A Butler matrix consists of a passive $N \times N$ phased antenna array network that has the ability to steer the main beam in the desired direction and/or to form nulls in the direction of strong interference or jamming. Practically, it consists of a combination of both hybrid couplers and phase shifters. The type of hybrid couplers used in its implementation determines the type of Butler matrix which can be either symmetrical or asymmetrical network. If the Butler matrix uses quadrature or 90° hybrids, the network becomes symmetrical while the asymmetric one uses out-of-phase or 180° hybrids.

The standard symmetric $N \times N$ Butler matrix has ($N = 2^n$) input ports and N output ports associated with N antenna elements. When it is fed by N-element linear antenna array, N orthogonal beams of the same gain as the whole array are obtained. Generally, the $N \times N$ Butler matrix can be constructed by cascading $H_n = Nn/2$ hybrid couplers and $P_n = N(n-1)/2$ phase shifters. In case of planar matrices with crossovers, the total number of crossovers C_n is calculated from Eq. (2.4) [118]

$$C_n = 2C_{n-1} + 2^{n-2}(2^{n-2} - 1), \qquad C_1 = 1 \tag{2.4}$$

For example, for a 4 × 4 Butler matrix shown in Figure 2.17; $N = 4 = 2^2$, $n = 2$ the matrix has four 90° hybrid couplers, two 45° phase shifters and two crossovers. Table 2.1 shows the number of hybrids, phase shifters and crossovers in different Butler matrices. The number of crossovers increases in a rapid manner by increasing the matrix order n and those crossovers will degrade the overall performance of the matrix. To avoid using crossovers in designing a Butler matrix, a two-layer PCB topology is to be used. Figure 2.18 shows a layout of 4 × 4 Butler matrix proposed in a two-layer topology.

The linear phase progression φ at the output ports for each input port can be calculated from Eq. (2.5) [21]

$$\varphi = (2m-1)\frac{\pi}{N}, \qquad m \text{ integer}, m \in [1 - N/2, N/2] \tag{2.5}$$

Due to this linear phase progression φ at the output ports, the main beam will be directed towards a certain angle θ_o which can be calculated from Eq. (2.6) [21]

$$\theta_o = sin^{-1}\left(\frac{\lambda}{d}\frac{\varphi}{2\pi}\right) \tag{2.6}$$

where d is the inter-element spacing of the linear antenna array, m is assigned for each input port and λ is the free space wavelength at the operating frequency. Table 2.2 shows the linear phase progression φ at the output ports and main beam direction θ_o for a 4 × 4 Butler matrix when the inter-element spacing of the linear antenna array is d = λ/2.

Table 2.1 Number of Hybrid Couplers, Phase Shifters and Crossovers in Butler Matrices

Number of ports, $\boldsymbol{N = 2^n}$	Matrix order $\boldsymbol{n}$	Number of 3dB/90° hybrid couplers, $\boldsymbol{Nn/2}$	Number of phase shifters, $\boldsymbol{N(n-1)/2}$	Number of crossovers, Eq. (2.4) $\boldsymbol{C_n}$
2 × 2	1	1	0	0
4 × 4	2	4	2	2
8 × 8	3	12	8	16
16 × 16	4	32	24	88
32 × 32	5	80	64	416
64 × 64	6	192	160	1,824

Table 2.2 Linear Phase Progression φ at the Output Ports and Main Beam Direction θ_o for a 4 × 4 Butler Matrix

	5	6	7	8	$\boldsymbol{\beta}$	$\boldsymbol{\theta_o}$
1	45°	90°	135°	180°	– 45°	+ 14.5°
2	135°	0°	225°	90°	+ 135°	– 48.6°
3	90°	225°	0°	135°	– 135°	+ 48.6°
4	180°	135°	90°	45°	+ 45°	– 14.5°

225° = – 135°

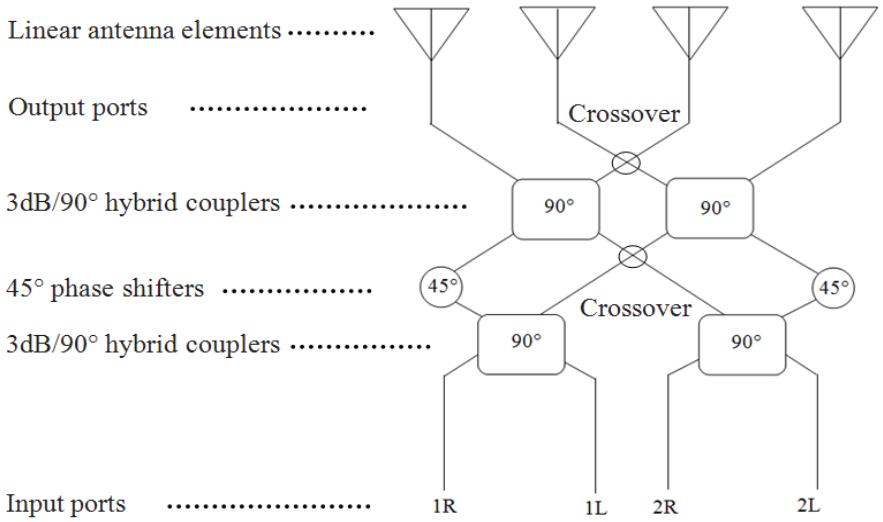

Figure 2.17 Schematic block diagram of 4 × 4 Butler matrix.

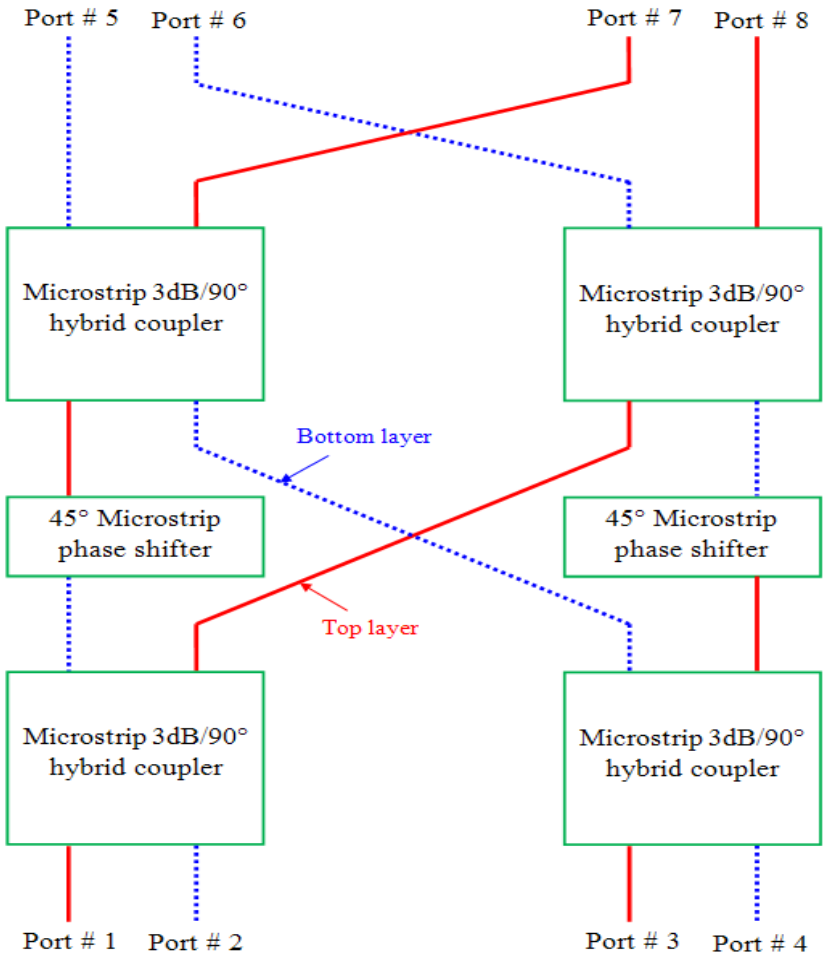

Figure 2.18 Block diagram of the proposed two-layer 4 × 4 UWB Butler matrix without crossovers.

2.7 Summary

In this chapter, the state of art of UWB antennas together with feed networks and other microwave associated components for UWB applications has been presented. It started by describing the UWB technology and its advantages for future wireless communication systems. This was followed by investigating several relevant works related to UWB antenna element designs and antenna arrays. The chapter presented several UWB feed networks and other associated UWB microwave components such as vertical transitions, 90° hybrid couplers and phase shifters. Then background information about UWB beamforming techniques was addressed with a focus on the architecture of a Butler matrix as a suggested beamforming network for generating multiple fixed orthogonal beams. The layout of 4 × 4 UWB Butler matrix without crossovers was presented on two-layered microstrip PCB technology.

Chapter 3

Theoretical Background and Analysis

3.1 Introduction

The design of compact and inexpensive ultra-wideband antennas and microwave components for beamforming antenna system is our target in this thesis. As mentioned in Chapter 2, various types of antennas and other associated microwave components have been recently considered for wideband and ultra-wideband applications. This chapter focuses on the theoretical background and design methodology used in designing those antennas and other microwave components for UWB operation. Starting from the initial design for the microstrip-line-fed printed circular disc monopole antenna, we developed different novel antenna structures for future UWB applications. The initial parameters of the UWB printed circular disc monopole antenna are also given in this chapter. The operation mechanism of those kinds of UWB antennas are introduced and discussed. The idea of integrating a bandstop filtering element on the reference circular disc monopole antenna is also addressed here. The methodology used in designing UWB feed networks and associated microwave components such as vertical transitions, hybrid couplers and phase shifters will be presented in Chapter 5.

This chapter is organized as follows: Section 3.2 presents the numerical and analytical techniques used in designing all UWB antennas and microwave components in

this thesis. Those techniques are based on Finite Element (FE) method as used in Ansoft High Frequency Structure Simulator (HFSS) and Finite Integration Technique (FIT) as in Computer Simulation Technology Microwave Studio (CST MWS). The operation principles and design methodologies of UWB disc monopole antennas and hybrid antennas based on the investigation of the antenna performance and characteristics are addressed in Section 3.3. Finally, conclusions are summarized in Section 3.4.

3.2 Numerical/Analytical Techniques

The principles of electromagnetic fields and waves are very important for the design and development of antennas as well as microwave devices and components as key elements of any wireless communication system. All proposed antennas and other associated microwave components in this thesis such as feed networks, vertical transitions, hybrid couplers, phase shifters and Butler matrices are analyzed and designed by solving the well-known Maxwell's equations. These equations describe all electromagnetic phenomena of different structures and configurations. They can be expressed in their either differential or integral forms as [88]

Differential form	Integral form	
$\nabla \cdot \vec{D} = \rho_v$	$\oiint \vec{D} \cdot d\vec{S} = Q_{enc}$	(3.1)
$\nabla \cdot \vec{B} = 0$	$\oiint \vec{B} \cdot d\vec{S} = 0$	(3.2)
$\nabla \times \vec{E} = -\frac{\partial \vec{B}}{\partial t}$	$\oint \vec{E} \cdot d\vec{l} = -\frac{\partial \Phi_B}{\partial t}$	(3.3)
$\nabla \times \vec{H} = \mathrm{J} + \frac{\partial D}{\partial t}$	$\oint \vec{H} \cdot d\vec{l} = i_{enc} + \varepsilon \frac{\partial \Phi_E}{\partial t}$	(3.4)

where the vectors $\vec{E}$ and $\vec{H}$ are the electric and magnetic field intensities and are measured in units of [V/m] and [A/m], respectively. The vector quantities $\vec{D}$ and $\vec{B}$ are the electric and magnetic flux densities and are in units of [C/m^2] and [Wb/m^2]. The scalar quantities $\Phi_E = \iint \vec{D} \cdot d\vec{S}$ and $\Phi_B = \iint \vec{B} \cdot d\vec{S}$ are the electric and magnetic fluxes and are in units of [C] and [Wb], respectively.

When the EM field problem is complex, an exact solution in a closed form may be difficult to obtain and hence we should solve them by applying numerical techniques. Because of the complexity of proposed antenna structures and other microwave components in this thesis, all proposed structures are modeled using commercial simulation software programs which enable us to design, simulate, tune and optimize structure's physical parameters to reach the best design before fabricating prototypes. Currently, there are several numerical techniques that can be used to solve the EM problems, such as the Finite Element (FE) method [149], the Method of Moments (MoM) [150], the Finite Difference Time Domain (FDTD) [151] and the Finite Integration Technique (FIT) [152]. The first two methods solve the EM problems in the frequency domain while the other two methods use the time domain. Depending on the type of problem, we can choose the appropriate numerical technique. A comparison among those numerical techniques is summarized in Table 3.1. All simulations done in this thesis are performed using two different computer aided design (CAD) tools which are based on computational EM modeling techniques [149-152] to check the accuracy of simulated results before the fabrication process phase. Two independent CAD tools are selected: one is a frequency domain solver while the other is a time domain solver. We compare them with respect to their storage capacity, running speed and accuracy.

Table 3.1 Comparison Among Several Numerical Techniques

Numerical technique	MoM [150]	FE [149]	FDTD [151]
Storage capacity	Moderate	Large	Large
CPU runtime	Moderate	Moderate/Large	Large
Full/Sparse matrix	Full	Sparse	Sparse
Analytical load	Moderate	Small	Nil
Structure complexity	Good	Very Good	Good
Material generality	Limited	Very Good	Good
Nonlinearity/inhomogeneity	Difficult	Easy	Easy
Open boundary support	Easy	Difficult	Difficult

3.2.1 Finite Element Method using Ansoft HFSS

The first simulation software program is Ansoft High Frequency Structure Simulator (HFSS) [119]. Ansoft HFSS is currently considered to be one of the top industry-standard software programs and a powerful EM field simulation tool for many years. It is based on a three-dimensional (3D) full-wave finite element (FE) method which is a frequency-domain numerical technique for solving Maxwell's equations. Because of its high accuracy and performance, Ansoft HFSS can be used by engineers in industry or researchers and scientists in academia to analyze and design different complex structures for high-frequency applications.

Ansoft HFSS uses the FE numerical technique in order to generate an EM field solution for different 3D problems. First, the finite element technique is based on divid-

ing the whole big problem space into small regions or sub-regions called elements. Then the fields in each finite element are formulated by local functions. Ansoft HFSS automatically converts the whole problem structure into a finite element mesh which consists of a large number of very small 3D tetrahedral shapes as shown in Figure 3.1. Each single tetrahedron is a four-sided pyramid as presented in Figure 3.2. It can be seen that the meshing or discretization operation done by Ansoft HFSS is very coarse in almost the whole structure while it is very fine at some regions which need more accuracy such as near wave port, metallic edges or discontinuities. After finalizing the mesh operation of the whole structure, the solution process starts with two-dimensional (2D) port solutions as the structure excitation then followed by the field solution of the full 3D problem including fields at all vertices, midpoints and interior points as in Figure 3.2. The program exploits the computed 2D fields on ports to be used as boundary conditions to solve the 3D fields of the whole structure.

During the numerical iterative solution, Ansoft HFSS solves the electric field for a given problem based on the following matrix equation (for a lossless case) [119]:

$$[A]\overline{x} + k_o^2[B]\overline{x} = c \tag{3.5}$$

where [A] and [B] are square matrices and their sizes depend on the geometry of the problem and the size of the mesh, $\overline{x}$ is the electric field vector, k_o is wave number in free space and c is the value of the source or excitation defined for the given problem. Then the magnetic field solution is calculated from the following relationship with the electric field:

$$\vec{H} = -\frac{1}{j\omega\mu}\nabla \times \vec{E} \tag{3.6}$$

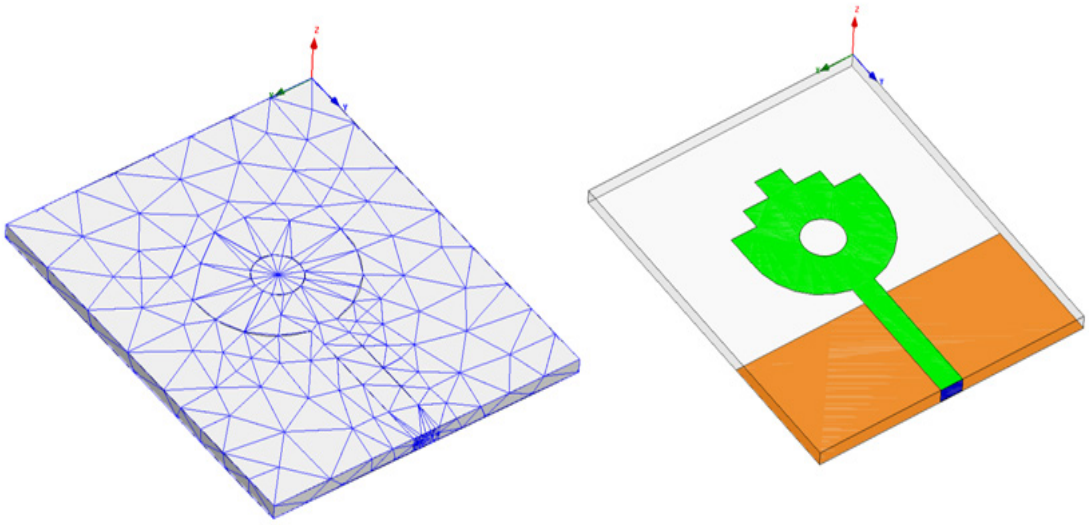

Figure 3.1 Meshing based on tetrahedral shapes of an antenna structure in Ansoft HFSS.

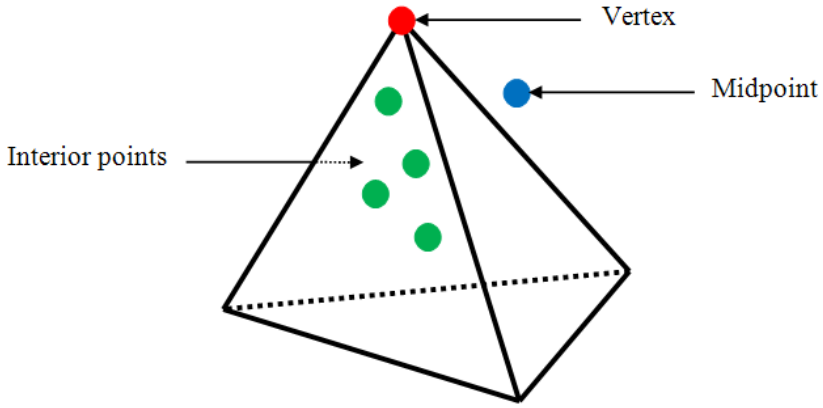

Figure 3.2 A single tetrahedral mesh shape used in Ansoft HFSS.

3.2.2 Finite Integration Technique using CST

The other simulation software program is called Computer Simulation Technologies Microwave Studio (CST MWS) [120]. CST MWS is a tool for fast and accurate 3D EM simulation of high frequency problems. Currently, it is considered to be industry-standard software programs and a powerful 3D EM field simulation tool. CST MWS is

based on the Finite Integration Technique (FIT) [121] which is equivalent to FDTD. Unlike the FE method, FIT is a time-domain numerical technique for solving Maxwell's equations. Using the function of parametric study in both Ansoft HFSS and CST MWS simulation programs, we can tune and optimize the structure physical parameters to obtain the best design before going to the fabrication process. CST MWS has different kinds of solvers not only a transient solver but also a frequency domain solver, an eigen mode solver and an integral equation solver.

In a transient or time-domain solver, the value of the vector electric $\vec{E}$ or magnetic $\vec{H}$ field quantities are computed through time at discrete spatial locations and at discrete time samples. The maximum time step Δt used in the simulation program depends on the minimum mesh step size which can be determined by the density of the mesh used in the meshing process of the whole structure. Therefore the program takes more time to run simulation if the mesh is dense. Once the spatial mesh or discretization is performed by the CST program, the finite integration method is employed. CST has two different mesh types available, i.e. hexahedral and tetrahedral meshes. Another mesh type used by the Integral Equation (IE) solver is called surface mesh. Figure 3.3 shows a single hexahedral tetrahedral and surface mesh element used in CST program. For complex structures, CST uses a hexahedral mesh in meshing or discretization because it is considered to be very robust. Other solvers use a tetrahedral or surface mesh method. Figure 3.4 shows the meshing based on hexahedral shapes of an antenna structure in CST.

The finite integration technique converts the well-known Maxwell equations in their integral form into set of discrete matrix equations called Maxwell grid equations (MGE) as follows [121]:

Integral form		Matrix form	
$\oiint_{\partial\tilde{V}} \vec{D} \cdot d\vec{A} = \iiint_{V} \rho_v \cdot d\vec{V}$	$\Rightarrow$	$[\tilde{S}]d = q$	(3.7)
$\oiint_{\partial V} \vec{B} \cdot d\vec{A} = 0$	$\Rightarrow$	$[S]b = 0$	(3.8)
$\oint_{\partial A} \vec{E} \cdot d\vec{l} = -\iint_{A} \frac{\partial \vec{B}}{\partial t} \cdot d\vec{A}$	$\Rightarrow$	$[C]e = -\frac{d}{dt}b$	(3.9)
$\oint_{\partial\tilde{A}} \vec{H} \cdot d\vec{l} = \iint_{\tilde{A}} \left[\frac{\partial \vec{D}}{\partial t} + \vec{J}\right] \cdot d\vec{A}$	$\Rightarrow$	$[\tilde{C}]h = \frac{d}{dt}d + j$	(3.10)

where $[C]$, $[\tilde{C}]$, $[S]$ and $[\tilde{S}]$ are square matrices represent the discrete curl and divergence operators, respectively and their sizes depend on the problem geometry. e and h represent the electric and magnetic grid voltages and they are related to the electric and magnetic fields according to $e = \int_{\partial A} \vec{E} \cdot d\vec{l}$ and $h = \int_{\partial\tilde{A}} \vec{H} \cdot d\vec{l}$. d and b are the electric and magnetic facet flux vectors over the mesh cell.

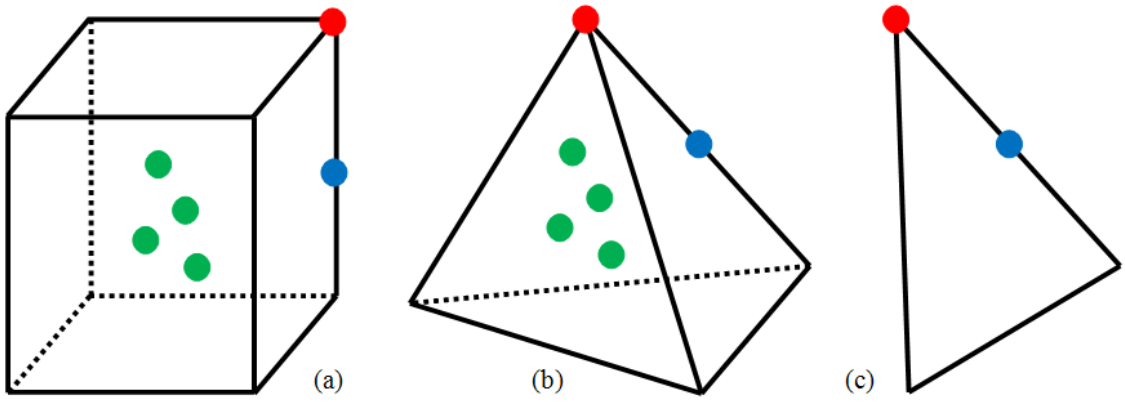

Figure 3.3 A single (a) hexahedral, (b) tetrahedral and (c) surface mesh element used in CST.

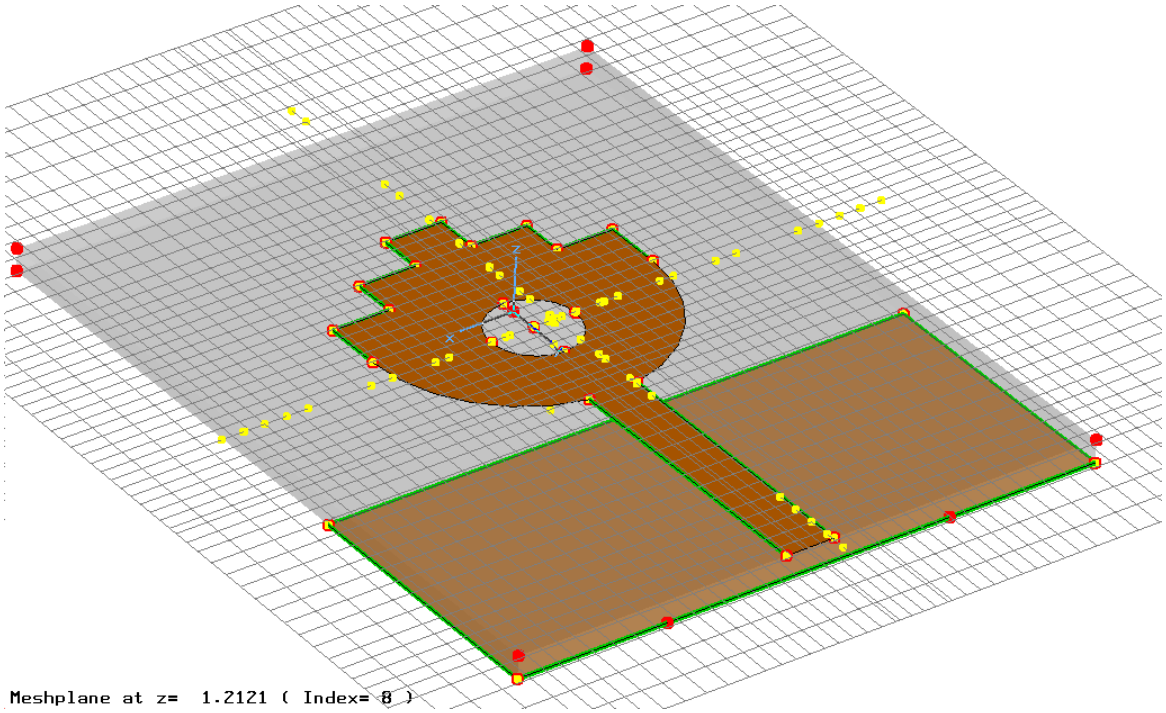

Figure 3.4 Meshing based on hexahedral shapes of an antenna structure in CST.

3.3 UWB Antenna Design Methodology

This section discusses the design methodology for determining initial parameters for UWB antennas. Two types of UWB antenna designs are presented; the first antenna design is based on the printed circular disc monopole antenna while the second design uses a hybrid technique of a printed monopole loaded with dielectric resonator. The first antenna type which is based on the printed circular disc monopole is a good candidate for achieving UWB impedance bandwidth with an almost stable dipole-like radiation pattern and constant gain across the whole desired frequency range. However, the antenna size is relatively large because the ground plane width should be at least twice the diameter of the circular disc otherwise the antenna impedance matching performance will be degrad-

ed. To achieve the antenna miniaturization along with UWB performance, the hybrid technique of using printed monopoles loaded with dielectric resonators (DRs) is considered as an efficient solution to achieve both bandwidth enhancement and size reduction. In addition, they offer some good advantages compared to other conventional metallic antennas such as high efficiency and low cost needed for wideband wireless applications. Another advantage of such kinds of hybrid antennas compared to printed circular disc monopoles is their ability to have more degree of freedoms by using different monopole and dielectric material parameters in order to control the antenna characteristics. Both antenna types have similar radiation characteristics and gains for short-range wireless communications. The design methodology used in designing UWB feed networks for linear antenna arrays are presented in Appendix A. In addition, the theoretical background for the design of microwave vertical transitions and hybrid couplers needed for the development of UWB beamforming networks is detailed in Appendix B.

3.3.1 UWB Printed Disc Monopole Antennas

Printed disc monopole antennas are considered to be good candidates for UWB applications because they have a simple structure, easy fabrication, wideband characteristics, and omni-directional radiation patterns [56]-[69]. The geometry of the reference printed circular disc monopole antenna is shown in Figure 3.5. To determine the initial parameters of the printed circular disc monopole antenna, we should first understand their operation mechanism. It has been shown that disc monopoles with a finite ground plane are capable of supporting multiple resonant modes instead of only one resonant mode (as in a conventional circular patch antenna) over a complete ground plane [122]. Overlap-

ping closely spaced multiple resonance modes ($f_1, f_2, f_3, \ldots, f_N$) as shown in Figure 3.6 can achieve a wide bandwidth and this is the idea behind the UWB bandwidth of circular disc monopole antennas. The frequency of the first resonant mode can be determined by the size of the circular disc. At the first resonance f_1, the disc antenna tends to behave like a quarter-wavelength monopole antenna, i.e. λ/4. That means the diameter of the circular disc is $2r = \lambda/4$ at the first resonant frequency.

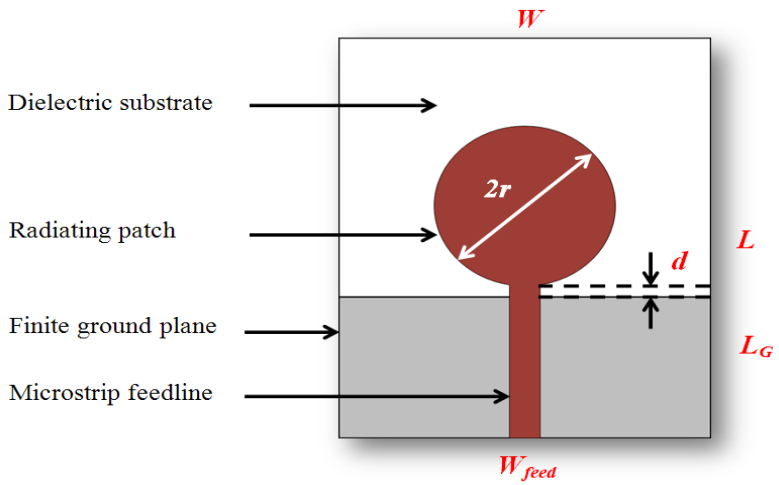

Figure 3.5 The configuration of the reference printed circular disc monopole antenna showing the necessary antenna parameters.

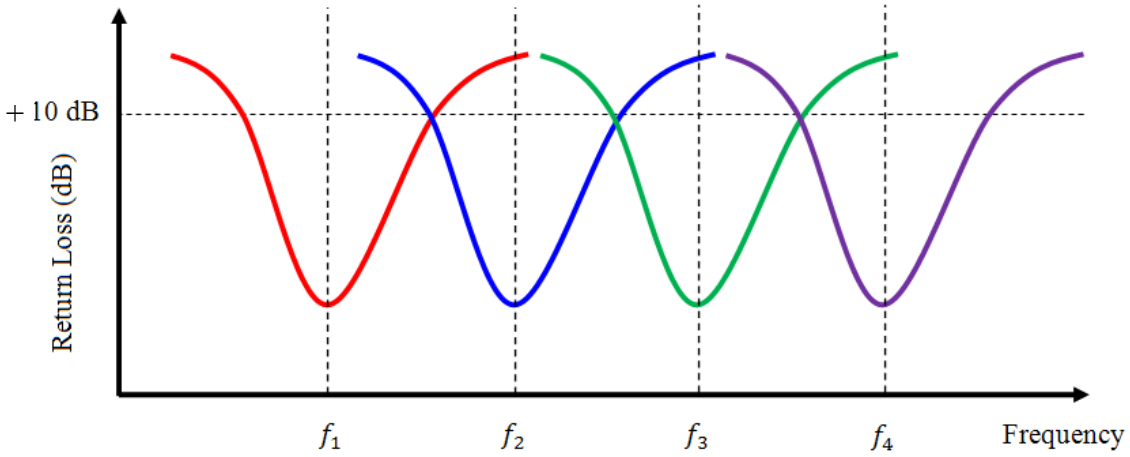

Figure 3.6 The concept of overlapping closely-spaced multiple resonance modes for the reference circular disc monopole antenna (reproduced from [123]).

Then the higher order modes $f_2, f_3, \ldots, f_N$ will be the harmonics of the first or fundamental mode of the disc. Unlike the conventional patch antennas with a complete ground plane, the ground plane of disc monopole antennas should be of a finite length L_G to support multiple resonances and hence achieve wideband operation. The width of the ground plane W is found to be approximately twice the diameter of the disc or $W = \lambda/2$ at the first resonant frequency [123].

The printed disc monopole antenna can be fed using different feeding techniques such as microstrip line, coplanar waveguide (CPW), aperture coupling, or proximity coupling. In the case of a microstrip line feed, the width of the microstrip feed line W_{feed} is chosen to achieve a 50Ω characteristic impedance. The other antenna parameters such as the feed gap between the finite ground plane and the radiating circular disc d and the length of the finite ground plane L_G can be determined using a full-wave EM numerical modeling techniques. The small feed gap between the finite ground plane and the radiating circular disc d is a very critical parameter which greatly affects the antenna impedance matching between the microstrip feedline and the radiating disc.

To avoid interference with some existing wireless systems in the 5.15–5.825 GHz frequency band, a filter with bandstop characteristics may be integrated with UWB antennas to achieve a notch function at the interfering frequency band. The idea of integrating a bandstop filtering element to the reference circular disc monopole antenna is illustrated graphically in Figure 3.7. Recently, several techniques have been introduced to achieve a single band notch within this frequency band. The most popular and easiest technique is embedding a narrow slot into the radiating patch. The slot may have different shapes such as C- shaped [70], slit ring resonator (SRR) [74], L- shaped [76], U- or

V- shaped [78], π-shaped slot [81].…etc. Some other techniques are based on using parasitic strips, i.e., inverted C-shaped parasitic strip [72]. Other techniques are based on using a slot defected ground structure in the ground plane, i.e., H-shaped slot DGS [71].

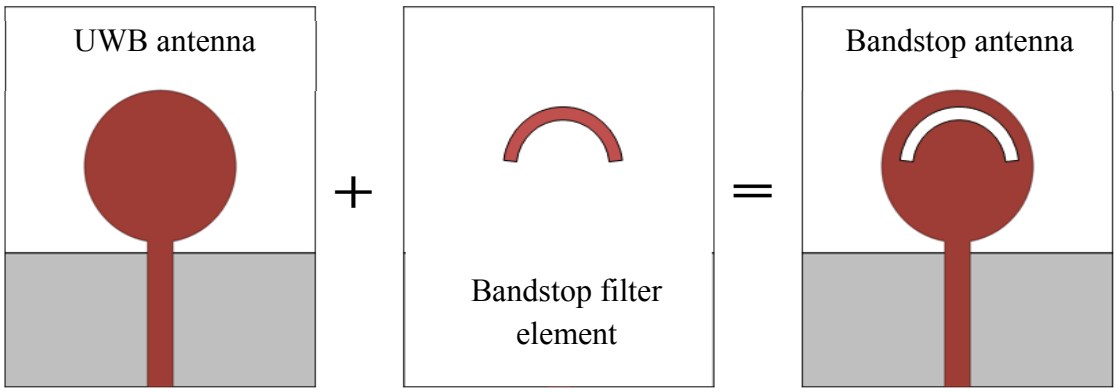

Figure 3.7 The idea of integrating a bandstop filtering element to the reference circular disc monopole antenna.

3.3.2 UWB Hybrid Monopole DR Antennas

Recently, DRAs have shown great attractive characteristics such as high radiation efficiency, low dissipation loss, small size, and light weight. Recent DRA antenna designs focus on enhancing the operational bandwidth by exploiting their advantage of having high degree of design flexibility [124]-[131]. Various techniques have been proposed to achieve bandwidth enhancement such as using different stacked DRAs to obtain multiple-resonance operation [126], using different configurations such as conical, elliptical, tetrahedral [128] … etc, or using different feeding techniques [127], [129]. It has been found that using the above techniques, the achieved DRA bandwidth ranges from 25% to 80%. Also, hybrid techniques of both monopoles and DRAs can be used to achieve wide bandwidth characteristics [125] and those hybrid monopoles and DRAs are considered very promising for achieving large bandwidth with a compact size.

3.4 Summary

In this chapter, the theoretical background and design methodology used in designing UWB antenna elements were discussed. We started with the design methodology to determine the initial parameters for the microstrip-line-fed printed circular disc monopole antenna as a reference antenna used to develop novel antenna structures for future UWB applications. It was shown that UWB characteristic was achieved due to the overlapping of the closely spaced resonances over the frequency band. The numerical/analytical background of the EM modeling techniques for both Ansoft HFSS and CST MWS simulation tools used in designing and optimizing most of all antennas and microwave components in this thesis are also addressed in the chapter. The design methodology used in designing UWB feed networks for linear antenna arrays are presented in Appendix A. In addition, the theoretical background for the design of microwave vertical transitions and hybrid couplers needed for the development of UWB beamforming network is detailed in Appendix B.

Chapter 4

UWB Printed Disc Monopole Antennas

4.1 Introduction

This chapter focuses on the development of different novel UWB microstrip-line-fed printed disc monopole and hybrid antennas with an emphasis of their frequency domain performance. Different antenna configurations are proposed and designed in order to find a best candidate for UWB operation. The best antenna candidate should have UWB performance with small size, constant gain, radiation pattern stability and phase linearity through the frequency band of interest. Also, the designed UWB antenna should have ease of manufacturing and integration with other microwave components on the same PCB such as feed networks, vertical transitions, hybrid couplers and phase shifters to construct UWB beamforming antenna array system. We have simulated, designed, fabricated and then tested experimentally different printed disc monopole antenna prototypes for UWB short-range wireless communication applications. The printed disc monopole antennas are chosen because they have small a size and omni-directional radiation patterns with large bandwidth. In order to understand their operation mechanism that leads to the UWB characteristics, those antenna designs are numerically studied. Also, the important physical parameters which affect the antenna performances are investigated numerically using extensive parametric studies in order to obtain some quantitative guide-

lines for designing these types of antennas. Because of the size limitations in the printed disc monopoles, hybrid monopole and dielectric resonator antennas are suggested to be used for achieving both bandwidth enhancement and size reduction.

This chapter is organized as follows; Section 4.2 presents the simulated and experimental results of a novel UWB printed circular disc monopole antenna with two steps and a circular slot. Parametric studies to see the effect of some antenna parameters on its performance are investigated in the subsection 4.2.1. Also, a design for band-notched UWB antenna to avoid interference with other existing WLAN systems is addressed in the same section. Novel printed maple-leaf shaped monopole antenna with two different band-notch designs are proposed in Section 4.3. Section 4.4 studies two other new antenna designs, i.e. a butterfly-shaped and a trapezoidal printed monopole antenna with bell-shaped cut. The compact hybrid printed monopole and DR antenna is discussed in Section 4.5. Finally, conclusions are summarized in Section 4.6.

4.2 Novel Printed Circular Disc Monopole Antenna with Two Steps and a Circular Slot

For better understanding the antenna characteristics, the antenna reflection coefficient (S11) curves are plotted in decibel or dB scale, i.e. ($S11_{dB} = 20 \log|S11| = -$Return loss RL). The geometry and photograph of the proposed printed circular disc monopole antenna with two steps and a circular slot is shown in Figure 4.1. The radiating element is fed by a 50Ω microstrip feed line with width of W_f = 4.4 mm. The substrate used in our design is Rogers RT/duroid 5880 high frequency laminate with thickness of h = 1.575

mm, relative permittivity of ε_r = 2.2 and loss tangent of $tan\delta$ = 0.0009. A finite ground plane of length L_G and width W lies on the other side of the substrate. The feed gap of width d between the finite ground plane and the radiating patch is a very critical parameter for antenna matching purposes and to obtain wide bandwidth performance.

This proposed antenna has a reduction in the overall antenna surface area compared to those reported in [64] and [66]. A parametric study is carried out to investigate the effect of antenna physical parameters such as the width of the substrate W, the width of the feed gap d, the radius of circular slot R_S and the steps dimensions W_1, W_2, L_1 and L_2 on the performance of the proposed UWB antenna.

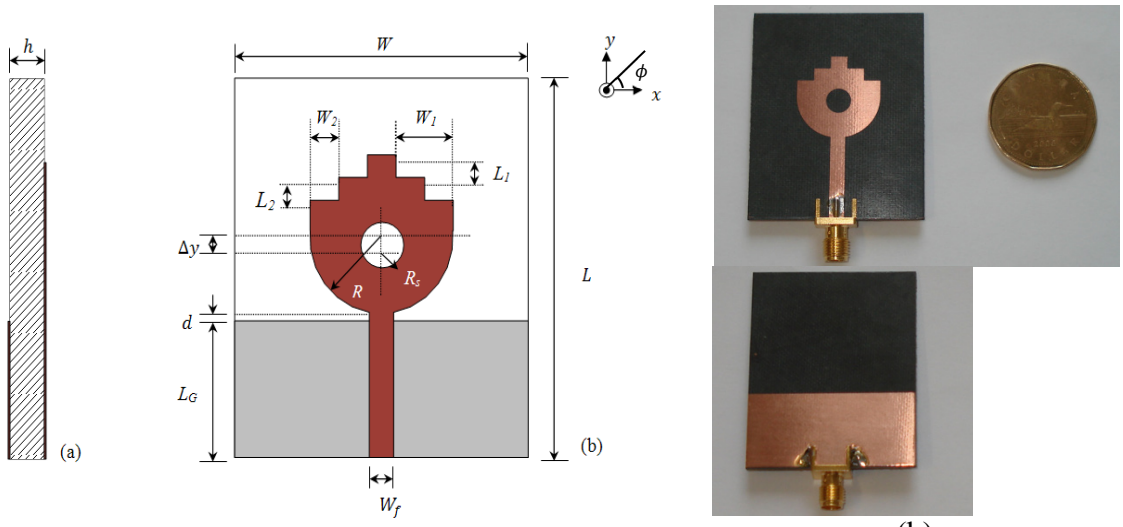

(a) (b)

Figure 4.1 (a) Geometry and (b) photograph of the proposed microstrip line fed monopole antenna.

4.2.1 Effect of the Antenna Parameters on its Performance

During the parametric study, one parameter varies while all other parameters are kept fixed. The optimized antenna parameters are: W = 41 mm, L = 50 mm, L_G = 18 mm, R = 10 mm, Δy = 2 mm, R_S = 3 mm, W_1 = 8 mm, W_2 = 4 mm, L_1 = 3 mm and L_2 = 3 mm.

Figure 4.2 shows the simulated antenna reflection coefficient (20 log|S11|) curves using CST MWS for different values of substrate width W, feed gap width d, slot radius R_S and the steps dimensions W_1, W_2, L_1 and L_2. It can be noticed from results that the smallest substrate width for obtaining the maximum available bandwidth is W = 41 mm. It can be also seen that the reflection coefficient impedance bandwidth is greatly dependent on both the feed gap width d and the circular slot radius R_S and by controlling these two parameters, the impedance matching between the radiating patch and the feed line can be easily controlled. By tuning the width of the feed gap d, the maximum achieved impedance bandwidth is determined. The circular slot inside the radiating patch acts as an impedance matching element which controls the antenna impedance matching as well as the antenna impedance bandwidth. Also, the circular slot inside the radiating patch can be used for miniaturizing the monopole antenna. Also, it can be noticed that the rectangular steps have no remarkable effect on the overall antenna impedance bandwidth. The optimum values for feed gap width, slot radius and steps dimensions are d = 1 mm, R_S = 3 mm and W_1 (= $2W_2$) = 8 mm and L_1 (= L_2) = 3 mm, respectively.

Cutting out two rectangular steps and a circular slot from the radiating patch to reduce the overall metallic area and hence reduce the antenna copper losses without affecting the antenna operation or disturbing the current distribution of the antenna is a challenging task. This can be done by investigating the antenna surface current distributions. Figure 4.3(a) & (b) presents the antenna surface current and electric field distributions for the proposed disc monopole antenna. From the electric field distributions, it is noticed that the monopole antenna supports multiple resonant modes. It can be seen that the current distribution is mainly located close to the radiating patch edges rather than in

the center. For increasing the maximum achieved impedance bandwidth, the lower resonant frequency should be decreased. This can be done by increasing the antenna perimeter which directly affects lower resonant frequency and then the antenna impedance bandwidth. To increase the antenna perimeter, cutting out steps from the radiating patch are used here. This is simply because the surface current will take longer path when the antenna perimeter p is larger and the new antenna with larger perimeter p appears to be like a longer length monopole antenna and then the lowest resonance frequency f_L will be decreased according to [63]:

$$\varepsilon_{eff} \approx (\varepsilon_r + 1)/2 \tag{4.1}$$

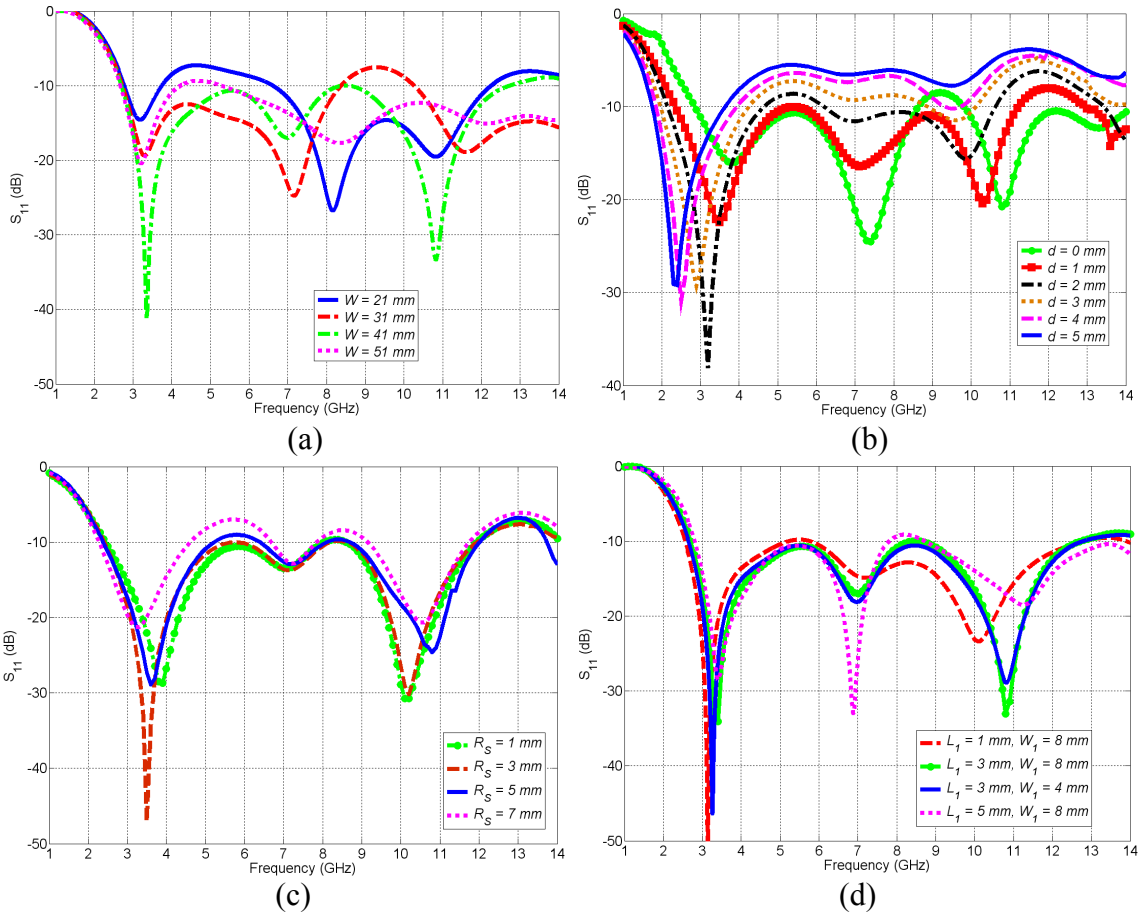

Figure 4.2 Parametric studies of effect of (a) substrate width W (b) feed gap width d (c) circular slot radius R_S and (d) steps dimensions W_1 (= $2W_2$) and L_1 (= L_2) on antenna reflection coefficient.

$$f_L \text{ (GHz)} = 300/p\sqrt{\varepsilon_{eff}} \tag{4.2}$$

where ε_{eff} is the effective dielectric constant and the perimeter p units are in millimeters.

For example, in the proposed antenna design, p = 71.4 mm, ε_r = 2.2, then ε_{eff} = 1.6 and the calculated lower resonant frequency using Eq. (4.2) is found to be $f_L \approx$ 3.3 GHz. From the simulated and measured reflection coefficient results shown in Figure 4.4, the lower resonant frequency is $f_L \approx$ 3.3 GHz which agrees well with the calculated value.

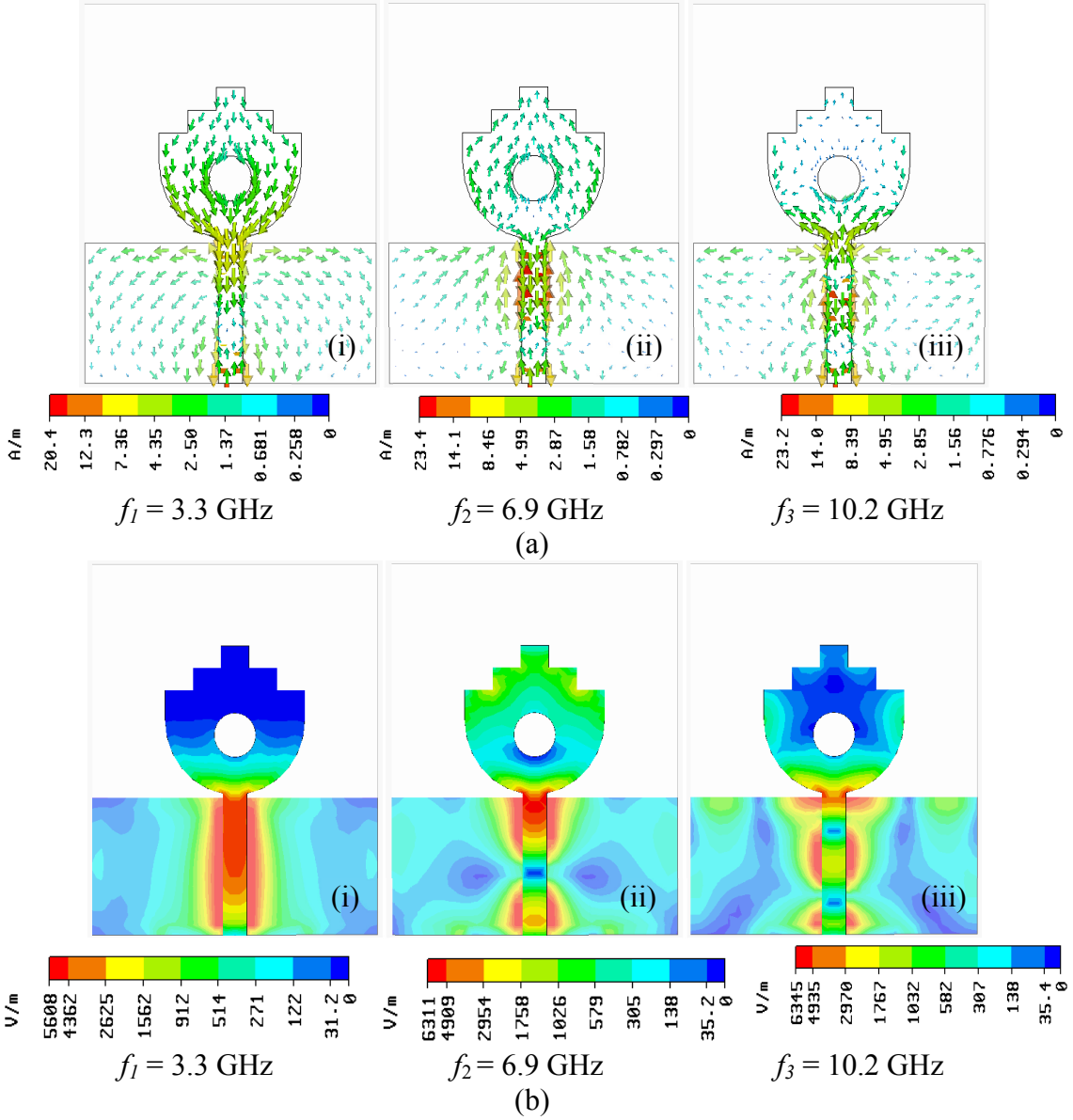

Figure 4.3 Simulated (a) surface current and (b) electric field distributions at the three resonant frequencies 3.3, 6.9 and 10.2 GHz.

4.2.2 Experimental and Simulation Results

A prototype of the microstrip-line-fed monopole antenna with optimized dimensions was fabricated as shown in Figure 4.1 and tested experimentally in the Applied Electromagnetics Laboratory at Concordia University. All scattering parameters measurements were carried out using Agilent E8364B programmable network analyzer (PNA). The measured and simulated reflection coefficient (S11) curves are presented in Figure 4.4. It can be noticed that both measured and simulated results are in good agreement with each other and the measured 10 dB return loss bandwidth ranges from 3.0 to 11.4 GHz which covers the entire UWB frequency spectrum. Compared to the simulated results, the second resonant frequency at 7 GHz is shifted up while the third resonant frequency at 10 GHz is shifted down. This may be due to the sub-miniature version A (SMA) connector losses and/or substrate losses especially at high frequencies (7-10 GHz). Even the loss effect of the substrate is modeled correctly and taken into account in the simulations; the simulation results did not change too much and did not agree with the measured results. In general, the proposed antenna exhibits an UWB impedance bandwidth (3.1-10.6 GHz) in both simulated and measured results.

For further understanding the antenna performance, the Ansoft HFSS simulated maximum realized total directive gain in the boresight direction and the phase of reflection coefficient ∠S11 for the proposed antenna are presented in Figure 4.5. The boresight of directional antenna is defined as the direction of maximum gain of the antenna. For most of antennas, the boresight is the axis of symmetry of the antenna, i.e. z-axis. It can be seen that the antenna has good gain stability across the frequency band of interest (3.1-10.6 GHz). It ranges from 3.4 dB to 5.2 dB with gain variation of about 2 dB. The behav-

ior of the phase of reflection coefficient ∠S11 versus frequency is also studied and shown in the same figure. It can be noticed that the phase seems to be linear across the whole UWB frequency range.

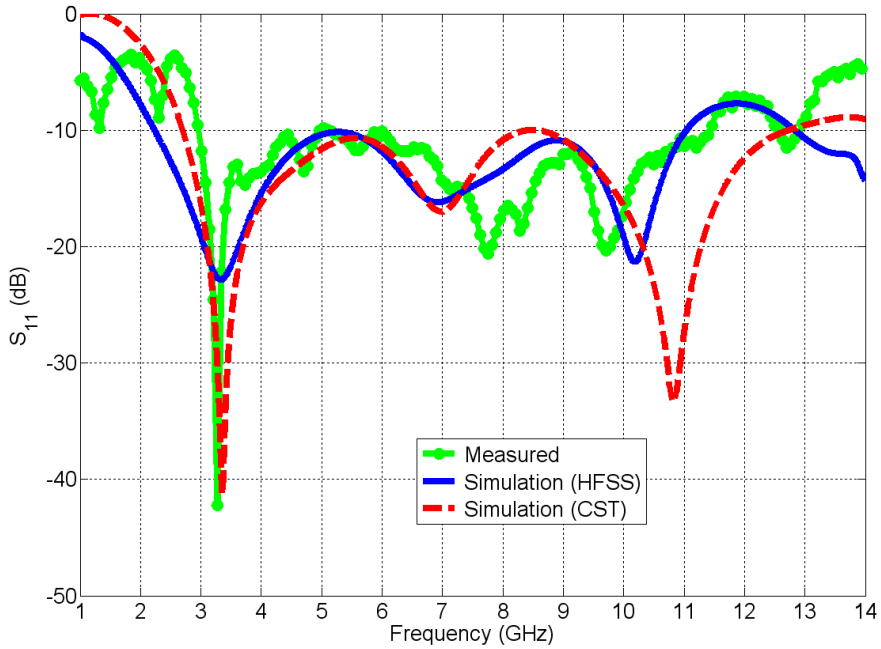

Figure 4.4 Measured and simulated reflection coefficient curves of the proposed microstrip line fed monopole antenna.

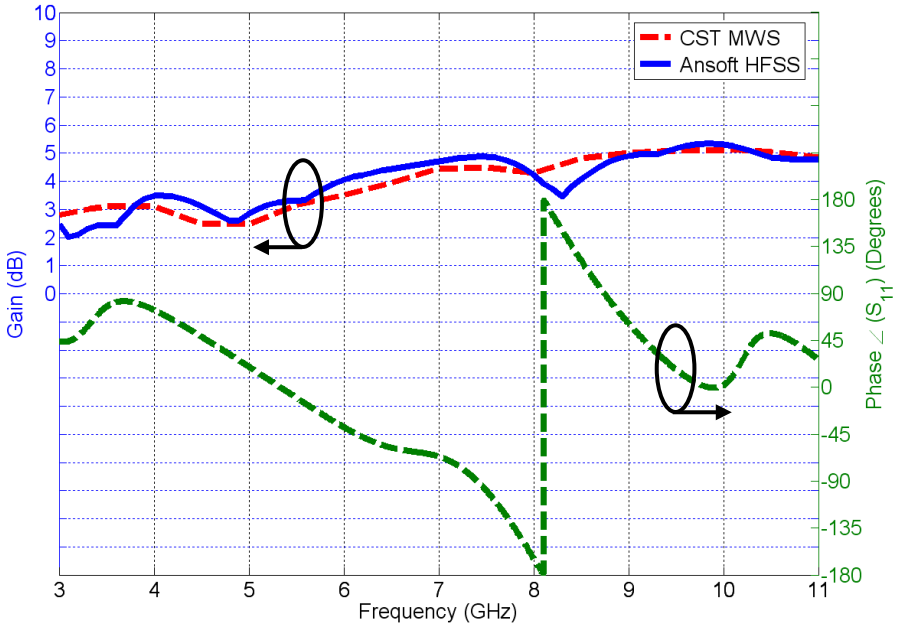

Figure 4.5 The simulated gain and phase of reflection coefficient ∠S11 versus frequency of the proposed microstrip-line-fed monopole antenna.

Figure 4.6 shows the radiation characteristics for the proposed antenna. Both yz-cut plane (*E*-plane) and xz-cut plane (*H*-plane) radiation patterns have been simulated using Ansoft HFSS and measured in an anechoic chamber at the three resonant frequencies 3.3, 6.8, and 10.2 GHz. From the measured results, the proposed antenna has omni-directional radiation pattern in *H*-plane at lower frequency (3.3 GHz) and near omni-directional at higher frequencies (6.9 and 10.2 GHz) with good agreement with simulations. The measured *E*-plane radiation patterns agree with the simulations especially at lower frequency (3.3 GHz) while the agreement is not as good as the *H*-plane patterns at higher frequencies (6.9 and 10.2 GHz). There are some ripples and discrepancies in the measured radiation patterns especially at the higher frequencies which may be due to sensitivity and accuracy of the measuring devices at higher frequencies in addition to the effects of the SMA feed connector and the coaxial cable. The *E*-plane is identified by most of UWB antenna patterns which is perpendicular to *H*-plane (almost symmetric). Researchers in UWB antenna typically define *E*-plane as the plane containing the feedline and the maximum radiation of the antenna. *H*-plane is the plane perpendicular to *E*-plane.

We have investigated both simulated and measured *E*-plane patterns. From simulations, nulls in *E*-plane at $\theta = 90°$ depend on the size of the finite ground plane and the contact point of SMA feed connector in particular at the upper edge frequency. By searching several published UWB antennas of similar disc monopole antennas, similar behavior of measured results are reported in many papers including [59], [153]-[156].

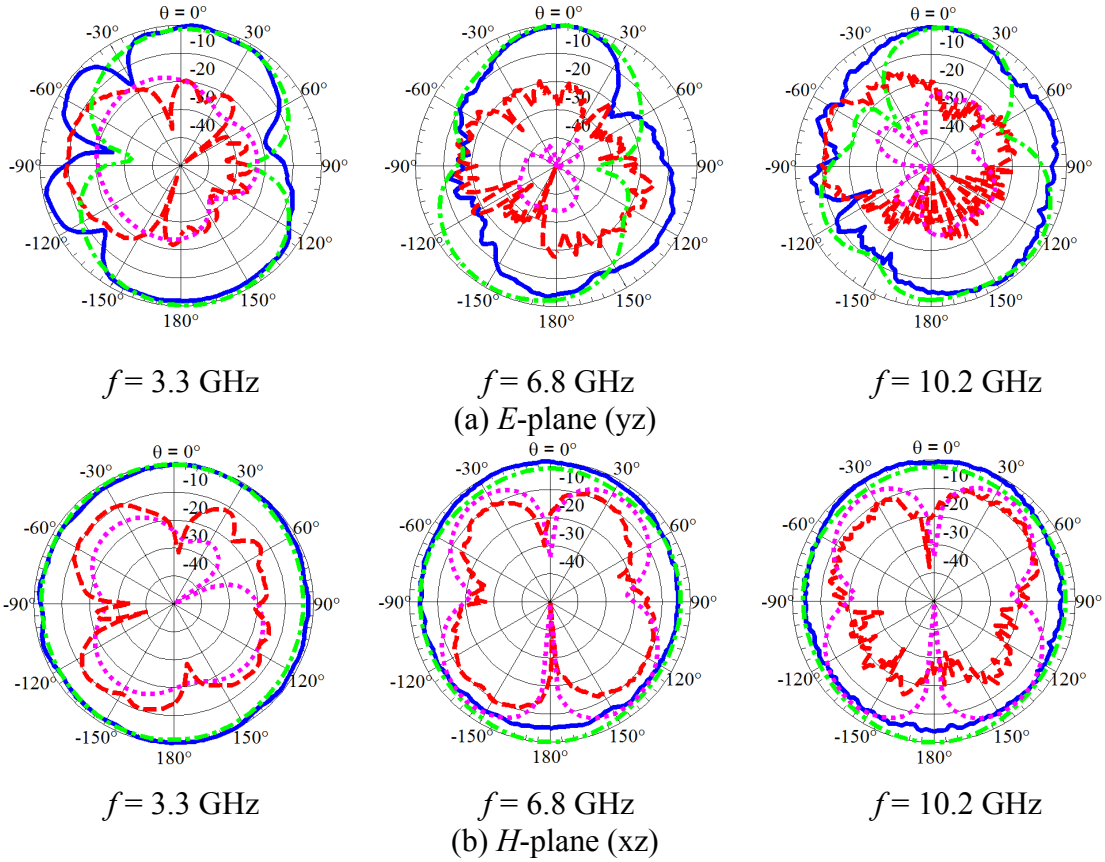

f = 3.3 GHz *f* = 6.8 GHz *f* = 10.2 GHz

(a) *E*-plane (yz)

f = 3.3 GHz *f* = 6.8 GHz *f* = 10.2 GHz

(b) *H*-plane (xz)

Figure 4.6 Measured co-pol (blue solid line), cross-pol (red dashed line), Ansoft HFSS simulated co-pol (green dash-dotted line) and cross-pol (magenta dotted line), (a) *E*-plane and (b) *H*-plane radiation patterns of the proposed antenna.

A modification can be made to the above designed antenna for achieving the bandstop function to avoid possible interference to other existing WLAN systems. A very narrow arc-shaped slot is cut away from the radiating patch as shown in Figure 4.7(a) will act as a filter element to make the antenna will not respond at the bandstop frequency. For perfect band-rejection performance of UWB antenna, the return loss of the stop-band notch should be almost 0dB or the reflection coefficient is almost 1.0. However, in our first band-stop antenna design, we could achieve voltage standing wave ratio (VSWR) of about 8 (reflection coefficient is 0.78 or -2.1dB). The arc-shaped slot filter element di-

mensions will control both the bandstop frequency f_{notch} and the rejection bandwidth of the band-notched filter BW_{notch}. The arc-shaped slot filter dimensions are: the radius of the slot R_1, the thickness of the slot T and the slot angle 2α. Figure 4.7(b) illustrates the simulated reflection coefficient curves using both HFSS and CST MWS for comparison. From the simulation results, it can be seen that the band-notched characteristic in the 5.0-6.0 GHz band is achieved with good agreement between them.

Parametric studies were carried out to address the effect of arc-shaped slot dimensions on the band-notched performance. Figures 4.8 shows the effect of varying the slot radius R_1, slot thickness T and the slot angle 2α parameters on the simulated antenna reflection coefficient, respectively. From results in Figure 4.8(a) & (c), it can be seen that the notch frequency f_{notch} decreases by increasing both the arc-shaped slot radius R_1 and the angle 2α while the notch bandwidth BW_{notch} is almost the same. On the other side, both the notch frequency and bandwidth increase at the same time by increasing the slot thickness T. For achieving a band-notched performance in the 5-6 GHz frequency band, the arc-shaped slot parameter dimensions are: $R_1 = 7.5$ mm, $T = 0.7$ mm and $2\alpha = 160°$.

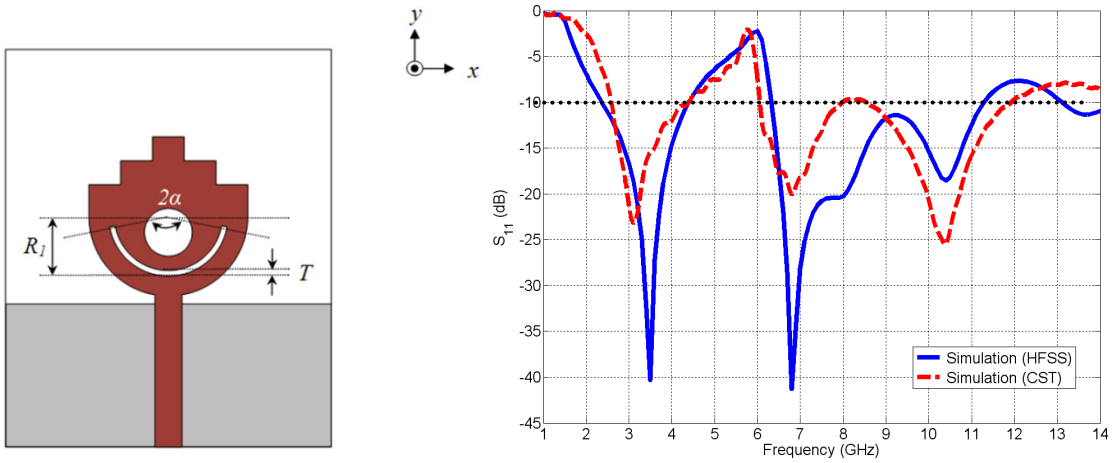

(a) (b)

Figure 4.7 (a) Geometry of the band-notched antenna, $R_1 = 7.5$ mm, $T = 0.7$ mm and $2\alpha = 160°$ (b) Simulated reflection coefficient curves versus frequency.

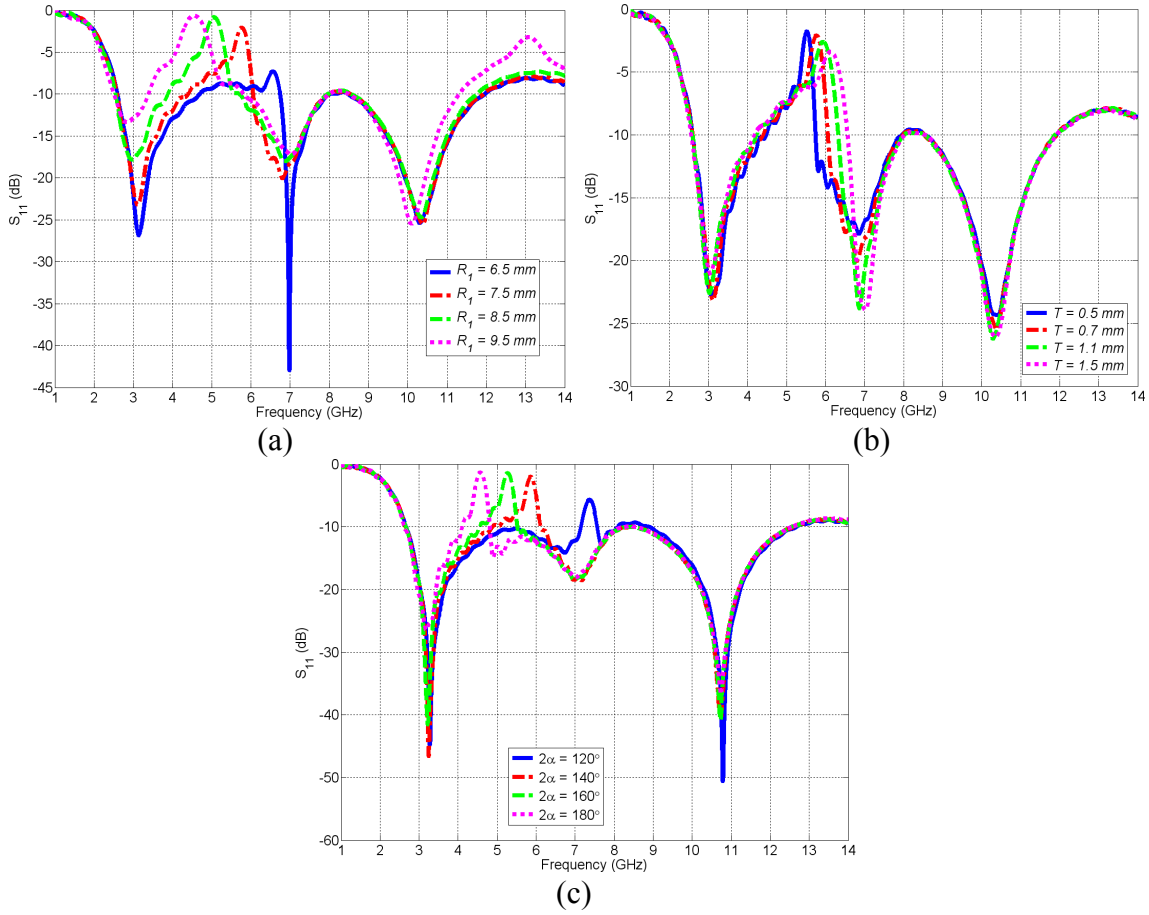

Figure 4.8 Simulated reflection coefficient curves versus frequency for different values of (a) arc-shaped slot radius R_1, (b) thickness of the slot T and (c) the slot angle 2α.

4.3 Maple-leaf Shaped Monopole Antennas

In this section, we developed different maple-leaf shaped monopole antennas with two band-rejection techniques for the 5.0-6.0 GHz frequency band. Figure 4.9(a) & (b) show the geometrical configuration and the photograph of the proposed UWB maple-leaf-shaped monopole antenna prototype. The radiating element consists of a maple-leaf-shaped patch as a radiating element which represents the Canada flag symbol. The radiating patch is fed by a microstrip line and both are etched on a Rogers RT Duroid 5880 substrate with dielectric constant ε_r = 2.2, dielectric loss tangent $tan\delta$ = 0.0009, and

thickness h = 1.575 mm. The proposed antenna parameters $L_1 \sim L_{10}$ are determined using an extensive parametric study and optimization in both Ansoft HFSS and CST MWS to address the effect of those parameters on the overall performance of the antenna. Details of the optimized parameters are summarized in Table 4.1. Our target here is to design a compact antenna for UWB operation. So, we tried to reduce the overall antenna size by reducing the substrate dimensions from 50 × 41 mm^2 as in the previous antenna design to 35.48 × 30.56 mm^2 as in the present antenna design. Here, there is a reduction in the antenna size by almost 47% compared to our first proposed antenna prototype, i.e. circular disc monopole antenna with two steps and a circular slot.

The maple-leaf shaped monopole antenna is used to achieve wider impedance matching bandwidth by introducing many leaf arms into the main radiating patch. This will lead to increasing the overall perimeter of the antenna and hence the monopole antenna looks bigger in size than its real physical size. This is simply because the current takes paths close to the edges rather than inside the radiating patch. The proposed maple-leaf shaped monopole antenna has a wider bandwidth with smaller size compared to the first UWB antenna design (stepped monopole antenna).

Table 4.1 Maple-leaf Shaped Printed Monopole Antenna Dimensions (Units in mm)

W	L	L_G	W_1	W_f	d	L_1	L_2
30.48	35.56	12.95	5.59	4.06	0.84	2.27	7.47
L_3	L_4	L_5	L_6	L_7	L_8	L_9	L_{10}
2.65	4.10	4.34	3.05	5.39	7.73	4.02	5.24

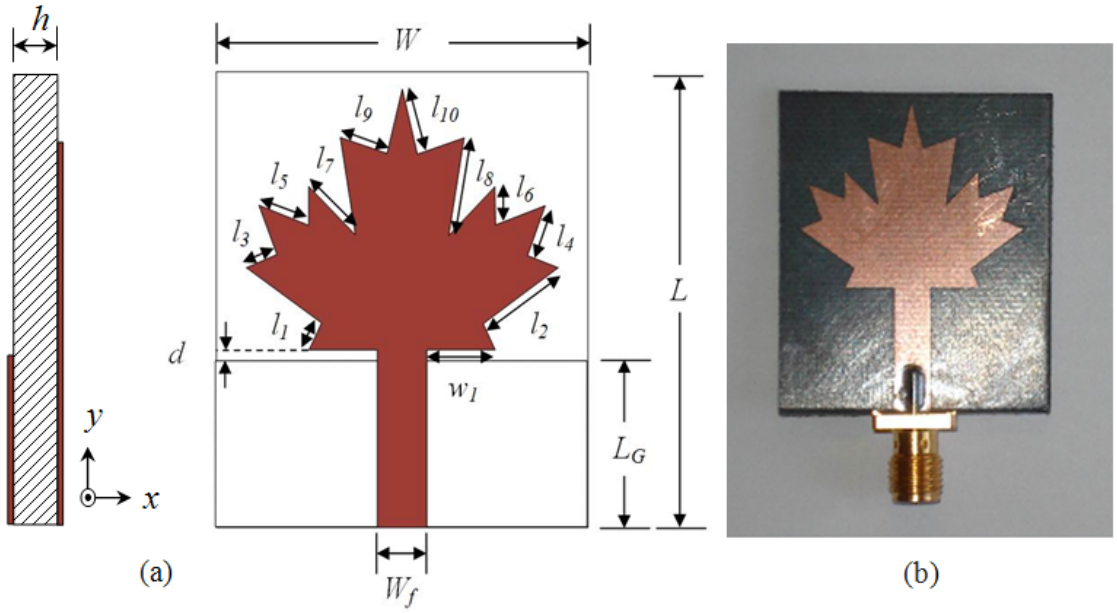

Figure 4.9 (a) Geometry and (b) photograph of the proposed maple-leaf shaped printed monopole antenna prototype.

Figure 4.10(a) illustrates the simulated and measured reflection coefficient curves against the frequency for the designed maple-leaf antenna. It can be noticed from the results that the proposed antenna exhibits a simulated impedance bandwidth from 3 to 13 GHz with good agreement between Ansoft HFSS and CST simulation programs while the measured impedance bandwidth becomes dual-band, one in 4.1-7.0 GHz and the other one in 8.7-13.3 GHz. The explanation for the difference between the measured and simulated results can be easily understood if we mention that both simulated reflection coefficient curves are already very close or even touch the -10 dB level in the region 7.0-9.0 GHz frequency band. So, if there is any manufacturing error in the antenna parameters $L_1 \sim L_{10}$ during the fabrication proposes of the antenna prototype will be a big issue. This is in addition to calibration errors during S-parameters measurement and the effect of SMA connector which was not taken into account during simulations. Also, the manufacturing tolerance as well as the effect of SMA connector have been simulated in CST MWS pro-

gram and simulation results are shown in Figure 4.10(b) and it is found from the obtained result that it confirms the above explanation.

The antenna radiation characteristics across the whole UWB frequency band were also investigated. Figure 4.11 shows both the measured and simulated *E*- and *H*-plane radiation patterns at frequencies 3, 5, 7, and 9 GHz, respectively. The measured *H*-plane radiation patterns are very close to those obtained in the simulation. It can be noticed that the *H*-plane patterns are omni-directional at all frequencies of interest. The measured *E*-plane patterns follow the shapes of the simulated ones, though the agreement is not as good as the *H*-plane patterns. There are some fluctuations, ripples and distortions on the measured curves, which may be caused by the SMA feed connector and the coaxial cable.

We developed two different band-notched antennas using two different techniques for band rejection. Figure 4.12(a) introduces the first proposed band-notched antenna which is designed by modifying the above maple-leaf antenna by cutting a narrow H-shaped slot away from the radiating patch. The H-slot acts as a filtering element where slot dimensions control the rejection band of the band-notched filter. Figure 4.12(b) presents the second proposed band-notched antenna which is designed by cutting two narrow rectangular slits in the ground plane making a DGS. In the maple-leaf band-stop antennas, we achieved VSWR of 10 (reflection coefficient is 0.82 or -1.7dB) with H-shaped slot and VSWR of 24 (reflection coefficient is 0.92 or -0.7dB) with two slits in the ground. It can be concluded that using two slits in the ground plane achieves better rejection characteristics compared to using narrow slots (either arc-shaped or H-shaped) in the radiating patch.

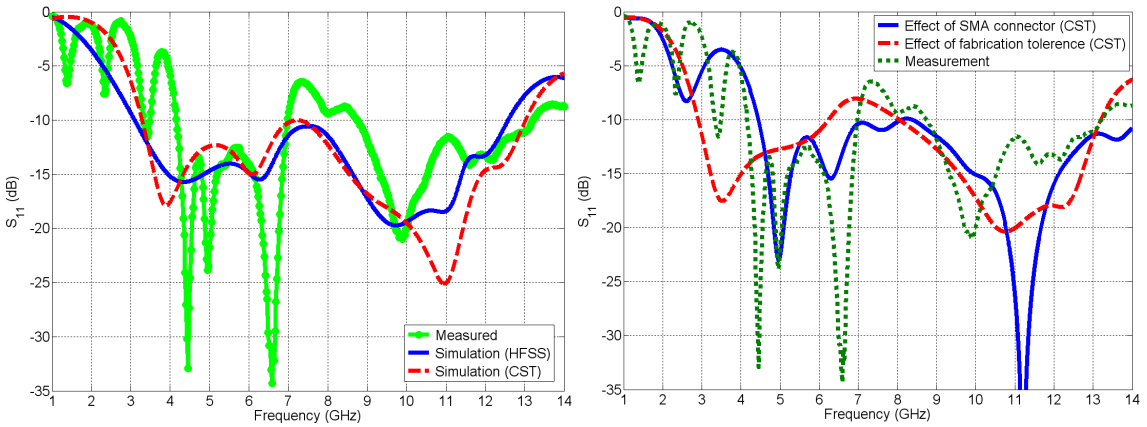

(a) (b)

Figure 4.10 (a) Measured and simulated reflection coefficient curves of the maple-leaf antenna (b) effect of fabrication tolerance on the performance of maple-leaf antenna.

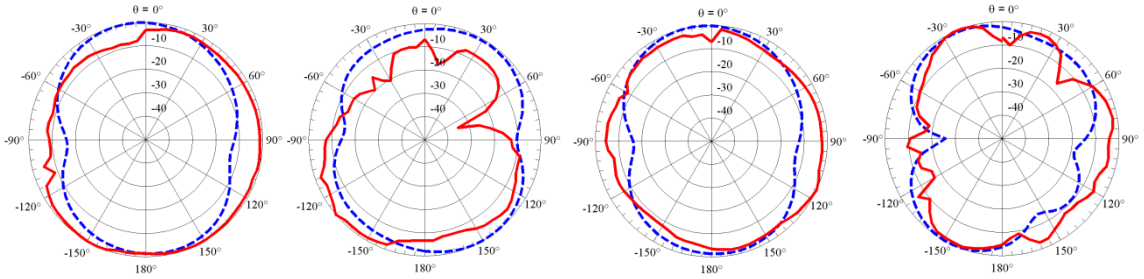

f = 3 GHz f = 5 GHz f = 7 GHz f = 9 GHz

(a) E-plane (yz)

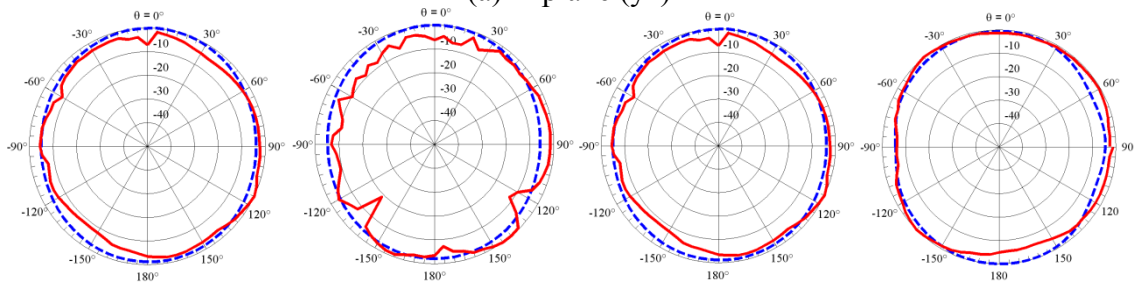

f = 3 GHz f = 5 GHz f = 7 GHz f = 9 GHz

(b) H-plane (xz)

Figure 4.11 Measured (red solid line) and simulated (blue dashed line) (a) E-plane and (b) H-plane radiation patterns of the maple-leaf antenna.

In both techniques, we can control both the notch center frequency f_{notch} and the bandwidth BW_{notch} by adjusting the H-slot and the two slits dimensions, respectively. In the first band-notched antenna, we adjust the slot length L_S, thickness W_S, and location

from the substrate edge D_S to control the bandstop characteristic. In the second band-notched antenna, we control the bandstop characteristic by adjusting the two rectangular slits length L_S, thickness W_S, and distance between them S. The remarkable thing here is that the notch center frequency f_{notch} is controlled by adjusting the mean length of the slot or the two slits to be about one half-wavelength, i.e. λ/2 at the desired notched frequency. For example, the calculated mean length of the H-shaped slot is about 26 mm and the calculated λ/2 at the notch frequency f_{notch} = 5.5 GHz is 27.7 mm. It is found that the notch bandwidth BW_{notch} can be controlled by adjusting the thickness of the slot or the two slits.

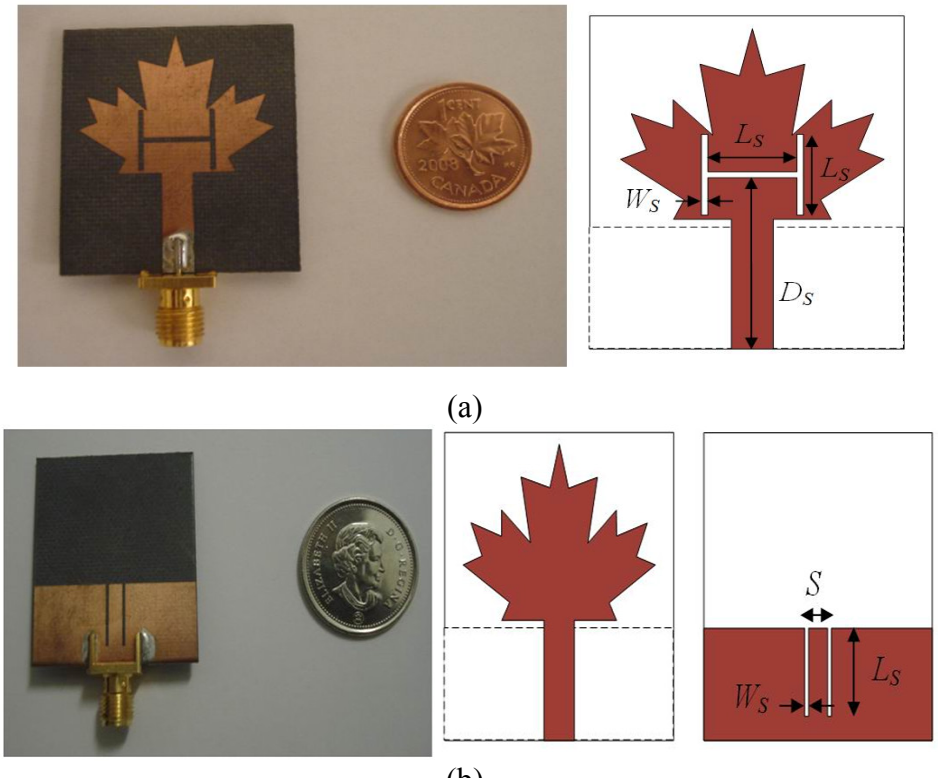

Figure 4.12 Photograph and geometry of the proposed bandstop antennas using (a) H-slot (b) two slits.

Figure 4.13(a) & (b) present the simulated and measured reflection coefficient curves of both band-notched antennas with H-slot and two slits, respectively. It is obvious from the results that the bandstop function in the 5.0-6.0 GHz is successfully achieved for both antenna designs. The discrepancies in the 7-9 GHz frequency band come from the maple-leaf antenna itself not from the filter elements for band rejection. It can also be noticed that these discrepancies in the 7-9 GHz frequency band are more remarkable in the first prototype than the second one. This is may be due to the effect of using DGS in the finite ground plane enhanced the antenna performance in the 7-9 GHz frequency band.

Figure 4.14 and Figure 4.15 show the CST simulated surface current distributions over different frequencies, i.e. 3, 5.5 and 7 GHz for both band-notched antenna designs with H-slot and two slits, respectively. It can be noticed that at the bandstop frequency 5.5 GHz, nearly all the currents are trapped at the H-shaped slot or two slits which are preventing the current from radiation while at the radiation frequencies 3 and 7 GHz, the current is uniformly distributed through the whole radiating patch.

The CST simulated antenna maximum realized gains in the bore-sight direction versus frequency for the maple-leaf antenna, band-notched antennas with H-slot and two slits are presented in Figure 4.16. It can be seen that the maple-leaf antenna gain is almost stable over the whole frequency band and it ranges from 2 dB to 4.3 dB with gain variation about 2.3 dB through the whole frequency band of interest. For band-notched antenna designs with H-slot and two slits, a sharp gain decrease is remarkably happened in the 5.0-6.0 GHz frequency band. Gain results ensure that the band-notched antennas are not responding in the bandstop frequency range between 5.0 and 6.0 GHz.

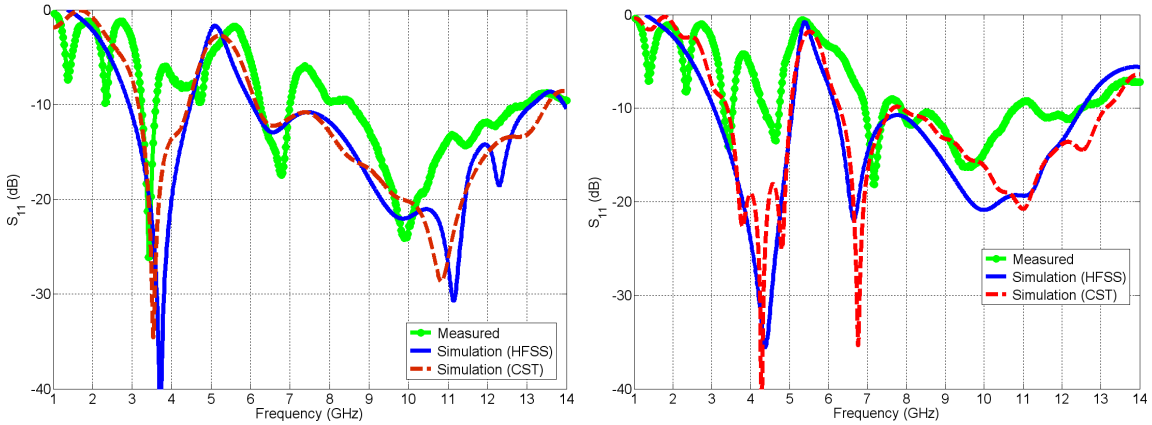

Figure 4.13 Measured and simulated reflection coefficient curves for bandstop antennas (a) using an H-slot (W_S = 0.65 mm, L_S = 8.6 mm and D_S = 18.6 mm) and (b) using two slits (W_S = 0.5 mm, L_S = 10.2 mm, and S = 3 mm).

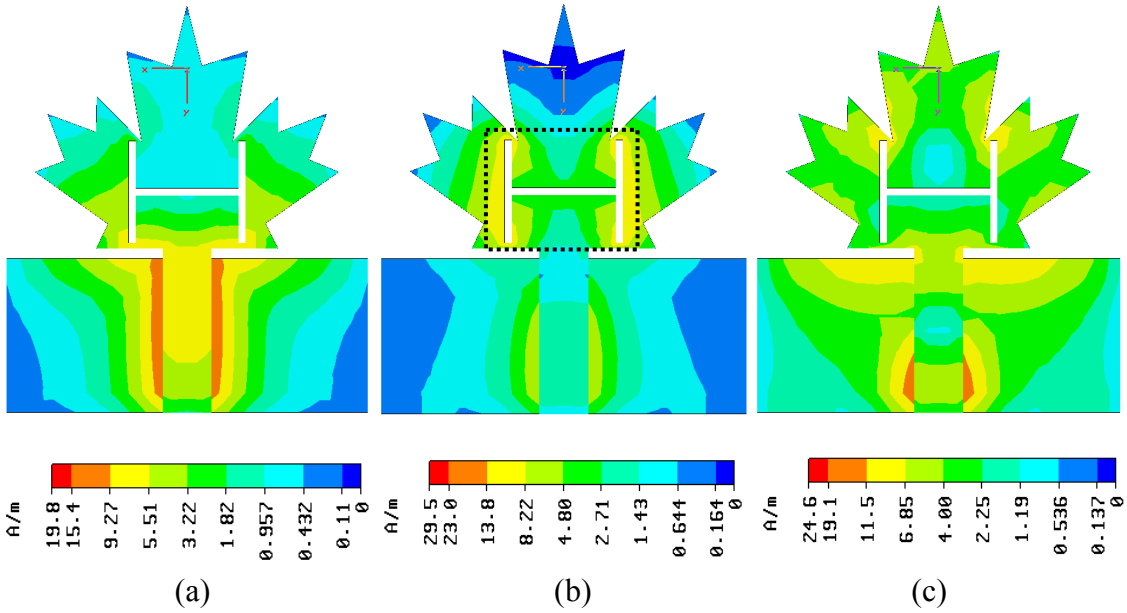

Figure 4.14 Surface current distributions for the first bandstop antenna at the (a) radiating frequency f_1 = 4 GHz, (b) bandstop frequency f_2 = 5.5 GHz and (c) the radiating frequency f_3 = 7 GHz.

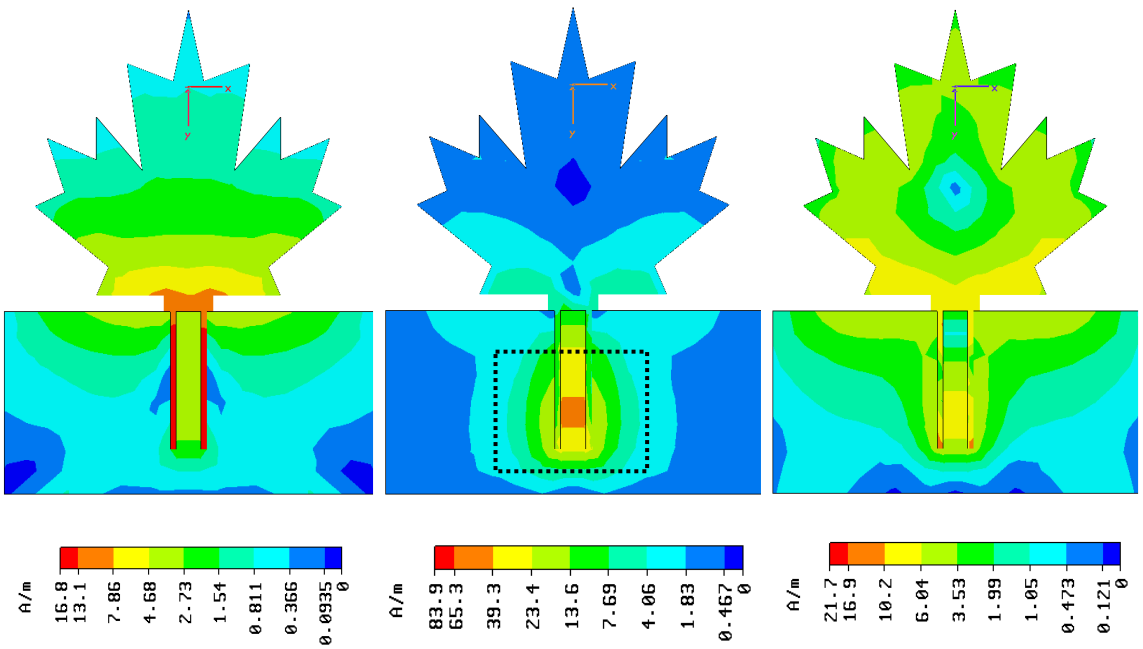

(a) (b) (c)

Figure 4.15 Surface current distributions for the second bandstop antenna at the (a) radiating frequency f_1 = 4 GHz, (b) bandstop frequency f_2 = 5.5 GHz and (c) the radiating frequency f_3 = 7 GHz.

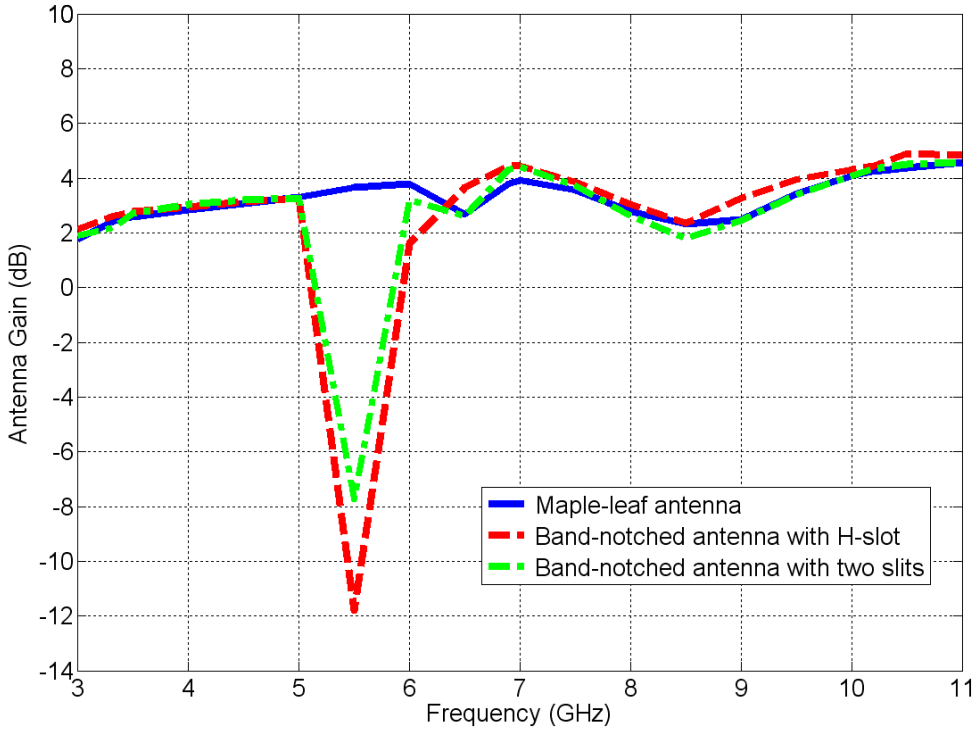

Figure 4.16 Simulated gain curves versus frequency for all three maple-leaf antennas.

4.4 Other Shapes of Monopole Antennas

In this section we continue to enhance the UWB antenna performance to obtain a compact in size antenna with maximum possible impedance bandwidth for UWB operation. We are considering the design of two compact omni-directional UWB antennas with different shape of radiating patches. The first design is the butterfly-shaped monopole antenna while the second one is trapezoidal-shaped monopole antenna with a bell-shaped cut as shown in Figure 4.17 (a) and (b), respectively. The butterfly-shaped monopole antenna size is 35 × 35 mm^2 which is bigger than the previous maple-leaf-shaped antenna (35.5 × 30.5 mm^2) by about 13%. The other proposed design is the trapezoidal-shaped monopole antenna of size 34 × 30 mm^2 which is smaller than the maple-leaf-shaped antenna by about 6%. The best candidate among all printed disc monopole antennas from the antenna size point of view is the trapezoidal antenna with bell-shaped cut. Moreover, the candidate antenna still has UWB impedance bandwidth with reasonable stable radiation characteristics and constant gain through the desired frequency range.

Both proposed antennas are etched on 1.575mm-thick Rogers RT 5880 substrate (ε_r = 2.2 and $tan\delta$ = 0.0009) and fed by 50Ω characteristic impedance microstrip line. The finite ground plane length is L_G = 10 mm and the feed gap width is d = 0.5 mm. The butterfly-shaped antenna consists of a radiating element of two overlapped elliptical discs of major radius a = 16.6 mm and a minor radius b = 10.4 mm (elliptically ratio $a/b \approx 1.6$ forming the two wings of the butterfly). Two annular slot rings of an outer radius r_1 = 2 mm and an inner radius r_2 = 1 mm have been cut out from the radiating patch. They are located at distance c (= e) = 5.2 mm from the two ellipses' edges. These slot rings can

increase the bandwidth of the proposed antenna and they are useful to reduce the overall metallic area.

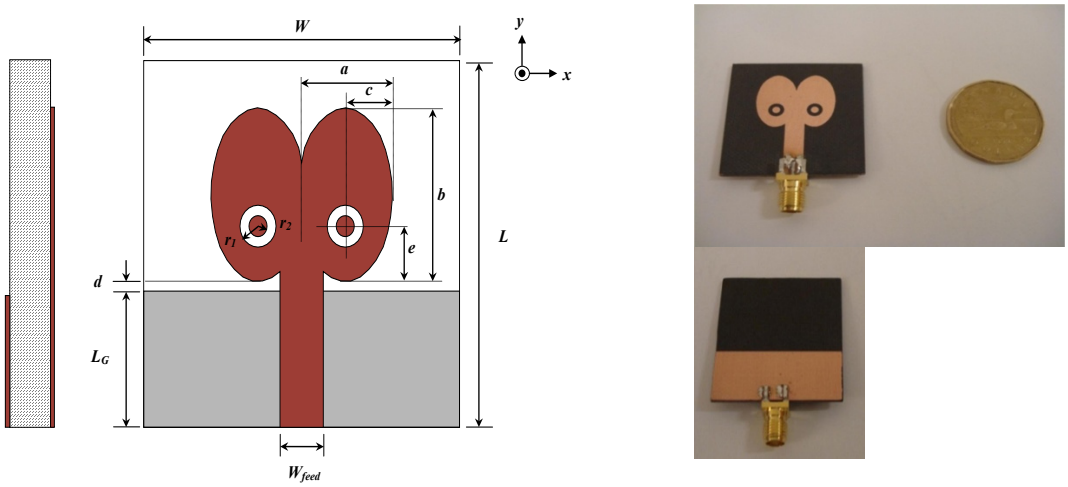

(a)

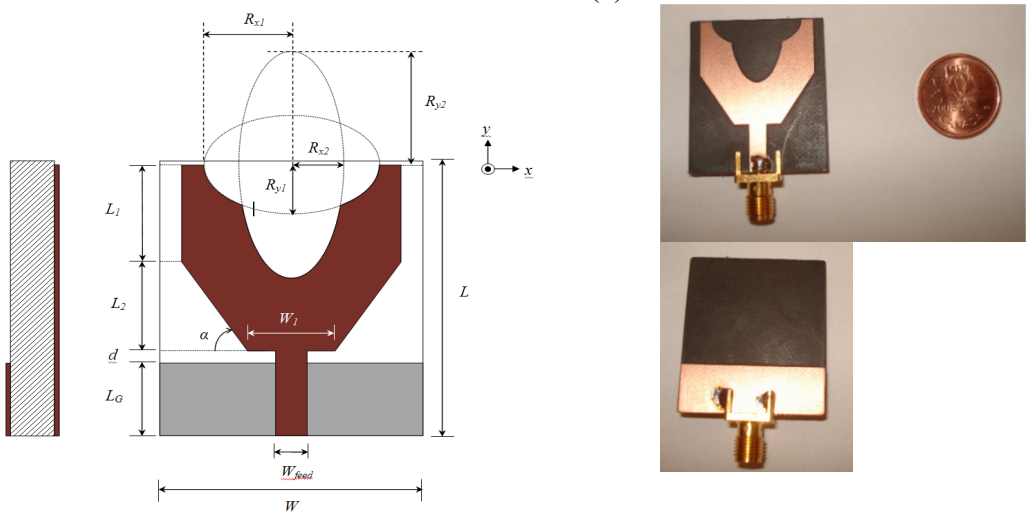

(b)

Figure 4.17 Geometry and photograph of the (a) butterfly-shaped (b) trapezoidal-shaped monopole antenna.

The trapezoidal-shaped antenna consists of a trapezoidal patch of dimensions L_1 = 12 mm, L_2 = 11 mm, W_1 = 10 mm and bevel angle α = 55.7°. Two elliptical cuts have been cut out from the radiating patch forming a bell shaped cut. The first elliptical cut is of a major radius R_{x1} = 10 mm and a minor radius R_{y1} = 6 mm (elliptically ratio R_{x1}/R_{y1} = 1.67). The second elliptical cut is of a minor radius R_{x2} = 6 mm and a major radius R_{y2} =

14 mm (elliptically ratio R_{y2}/R_{x2} = 2.33). An antenna prototype of both structures with optimized parameters has been fabricated for experimental investigation.

The measured and simulated reflection coefficient curves against frequency for butterfly and trapezoidal antennas are plotted in Figure 4.18, respectively. It is observed from the results that the simulated reflection coefficient with Ansoft HFSS and CST are almost in good agreement and both antennas exhibit wide impedance bandwidth from 3 GHz to beyond 12 GHz (FBW is > 110%) for both antennas. The measured results shows that the both antenna designs still have wide impedance bandwidth covering the UWB frequency range. It is shown that there are different resonances occur at different frequencies across the UWB frequency range and the overlap among these resonances achieve the wide bandwidth characteristic of those types of printed monopole antenna. The measured and simulated *E*- and *H*-plane radiation patterns at frequencies 3, 5, 7 and 9 GHz are illustrated in Figure 4.19 and Figure 4.20, respectively. As expected, both antennas exhibit a dipole-like radiation patterns in *E*-plane and good omni-directional radiation patterns in *H*-plane.

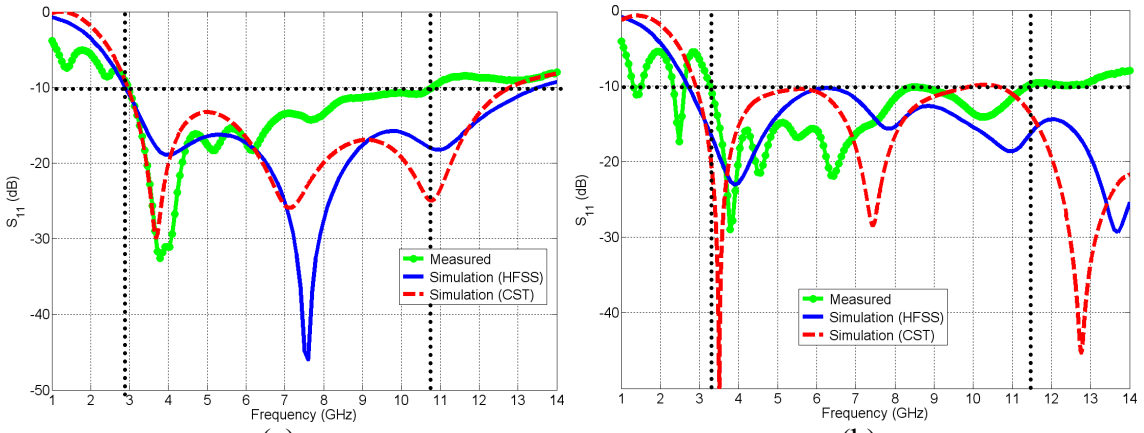

Figure 4.18 Measured and simulated reflection coefficient curves of the (a) butterfly antenna and (b) trapezoidal antenna.

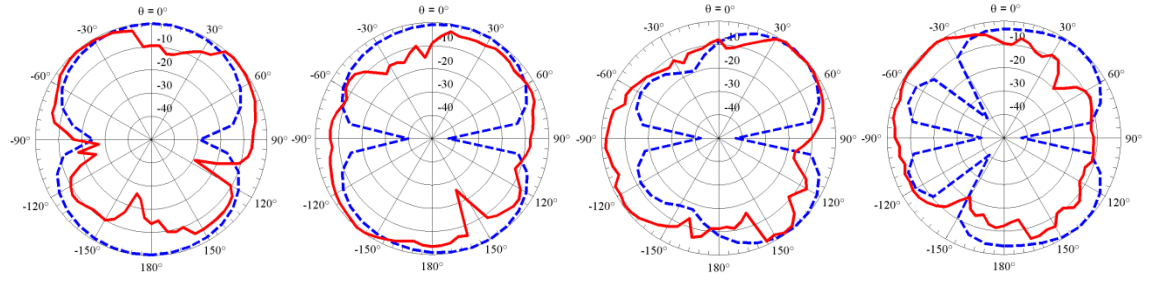

f = 3 GHz f = 5 GHz f = 7 GHz f = 9 GHz

(a) *E*-plane (yz)

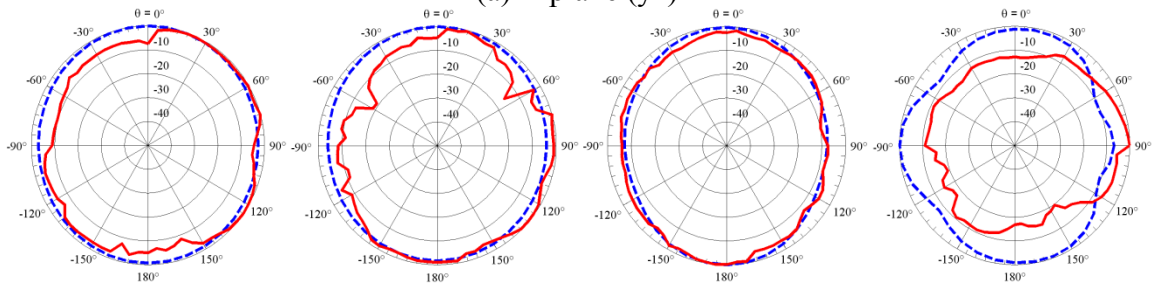

f = 3 GHz f = 5 GHz f = 7 GHz f = 9 GHz

(b) *H*-plane (xz)

Figure 4.19 Measured (red solid) and simulated (blue dashed) (a) *E*-plane and (b) *H*-plane radiation patterns for butterfly antenna.

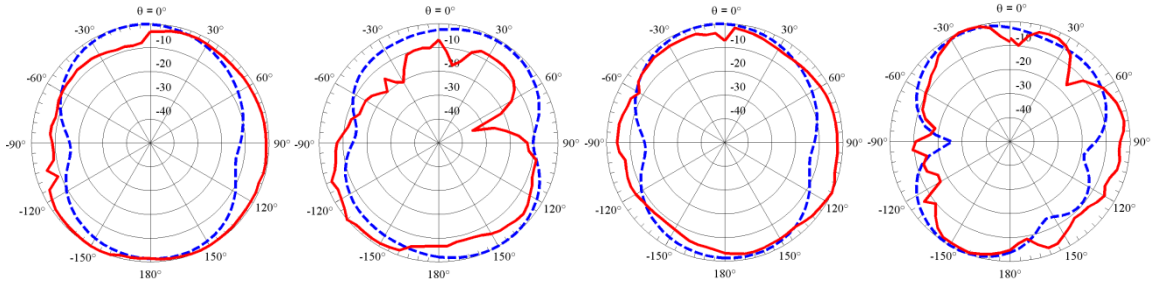

f = 3 GHz f = 5 GHz f = 7 GHz f = 9 GHz

(a) *E*-plane (yz)

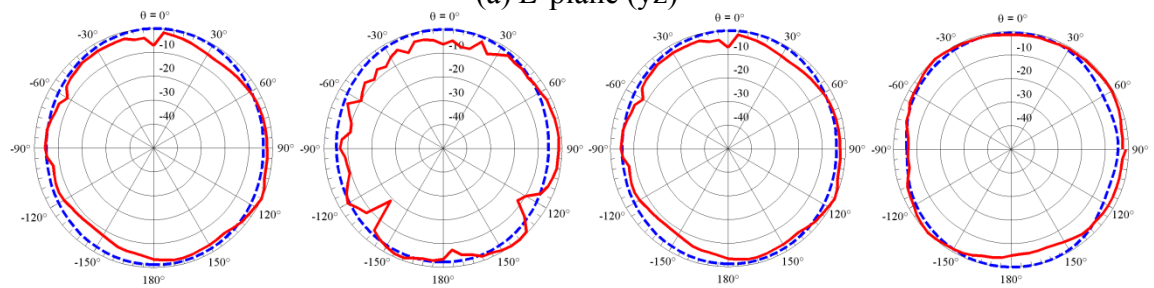

f = 3 GHz f = 5 GHz f = 7 GHz f = 9 GHz

(b) *H*-plane (xz)

Figure 4.20 *E*- and *H*-plane radiation patterns of the trapezoidal antenna. Blue dashed lines for simulated and red solid lines for measured.

4.5 Compact Hybrid Monopole Antenna Loaded with a Dielectric Resonator

In this section, we present a new compact hybrid printed monopole antenna loaded with a dielectric resonator (DR). The antenna consists of a microstrip-line-fed monopole with a finite truncated ground plane printed on a Rogers RT/duroid5880 high frequency laminate with thickness of h = 0.787 mm, loss tangent of $tan\delta$ = 0.0009 and relative permittivity of ε_r = 2.2. The printed monopole is then loaded with a DR of a quarter elliptical cylinder of Rogers RO3010. The printed monopole of width W_2 and length L_2 is installed on the lower side of the substrate at a distance d_x from the substrate edge and is fed by a 50Ω microstrip line of width W_1 and length L_1. The DR has a shape of quarter elliptical cylinder of Rogers RO3010 with relative permittivity of ε_r = 10.2, thickness of H, minor and major radii of A and B, respectively. The reason of using this hybrid combination of a printed monopole with truncated ground of length L_G and DR is to achieve wide bandwidth required for UWB operation. It is obvious that both the ground plane and microstrip line together act as a monopole antenna. The antenna impedance bandwidth can be enhanced in three ways; by loading the monopole antenna with a DR; second by making an inner air groove of radius R inside the DR at distance X and Y from the DR edges and, third by controlling the tuning arm of length L_S in the truncated ground plane for matching purposes and to increase the antenna impedance bandwidth. The role of both inner groove inside DR and the tuning arm is numerically studied and presented in details in [132]. Compared to the antenna in [133], the proposed antenna has a size reduction by 62%, with achieved bandwidth increase of 4%. The optimized antenna parameters are tabulated in Table 4.2.

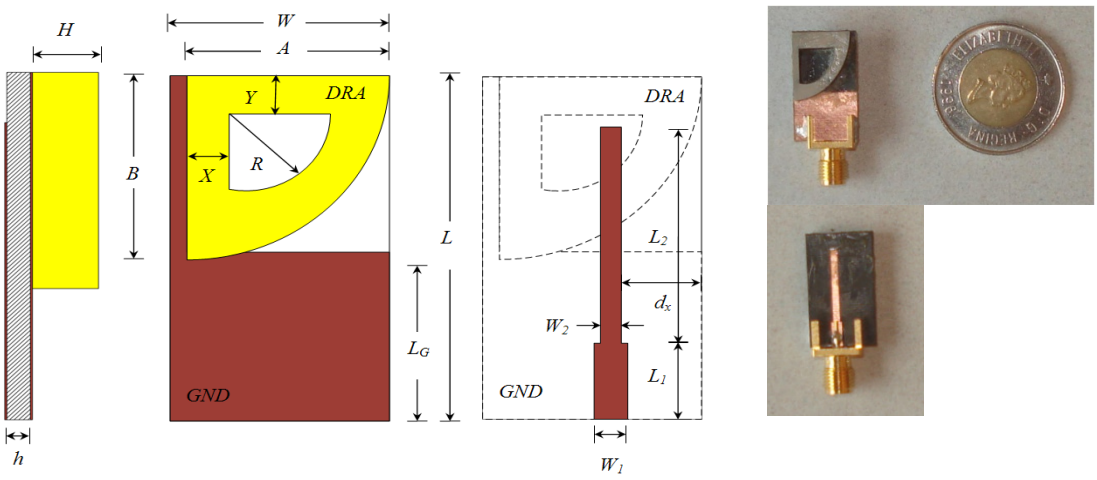

(a) (b)

Figure 4.21 (a) Geometry and (b) photograph of the compact hybrid DR antenna.

Table 4.2 Optimized Parameters for the Proposed Compact Hybrid DR Antenna

Parameter	W	L	A	B	R	X	Y	L_G
Value (mm)	13.0	22.5	12.0	14.0	7.0	1.5	3.5	11.0
Parameter	W_1	L_1	W_2	L_2	L_S	d_x	H	h
Value (mm)	2.0	5.0	1.24	14.2	12.5	4.76	2.54	0.787

The measured and simulated reflection coefficient curves for the proposed compact hybrid DR antenna using Ansoft HFSS and CST are illustrated in Figure 4.22. The simulated impedance bandwidth is from 3.6 to 11.2 GHz while the antenna exhibits a measured impedance bandwidth of dual-band in 3.9-4.4 GHz and in 4.8-10.6 GHz. Figure 4.23(a) and (b) introduce the simulated input impedance, the simulated maximum realized total directive gain in the boresight direction and measured antenna group delay, respectively. The antenna input impedance has almost a real part of 50Ω and imaginary part of 0Ω at most of frequencies in the desired frequency band. It can be noticed that the proposed antenna total directive gain is almost stable over the whole frequency band of interest. The measured and simulated *E*- and *H*-plane radiation patterns at 4, 6 and 8 GHz for the proposed antenna prototype are plotted in Figure 4.24(a) and (b), respectively.

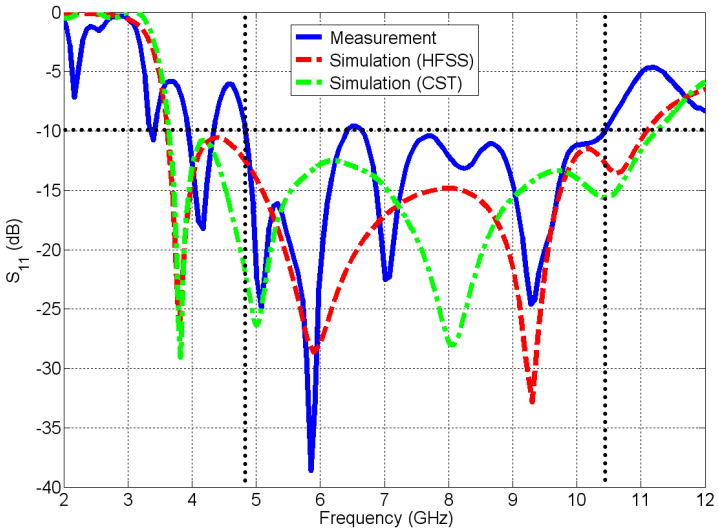

Figure 4.22 Simulated and measured reflection coefficient curves for the proposed compact hybrid DR antenna.

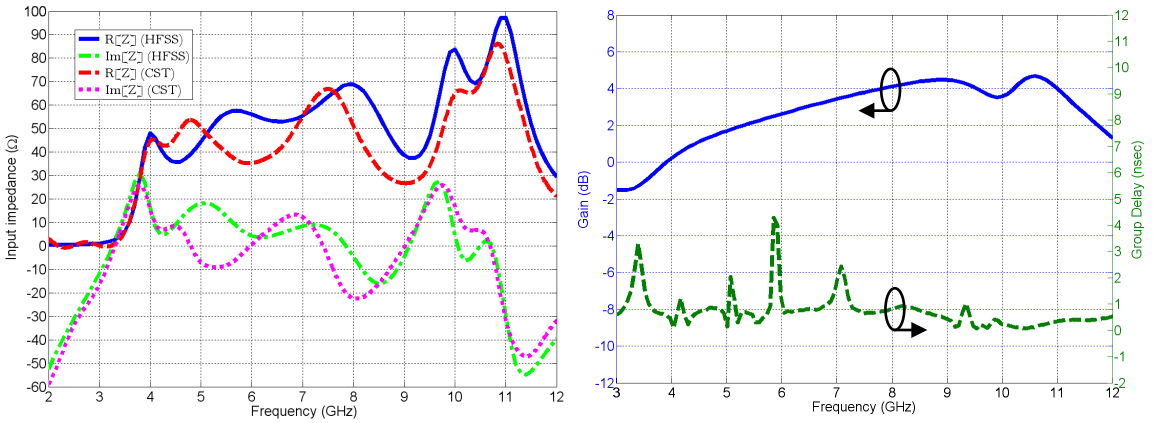

(a) (b)

Figure 4.23 Simulated (a) input impedance and (b) realized total directive gain and measured group delay for the proposed compact hybrid DR antenna.

The surface area of the proposed hybrid monopole loaded with DR is 13 × 22.5 mm^2 which is considered 71% less compared to the surface area of the previously designed trapezoidal antenna with bell-shaped cut (34 × 30 mm^2). Taking the antenna height along z-axis into account, the overall size of the proposed hybrid DR antenna is 13 × 22.5 × 3.327 mm^3 which is considered 39.5% less compared to the overall size of the

previously designed trapezoidal antenna with bell-shaped cut (30 × 34 × 1.575 mm^3). A comparison among all different UWB antenna design prototypes is summarized in Table 4.3. The trapezoidal monopole antenna with bell-shaped cut is considered the best candidate for UWB operation because it has a large bandwidth of 112% covering almost the whole UWB frequency range with small size and good gain stability.

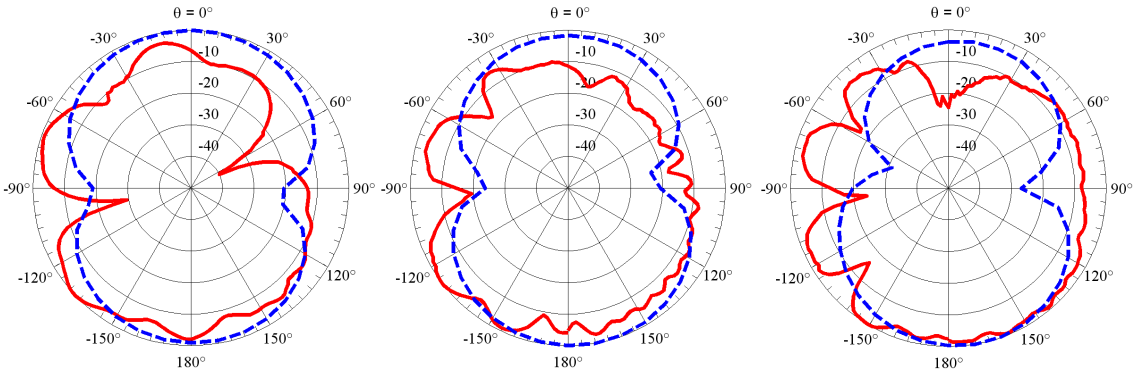

f = 4 GHz f = 6 GHz f = 8 GHz

(a) *E*-plane (yz)

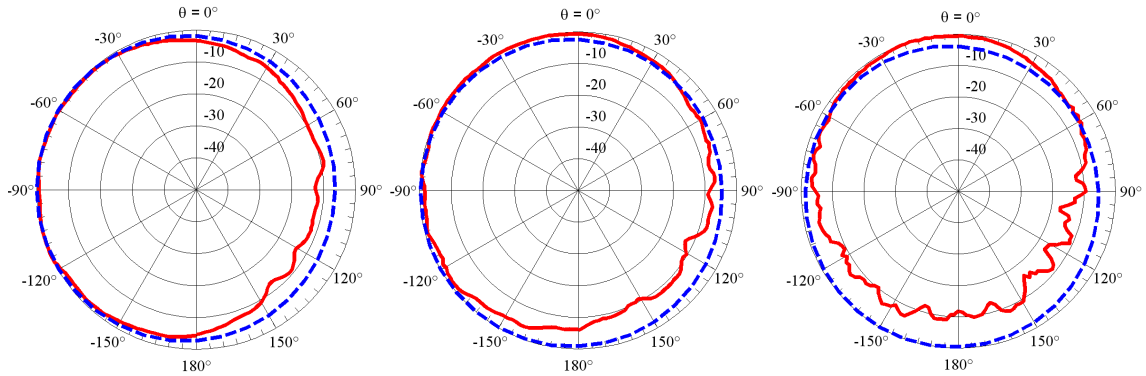

f = 4 GHz f = 6 GHz f = 8 GHz

(b) *H*-plane (xz)

Figure 4.24 Measured (red solid line) and simulated (blue dash line) *E*- and *H*-plane radiation patterns for the proposed compact hybrid DR antenna at 4, 6 and 8 GHz.

Table 4.3 Comparison Among Different UWB Antenna Design Prototypes

Parameter	Circular disc monopole with two steps and a circular slot	Maple-leaf antenna	Butterfly antenna	Trapezoidal antenna with bell-shaped cut	Hybrid monopole DR antenna
Dimensions (mm)	41 × 50 × 1.575	30.5 × 35.5 × 1.575	35 × 35 × 1.575	30 × 34 × 1.575	13 × 22.5 × 3.327
10 dB RL bandwidth (GHz)	3.0~11.5	(Dual-band) 4.1~7.0, 8.7~13.3	3.0~10.8	3.2~11.4	(Dual-band) 3.9~4.4, 4.8~10.6
10 dB RL bandwidth (%)	117%	52%, 42%	113%	112%	12%, 75%
Realized gain (dB)	3.4~5.2 ±1.8	2.0~4.3 ±2.3	2.0~4.7 ±2.7	2.7~5.3 ±2.6	0.2~4.4 ±4.2
Group delay (ns)	4.2	2.7	1.5	4.2	4.2

4.6 Summary

In this chapter, different UWB disc monopole antennas have been developed in microstrip PCB technology to achieve low profile and ease of integration. Parametric studies to see the effect of some antenna parameters on its performance have been numerically investigated. For further understanding the behavior of the proposed antennas, surface current distributions have been simulated and presented. Different techniques for obtaining bandstop function in the 5.0-6.0 GHz frequency band to avoid interference with other existing WLAN systems have been numerically and experimentally presented. The effects of band-notched parameters on the band-notch frequency and bandwidth have been studied. A hybrid technique of combining both printed monopole antenna with DR has also been used to achieve wide bandwidth along with a very compact structure. It has been shown that UWB characteristic was achieved due to the overlapping of the closely spaced resonances over the frequency band. The chapter has investigated the frequency domain performances of different printed disc monopole antennas and hybrid antenna. Experimental as well as the simulated results have confirmed UWB characteristics of the proposed antennas with nearly stable omni-directional radiation properties over the entire frequency band of interest. These features and their small sizes make them attractive for future UWB applications.

Chapter 5

UWB Feed Networks and Associated Components

5.1 Introduction

Due to the rapid increase in using UWB technology for short-range wireless communications, researchers are now developing various components that can operate in the UWB frequency range. Feed networks, transitions, couplers, and phase shifters are considered fundamental passive components and key elements extensively used in different microwave circuits and systems such as antenna array feed networks, amplifiers, mixers, modulators, and beamforming systems [88]. This chapter addresses the development of different structures for UWB feed networks, vertical transitions, hybrid couplers, and phase shifters in inexpensive microstrip PCB technology. The design of UWB feed networks based on modifying the traditional Wilkinson power divider is introduced. The equivalent circuit models for those components are given and analyzed in details in Appendix A. To optimize the performance of those structures, EM simulation is used to tune their physical dimensions. For achieving a higher gain for certain applications, antenna arrays may be used. The previously designed feed network is used to construct compact and inexpensive microstrip printed two-element and four-element UWB linear antenna

arrays with increased directivity. The UWB antenna element used is the previously designed antenna discussed in Chapter 4.

The proposed vertical transitions, hybrid couplers and phase shifters can provide a large dynamic coupling range with low insertion losses across the UWB frequency band. These advantages can make the designed transitions, couplers and phase shifters good candidates for the design of UWB subsystems as beamforming matrices in compact two-layer microstrip PCB topologies. The analysis of the proposed two-layer microstrip-to-microstrip vertical transition is performed by assuming the structure as a four-port coupler with one input port, one output port and the other two ports are terminated with open circuit loads. Details of the analysis based on the even-odd mode quasi-static analysis are presented in Appendix B.

The designed vertical transitions are then used to develop two-layer 90° 3dB hybrid couplers for UWB applications. Starting from the design parameters of the transitions, the full wave EM simulation programs are used to optimize those parameters to meet the design requirements for the UWB hybrid couplers such as good return loss and isolation with reasonable insertion losses across the whole UWB frequency band. Moreover, the phase between the direct and the coupled signals should be 90° throughout the frequency range of interest. Also, the designed vertical transitions are then used to develop two-layer 45° phase shifters for UWB applications.

The chapter is organized as follows; Section 5.2 shows the numerical and experimental results for the design of UWB feed network based on a modified two-section Wilkinson power divider/combiner. Section 5.3 focuses on the design of two-element and

four-element UWB linear antenna arrays by exploiting the previously designed antenna elements and feed networks. The design of two different shapes of vertical microstrip transitions is presented in Section 5.4. The design of trapezoidal- and butterfly-shaped vertical microstrip transitions are addressed in subsections 5.4.1and 5.4.2, respectively. From the previously designed two-layer vertical microstrip transitions, we developed the two-layer 90° 3 dB hybrid couplers for UWB applications presented in Section 5.5. Subsections 5.5.1 and 5.5.2 describe the design of trapezoidal- and butterfly-shaped microstrip hybrid couplers, respectively. Then Section 5.6 presents the design of UWB phase shifters and finally the conclusion is outlined in Section 5.7.

5.2 UWB Feed Networks

In this section, two different UWB feed network structures based on a modified two-section Wilkinson power divider for UWB applications are presented. The first feed network is designed and simulated numerically. The second one is designed, simulated, fabricated and tested experimentally. From the equations in Appendix A, according to the desired bandwidth ratio, the initial values for the feed network parameters can be determined. With the aid of EM simulation tools, we can optimize the parameters of the feed network by using full-wave analysis of the whole structure to achieve the desired performance. Both simulated and measured results show that the proposed feed networks have almost equal power split with low insertion loss and good return loss at all ports. The isolation between the two output ports are found to be better than 10 dB which make these feed networks good as dividers and/or combiners at the same time.

5.2.1 Design Methodology for UWB Feed Network

For designing a UWB feed network, a modified Wilkinson power divider is proposed. Figure 5.1 shows the schematic diagram of the proposed feed network for UWB operation. It simply consists of modified one-section Wilkinson power divider with characteristic impedance of Z_1 and electrical length of θ_1. Broadening the bandwidth is achieved by adding stub matching network to each branch with additional transmission lines at the end. The first transmission lines are extended (Z_1, θ_1') and one open circuit (OC) stub with (Z_S, θ_S) are added to each branch. Also, we added another section of Wilkinson power divider with (Z_2, θ_2) at the end of the stub matching network. The resistor at the end of the second section of Wilkinson power divider can be removed without affecting the feed network performance. By adjusting the length and width of the OC stubs, the bandwidth can be broadened. To determine the divider basic parameters for UWB frequency operation, the even-odd mode decomposition analysis is to be performed. Details of the even-odd mode decomposition analysis of such kind of modified two-section Wilkinson power dividers are outlines in Appendix A.

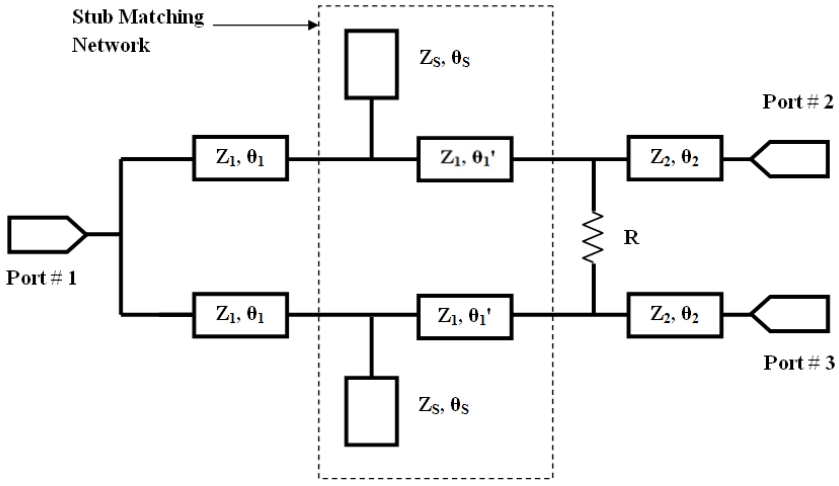

Figure 5.1 Schematic of the proposed UWB 1-to-2 feed network.

The design procedure is relatively simple. First, a traditional Wilkinson power divider should be designed with its center frequency f_0 at 6.85 GHz and the bandwidth ratio of 3.5:1 covering the whole UWB frequency range (3.1-10.6 GHz). Second, from the design equations given in Appendix A, according to the desired bandwidth ratio f_U/f_L, the initial values for the divider parameters $\theta_1, Z_1, \theta_2, Z_2,$ and B_s can be determined by means of elementary transmission line theory [89]. Then, the length of the extended line is chosen arbitrarily to be different than that of the main line, i.e. $\theta_1' \neq \theta_1$ to obtain more flexibility and degree of freedom and hence the bandwidth can be enhanced. With the aid of full-wave EM numerical modeling techniques, all other optimized parameters can be determined by using full-wave analysis of the whole structure. Simulations are carried out using both Ansoft HFSS and CST simulation programs. To validate the proposed design, a prototype is designed, fabricated and tested experimentally. Measured results show good performance within the whole UWB frequency range.

5.2.2 Modified Two-Section Wilkinson Power Divider

The initial investigations of the second proposed UWB feed network parameters were made from the formulas in Appendix A and results are summarized in Table 5.1. Full-wave analysis has been carried out using both EM simulator Ansoft HFSS and CST for comparison. The proposed UWB feed network is designed, fabricated and then experimentally tested. The circuit layout and the photograph of the UWB feed network prototype are presented in Figure 5.2(a) & (b), respectively. The substrate used is Rogers RT5880 with a thickness of 0.787 mm, relative permittivity ε_r = 2.2, and loss tangent $tan\delta$ = 0.0009. The overall size of the proposed divider is 22 mm × 19.6 mm. The parameters

of the proposed feed network were optimized to attain good return loss at all ports and good isolation over the whole UWB frequency range. The final dimensions and parameters for the proposed feed network are summarized in Table 5.2.

The simulated S-parameters for the proposed feed network are shown in Figure 5.3(a). It can be seen that the power is divided equally between the output ports with very small insertion loss ranges from 0.1 dB to 0.5 dB (HFSS) or from 0.5 dB to 1.0 dB (CST). The simulated return losses at all three ports are also presented in the same Figure. The return loss at the input port (S_{11}) is better than 13 dB and it reaches to less than 35 dB at some frequencies while the return losses at the output ports (S_{22} and S_{33}) are lower than 10 dB with better than 29 dB at some frequencies through the whole UWB frequency range. The isolation between the two outputs ports $S_{23} = S_{32}$ is found to be better than 10 dB throughout the desired frequency range.

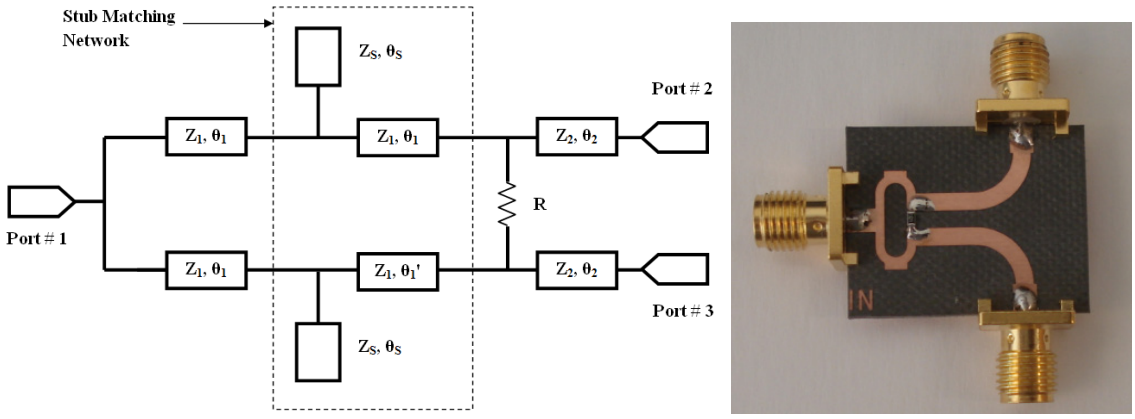

(a) (b)

Figure 5.2 (a) Circuit and (b) photograph of the proposed UWB feed network

Table 5.1 Initial Parameters for the Proposed UWB Feed Network.

Parameter	Z_1	θ_1	θ_1'	Z_2	θ_2	Z_S	θ_S
value	89.2 Ω	48.76°	27.1°	61Ω	137°	52.1 Ω	11.2°

For further investigating the performance of the proposed UWB feed network, the phase difference and the group delay between the two outputs ports are simulated using HFSS and shown in Figure 5.3(b). It can be noticed that the output signals are in phase with phase difference is 0°±0.5° across the whole frequency range. Also, the simulated group delay is almost constant and less than 0.14 ns which show good linearity within the UWB frequency range. The S-parameters for the feed network are measured using Agilent E8364B programmable network analyzer and shown in Figure 5.4. It can be seen that the proposed UWB feed network still have good return losses, insertion losses and isolation between output ports across most frequencies in the UWB frequency range.

Table 5.2 Optimized Parameters of the Proposed UWB Feed Network (Unit: mm)

Parameter	W_o	L_o	W_1	L_1	W_1'
Value	2.4	5.0	0.9	4.0	0.9
Parameter	L_1'	W_2	L_2	W_S	L_S
Value	2.5	1.8	5.0	2.3	0.8

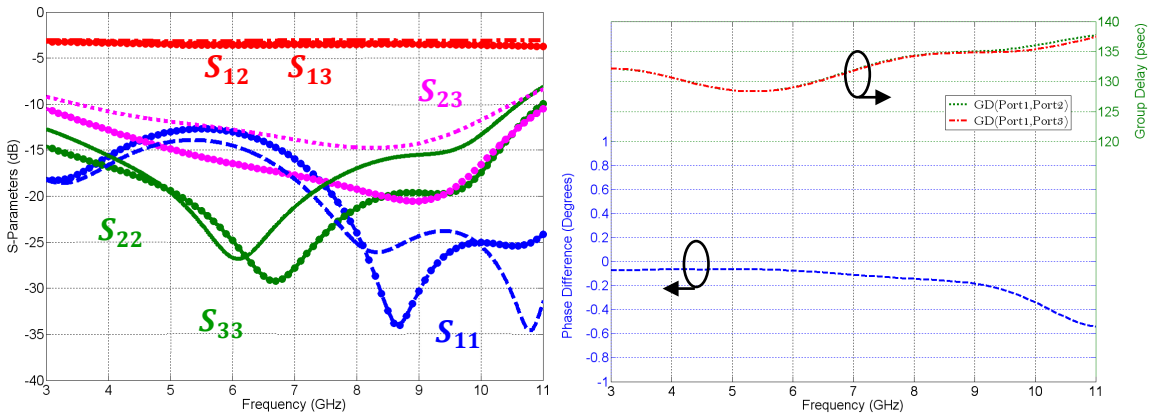

(a) (b)

Figure 5.3 Simulated (a) return loss, insertion loss, and isolation (HFSS: with marker, CST: without marker) (b) phase difference and group delays between ports.

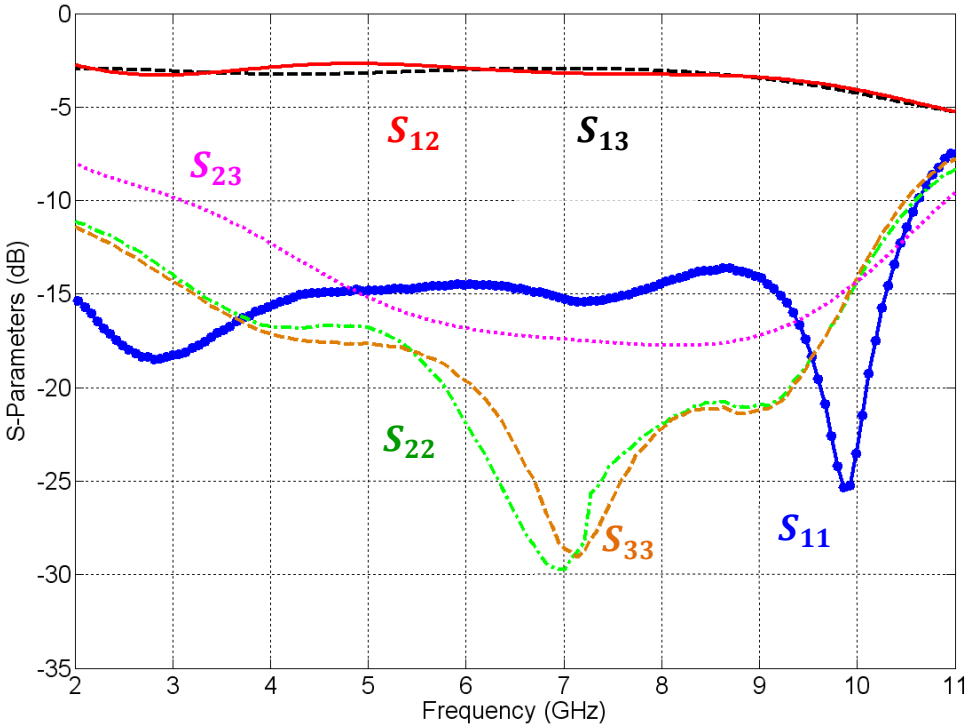

Figure 5.4 Measured return loss, insertion loss, and isolation for the UWB feed network.

5.3 Two- and Four-Element UWB Antenna Arrays

The two-element and four-element UWB linear antenna arrays are constructed by feeding two or four UWB antenna elements with previously designed UWB feed networks. The geometry and photograph of the proposed two-element and four-element linear antenna array prototypes are shown in Figure 5.5(a) and (b), respectively. The inter-element spacing between the antenna elements has a great effect on the overall performance of the array. Also, the addition of feed networks to the array may affect the array performance. In order to investigate the effect of different design parameters on the array performance, extensive parametric studies were carried out using full-wave analysis of the whole arrays. The target here is to design a two-element and four-element linear antenna arrays with good impedance matching characteristics across the desired UWB fre-

quency range. Moreover, the designed arrays should attain higher gain, stable radiation patterns, phase linearity, and constant group delay characteristics throughout the desired frequency band of interest.

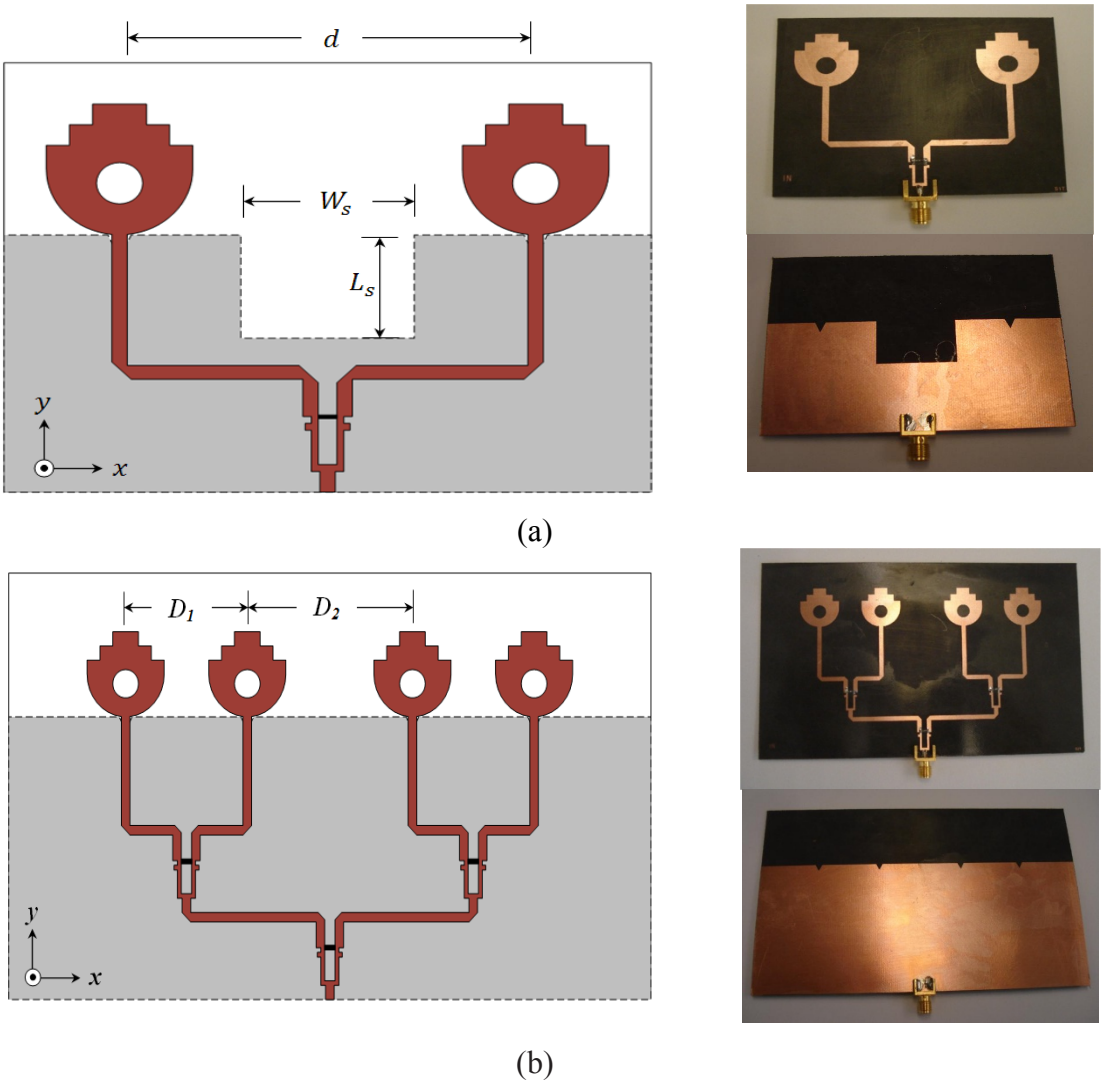

Figure 5.5 Geometry and photograph of the proposed (a) two-element and (b) four-element UWB printed disc monopole antenna array.

It has been found from the parametric studies that using a rectangular cut in the common ground plane of dimensions (W_S and L_S) in the two-element antenna array, a good array performance can be achieved through the entire UWB frequency range. The

reason behind using the rectangular cut in the common ground plane is to enhance the impedance matching characteristics of the array by reducing the mutual coupling effect between the closely adjacent two antenna elements. The center-to-center distance between the two antenna elements are chosen to be close to the half wavelength at the UWB lower edge frequency f_L = 3.1 GHz which is d = 54 mm. However the chosen inter-element spacing is higher than the minimum requirement to avoid grating lobes, the achieved array impedance matching bandwidth is better. The optimized values for the rectangular cut in the common ground plane are: W_S = 22 mm and L_S = 15 mm.

Properly adjusting the interspacing distance parameters D_1 and D_2 between the antenna elements, the impedance matching characteristics of the four-element array and the array performance can be controlled. This can be done by applying full-wave analysis of the whole structure and using extensive parametric study and different optimization techniques. For maximum achieved bandwidth, the optimized interspacing distances between the four antenna elements were found to be D_1 = 28.5 mm and D_2 = 38.5 mm. The non-uniform array is chosen here to achieve better array impedance matching bandwidth than that of the uniform array. Using uniform array with large inter-element spacing will result in higher grating lobes. With the proposed non-uniform array, the array impedance bandwidth is enhanced with better grating lobe levels compared to the large uniform array. D_2 is chosen to be smaller than D_1 to reduce the effect of mutual coupling among center elements which results in better impedance matching performance. The measured and simulated reflection coefficient curves of two- and four-element antenna arrays are shown in Figure 5.6(a) and (b), respectively. It can be noticed from the results that the measured and simulated reflection coefficient curves versus frequency using both HFSS

and CST are in good agreement. The two-element array has impedance bandwidth starting from 3.1 to 10.6 GHz covering the whole UWB frequency range. There are some factors that negatively affect the overall array performance in case of four-element array. One factor is the mutual coupling among the four antenna elements which is greater than that of two-element array. Also the use of three feed networks in four-element array compared to only one in two-element array badly affects the array performance. According to the previously mentioned factors, the four-element array impedance bandwidth is multi-band instead of ultra-wideband within the UWB range, i.e. 3.26-3.5 GHz, 4.16-4.52 GHz, 5.18-9.14 GHz, and 9.62-10.22 GHz. The simulated maximum realized total directive gain in the boresight direction of both two- and four-element antenna arrays are presented in Figure 5.7. The gain of the single antenna element is plotted here for comparison purposes. The average gain of the two- and four-element arrays are about 3 dB and 6 dB higher than that of the single element as expected, respectively.

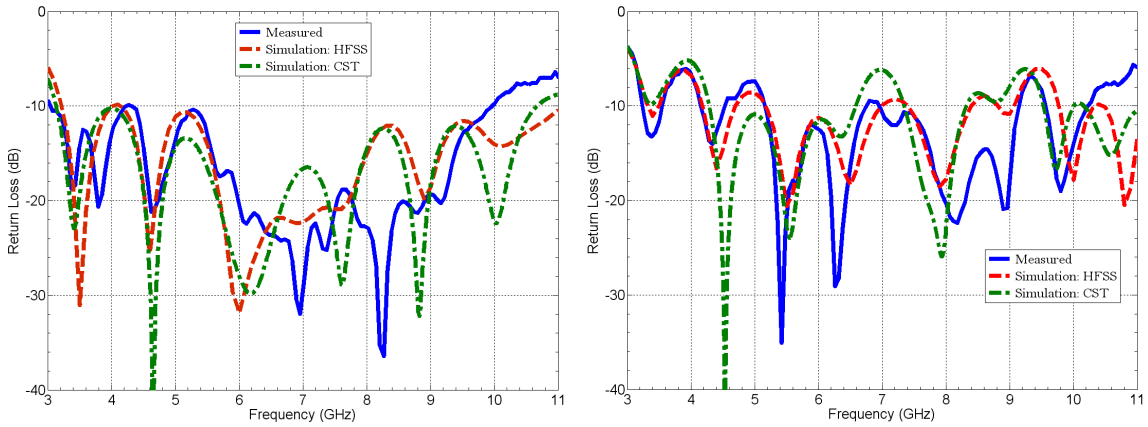

(a) (b)

Figure 5.6 Measured and simulated reflection coefficient curves versus frequency for the (a) two-element and (b) four-element antenna array.

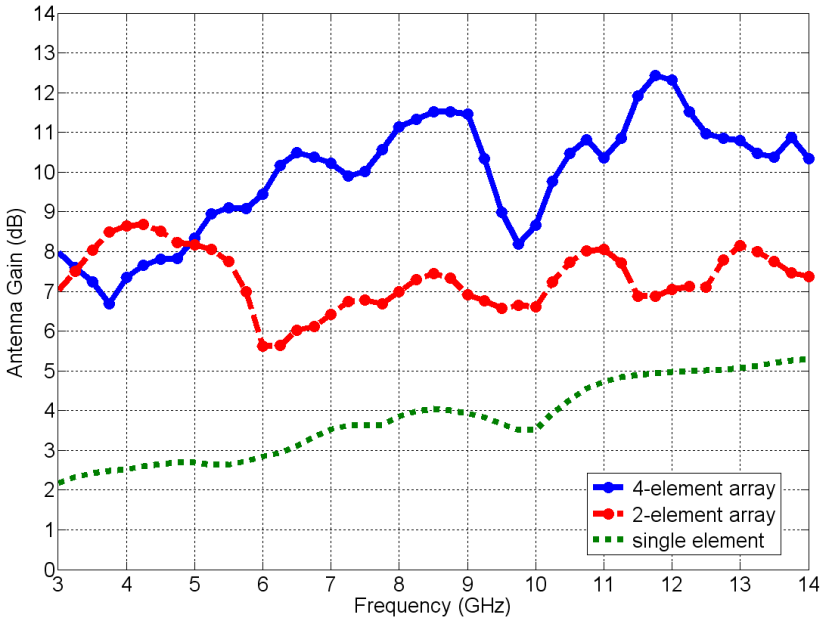

Figure 5.7 Simulated gains of the two-element and four-element antenna array compared to a single antenna element.

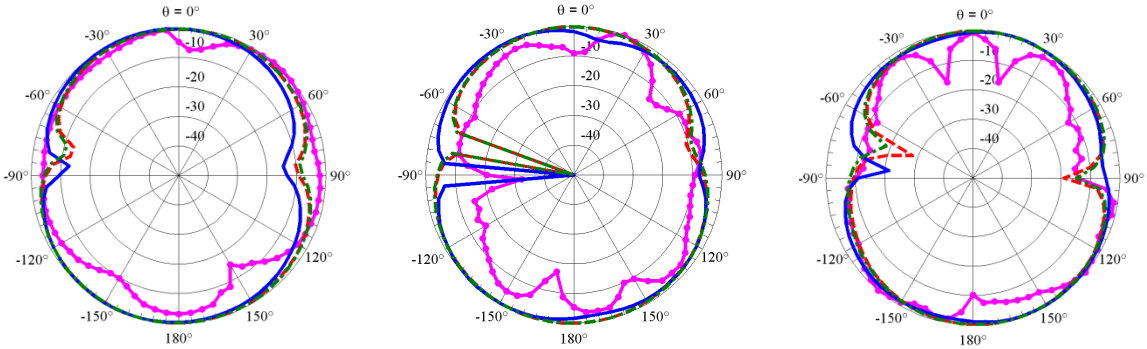

f = 3 GHz f = 5 GHz f = 7 GHz

(a) *E*-plane

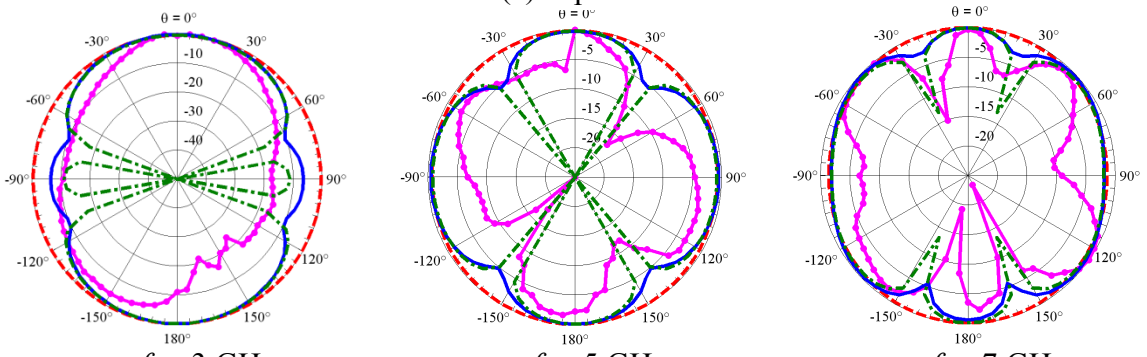

f = 3 GHz f = 5 GHz f = 7 GHz

(b) *H*-plane

Figure 5.8 The normalized *E*- and *H*-plane radiation patterns of the two-element array at 3, 5 and 7 GHz. (solid: antenna array, dash-dot: without mutual coupling, dash: single antenna element, marker: measured).

The normalized *E*- and *H*-plane radiation patterns of the two- and four-element arrays at different frequencies, i.e. 3, 5 and 7 GHz are shown in Figure 5.8 and Figure 5.9, respectively. In those figures, the effect of mutual coupling among the antenna elements on the array radiation characteristics is numerically studied. The radiation patterns of both the two- and four-element arrays with and without mutual coupling effect are simulated. The measured radiation patterns of both antenna arrays are also presented. The radiation patterns of the single antenna element are shown for comparison purposes.

The *E*-plane radiation patterns of both two- and four-element arrays are almost the same like the single antenna element with no big change. The *H*-plane radiation patterns of both arrays are bi-directional compared to the omni-directional pattern of the single antenna element with good stability with frequency.

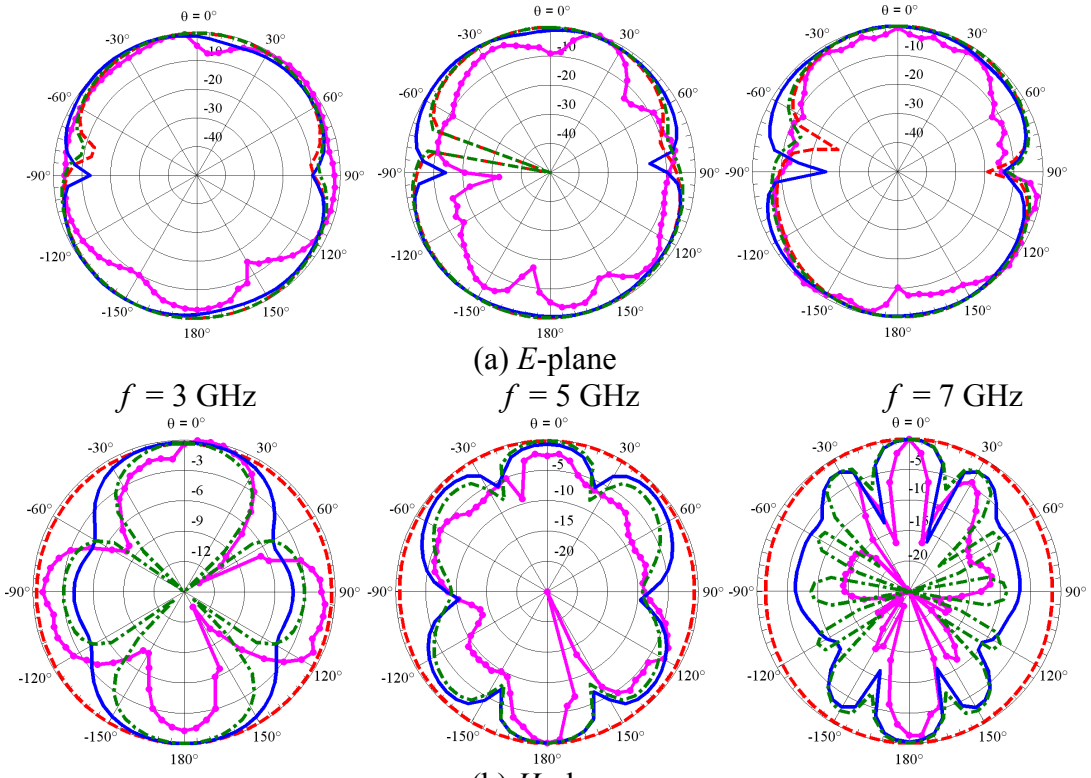

(a) *E*-plane

f = 3 GHz *f* = 5 GHz *f* = 7 GHz

(b) *H*-plane

Figure 5.9 The normalized *E*- and *H*-plane radiation patterns of the four-element array at 3, 5 and 7 GHz. (solid: antenna array, dash-dot: without mutual coupling, dash: single antenna element, marker: measured).

5.4 UWB Two-Layer Microstrip Vertical Transitions

The Fabrication of all dual layer structures has been performed in the Poly-Grames research center in Ecole Polytechnique at University of Montreal. Poly-Grames research center has the ability to manufacture printed circuits on all types of microwave substrates. Their present fabrication capabilities are limited to two layers (double sided) and hole (via) metallization are limited to circuits no larger than 4''x 4'' for copper. The process starts with fabricating each layer separately as a single layer then both layers are stacked together by a special type of adhesive materials, i.e. epoxy glue using a specialized machine for that purpose. Epoxy adhesives are better in heat and chemical resistance than other common adhesives. The alignment between substrates is made using 0.125'' pins at 2.5'' center to center. It is well-known that the big problem with dual layer structures is the problem of misalignments between the two stacked layers and hence this will lead to degradation in the circuit performance in measurement compared to simulations results.

In this section, two different designs for aperture or slot-coupled vertical microstrip-to-microstrip transitions for UWB applications are presented. In those proposed designs, the microstrip coupling patches have either trapezoidal- or butterfly-shaped structures while the coupling slots have rectangular structures. The microstrip coupling patches may take any shape such as rectangular, circular or any arbitrary shape …etc. Trapezoidal- and butterfly-shaped coupling patches have been chosen for our proposed transitions based on a comparison was done among different shapes for the microstrip coupling patches seeking for the best candidate for designing a good UWB microstrip vertical transition. It has been found that both the trapezoidal and butterfly shapes are bet-

ter than the other two rectangular and circular shapes for the microstrip coupling patches. The simulated results using Ansoft HFSS and CST show that the proposed transitions have small insertion loss values and high return loss values over the UWB frequency range (3.1-10.6 GHz). All proposed transition designs are built using two RT Duroid 5880 substrates with thickness of h = 0.508 mm, relative permittivity of ε_r = 2.2 and loss tangent of $tan\delta$ = 0.0009. The overall dimensions of proposed transitions are 20×20 mm^2.

5.4.1 Design Methodology for UWB Vertical Transitions

The arbitrary structure of the proposed UWB microstrip vertical transition as a four-port coupler is shown in Figure 5.10. It simply consists of two arbitrary-shaped microstrip patches connected to the input and output microstrip lines and they are located on the top and bottom layers of the structure. The coupling between these microstrip patches is achieved by cutting an arbitrary-shaped slot in the common ground plane located at the middle layer. First, the analysis should be performed for those UWB transitions to come up with the necessary design parameters. Those kinds of transitions with complex-shaped patches are difficult to be analyzed using the even–odd mode quasi-static analysis of broadside slot-coupled microstrip lines [88], [112]. Transitions with rectangular-shaped patches can be easily analyzed and the equivalent rectangular-shaped patch parameters can be obtained instead. Details of the analysis of such kind of two-layer microstrip vertical transition structures are discussed in Appendix B.

The target here is to design a microstrip two-layer vertical microstrip transition for UWB operation from 3.1 GHz to 10.6 GHz. So it is better to design the transition at

the center frequency of operation f = 6.85 GHz with a bandwidth of 7.5 GHz to cover the whole UWB frequency range. Initially, the value of the patch and coupling slot length l is set to quarter of the effective wavelength at the centre frequency, i.e. 7.8 mm. The microstrip transmission lines at the top and bottom layers have 50Ω characteristic impedance and hence their widths W_m can be found from the microstrip design equations [107]. For a given coupling value C, the even- and odd-mode characteristic impedances can be calculated using Eq. (B.9) and Eq. (B.10). Table 5.3 shows the relationship between the even- and odd-mode characteristic impedances for different transition coupling values.

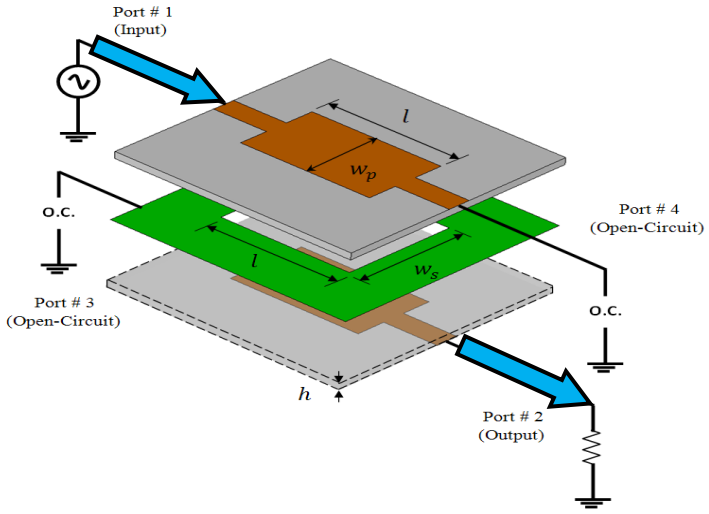

Figure 5.10 The arbitrary microstrip vertical transition as a four-port coupler.

Table 5.3 Even- and Odd-mode Impedances for Different Coupling Values

	Coupling Values C (dB)					
Characteristic Impedances	0.3 (10.46 dB)	0.4 (7.96 dB)	0.5 (6.02 dB)	0.6 (4.44 dB)	0.7 (3.1 dB)	0.8 (1.94 dB)
$Z_{0e}(\Omega)$	68.1	76.3	86.6	100	119	150
$Z_{0o}(\Omega)$	36.7	32.7	28.8	25	21	16.7

It can be noticed that by increasing the coupling values, even-mode characteristic impedance (Z_{0e}) increases while the odd-mode characteristic impedance (Z_{0o}) decreases. From the equivalent rectangular-shaped patch initial parameters and the calculated even- and odd-mode characteristic impedances for the desired coupling value, the full-wave analysis is used to optimize the complex-shaped transition parameters to achieve the UWB operation with good performances.

Two different transition configurations using different patch shapes are presented. The first configuration uses trapezoidal-shaped patches on the top and bottom layers and a rectangular coupling slot in the middle ground plane layer. The performance of this transition can be controlled by adjusting the trapezoidal parameters (minor width, major width) and the coupling slot dimensions (width and length). The other configuration has butterfly-shaped patches and a rectangular slot in the common ground plane. In this design, the transition characteristics are controlled by the butterfly patch dimensions (radius, angle and stub length) and the coupling slot dimensions (width and length). This configuration has five parameters to adjust and hence it offers more degree of freedom to achieve the design goal compared to the trapezoidal transition.

5.4.2 Trapezoidal-Shaped Microstrip Vertical Transition

The proposed two-layer trapezoidal-shaped microstrip vertical transition is shown in Figure 5.11. The patches used here in this proposed transition are of trapezoidal shapes with minor and major widths of W_{p1} and W_{p2}, respectively and the rectangular coupling slot of width W_S. The length of the microstrip trapezoidal coupling patch L_p which is

equal to the length of the rectangular coupling slot L_S, i.e. $L_p = L_S$. The initial parameters of the proposed transition can be determined from Eq. (B.11) through Eq. (B.15) in Appendix B. The electrical equivalent circuit of the proposed two-layer microstrip vertical transition is not easy to obtain, especially it employs arbitrary shaped patches such as trapezoidal ones and a coupling slot. For that reason, the application of extensive parametric studies becomes very important and helpful to study the effect of the trapezoidal patches and coupling slot parameters on the overall transition performance. The simulated transition parameters for different coupling values C have been simulated and then presented in Table 5.4.

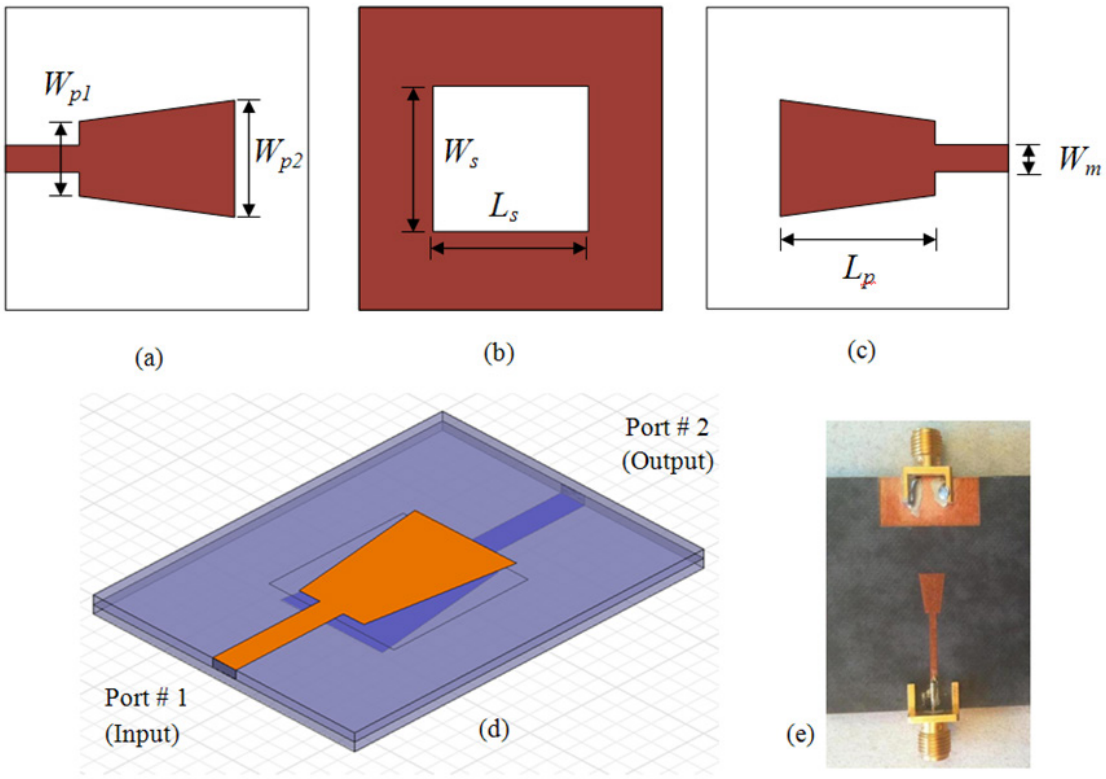

Figure 5.11 Configuration of the proposed UWB trapezoidal vertical transition. (a) Bottom layer, (b) mid layer, (c) top layer (d) the whole structure and (e) photograph of fabricated transition.

Table 5.4 Parameters of the Trapezoidal Transition for Different Coupling Values (Units: mm)

	Coupling Values C (dB)		
Transition Parameters	0.7 (3.1 dB)	0.8 (1.94 dB)	0.9 (0.92 dB)
W_{p1}	3.7	4.1	5.2
W_{p2}	5.8	5.0	4.6
W_S	6.5	7.4	8.0

It has been found that to achieve UWB bandwidth of operation, the coupling value should be in the range from 0.7 to 0.9, and this is why we simulated the transition parameters at those coupling values seeking the best value. It can be noticed from the values given in Table 5.4 that by increasing the coupling values, both the trapezoidal minor width W_{p1} and the coupling slot width W_S increase while the trapezoidal major width W_{p2} decreases. By adjusting the transition physical parameters, we can easily control the coupling between the trapezoidal patches. For UWB operation, the optimized transition parameters are: W_{p1} = 3.7 mm, W_{p2} = 5.8 mm, W_S = 7.2 mm, L_p (= L_S) = 7.7 mm and W_m = 1.3 mm.

Figure 5.12 (a) shows the simulated return losses and insertion losses between the input and output ports for the proposed UWB transition using both HFSS and CST with good agreement between them. Because of symmetry, we present only results S_{11} (=S_{22}) and S_{21} (=S_{12}). The return loss S_{11} is better than 16 dB at the center frequency and reaches 40 dB at some frequencies while the insertion loss S_{21} between the input and output ports is less than 1 dB in the UWB frequency range. The measured S-parameters S_{11}, S_{12}, S_{21} and S_{22} for the proposed transition are presented in Figure 5.12(b). It is obvious that the measured return loss at the input port S_{11} is different than measured return loss at the

output port S_{22} especially at high frequencies more than 9.5 GHz although the structure is symmetric. This may be due to the fabrication error in the alignment between the two layers during fabrication process. Discrepancies in the measured insertion losses above 7 GHz may be due to the substrates losses especially at higher frequencies. We have to take into account the material used to stick the two layers together and its thickness which may affect the performance of the fabricated prototypes.

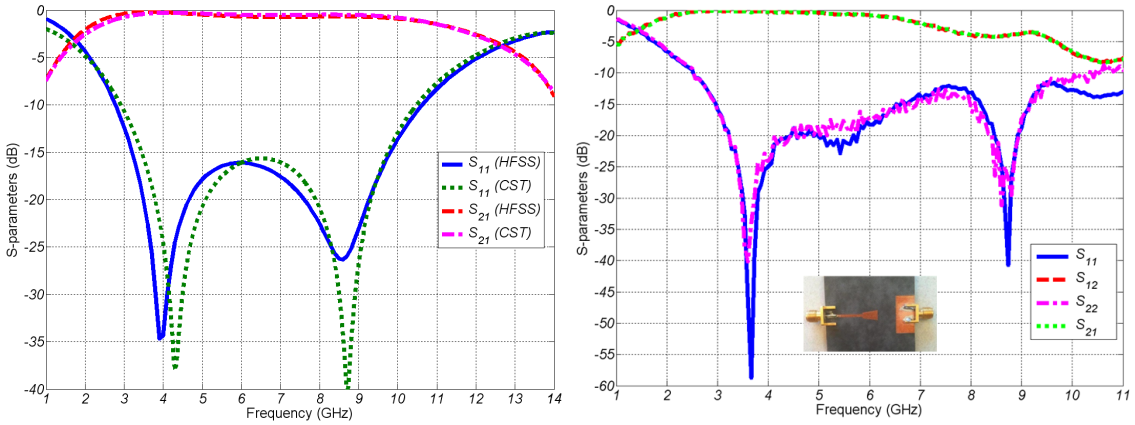

(a) (b)

Figure 5.12 (a) Simulated and (b) measured S-parameters of the proposed trapezoidal vertical transition.

5.4.3 Butterfly-Shaped Microstrip Vertical Transition

Figure 5.13 shows the butterfly-shaped microstrip-to-microstrip vertical transition. In this new design, butterfly-shaped microstrip patches are used at the top and bottom layers and they are connected to the input and output microstrip lines. The butterfly-shaped patches consist of two circular arcs connected back to back with radius R and angle θ. An open circuit stub of length d is attached to the butterfly microstrip patches to tune the coupling and the impedance matching bandwidth. The coupling between these patches is achieved by cutting a rectangular-shaped slot of length L_S and width W_S from

the common ground plane which is located at the middle layer. The simulated transition parameters for different coupling values are tabulated in Table 5.5. It can be noticed that by increasing the coupling values, both the butterfly radius R and the coupling slot width W_S increase while both the butterfly angle θ and the OC stub length d decreases. By adjusting the transition physical parameters, we can easily control the coupling between the butterfly patches. For UWB operation, the optimized transition parameters are: R = 2.2 mm, $\theta = 90°$, $W_S = 7.3$ mm, $L_S = 6.0$ mm, $d = 4.5$ mm and $W_m = 1.3$ mm.

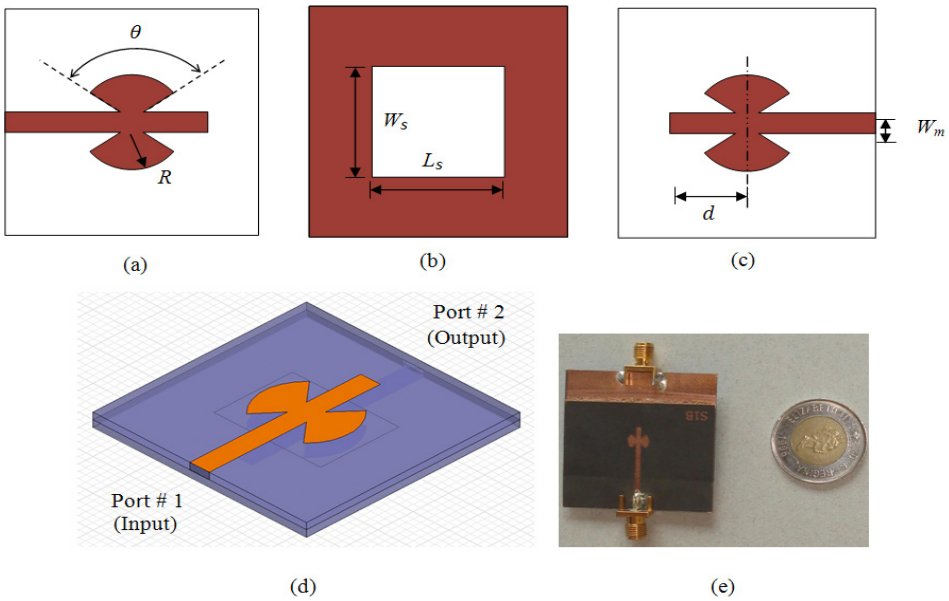

Figure 5.13 Configuration of the proposed UWB butterfly vertical transition. (a) Bottom layer, (b) mid layer, (c) top layer, and (d) the whole structure and (e) photograph of fabricated transition.

Table 5.5 Parameters of the Butterfly Transition for Different Coupling Values

	Coupling Values C (dB)		
Transition Parameters	0.7 (3.1 dB)	0.8 (1.94 dB)	0.9 (0.92 dB)
R (mm)	0.9	1.7	1.6
$\theta°$	90°	75°	50°
W_s (mm)	4.8	8.8	11.5
d (mm)	4.5	3.5	3.0

Figure 5.14(a) shows the simulated return losses and insertion losses between the input and output ports for the proposed UWB transition using both HFSS and CST with good agreement between them. The return loss $S_{11} = S_{22}$ is better than 16 dB at 8.8 GHz with better than 42 dB at some frequencies while the insertion loss $S_{21} = S_{12}$ between the input and output ports is less than 1 dB in the desired frequency range. The measured S-parameters for the proposed butterfly transition are presented in Figure 5.14(b). Also, it is obvious that there is difference between the measured return losses at both input port S_{11} and output port S_{22} especially at higher frequencies although the structure is symmetric. This may also be due to the misalignment between the two layers during fabrication process.

From the simulated and measured results for both proposed transitions, it is obvious that the second transition with butterfly-shaped patches has improved characteristics compared to the trapezoidal-shaped transition. This is because the butterfly transition has curved structure with less sharp edges compared to the trapezoidal transition which minimizes the radiation losses from the microstrip patches and hence improves its overall performance across the whole UWB frequency range. Measured results in Figure 5.12(b) and 5.14(b) for both transitions prove our conclusions especially for the insertion loss S_{21}. It can be noticed that the insertion loss S_{21} increases rapidly with frequency especially above 8 GHz in the trapezoidal transition which does not occur in the butterfly transition even above 10 GHz.

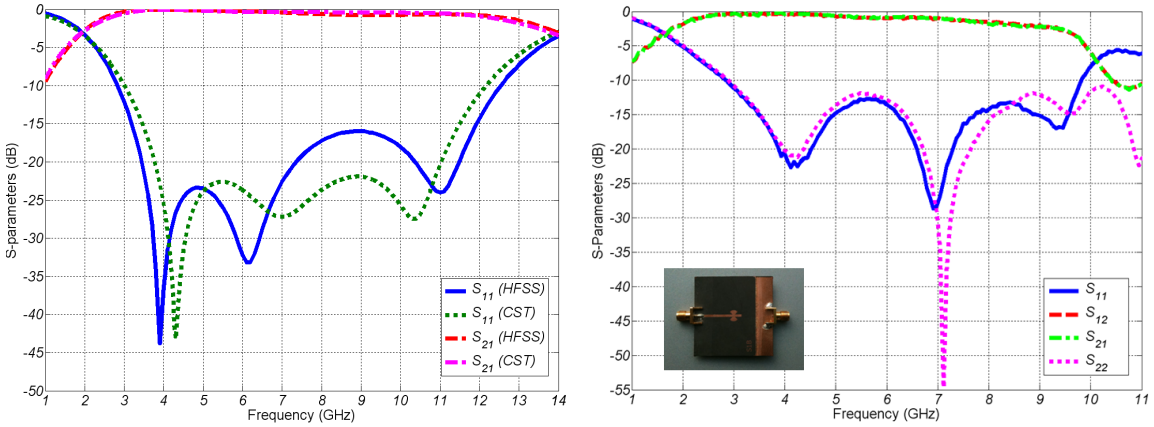

(a) (b)

Figure 5.14 (a) Simulated and (b) measured S-parameters of the proposed butterfly vertical transition.

5.5 UWB Two-Layer Microstrip 90° Hybrid Couplers

In this section, we are developing trapezoidal- and butterfly-shaped two-layer microstrip 90° backward hybrid couplers with rectangular slot-coupling from the previously designed trapezoidal- and butterfly-shaped transitions. The first configuration uses trapezoidal-shaped patches on the top and bottom layers and a rectangular coupling slot in the middle ground plane layer. The performance of this coupler can be controlled by adjusting the trapezoidal parameters and the coupling slot dimensions to achieve good UWB return loss and isolation with acceptable transmission magnitudes and phases. The other configuration has butterfly-shaped patches and a rectangular slot in the ground plane. In this design, the coupler characteristics are controlled by the butterfly patch dimensions and the coupling slot dimensions. Here, configuration 2 has five parameters to adjust and hence has more degree of freedom to achieve the design goal. The main advantage for those couplers is the flexibility in their design parameters than the conventional circular,

rectangular … etc shaped couplers. For all proposed coupler designs, the substrates used are the same like what we used in the previously designed transitions.

5.5.1 Design Methodology for UWB 90° Hybrid Couplers

The geometry of an arbitrary microstrip hybrid four-port coupler is shown in Figure 5.15. The shown four-port microstrip hybrid coupler generally consists of two dielectric substrates and three microstrip layers. The top layer includes an arbitrary-shaped patch connected to a microstrip line with port # 1 (input) and port # 2 (direct output) at both ends. The bottom layer is identical to the top layer. It contains another arbitrary-shaped patch facing the top one and connected to a microstrip line with port # 3 (coupled output) and port # 4 (matched) at both ends. Port # 4 is called matched or isolated port because there is no output power goes to that port and hence it should be connected to a 50Ω matched load. The middle layer contains the common ground plane and by cutting a rectangular-shaped slot, the coupling between the microstrip patches can be achieved.

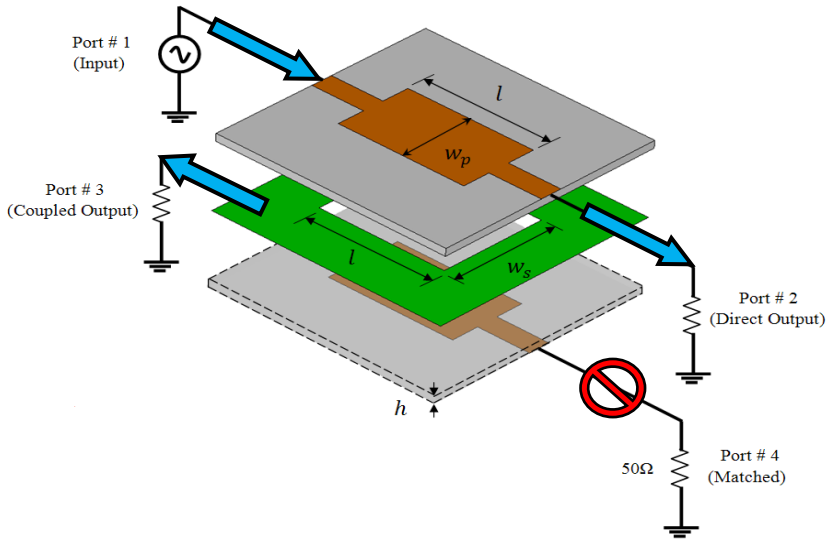

Figure 5.15 The arbitrary microstrip hybrid four-port backward coupler.

Because the proposed UWB hybrid couplers have complex-shaped patches, the analysis of those kinds of couplers is difficult and hence it is preferred to simplify those complex-shaped patches into their equivalent rectangular-shaped patches of width W_p, length L_p, the coupling slot width of W_S and the coupling slot length of L_S (= L_p) as shown in Figure 5.15. The analysis procedure for the equivalent rectangular-shaped microstrip hybrid couplers is similar to the one described in [107], [112]. To design a UWB hybrid coupler, it is important to make sure that it covers the whole UWB range with acceptable performance. A suitable coupling value C_{dB} should be selected to achieve the desired UWB bandwidth. Then the even-mode (Z_{0e}) and odd-mode (Z_{0o}) characteristic impedances can be determined from:

$$Z_{0e} = Z_0 \sqrt{\frac{1 + 10^{-C_{dB}/20}}{1 - 10^{-C_{dB}/20}}} \tag{5.1}$$

$$Z_{0o} = Z_0 \sqrt{\frac{1 - 10^{-C_{dB}/20}}{1 + 10^{-C_{dB}/20}}} \tag{5.2}$$

where the multiplication of both even- and odd-mode characteristic impedances is $Z_{0e}Z_{0o} = Z_0^2$. For example, in case of a 3 dB hybrid coupler, C_{dB} = 3 dB and hence the values of even- and odd-mode characteristic impedances calculated from Eq. (5.1) and Eq. (5.2) are 120.9Ω and 20.6Ω, respectively.

After calculating the required values of even- and odd-mode characteristic impedances, the dimensions of the equivalent rectangular-shaped couplers can be determined using the approach in [107]. Both the rectangular-shaped patch width W_p and the coupling slot width W_S can be determined from the odd- and even-mode characteristic im-

pedances, respectively. The rectangular-shaped patch length L_p which is equal to the coupling slot length L_S is set to quarter of the effective wavelength at the centre frequency of operation, i.e. f_c = 6.85 GHz. Now, the initial parameters for the equivalent rectangular-shaped couplers are determined. The optimized parameters for the proposed UWB hybrid couplers with complex-shaped patches can be evaluated using full wave EM simulation of the whole structure with the aid of extensive parametric study or different optimization techniques.

5.5.2 Two-Layer Trapezoidal-shaped Microstrip 90° Hybrid Coupler

The configuration and the photograph of the proposed trapezoidal-shaped microstrip hybrid coupler are shown in Figure 5.16. Extensive parametric studies are carried out to justify the effect of coupler physical parameters on both the coupling level and the phase difference between both direct and coupled ports. For designing UWB 90° hybrid coupler, the optimized trapezoidal-shaped coupler parameters for different coupling values, i.e. C_{dB} = 3, 6 and 10 dB are summarized in Table 5.6. For UWB operation, the optimized coupler parameters for 3db/90° coupler are: W_{p1} = 3.7 mm, W_{p2} = 4.5 mm, W_S = 7.2 mm, L_p (= L_S) = 7.7 mm and W_m = 1.3 mm.

Figure 5.17(a) shows the simulated return loss S_{11} and isolation S_{41} of the designed coupler using both HFSS and CST with good agreement between them. From the results, it is clear that the designed coupler features good characteristics across the desired frequency range. The return loss is better than 17 dB (20 dB on average) across the whole UWB frequency range. The isolation is higher than 14 dB (20 dB on average) for

the same band. The simulated insertion losses (both through S_{21} and coupled S_{31}) of the designed coupler are shown in Figure 5.17(b). The results indicate that the coupling is 3±1.25 dB for the UWB frequency band.

Figure 5.18 presents the simulated phase and phase difference between port # 2 (direct) and port # 3 (coupled), respectively. It is obvious that the phase is quite linear in the UWB frequency band and the phase difference is 90°±2.5° through the whole frequency band of interest. The measured S-parameters as well as the phases and the phase difference between the direct and coupled ports of the trapezoidal coupler are plotted in Figure 5.19. The measured phase difference is acceptable in the 3.0-8.0 GHz frequency band while it changes too much when the frequency increases more than 8 GHz.

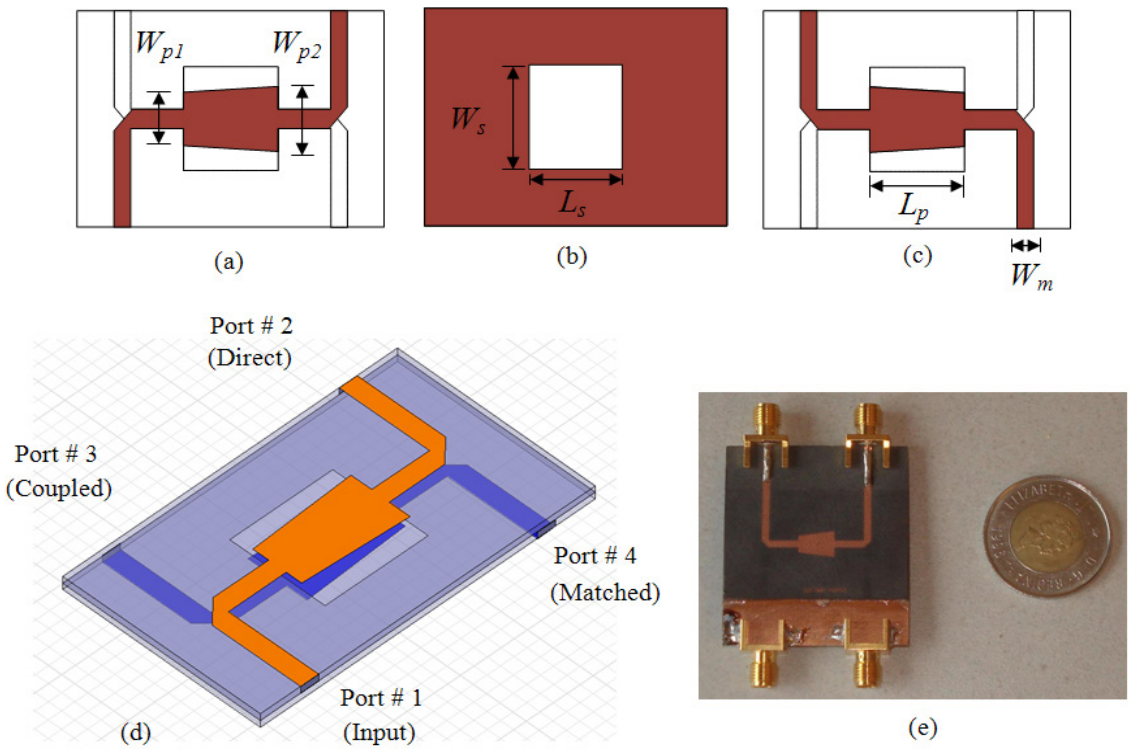

Figure 5.16 Configuration of the UWB trapezoidal 90° hybrid coupler. (a) Bottom layer, (b) mid layer, (c) top layer, and (d) the whole structure and (e) photograph of fabricated transition prototype.

Table 5.6 Parameters of the Trapezoidal Hybrid Coupler for Different Coupling Values (Units in mm)

	Coupling Values C_{dB}		
Coupler Parameters	3 dB	6 dB	10 dB
W_{p1}	3.7	2.2	2.2
W_{p2}	4.5	3.0	2.5
W_s	7.2	3.62	2.65

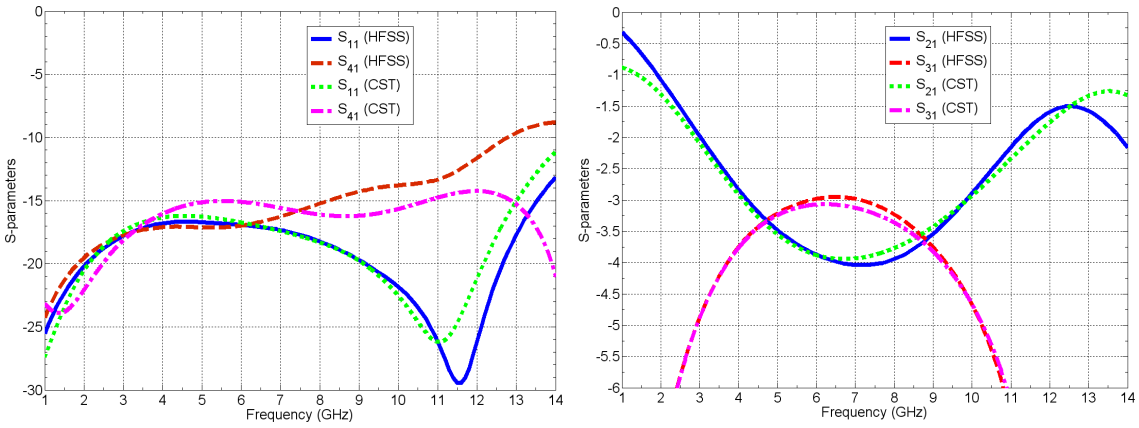

(a) (b)

Figure 5.17 Simulated (a) return losses and isolation, (b) coupling and insertion losses of the trapezoidal coupler.

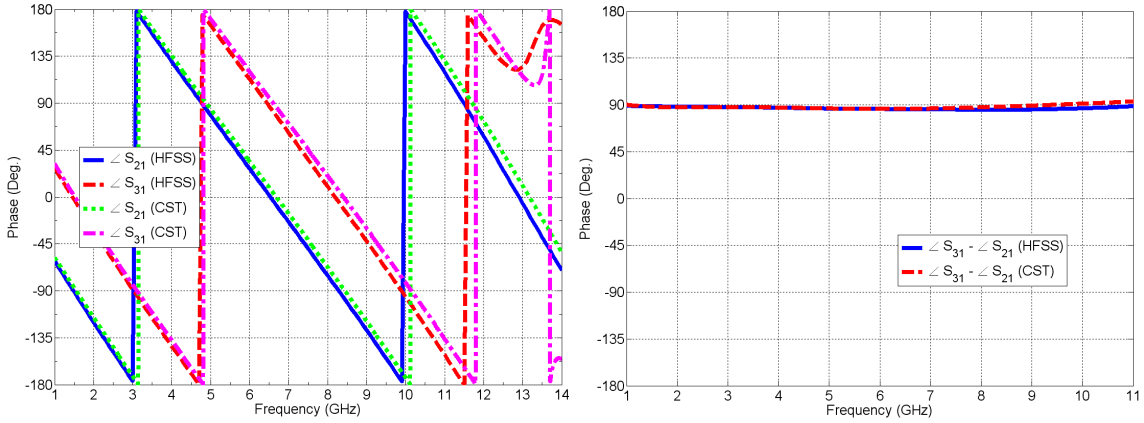

(a) (b)

Figure 5.18 Simulated (a) phases and (b) phase difference between ports 2 and 3 of the trapezoidal coupler.

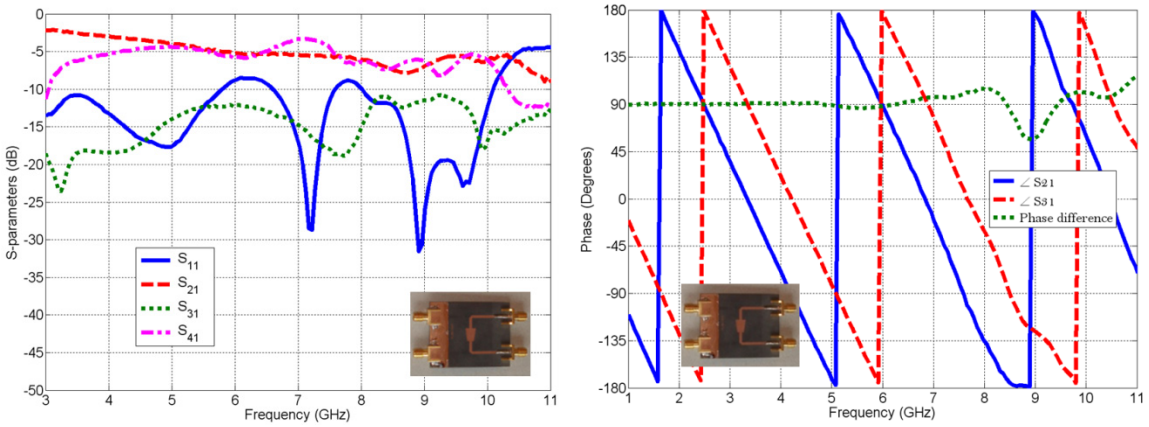

(a) (b)

Figure 5.19 Measured (a) S-parameters and (b) phases and phase difference between the direct and coupled ports for the trapezoidal coupler.

5.5.3 Two-Layer Butterfly-shaped 90° Microstrip Hybrid Coupler

This section presents the other design for the two-layer 90° hybrid coupler built in microstrip PCB technology. Figure 5.20 presents the geometrical configuration of the proposed butterfly-shaped microstrip 90° hybrid coupler. The proposed coupler has butterfly-shaped microstrip patches connected to microstrip lines facing each other on the top and bottom. Full-wave analysis is used to determine the dimensional parameters of the butterfly-shaped patches R and θ and the slot width W_S numerically. The optimized butterfly-shaped coupler parameters for different coupling values C_{dB} = 3, 6 and 10 dB are tabulated in Table 5.7. For UWB operation, the optimized coupler parameters for 3db/90° coupler are: R = 2.83 mm, θ = 90°, W_S = 10 mm, L_S = 6.0 mm and W_m = 1.3 mm.

The simulated return loss, isolation and insertion losses for the designed UWB coupler using both HFSS and CST are plotted in Figure 5.21. It is obvious from the results that the designed coupler exhibits good performances across the desired UWB frequency band. The return loss is better than 14 dB and isolation is higher than 14 dB (be-

low 20 dB on average) across the whole range. Results also indicate that the coupling is about 3±2 dB for the UWB frequency band. The simulated phase and phase difference between port # 2 (direct output) and port # 3 (coupled output) are illustrated in Figure 5.22(a) and (b), respectively. It is clear that the phase is quite linear in the UWB frequency band and the phase difference is 90°±7° in the same frequency band.

The measured S-parameters and phase difference between the direct and coupled ports for the butterfly coupler are given in Figure 5.23(a) and (b), respectively. Results show good coupler performance especially in the lower frequency band. Compared to the previous trapezoidal coupler, the butterfly coupler features better characteristics through the whole UWB frequency range.

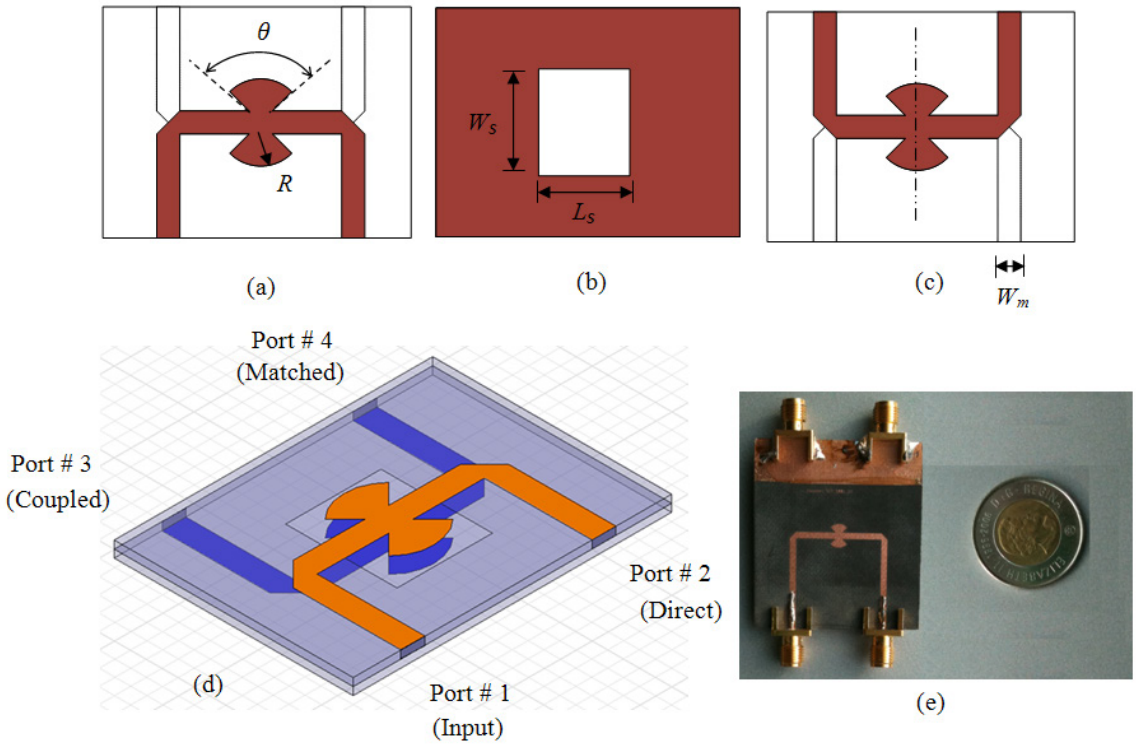

Figure 5.20 Configuration of the proposed UWB butterfly directional coupler. (a) Bottom layer, (b) mid layer, (c) top layer, and (d) the whole structure and (e) photograph of fabricated transition prototype.

Table 5.7 Parameters of the Butterfly Directional Coupler for Different Coupling Values

	Coupling Values C_{dB}		
Coupler Parameters	3 dB	6 dB	10 dB
R (mm)	2.83	3.0	1.7
$\theta°$	90°	95.4°	99.5°
W_s (mm)	10	4.5	2.9

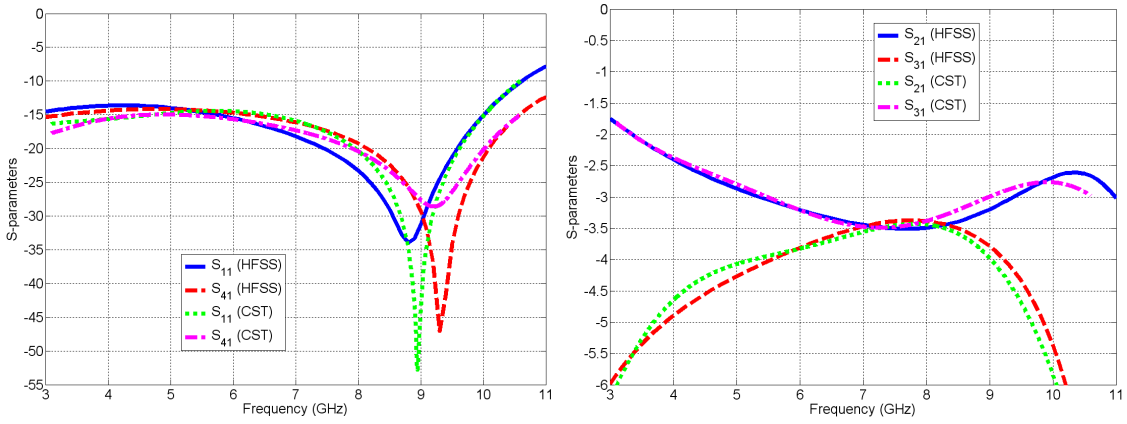

(a) (b)

Figure 5.21 Simulated (a) return loss and isolation, (b) coupling and insertion losses of the butterfly coupler.

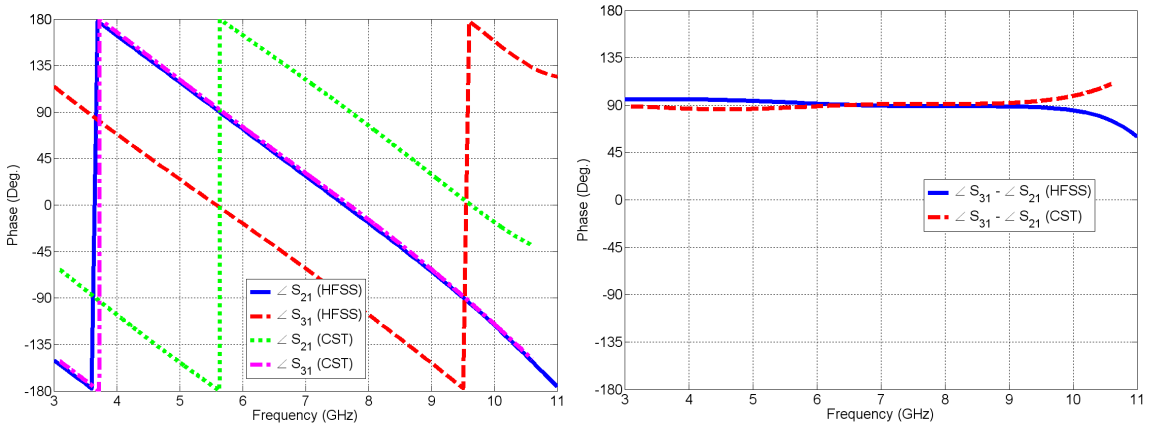

(a) (b)

Figure 5.22 Simulated (a) phases and (b) phase differences between ports 2 and 3 of the butterfly coupler.

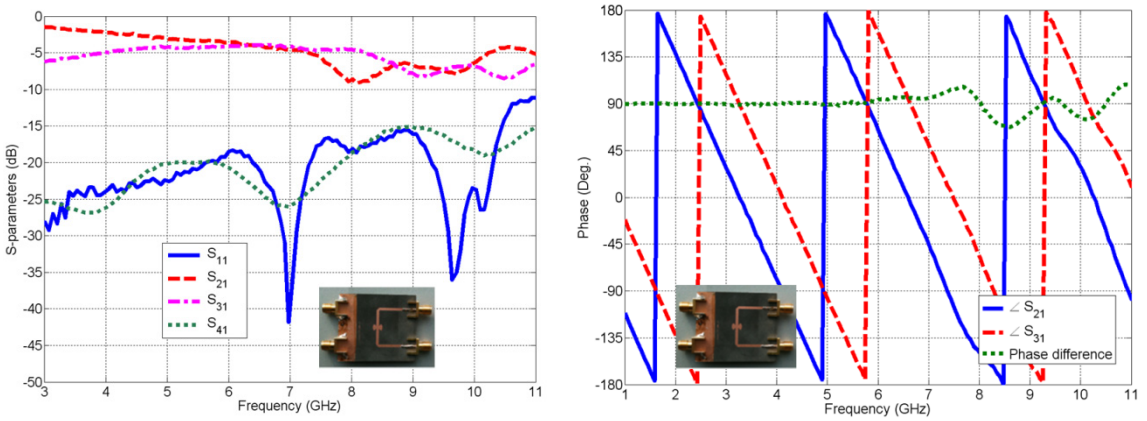

(a) (b)

Figure 5.23 Measured (a) S-parameters and (b) phase difference between the direct and coupled ports for the butterfly coupler.

5.6 UWB Two-Layer Microstrip Phase Shifters

In this section we continue using the previously designed trapezoidal- and butterfly-shaped vertical microstrip transitions to develop phase shifters for UWB applications. The problem with the conventional narrowband phase shifters is that the phase changes linearly with the frequency. To design a wideband phase shifter where the phase is almost constant with frequency, we exploit the wideband characteristics of the designed trapezoidal- and butterfly-shaped transitions and the conventional transmission lines. For all proposed phase shifter designs, the substrates used are the same as what we used in the previously designed transitions.

5.6.1 Two-Layer Trapezoidal-shaped 45° Phase Shifter

The configuration of the proposed trapezoidal-shaped 45° microstrip phase shifter is shown in Figure 5.24. It simply consists of the designed trapezoidal-shaped transition

connected to port # 1 and port # 2. The reference transmission line is installed on the top layer between port # 3 and port # 4. By controlling the transition parameters and the length of the reference transmission line, the suitable constant phase shift can be obtained over the desired bandwidth. The simulated and measured return and insertion losses for the 45° trapezoidal phase shifter are illustrated in Figure 5.25(a) and (b), respectively. It can be seen that the simulated return and insertion losses are better than 10 dB and 1.2 dB in the 3.1-10.6 GHz band, respectively. There is a good agreement between both HFSS and CST simulation results. The measured return and insertion losses are good in the lower frequency band from 3.3 GHz to 9.6 GHz. The phase difference ($\angle S_{43} - \angle S_{21}$) has been simulated and plotted in Figure 5.26(a). The simulated achieved phase difference is almost 45° with phase error of less than ±7° across the whole UWB frequency band. Also, the measured phases and phase difference between the ports (1, 2) and ports (3, 4) are shown in Figure 5.26(b). It can be noticed that phases are almost linear as a function of frequency and the measured phase difference achieved is varying around 45° but it deteriorated at higher frequencies above 8.0 GHz.

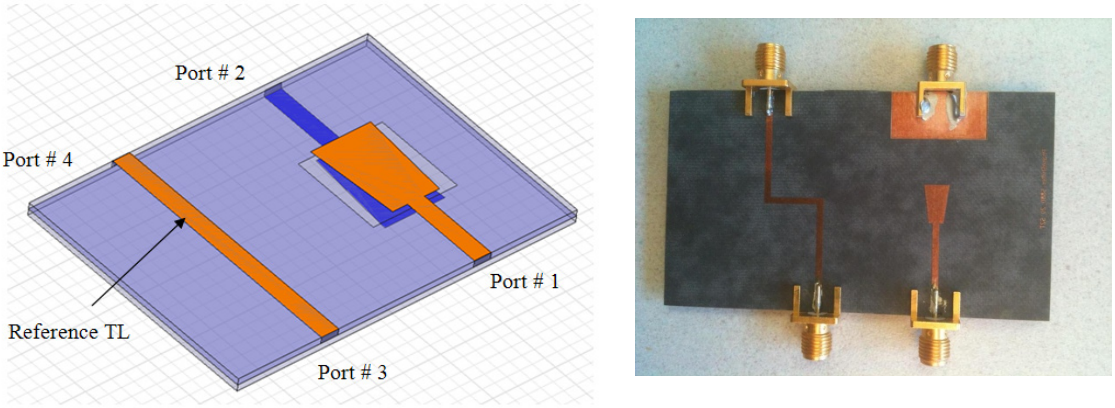

(a) (b)

Figure 5.24 Configuration of the proposed trapezoidal-shaped UWB 45° phase shifter. (a) The whole structure and (b) photograph of fabricated prototype.

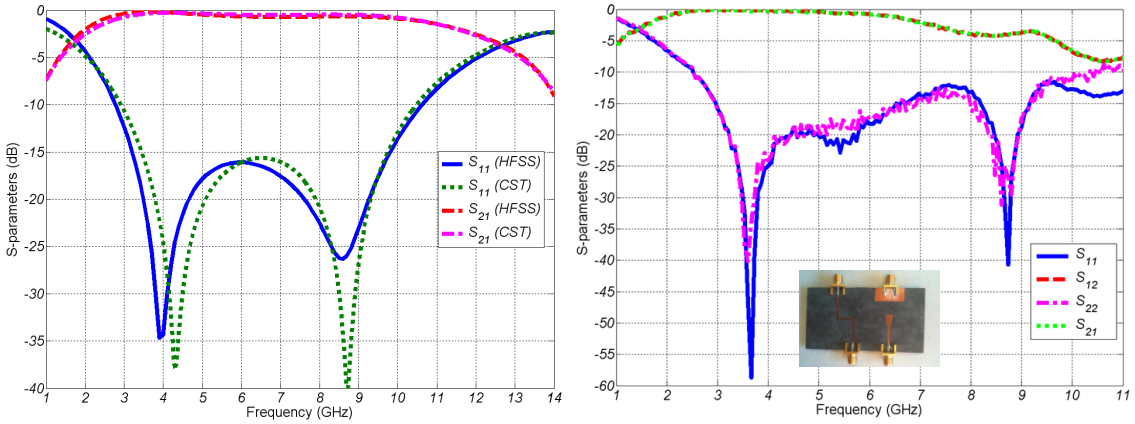

(a) (b)

Figure 5.25 (a) Simulated and (b) measured return and insertion losses of the proposed UWB 45° trapezoidal phase shifter.

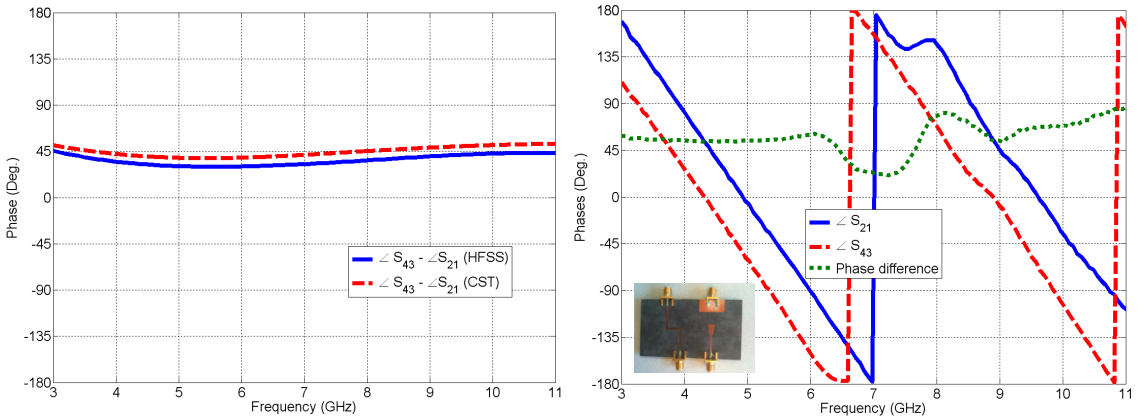

(a) (b)

Figure 5.26 (a) Simulated phase difference and (b) measured $\angle S_{21}$ & $\angle S_{43}$ phases and phase difference ($\angle S_{43} - \angle S_{21}$) of the proposed 45° trapezoidal phase shifter.

5.6.2 Two-Layer Butterfly-shaped 45° Phase Shifter

The other configuration of the proposed butterfly-shaped 45° microstrip phase shifter is shown in Figure 5.27. It is simply consists of the designed butterfly-shaped transition connected to ports 1 and 2. The reference transmission line is installed on the top layer between ports 3 and 4. The desired constant phase shift over the maximum available bandwidth can be obtained by controlling the transition parameters and the length of

the reference transmission line. The simulated and measured return and insertion losses for the 45° butterfly phase shifter are illustrated in Figure 5.28(a) and (b), respectively. It can be noticed that the return and insertion losses are better than 13 dB and 0.8 dB across the whole UWB band. The measured return and isolation losses are good in the 2.8-9.8 GHz frequency band. The simulated and measured phases between ports (1, 2) and ports (3, 4) and the phase difference are presented in Figure 5.29(a) and (b), respectively. It can be seen that the phase is almost linear with frequency. The achieved phase difference is almost 45° with acceptable phase error especially in the lower frequency band.

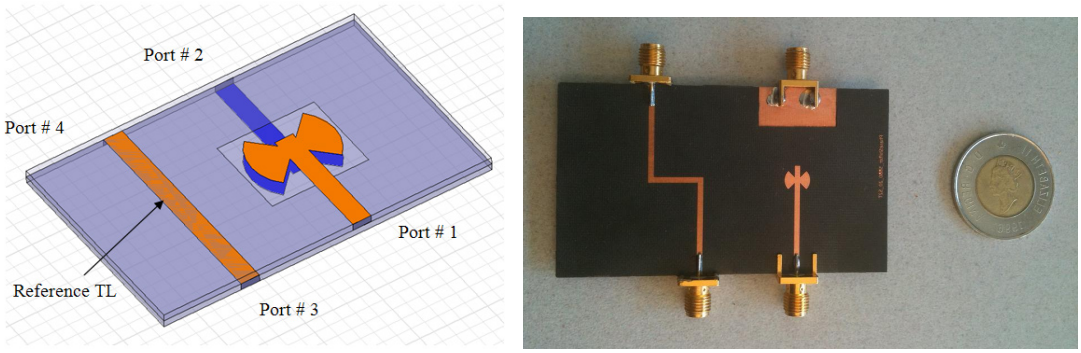

(a) (b)

Figure 5.27 Configuration of the proposed butterfly-shaped UWB 45° phase shifter. (a) The whole structure and (b) photograph of fabricated phase shifter prototype.

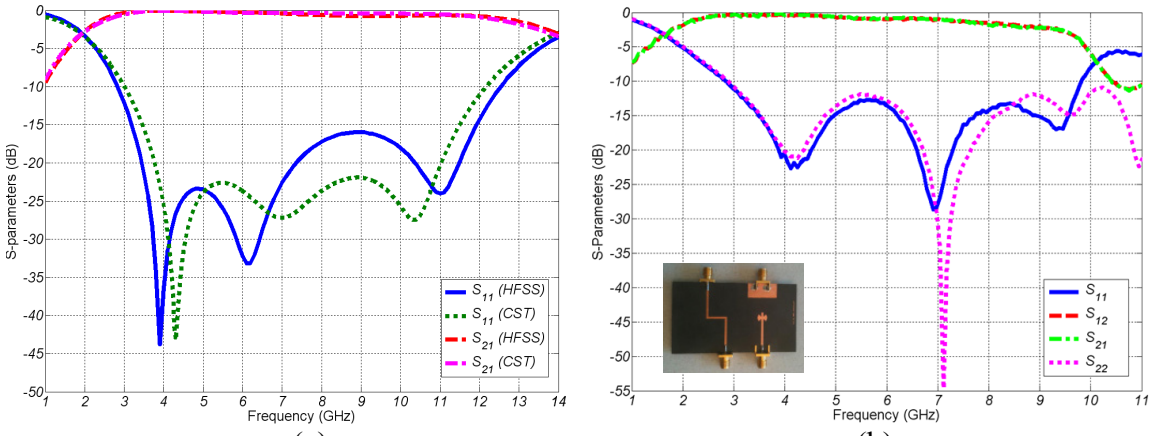

(a) (b)

Figure 5.28 (a) Simulated and (b) measured return and insertion losses of the proposed 45° butterfly phase shifter.

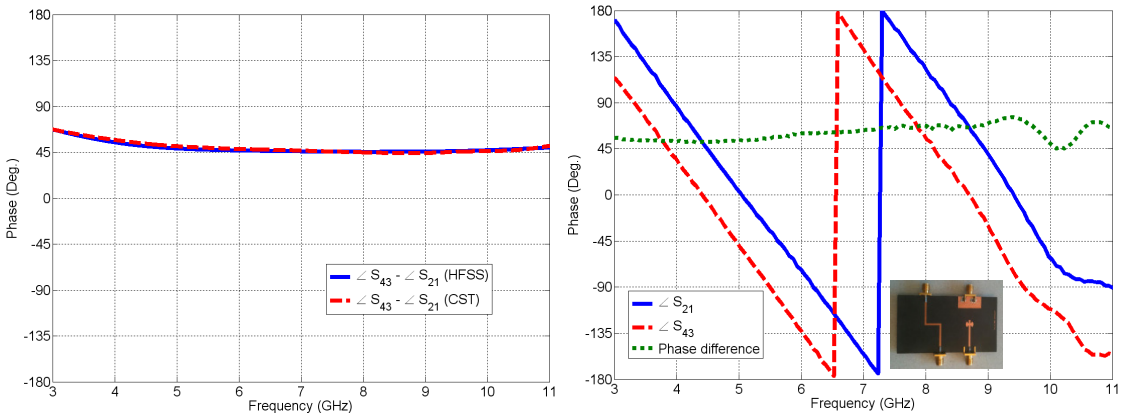

Figure 5.29 (a) Simulated phase difference and (b) measured $\angle S_{21}$ & $\angle S_{43}$ phases and phase difference ($\angle S_{43} - \angle S_{21}$) of the proposed 45° butterfly phase shifter.

5.7 Summary

A UWB feed network prototype has been proposed and designed. This prototype is based on a modified two-section Wilkinson power divider by adding stub matching network to each branch with additional transmission lines at the end and saving the resistor of the second section. This prototype has been fabricated and tested at UWB frequency band. It has been used in constructing two- and four-element UWB antenna arrays. Both simulated and measured results show that the proposed feed network has acceptable insertion loss, satisfactory isolation and good return loss of all ports within the whole UWB frequency range. The two- and four-element antenna arrays have been developed from the designed antenna elements and feed networks. Both measured and simulated results show that the two-element antenna array has UWB impedance performance, with antenna array gain of about 5.5–8.5 dBi within the whole UWB frequency range. For the four-element antenna array, the achieved impedance matching is multi-band within the UWB frequency range, and the gain of the antenna array is about 7.5–11.5 dBi. In addition, the radiation patterns of the antenna array are quite stable with frequency.

The design of two UWB slot-coupled vertical microstrip-to-microstrip transitions has been presented. The proposed transitions utilize broadside coupling between complex-shaped microstrip patches of trapezoidal and butterfly shapes located at the top and bottom layers. The coupling mechanism between those layers is achieved by cutting a rectangular-shaped slot at the common ground plane or the middle layer. For achieving the maximum possible bandwidth where the transition performances remain acceptable, the coupling value between the microstrip patches is found to be between 0.7 and 0.8. Both simulated and measured results have shown that the proposed transitions have a

good return loss and an acceptable insertion loss across the desired UWB frequency range while the phase is almost linear with frequency. The designed transitions have been used to develop two different 3dB/90° hybrid couplers with good return losses, insertion losses, coupling and isolation characteristics across the desired frequency range. Then two different 45° phase shifters have been designed to be used in building 4 × 4 Butler matrices in the next chapter.

Chapter 6

UWB Microstrip Beamforming Networks

6.1 Introduction

This chapter focuses on the design of UWB compact and inexpensive Butler matrices employing the previously developed two-layer microstrip components reported in Chapter 5. The microstrip two-layer layout for a 4 × 4 Butler matrix to avoid using any cross lines or crossovers is presented in Figure 2.18 in Chapter 2. In the previously designed Butler matrices with crossovers, the maximum achievable bandwidth is greatly affected by those elements. Moreover, the structure complexity of those Butler matrices will be increased using crossovers and hence there will be some fabrication problems and limitations as well as the expected losses will be increased which limit their performance [135]. The proposed 4 × 4 Butler matrices using microstrip PCB technology are compact, inexpensive and offering wideband performances for both transmission magnitudes and phases with good return losses and isolation characteristics. The use of microstrip PCB technology is good choice for designing a compact size and low cost beamforming network [27]. Two different 4 × 4 Butler-matrix configurations are designed, fabricated and then tested based on the previously presented microwave components with trapezoidal and butterfly patch shapes. It has been found that separate elements as well as the constructed Butler matrices have good simulated and measured results.

This chapter is organized as follows: Section 6.2 focuses on the design of two different 4 × 4 Butler-matrix configurations for the UWB applications. It starts with Section 6.2.1 which introduces the design and implementation of trapezoidal-shaped 4 × 4 Butler matrix based on using the previously developed trapezoidal-shaped components in Chapter 5. Another configuration in Section 6.2.2 is the butterfly-shaped 4 × 4 Butler matrix based on previously developed butterfly-shaped hybrid couplers and phase shifters. Both numerical and experimental investigations are introduced and discussed in details for different Butler-matrix configurations. All matrix characteristics including the calculation of transmission magnitudes and phases as well as the return losses and isolations are simulated numerically using both Ansoft HFSS and CST Microwave Studio. To demonstrate the functionality of the designed UWB 4 × 4 Butler-matrix configurations, four identical patch antenna elements designed at f = 5.8 GHz are connected to four output ports of the Butler matrix and the radiation pattern characteristics are simulated, presented and discussed. Finally, conclusions of this chapter are summarized in Section 6.3.

6.2 UWB 4 × 4 Two-Layer Butler Matrix

The proposed 4×4 Butler matrices are designed and optimized numerically using EM simulation programs: HFSS and CST. The Butler matrix components are the 3dB/90° hybrid couplers and 45° phase shifters as discussed in Chapter 5. The substrates used in all prototypes are Rogers RT/duroid 5880 with thickness of h = 0.508 mm, and relative permittivity of ε_r = 2.2. S-parameter measurements for testing the fabricated matrix prototypes are carried out using Agilent E8364B programmable network analyzer.

6.2.1 Configuration One

Figure 6.1 shows the developed 4 × 4 trapezoidal-shaped UWB Butler matrix using 3dB/90° hybrid couplers and 45° phase shifters of trapezoidal shapes. The physical dimensions of the components used to construct the 4 × 4 Butler matrix are the same as given in Chapter 5. Figure 6.2(a) presents the simulated results for the transmission magnitude parameters S_{51}, S_{61}, S_{71} and S_{81} with frequency when port # 1 is fed while the other ports are terminated with 50Ω matched loads. The transmission magnitude parameters S_{52}, S_{62}, S_{72} and S_{82} as functions of frequency when port # 2 is fed and keeping all the other ports terminated with matched loads are shown in Figure 6.2(b).

The return losses and isolation versus frequency for ports 1 and 2 are also simulated and presented in Figure 6.3(a) and (b), respectively. This Butler matrix is designed to operate in the UWB frequency range from 3.1 to 10.6 GHz. The designed 4 × 4 Butler matrix is fabricated and then tested experimentally. Figure 6.4(a) and (b) show the experimental results of the transmission magnitudes for port # 1 and port # 2, respectively while the other six ports are terminated with 50Ω matched loads. The measured return losses and isolation parameters for both ports are demonstrated in Figure 6.5(a) and (b), respectively. From both simulated and measured results, the proposed Butler matrix has a wideband performance across the UWB frequency range with reasonable insertion loss values especially in the mid-frequency band around 6.85 GHz. The simulated and measured return loss S_{11} (port # 1 is fed) is below -10 dB for most of frequencies and the same for S_{22} (port # 2 is fed). Also, the simulated and measured isolations when port # 1 is fed, S_{21}, S_{31}, and S_{41} are better than 10 dB, 27 dB and 18 dB, respectively. When port # 2 is fed, the isolations S_{12}, S_{32}, and S_{42} are better than 10 dB, 10 dB and 27 dB, respectively.

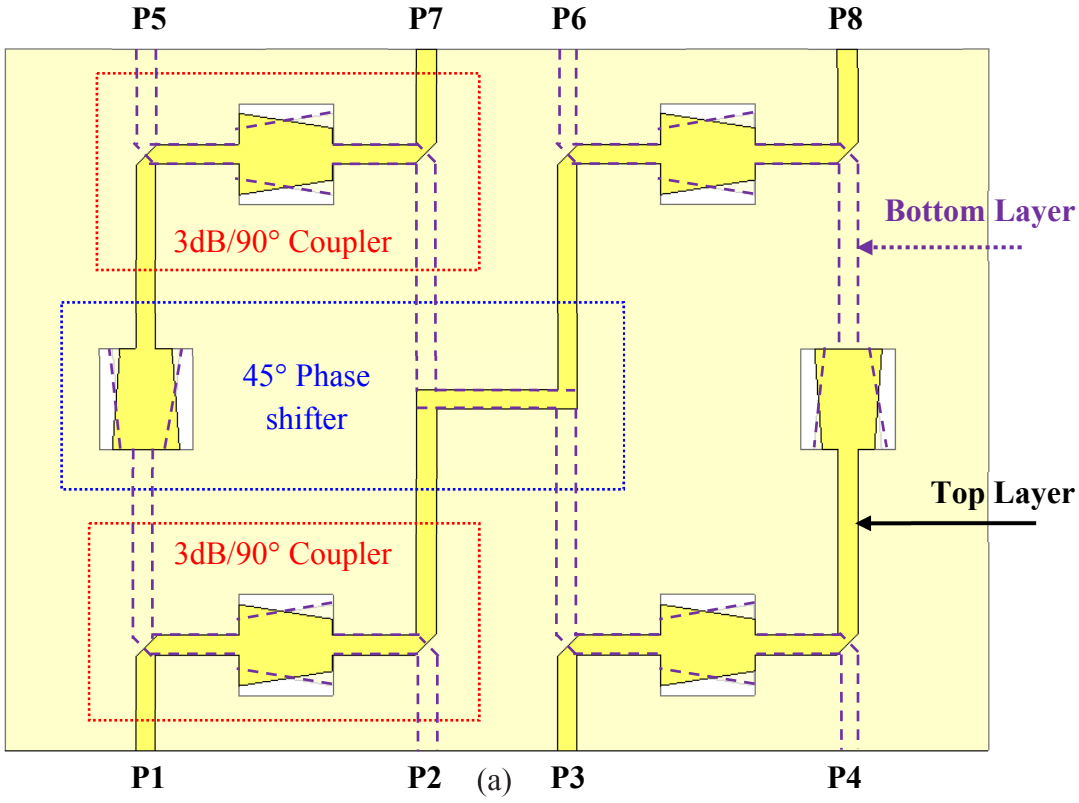

(a)

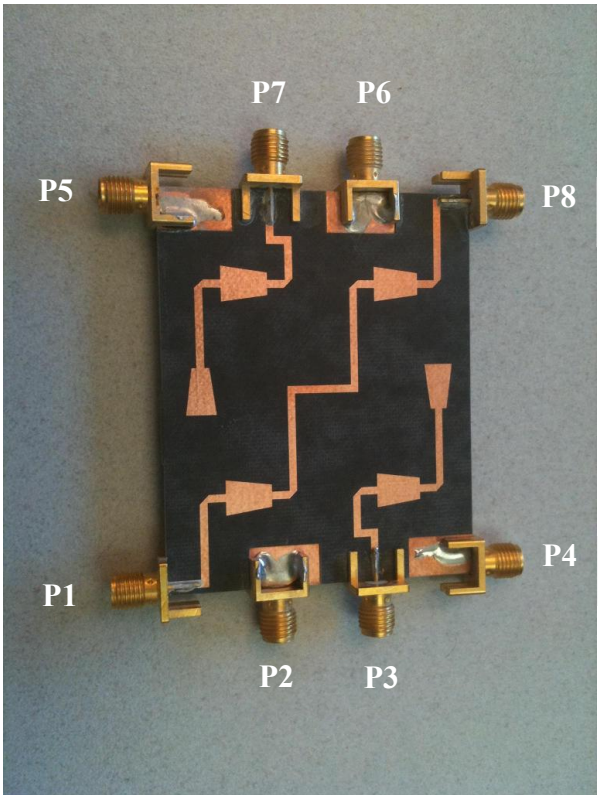

(b)

Figure 6.1 (a) Geometry and (b) photograph of the developed configuration one for the trapezoidal-shaped 4×4 Butler matrix prototype.

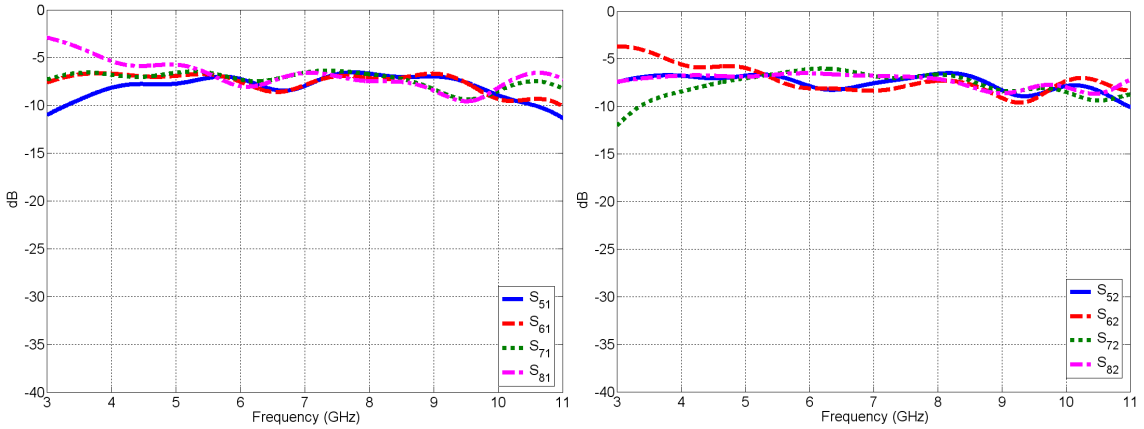

(a) (b)

Figure 6.2 Simulated transmission magnitudes of the trapezoidal-shaped 4×4 Butler matrix when: (a) port # 1 is fed, (b) port # 2 is fed.

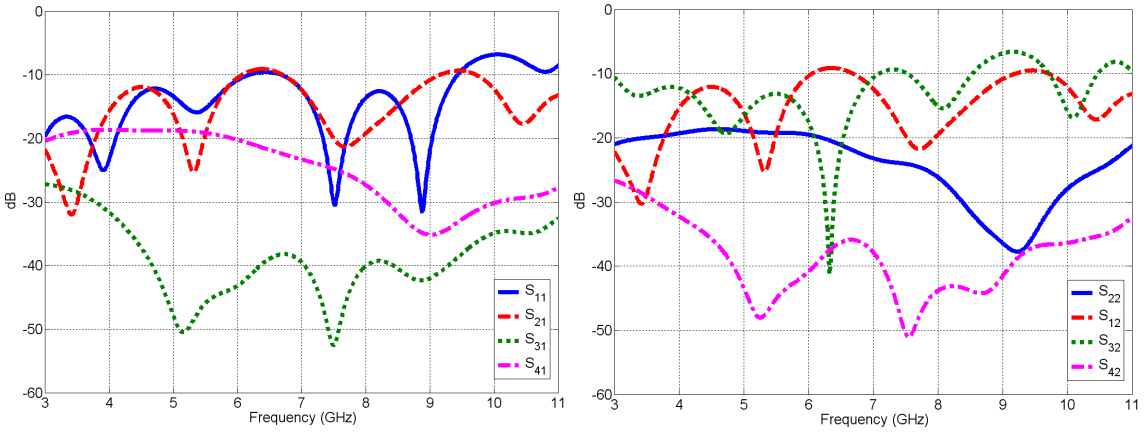

(a) (b)

Figure 6.3 Simulated return losses and isolations of the trapezoidal-shaped 4×4 Butler matrix when: (a) port # 1 is fed, (b) port # 2 is fed.

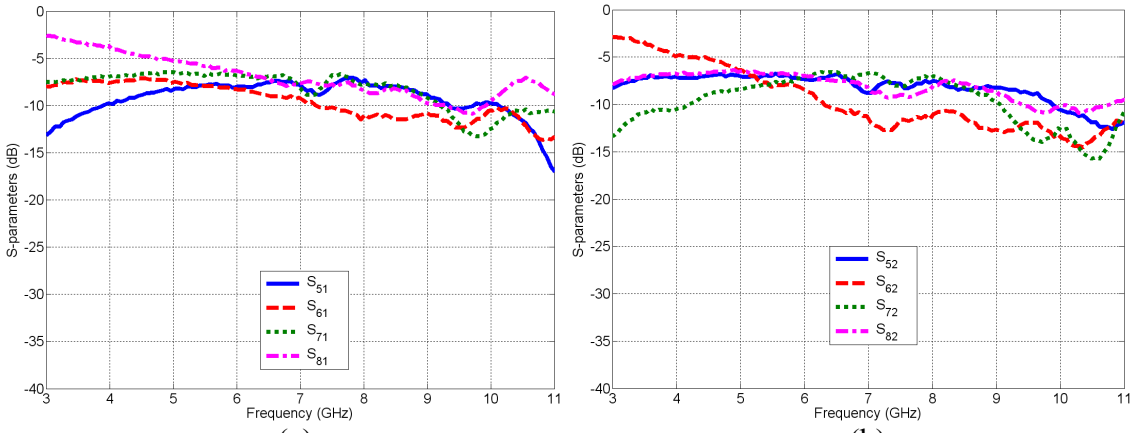

(a) (b)

Figure 6.4 Measured transmission magnitudes of the configuration one for the trapezoidal-shaped 4×4 Butler matrix when: (a) port # 1 is fed, (b) port # 2 is fed.

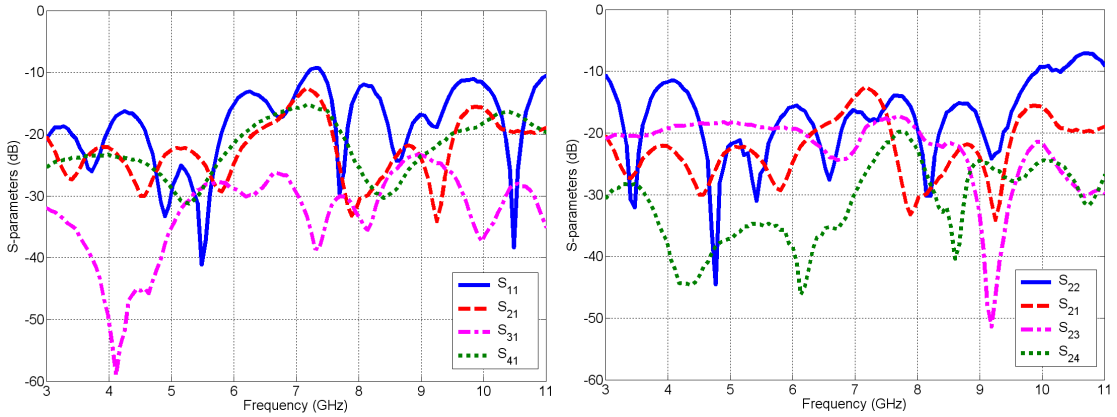

(a) (b)

Figure 6.5 Measured return losses and isolations of the developed configuration one for the trapezoidal-shaped 4×4 Butler matrix when: (a) port # 1 is fed, (b) port # 2 is fed.

The difference between simulated and measured results is may be due to the error in alignment during fabrication process and the substrates losses especially at higher frequencies. The simulated and measured differential phase characteristics of the proposed Butler matrix are shown in Figure 6.6 and Figure 6.7, respectively. The matrix has almost good differential phases of –45°, –90° and –135° when port # 1 is fed and +45°, –90° and +135° when port # 2 is fed within the UWB frequency. The phase differences α between consecutive output ports are –45° and +135° when ports 1 and 2 are fed, respectively.

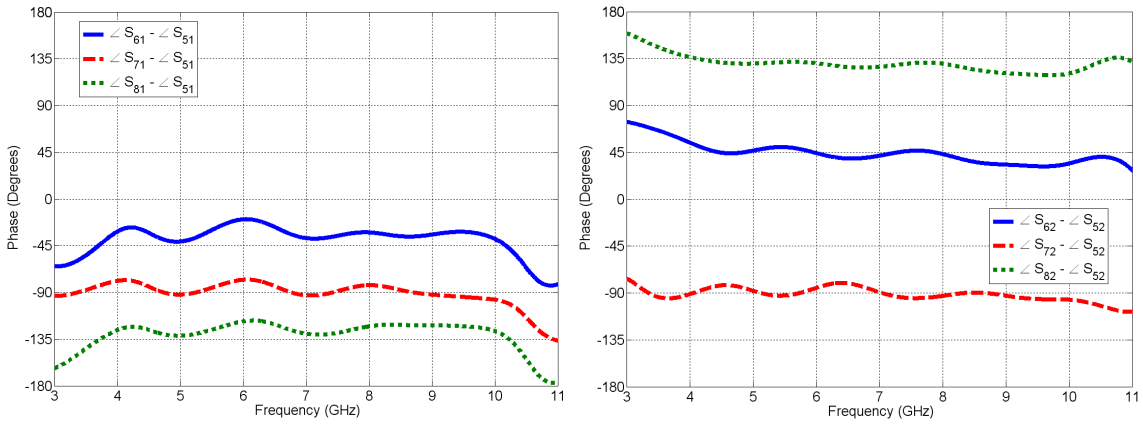

(a) (b)

Figure 6.6 Simulated differential phase characteristics of the trapezoidal-shaped 4×4 Butler matrix when: (a) port # 1 is fed, (b) port # 2 is fed.

Figure 6.8(a) and (b) presents the surface current distributions for the developed configuration one at the center frequency f = 6.85 GHz when ports 1 and 2 are fed, respectively.

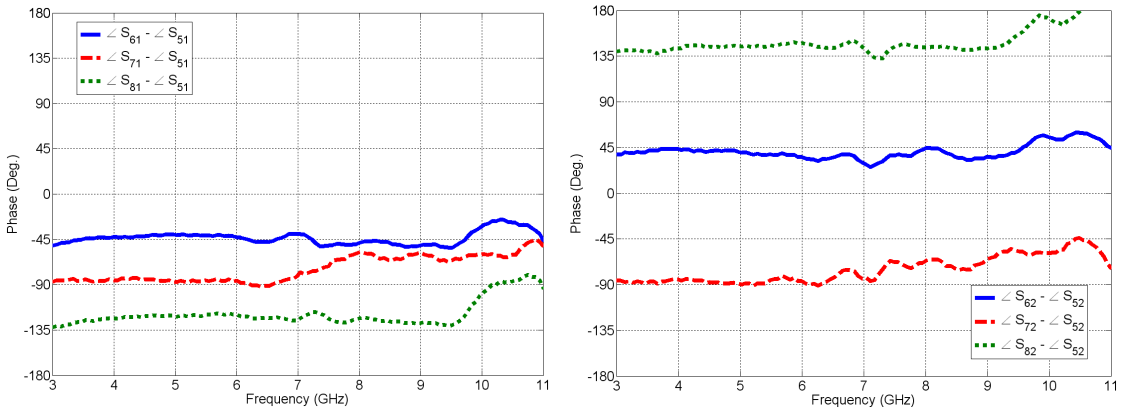

(a) (b)

Figure 6.7 Measured differential phase characteristics of the developed configuration one for the trapezoidal-shaped 4×4 Butler matrix when: (a) port # 1 is fed, (b) port # 2 is fed.

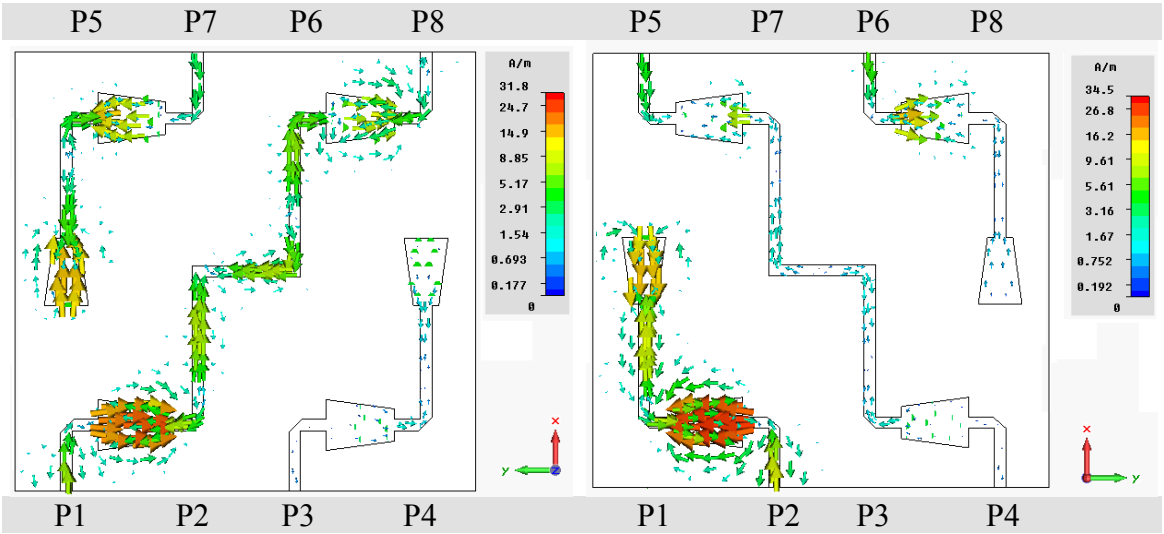

(a) (b)

Figure 6.8 Surface current distributions for the developed configuration one at center frequency f = 6.85 GHz when: (a) port # 1 is fed, (b) port # 2 is fed.

The designed Butler matrix is then used to feed four identical tapered slot antenna (TSA) [157] elements for a multi-beam antenna system as shown in Figure 6.9. This is to study the effect of both transmission magnitudes and phases of the designed Butler matrix on the main beam direction of the array. We can steer the main beam in four different directions according to the port fed. The TSA array inter-element spacing is designed at upper edge frequency to be one wavelength, i.e. d = 28.3 mm. It can be seen from Figure 6.10 that the main beam directions are +6°, –20°, +20° and –6° when ports 1, 2, 3 and 4 are fed with signals, respectively. Also, the array side-lobe level (SLL) is better than –3.9 dB in all cases with good angular 3dB beam-widths between 13° and 13.5°. The ideal values for main beam directions are +7°, –22°, +22° and –7° when ports 1, 2, 3 and 4 are fed with signals, respectively. The errors in the main beam locations are –1°, +2°, –2° and +1°, respectively.

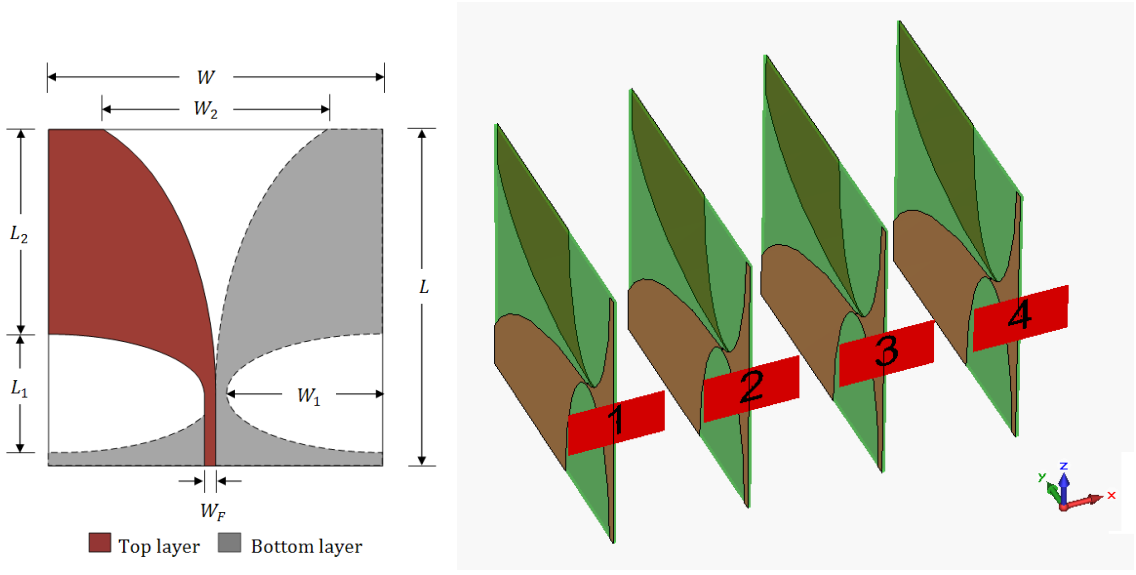

(a) (b)

Figure 6.9 Configuration and geometrical dimensions of (a) single TSA antenna element and (b) array model.

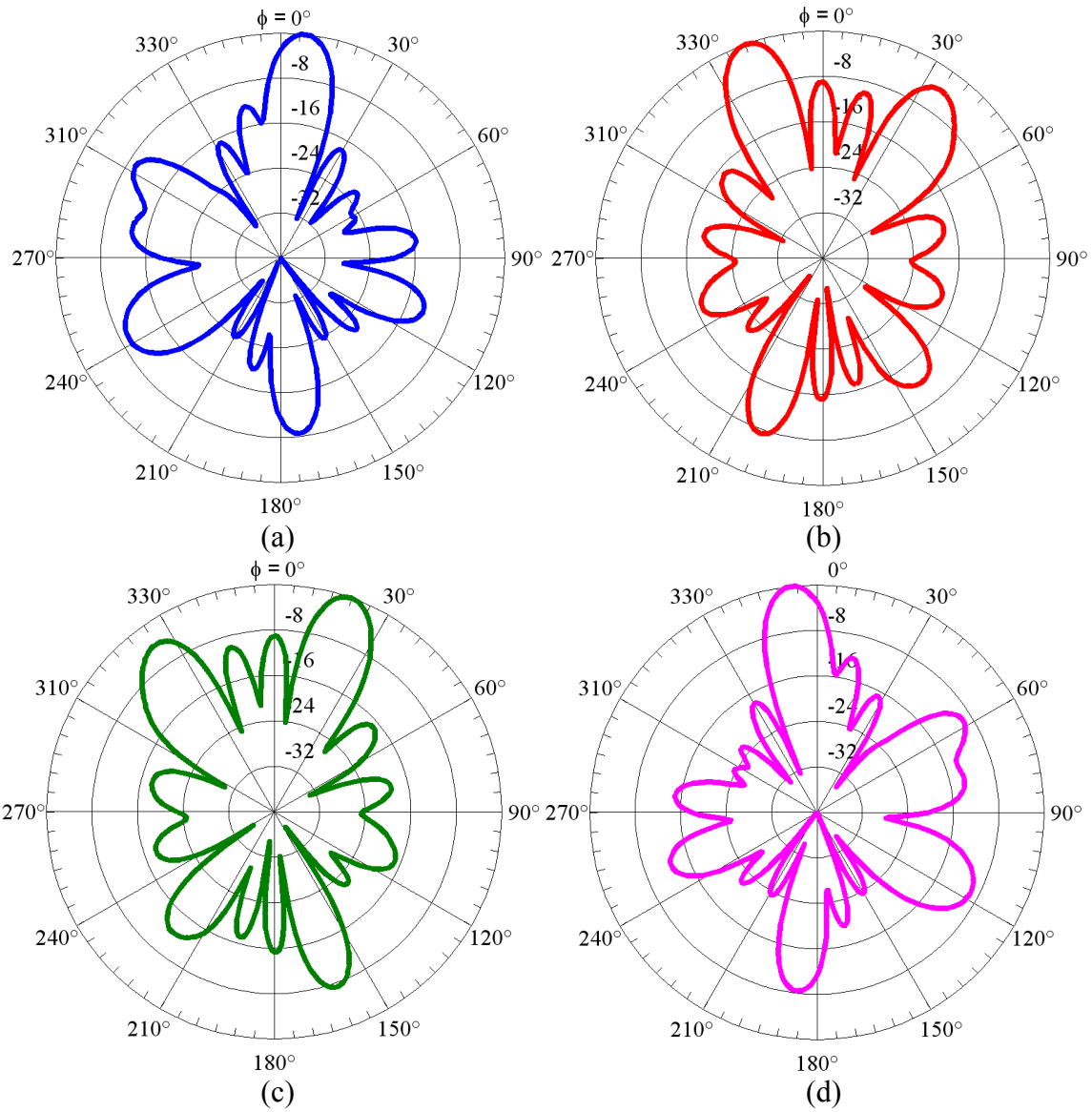

Figure 6.10 Simulated radiation patterns of four-element TSA array fed by the developed Butler matrix in configuration one at f = 10.6 GHz when: (a) port # 1 is fed, (b) port # 2 is fed, (c) port # 3 is fed and (d) port # 4 is fed.

6.2.2 Configuration Two

Figure 6.11 shows the developed 4 × 4 butterfly-shaped UWB Butler matrix using 3dB/90° hybrid couplers and 45° phase shifters of butterfly shapes. The physical dimensions of the components used to construct the 4 × 4 Butler matrix are the same as given in

Chapter 5. Figure 6.12(a) presents the simulated results for the transmission magnitude parameters S_{51}, S_{61}, $S_{71}$and S_{81} as a function of frequency when port # 1 is fed while the other ports are terminated with matched loads. The transmission magnitude parameters S_{52}, S_{62}, $S_{72}$and S_{82} as a function of frequency when port # 2 keeping all the other ports terminated with 50Ω matched loads are shown in Figure 6.12(b). The simulated return losses and isolation versus frequency are also plotted and presented in Figure 6.13(a) and (b), respectively. The measured transmission magnitudes, return losses and isolations are shown in Figure 6.14 and Figure 6.15, respectively.

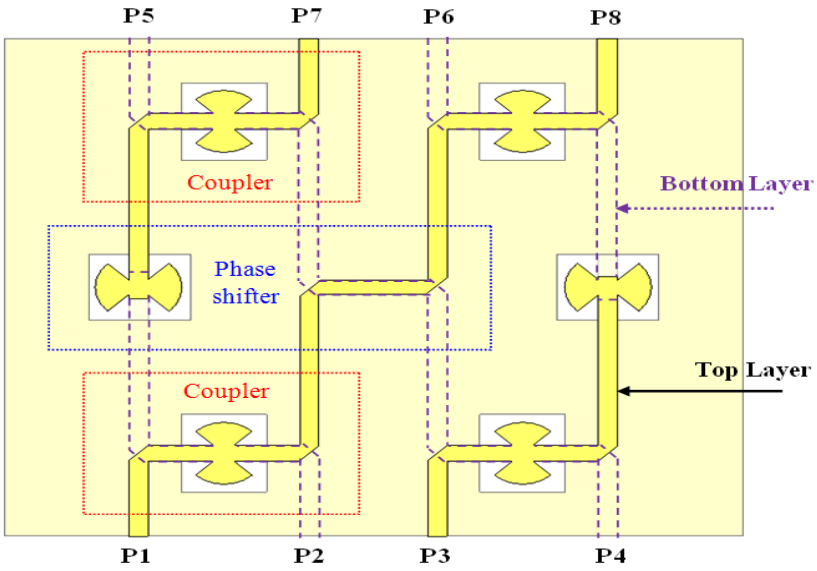

(a)

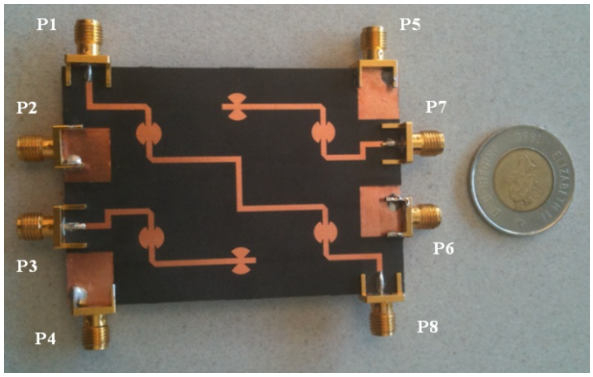

(b)

Figure 6.11 (a) Geometry and (b) photograph of the developed configuration two for the 4×4 butterfly Butler matrix prototype.

From both simulated and measured results, the proposed Butler matrix has wide-band performance across the UWB frequency range with reasonable insertion loss values especially in the 5.0-10 GHz frequency band. Both simulated and measured return losses S_{11} are better than 10 dB for most of frequencies and the same for S_{22}. Also, the simulated and measured isolations when port # 1 is fed, S_{21}, S_{31}, and S_{41} are better than 17 dB, 25 dB and 15 dB, respectively. When port # 2 is fed, the simulated and measured isolations S_{12}, S_{32}, and S_{42} are better than 17 dB, 17 dB and 24 dB, respectively.

Figure 6.18(a) and (b) presents the magnetic field distributions for the developed configuration two at the center frequency f = 6.85 GHz when both ports 1 and 2 are fed, respectively.

Compared to configuration 1, the measured return losses, isolations and insertion losses are better in case of configuration 2 with butterfly-shaped patches. This may be due to the curved shape of the butterfly compared to the trapezoidal structure and hence the radiation losses are less.

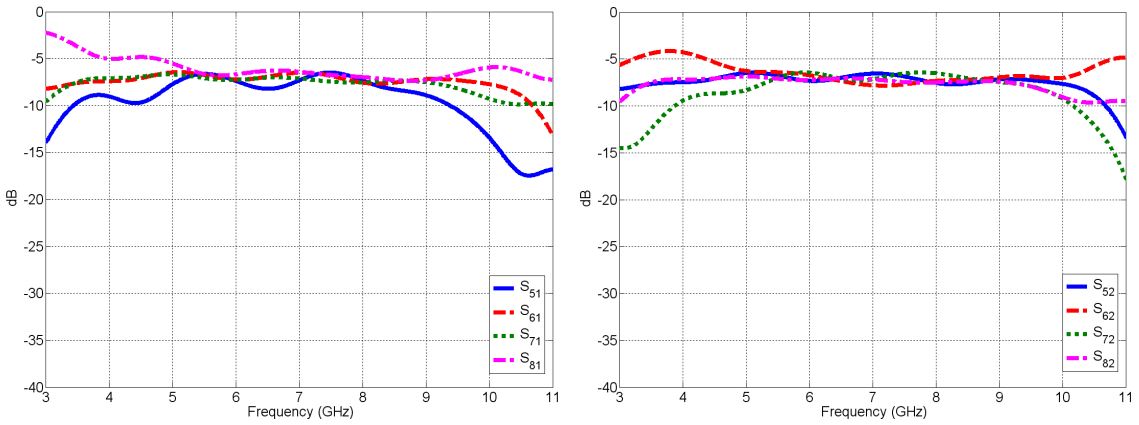

(a) (b)

Figure 6.12 Simulated transmission magnitudes of the butterfly 4×4 Butler matrix when: (a) port # 1 is fed (b) port # 2 is fed.

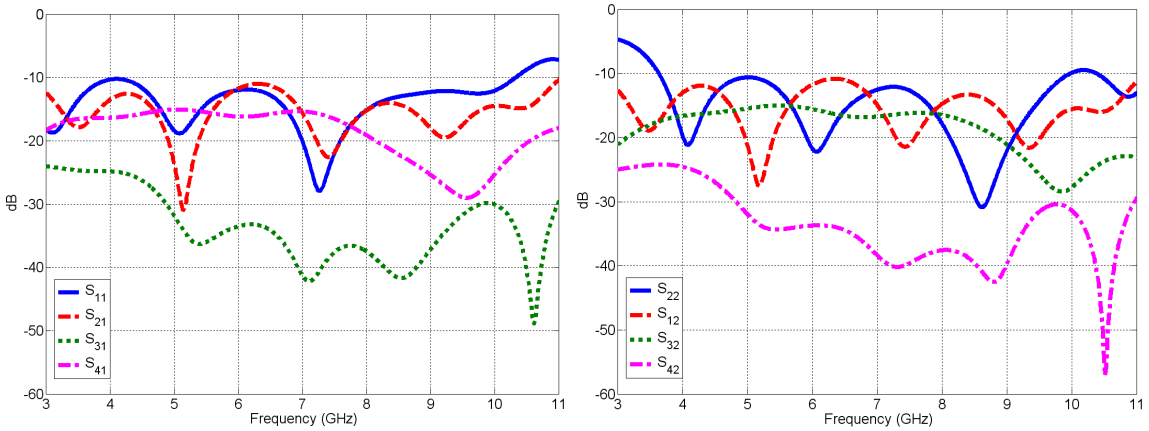

(a) (b)

Figure 6.13 Simulated return losses and isolations of the butterfly 4×4 Butler matrix when: (a) port # 1 is fed (b) port # 2 is fed.

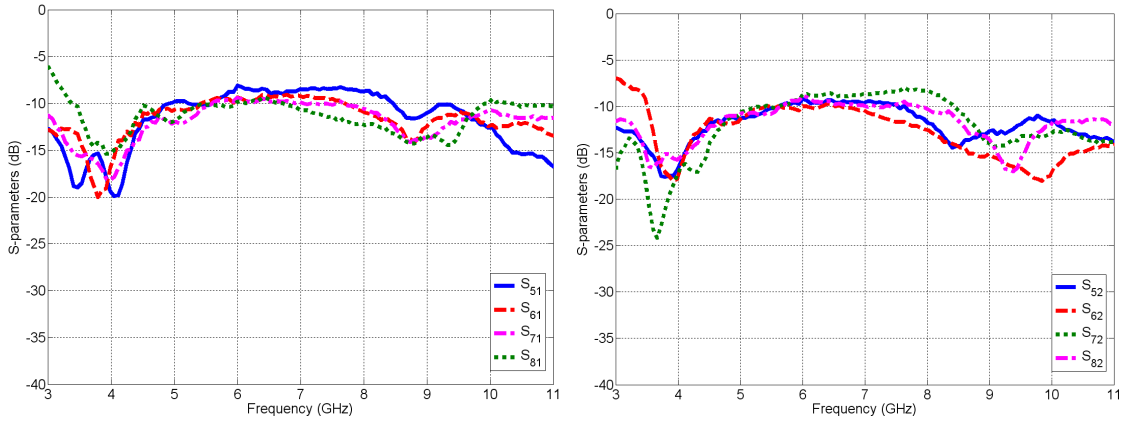

(a) (b)

Figure 6.14 Measured transmission magnitudes of the configuration two for the butterfly-shaped 4×4 Butler matrix when: (a) port # 1 is fed (b) port # 2 is fed.

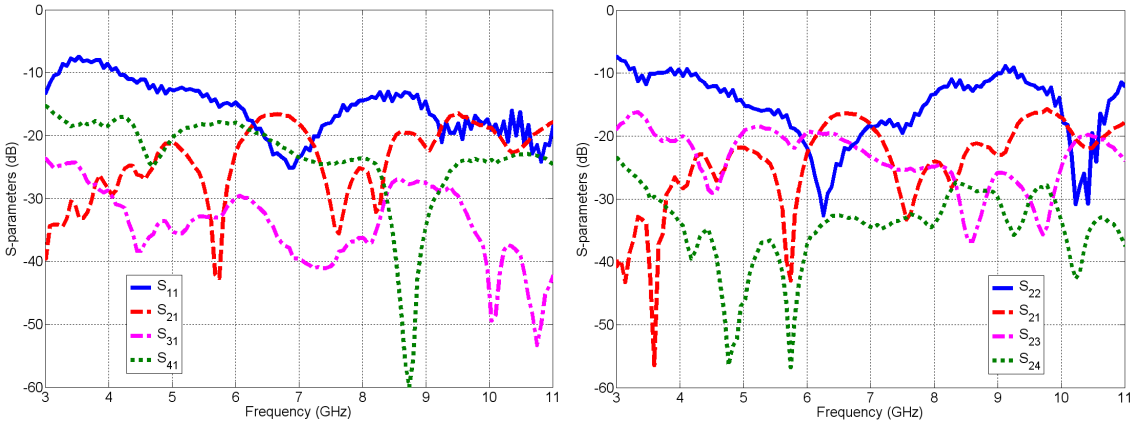

(a) (b)

Figure 6.15 Measured return losses and isolations of the developed configuration two for the butterfly-shaped 4×4 Butler matrix when: (a) port # 1 is fed (b) port # 2 is fed.

The simulated and measured transmission phases of the proposed Butler matrix are shown in Figure 6.16 and Figure 6.17, respectively. The matrix has almost good differential phases of –45°, –90° and –135° when port # 1 is fed and +45°, –90° and +135° when port # 2 is fed within the frequency band of interest especially in the 5.0-10 GHz frequency band.

To demonstrate the impact of Butler matrix transmission magnitudes and phases on the array main beam direction, the designed Butler matrix is fed by a four-element linear TSA array. The array inter-element spacing is chosen to be $0.5\lambda_o$= 28.3 mm at the upper edge frequency f = 10.6 GHz. Figure 6.19 shows the simulated array radiation patterns at the four output ports.

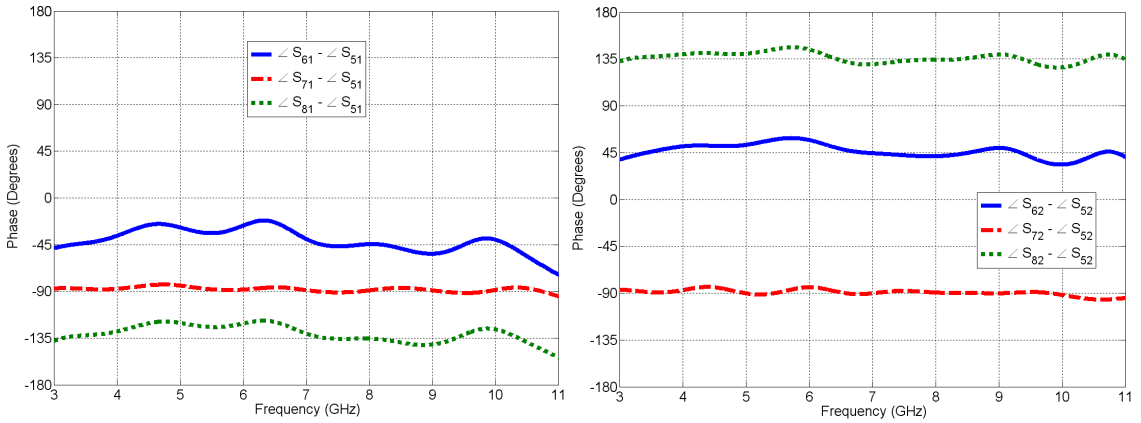

(a) (b)

Figure 6.16 Simulated differential phase characteristics of the butterfly 4×4 Butler matrix when: (a) port # 1 is fed (b) port # 2 is fed.

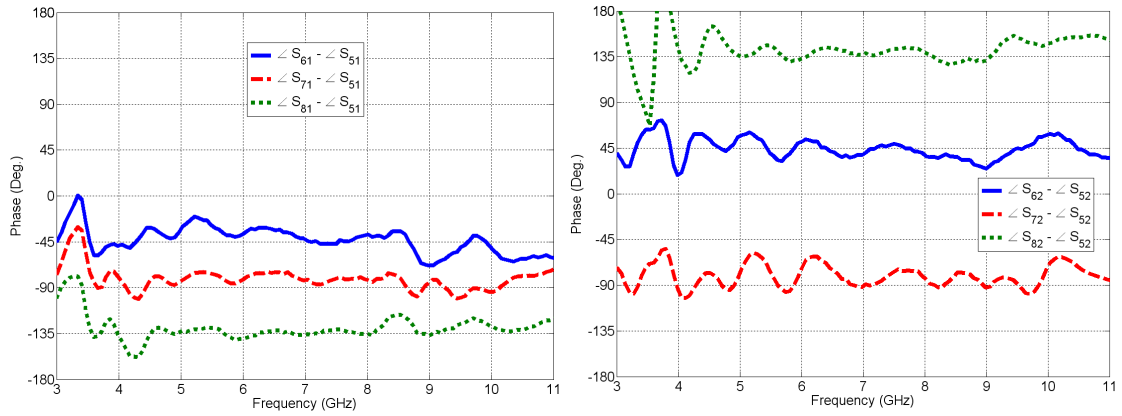

(a) (b)

Figure 6.17 Measured differential phase characteristics of the developed configuration two for the butterfly-shaped 4×4 Butler matrix when: (a) port # 1 is fed, (b) port # 2 is fed.

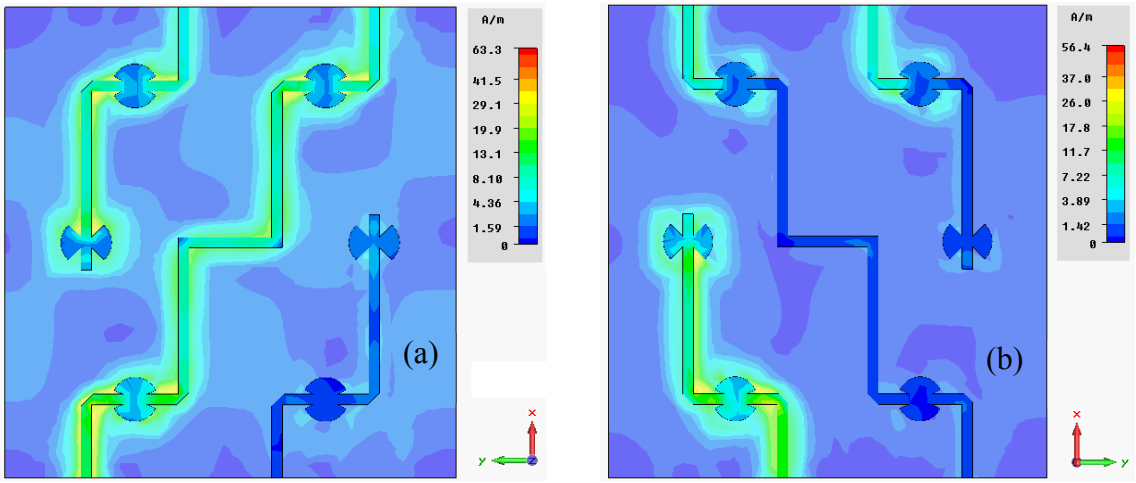

Figure 6.18 Magnetic field distributions for the developed configuration two at center frequency f = 6.85 GHz when: (a) port # 1 is fed, (b) port # 2 is fed.

It can be noticed from radiation characteristics that the proposed configuration-two beamforming antenna array system can steer the main beam in four different directions according to the port fed. The main beam directions are +7°, –20°, +20° and –6° when ports 1, 2, 3 and 4 are fed with signals, respectively. Also, the array side-lobe level (SLL) is better than –4.1 dB in all cases with good angular 3dB beam-widths between

13° and 13.5°. Compared to configuration 1, the obtained radiation patterns with configuration 2 at f = 10.6GHz exhibit better main beam directions and side lobe levels.

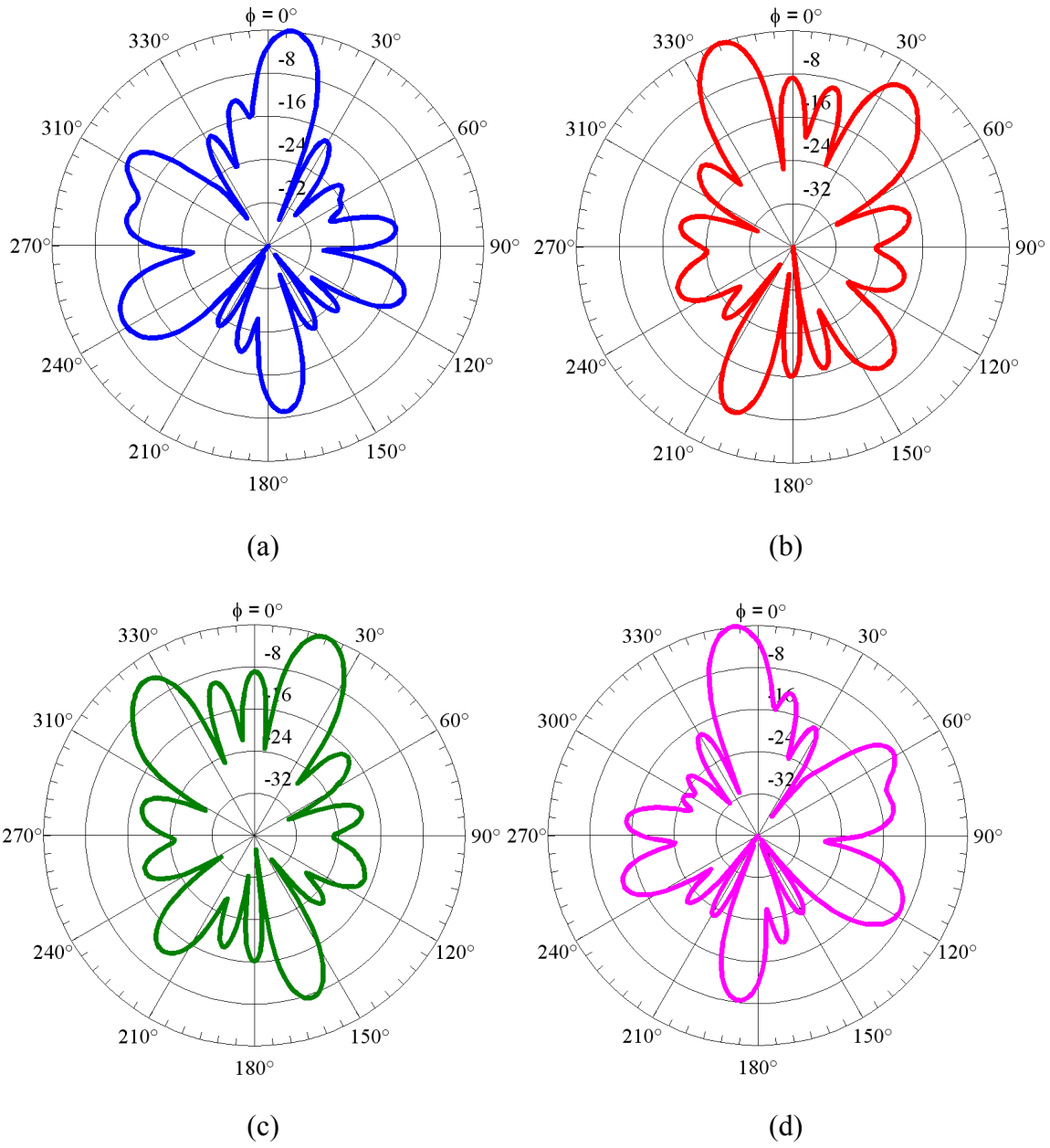

Figure 6.19 Simulated radiation patterns of four-element TSA array fed by the developed Butler matrix in configuration two at f = 10.6 GHz when: (a) port # 1 is fed, (b) port # 2 is fed, (c) port # 3 is fed and (d) port # 4 is fed.

6.3 Summary

This chapter has presented the design of two 4×4 Butler matrix prototypes based on two different shapes for compact and inexpensive beamforming networks. The constructed beamforming networks are based on using two-layered printed circuit board microstrip technology to design 4×4 Butler matrices. It has been shown that these beamforming matrices avoid using any crossing lines or crossovers and hence exhibit good bandwidth performance for UWB applications. Both simulation and experimental results including return loss, isolations, transmission magnitudes and phases are presented and discussed for both configurations. Furthermore, to study the effect of the obtained transmission magnitudes and phases on the performance of the proposed beamforming matrices, a four-element patch antenna array was connected to these matrices to construct multiple beam antenna systems. Simulations were performed on these beamforming systems and the obtained radiation characteristics are also introduced and discussed.

Chapter 7

Conclusions and Future Work

7.1 Conclusions

This thesis has presented the design methodology and results of antenna elements and arrays together with other associated microwave components and beamforming including feed networks, transitions, hybrid couplers and phase shifters over the UWB frequency band. Several UWB antenna elements have been designed, optimized, fabricated and tested seeking for better design for future UWB wireless communication systems. By introducing a simple and proper narrow slot either in the radiating element or in the feeding structure, frequency-notched characteristics are obtained and a good band-notched performance in the 5.0–6.0 GHz band is achieved. Also, a band rejection function is achieved by cutting narrow slots in the finite ground plane. The proposed antenna performance is suitable for UWB applications avoiding the interference of the existing IEEE 802.11a or HIPERLAN/2 wireless local area network systems. In addition, a UWB power divider/combiner network is developed and used to feed UWB two- and four-element linear array antennas. To demonstrate UWB antenna array beamforming networks, compact and inexpensive 4 × 4 Butler matrices for UWB applications are developed and fabricated using UWB two-layered microstrip PCB hybrid couplers and phase shifters integrating different UWB vertical microstrip transitions. Prototyping and measurement verification for different UWB elements are also presented and discussed.

UWB Antenna Elements

Optimized UWB printed disc monopole or hybrid monopole DR antenna prototypes have been fabricated and their electrical characteristics have been experimentally measured. Simulation and experimental results show an antenna impedance bandwidth with reflection coefficient or return loss better than 10 dB over the whole UWB frequency range (3.1–10.6 GHz) for all proposed antennas except for the maple-leaf antenna and hybrid monopole DR antenna where the achieved impedance bandwidth is dual-band. All proposed antennas exhibit reasonable omni-directional radiation patterns in the *H*-plane and good gain flatness over the frequency band of interest. The antenna phase is almost linear with good group delay variation across the desired frequency range. Compared to the other antenna designs, the trapezoidal monopole antenna with bell-shaped cut is considered to be the best candidate for UWB operation because it has a large bandwidth of 112% covering almost the whole UWB frequency range with small size ($30 \times 34 \times 1.575$ mm^3) and good gain stability (±2.6 from 2.7 dB to 5.3 dB).

UWB Power Dividers and Antenna Arrays

To design and construct a UWB array antenna system for high gain applications, UWB feed networks are necessary. For this purpose, a compact modified Wilkinson power divider prototype is introduced. This feed network is based on a modified version of the conventional two-section Wilkinson power divider with overall size 22×13.38 mm^2. The prototype is fabricated and experimentally tested. Simulation and measured results show that the designed feed network is working well over the UWB frequency range. It is then integrated with UWB antenna elements to develop two- and four-element

antenna arrays. The two-element antenna array demonstrates a UWB impedance performance, with antenna array gain of about 5.5–8.5 dBi within the whole UWB frequency band. For the four-element antenna array, the achieved impedance matching is multi-band within the UWB frequency band, and the gain of the antenna array is about 7.5–11.5 dBi. In addition, the radiation patterns of the antenna array are quite stable with frequency.

UWB Microstrip Vertical Transitions, Couplers and Phase Shifters

The design procedure and implementation of different UWB slot-coupled microstrip-to-microstrip vertical transitions are also introduced. The proposed transitions utilize broadside coupling between trapezoidal- and butterfly-shaped microstrip patches at the top and bottom layers. The coupling mechanism uses a rectangular-shaped slot at the common ground plane located at the middle layer. For achieving the maximum possible bandwidth for UWB operation where the transition performances remain acceptable, the coupling value between the microstrip-coupled patches should be between 0.7 and 0.8. The transitions and their subsequent use and integration are fully modeled by 3D electromagnetic numerical modeling techniques. The simulated results have shown that the proposed transitions have a good return loss and an acceptable insertion loss across the desired UWB frequency range while the phase is almost linear with frequency. The transitions are then used to develop 3dB/90° hybrid couplers with good return losses, insertion losses, and coupling and isolation characteristics through the frequency band of interest. By installing a conventional microstrip transmission line to a vertical transition, it can be used as a phase shifter with constant phase through a wide bandwidth of operation.

UWB Beamforming Networks

The design of two different prototypes based on two different shapes for compact and inexpensive beamforming networks is then presented. The constructed BF networks are based on using two-layered microstrip PCB technology to design 4 × 4 Butler matrices. These matrices avoid using any crossovers or crossing lines and hence exhibit wide bandwidth for UWB applications. To validate the proposed design, experimental prototypes of the proposed 4 × 4 Butler matrices were designed, fabricated and tested. Both simulation and experimental results including return loss, isolations, transmission magnitudes and phases are presented and discussed. Furthermore, to test the beam-steering functionality of the proposed matrices, four patch antenna elements were connected to these matrices to form multiple beam antenna systems. Simulations were performed on these beamforming systems and the radiation characteristics were also introduced and discussed.

7.2 Contributions

This work has provided an insight into the design of antenna elements, arrays and associated microwave components such as feed networks, vertical transitions, hybrid couplers and phase shifters for UWB wireless communication applications and will provide a platform for further research in the area. Several journal and conference publications are resulted and reported the contributions of this work in [60]-[62], [132]-[133] and [136]-[148].

The major contributions of the thesis are detailed below.

- From surface current distributions, it has been shown that disc monopole antennas with a finite ground plane are capable of supporting multiple resonant frequencies and the overlap of those multiple resonances leads to a large bandwidth required for UWB operation. This idea is considered to be the operation mechanism for UWB disc monopole antennas. Starting from the original circular disc monopole antenna, different printed disc monopoles presented in [60]-[62], [132]-[133], [136]-[138], [141]-[144], [146]-[148], have been developed in order to achieve better performance or even to reduce the antenna size for mobile and portable devices. In addition, it has been shown that using a hybrid combination of printed monopole and other materials such as dielectric resonators (DRs), a noticeable enhancement in the bandwidth is achieved with remarkable reduction in the overall size of the antenna.
- The proposed UWB antenna elements are integrated with bandstop filtering elements to achieve a notch function at potential interfering frequency band, i.e. 5.15–5.825 GHz to avoid interferences with other existing systems. Different techniques for band rejection have been used and presented in [60], [136]-[138], [141], [143], [146]-[147] such as cutting a narrow slot in the radiating element, feeding structure or even in the finite ground plane without affecting the performance of the antenna in other working frequency bands.
- A compact feed network prototype for UWB applications is also proposed in the thesis and presented in [140], [145]. With this feed network, two- and four-element linear antenna arrays discussed in [139] are implemented for obtaining high gain. The

impact of interaction or mutual coupling between antenna elements on the array radiation characteristics is also discussed in detail.

- Two novel shapes, i.e. trapezoidal and butterfly shapes have been used for designing two-layered vertical microstrip transitions, 3dB hybrid couplers and 45° phase shifters for UWB applications. The two designs for vertical microstrip transitions presented in Chapter 5 are combined and submitted as a full length journal paper to *IEEE Transactions on Microwave Theory and Techniques*. The two new designs for 3dB hybrid coupler as well as phase shifters will be combined and submitted as a full length journal paper each.
- Lastly, a compact size and low cost UWB beamforming network is designed and implemented for UWB communications applications. The proposed beamforming system is 4 × 4 Butler matrix constructed from the previously designed components such as transitions, hybrid couplers and phase shifters. The two new designs for 4 × 4 Butler matrices will be combined and submitted as a full length journal paper.

7.3 Future Work

Based on the completed work in this thesis, much future research may be carried out and outlined in the following tasks:

- Investigate new techniques to reduce the size along with enhancing the bandwidth of UWB printed disc monopole antennas for use in mobile and portable devices.

- Detailed understanding of resonant modes mechanism of hybrid printed monopole antennas loaded with dielectric resonator (DR) and the antenna performance at those different resonant modes to come up with improved design of UWB antennas.
- A better understanding of the operation of bandstop filters elements to achieve band rejection properties to minimize/eliminate potential interference with narrowband communication systems operating in the same UWB frequency band.
- Looking for different shapes, techniques or design approaches to design UWB microwave components such as transitions, hybrid couplers and phase shifters with better performances in the whole UWB frequency range.
- The developed UWB microwave components such as transitions, hybrid couplers and phase shifters will be used to design beamforming network. So enhancing those components and minimizing their losses as much as possible will lead to a better beamforming network.
- The design of 8 × 8 or even 16 × 16 Butler matrices which requires the design of 22.5° and 67.5° phase shifters in addition to 45° phase shifters.
- Design of other types of beamforming networks such as a 4 × 4 Nolen matrix exploiting the designed transitions and hybrid couplers. It needs three different types of couplers, i.e. 3 dB, 4.77 dB and 6 dB hybrid couplers.

References

[1] FCC, “First report and order, revision of part 15 of the commission's rules regarding ultra-wideband transmission systems FCC," 2002.

[2] M.-G. di Benedetto, T. Kaiser, A. F. Molisch, I. Oppermann, C. Politano, and D. Porcino (eds.), UWB Communications Systems: A Comprehensive Overview: Hindawi, 2006.

[3] B. Allen, M. Dohler, E. E. Okon, W. Q. Malik, A. K. Brown, and D. J. Edwards (eds.), Ultra-Wideband Antennas and Propagation for Communications, Radar and Imaging. London, UK: Wiley, 2006.

[4] R. J. Mailloux, Phased Array Antenna Handbook, Artech, Boston, second edition, 2005.

[5] Y. M. Kim, “Ultra Wide Band (UWB) Technology and Applications," technical report, NEST group The Ohio State University, July 10, 2003.

[6] A. Batra et al., “Multi-Band OFDM Physical Layer Proposal,” Document IEEE 802.15-03/267r2, 2003.

[7] M. Z. Win and R. A. Scholtz, “On the energy capture of ultra-wide bandwidth signals in dense multipath environments,” *IEEE Comm. Lett.,* vol. 2, no. 9, pp. 245–247, Sep. 1998.

[8] A. F. Molisch, "Ultrawideband propagation channels - theory, measurement, and modeling," *IEEE Trans. Veh. Technol.,* vol. 54, no. 5, pp. 1528–1545, Sept. 2005.

[9] Beamforming Boosts the Range and Capacity of WiMAX Networks, white paper of Fujitsu Microelectronics America, Inc., July 2008.

[10] C. Nerguizian, C. Despins, S. Affes, and M. Djadel, “Radiochannel characterization of an underground mine at 2.4 GHz wireless communication,” *IEEE Trans. on Wireless Commun.,* vol. 4, no. 5, pp. 2441–2453, Sept. 2005.

[11] G. Foschini, and M. Gans, “On Limits of Wireless Communications in a Fading Environment when Using Multiple Antennas,” Wireless Personal Communications, vol. 6, no. 3, pp. 311–335, 1998.

[12] I. E. Telatar, “Capacity of multi-antenna Gaussian channels,” European Trans. Tel., vol. 10, no. 6, pp. 585–595, 1999.

[13] M. I. Dessouky, H. A. Sharshar, and Y. A. Albagory, “Improving the cellular coverage from a high altitude platform by novel tapered beamforming technique,” *J. of Electromagn. Waves and Appl.,* vol. 21, no. 13, pp. 1721–1731, 2007.

[14] J. H. Winter, J. H., “Smart antennas for wireless systems,” *IEEE Personal Communications,* vol. 5, no. 1, pp. 23–27, Feb. 1998.

[15] P.H. Lehne and M. Pettersen, “An Overview of Smart Antenna Technology for Mobile Communications Systems,” *IEEE Communications Surveys,* vol. 2, no. 4, Fourth Quarter 1999.

[16] H. Ming-Ju, G.L. Stuber, and M. Austin, “Performance of switched beam smart antennas, for cellular radio systems,” *IEEE Trans. Veh. Technol.,* vol. 47, no. 1, pp. 10–19, Feb. 1998.

[17] A. F. Naguib, N. Sesh´adri, and A. R. Calderbank, “Increasing data rate over wireless channels,” *IEEE Signal Processing Magazine*, vol. 17, no. 3, pp. 76–92, 2000.

[18] P. S. Hall and S. J. Vetterlein, "Review of radio frequency beamforming techniques for scanned and multiple beam antennas," *IEE Proc. Microw. Antennas Propag.,* vol. 137, part H, no. 5, Oct. 1990.

[19] J. Blass, "Multidirectional Antenna: A New Approach to Stacked Beams," *IRE International Conference Record*, vol. 8, Part 1, 1960.

[20] S. Mosca, F. Bilotti, A. Toscano, and L. Vegni, "A novel design method for Blass matrix beam-forming networks," *IEEE Trans. Antennas Propag.,* vol. 50, no. 2, pp. 225–232, Feb. 2002.

[21] Y. T. Lo and S.W. Lee, Antenna Handbook. New York: Van Nostrand Reinhold, 1988.

[22] R. C. Hansen, Phased Array Antennas, Wiley, New York, Series in Microwave and Optical Engineering, 1998.

[23] W. Rotman and R. F. Turner, "Wide-angle microwave lens for line source applications," *IEEE Trans. Antennas Propag.,* vol. 11, no. 6, pp. 623–632, Nov. 1963.

[24] P. K. Singhal, P. C. Sharma, R. D. Gupta, "An Overview of Design and Analysis Techniques of Rotman Type Multiple Beam Forming Lens and Some Performance Results," IE(I)Journal-ET, vol. 84 , pp. 52–58, Jan. 2004.

[25] J. Butler and R. Lowe, "Beam-Forming Matrix Simplifies Design of Electronically Scanned Antennas," Electronic Design, vol. 9, pp. 170–173, April 1961.

[26] T. A. Denidni and T. E. Libar, "Wide band four-port Butler matrix for switched multibeam antenna arrays," *IEEE Proc. Personal, Indoor and Mobile Radio Communications*, vol. 3, pp. 2461–2464, Sept. 2003.

[27] M. Nedil, T. A. Denidni and T. E. Libar, “Novel Butler Matrix Using CPW Multi-layer Technology,” *IEEE Trans. Microwave Theory and Techniques,* vol. 54, no. 1, pp. 499–507, Jan. 2006.

[28] Y Huang, K Chan, G Niyomjan, B Cheesman, B Nair, X Zhu and Q Wang, “Some of the latest developments on antennas,” *IEEE Proceedings 2005 International Conference on Wireless Communications, Networking and Mobile Computing,* Wuhan, China, pp. 103–106, Sept. 2005.

[29] Z. N. Chen and X. Qing, “Research and development of planar UWB antennas,” *IEEE Microwave Conference Proceedings, 2005. APMC 2005. Asia-Pacific Conference Proceedings,* 4 pp., Suzhou, China, Dec. 2005.

[30] W. Q. Malik, B. Allen, and D. J. Edwards, “A simple adaptive beamformer for ultrawideband wireless systems,” *Proc. IEEE Int. Conf. Ultrawideband (ICUWB),* USA, pp. 453–457, Sept. 2006.

[31] Antenna Standards Committee of the IEEE Antennas and Propagation Society, IEEE Standard Definitions of Terms for Antennas, IEEE Std 145-1993, The Institute of Electrical and Electronics Engineers, Inc, New York, 1993.

[32] Barrett, W. Terence, “History of Ultra Wideband Communications and Radar: Part I, UWB Communications", Microwave Journal, January 1st, 2001.

[33] L. E. Miller, “Why UWB? A Review of Ultrawideband Technology", National Institute of Standards and Technology, MA, Tech. Rep., April 2003.

[34] I. Linardou, C. Migliaccio, J. M. Laheurte and A. Papiernik, “Twin Vivaldi antenna fed by coplanar waveguide", *Electron. Lett.,* vol.33, no. 22, pp. 1835–1837, Oct. 1997.

[35] E. Guillanton, J.Y. Dauvignac, Ch. Pichot and J. Cashman, “A New Design Tapered Slot Antenna for UWB Applications", *Microwave Opt. Technol. Lett.,* vol. 19, no.4, pp. 286–289, Nov. 1998.

[36] J. P. Weem, B. M. Notaros and Z. Popovic “Broadband Element Array Considerations for SKA", Conf. Proc. Perspectives on Radio Astronomy: Technologies for Large Antenna Arrays, pp.59–67, Dwingeloo, The Netherlands, April, 1999.

[37] E. Gazit, “Improved design of the Vivaldi antenna", *IEE Proc. Microw. Antennas Propag.,* vol. 135, part H, no. 2, pp. 89–92, 1988.

[38] S. G. Kim and K. Chang, “Ultra Wideband Exponentially-Tapered Antipodal Vivaldi Antennas", *IEEE Antennas and Propagation Society Symposium*, vo. 3, pp. 2273 – 2276, Monterey, CA, June 2004.

[39] Warren L. Stutzman and Gary A. Thiele, Antenna Theory and Design, 1998, by John Wiley & Sons, INC.

[40] A. Sibille, “Compared Performance of UWB Antennas for Time and Frequency Domain Modulation", 28th URSI General Assembly, NewDelhi, India, 2005.

[41] S. N. Samaddar. E. L Mokole, “Biconical Antennas with Unequal Cone Angles", *IEEE Transactions on Antenna and Propagation,* Vol 46, No 2, pp 181-193, 1998.

[42] S. Licul, J. A. N. Noronha, W. A. Davis, D. G. Sweeney, C. R. Anderson and T. M. Bielawa, “A parametric study of time-domain characteristics of possible UWB antenna architectures", *IEEE 58th Vehicular Technology Conference, VTC 2003*-Fall, vol. 5, 6-9 October, 2003.

[43] D. J. Sego, “Ultrawide Band Active Radar Array Antenna for Unmanned Air Vehicles", *Proc. IEEE Nat. Telesyst. Conf.,* pp. 13–17, 1994.

[44] E. Gschwendtner, W. Wiesbeck, “Ultra-Broadband Car Antennas for Communications and Navigation Applications", *IEEE Trans. Antennas Propag.,* vol. 51, no. 8, pp. 2020–2027, Aug. 2003.

[45] T. W. Hertel and G. S. Smith, “On the Dispersive Properties of the Conical Spiral Antenna and Its Use for Pulsed Radiation", *IEEE Trans. Antennas Propag.,* vol. 51, no. 7, pp. 1426–1433, July 2003.

[46] Z. Lou and J. M. Jin, “Modeling and Simulation of Broadband Antennas using the Time-Domain Finite-Element Method", *IEEE Trans. Antennas Propag.,* vol. 53, no. 12, pp. 4099–4110, Dec. 2005.

[47] M. J. Ammann, “Square planar monopole antenna", *Proc IEE National Conf Antennas Propagat.,* UK, pp. 37–40, 1999.

[48] M. J. Ammann, “Control of the impedance bandwidth of wideband planar monopole antennas using a beveling technique", *Microwave Opt. Technol. Lett.,* vol. 30, no. 4, pp. 229–232, Aug. 2001.

[49] S. W. Su, K. L. Wong, and C. L. Tang, “Ultra-wideband square planar monopole antenna for IEEE 802.16a operation in the 2–11 GHz band", *Microwave Opt. Technol. Lett.,* vol. 42, no. 6, pp. 463–466, Sept. 2004.

[50] Z. N. Chen, M. J. Ammann, and M. Y. W. Chia, “Broadband square annular planar monopoles", *Microwave Opt. Technol. Lett.,* vol. 36, no. 6, pp. 449–454, Mar. 2003.

[51] N. P. Agrawall, G. Kumar, and K. P. Ray, “Wide-Band Planar Monopole Antennas", *IEEE Trans. Antennas Propag.,* vol. 46, no. 2, pp. 294–295, Feb. 1998.

[52] Z. N. Chen, M. J. Ammann, M. Y. W. Chia and T. S. P. See, “Annular planar monopole antennas", *IEE Proc. Microw. Antennas Propag.,* vol. 149, no. 4, pp. 200–203, Aug. 2002.

[53] Z. N. Chen, and Y. W. M. Chia, “Impedance characteristics of trapezoidal planar monopole antennas,” *Microwave Opt. Technol. Lett.,* vol. 27, no. 2, pp. 120–122, Oct. 2000.

[54] S. Y. Suh, W. L. Stutzman, and W. A. Davis, “A New Ultrawideband Printed Monopole Antenna The Planar Inverted Cone Antenna (PICA)", *IEEE Trans. Antennas Propag.,* vol. 52, no. 5, pp. 1361–1365, May 2004.

[55] Z. N. Chen, “Broadband Roll Monopole", *IEEE Trans. Antennas Propag.,* vol. 51, no. 11, pp. 3175–3177, May 2003.

[56] H Deng, X He, S Liu, Y Xie, “A novel Ultra Wideband Planar Antenna,” *Global Symposium on Millimeter Waves (GSMM),* pp. 288–290, April 2008.

[57] S. Cheng, P. Hallbjorner, and A. Rydberg, “Printed Slot Planar Inverted Cone Antenna for Ultrawideband Applications,” *IEEE Antennas Wireless Propag. Lett.,* vol. 7, pp.18–21, 2008.

[58] J.-P. Zhang, Y.-S. Xu, and W.-D Wang, “Microstrip-Fed Semi-Elliptical Dipole Antennas for Ultrawideband Communications,” *IEEE Trans. Antennas Propag.,* vol. 56, no.1, pp. 241–244, 2008.

[59] A. Abbosh and M. Bialkowski, “Design of ultra wideband planar monopole antennas of circular and elliptical shape,” *IEEE Trans. Antennas Propag.,* vol. 56, no.1, pp.17–23, 2008.

[60] O. Ahmed and A.-R. Sebak, "A Printed Monopole Antenna with Two Steps and a Circular Slot for UWB Applications," *IEEE Antennas Wireless Propag. Lett.,* vol.7, pp. 411–413, 2008.

[61] O. Ahmed and A.-R. Sebak, "A Novel Ultra-Wideband Printed Monopole Antenna", *XXIX General Assembly of the International Union of Radio Science (URSI),* Chicago, USA, 2008.

[62] O. Ahmed and A.-R. Sebak, "A Novel Maple Leaf Shaped Printed Monopole Antenna for UWB Wireless Communications", *IEEE International Symposium on Antennas and Propagation and USNC/URSI National Radio Science Meeting (APS/URSI),* San Diego, USA, 2008.

[63] N. C. Azenui, and H. Y. D. Yang, "A printed crescent patch antenna for ultrawideband applications," *IEEE Antennas Wireless Propag. Lett.,* vol. 6, pp. 113–116, 2007.

[64] J. Liang, C.C. Chiau, X. Chen and C.G. Parini, "Study of a printed circular disc monopole antenna for UWB systems," *IEEE Trans. Antennas Propag.,* vol. 53, no. 11, pp. 3500–3504, Nov. 2005.

[65] C. Y. Huang and W. C. Hsia, "Planar elliptical antenna for ultra-wideband communications," *Electron. Lett.,* vol. 41, no. 6, pp. 296-297, Mar. 2005.

[66] C.-H. Hsu, "Planar multilateral disc monopole antenna for UWB application," *Microwave Opt. Technol. Lett.,* vol. 49, no. 5, pp. 1101–1103, May 2007.

[67] S. H. Choi, J. K. Park, S. K. Kim, and J. Y. Park, "A New UWB Antenna for UWB Applications," *Microwave Opt. Technol. Lett.,* vol. 40, no. 5, pp. 399–401, May 2004.

[68] Z. N. Chen, T. S. P. See, and X. Qing, "Small printed Ultrawideband antenna with reduced ground plane effect," *IEEE Trans. Antennas Propag.,* vol. 55, no. 2, pp. 383–388, Feb. 2007.

[69] M. A. Peyrot-Solis, G. M. Galvan-Tejada, and H. Jardon-Aguilar, "A novel planar UWB monopole antenna formed on a printed circuit board," *Microwave Opt. Technol. Lett.,* vol. 48, no. 5, pp. 933–935, May 2006.

[70] Chih-Yu Huang, Wei-Chun Hsia, and Jieh-Sen Kuo, "Planar ultra-wideband antenna with a band-notched characteristic," *Microwave Opt. Technol. Lett.,* vol. 48, no. 1, pp. 99–101, Oct. 2006.

[71] M. Naghshvarian-Jahromi, "Compact UWB bandnotch antenna with transmission-line fed," *Progress In Electromagnetics Research B,* vol. 3, pp. 283–293, 2008.

[72] C.-Y. Huang, S.-A. Huang, and C.-F. Yang, "Band-Notched Ultra-Wideband Circular Slot Antenna With Inverted C-Shaped Parasitic Strip," *Electron. Lett.,* vol. 44, no. 15, pp. 891–892, July 2008.

[73] C.-J. Pan, C. Lee, C.-Y. Huang, and H.-C. Lin, "Band-notched ultra-wideband slot antenna," *Microwave Opt. Technol. Lett.,* vol. 48, no. 12, pp. 2444–2446, Oct. 2006.

[74] J. Kim, C.S. Cho and J.W. Lee, "5.2 GHz notched ultra-wideband antenna using slot-type SRR," *Electron. Lett.,* vol. 42, no. 6, pp. 315–316, Mar. 2006.

[75] H. W. Liu, C. H. Ku, T. S. Wang, C.F. Yang, "Compact monopole antenna with band-notched characteristic for UWB applications", *IEEE Antennas Wireless Propag. Lett.,* vol. 9, pp. 397–400, 2010.

[76] Y. C. Lin and K. J. Hung, "Compact Ultrawideband Rectangular Aperture Antenna and Band-Notched Designs," *IEEE Trans. Antennas Propag.,* vol. 54, no. 11, pp. 3075–3081, Nov. 2006.

[77] M. Ojaroudi, G. Ghanbari, N. Ojaroudi, C. Ghobadi, "Small square monopole antenna for UWB applications with Variable frequency band-notch function", *IEEE Antennas Wireless Propag. Lett.,* vol. 8, pp. 1061–1064, 2009.

[78] B. Ahamadi, R. F. Dana, "A miniaturized monopole antenna for ultrawideband applications with band-notch filter", *IET Microwave antennas Propagations,* vol.3, pp.1224–1231, 2009.

[79] S. W. Qu, J. Li, and Q. Xue, "A Band-notched Ultrawideband Printed Monopole Antenna," *IEEE Antennas Wireless Propag. Lett.,* vol. 5, pp. 495–498, Dec. 2006.

[80] C.-Y. Hong, C.-W. Ling, I.-Y. Tarn, and S.-J. Chung, "Design of a Planar Ultrawideband Antenna with a New Band-Notch Structure," *IEEE Trans. Antennas Propag.,* vol. 55, no. 12, pp. 3391–3397, 2007.

[81] Y.-L. Zhao, Y.-C. Jiao, G. Zhao, L. Zhang, Y. Song, and Z.-B. Wong, "Compact Planar Monopole UWB Antenna with Band-Notched Characteristic," *Microwave Opt. Technol. Lett.,* vol. 50, no. 10, pp. 2656–2658, Oct. 2008.

[82] H. Z. Liu, J. C. Coetzee, and K. Mouthaan, "UWB antenna array for wireless transmission along corridors," *Microwave Opt. Technol. Lett.,* vol. 50, no. 4, pp. 886–890, Apr. 2008.

[83] Y.-Y. Yang and Q.-X. Chu, "Planar 4-element UWB antenna array and time domain characterization," *Microwave Opt. Technol. Lett.,* vol. 50, no. 12, pp. 3118–3123, Dec. 2008.

[84] M. Ameya, Y. Ito, M. Yamamoto and T. Nojima, “2-element UWB array antenna using leaf-shaped bowtie element,” *2007 IEEE AP-S Int. Symp. on Antennas and Propagation,* Honolulu, Hawaii, USA, pp. 1961–1964, June 2007.

[85] Y. Ito, M. Ameya, M. Yamamoto and T. Nojima, “Unidirectional UWB array antenna using leaf-shaped bowtie elements and flat reflector,” *Electron. Lett.,* vol. 44, no. 1, pp. 9–11, Jan. 2008.

[86] P. Li, J. Liang, X. Chen, and C. Parini, “A 4-Element Ultra-wideband Tapered-Slot-Fed Antenna Array,” *IEEE International Symposium on Antenna and Propagation (IEEE AP-S),* pp. 4475–4478, July 2006.

[87] Y. Yang, C. Zhang, S. Lin, and A. E. Fathy, "Development of an ultra wideband Vivaldi antenna array," *IEEE International Symposium on Antenna and Propagation (IEEE AP-S)*, vol. 1A, pp. 606–609, July 2005.

[88] D. Pozar, *Microwave Engineering*, 3rd ed. New York: Wiley, 2005.

[89] S. B. Cohn, “A Class of Broadband Three-Port TEM-Mode Hybrid,” *IEEE Trans. Microw. Theory Tech.*, vol. 19, no. 2, pp. 110–116, Feb. 1968.

[90] R. Pazoki, M. R. Ghafouri Fard and H. Ghafouri Fard, “A Modification in the Single-Stage Wilkinson Power Divider to Obtain Wider Bandwidth,” *Proc. Asia-Pacific Microw, Conf.,* pp. 2325–2328, Dec. 2007.

[91] X.-P. Ou and Q.-X. Chu, “A Modified Two-section UWB Wilkinson Power Divider”, *International Conference on Microwave and Millimeter Wave Technology ICMMT,* 2008.

[92] L. Yang, Q.-X. Chu, "Design of a Compact UWB Wilkinson Power Divider", *International Conference on Microwave and Millimeter Wave Technology ICMMT*, 2008.

[93] K. Yi and B. Kang, "Modified Wilkinson Power Divider for nth Harmonic Suppression," *IEEE Microw. Wireless Compon. Lett.*, vol. 13, no. 5, pp. 178–180, May 2003.

[94] A. Abbosh, "A compact UWB three-way power divider," *IEEE Microw. Wireless Compon. Lett.,* vol. 17, no. 8, pp. 598–600, Aug. 2007.

[95] D. Wu, Y. Fan, M. Zhao, and Y.-H. Zhang," Vertical transition in multilayer millimeter wave module using circular cavity," *Progress In Electromagnetics Research M,* vol. 5, pp. 91–100, 2008.

[96] S. Ya , Z. Jun," Design of vertical transition for broad-band T/R module applications with LTCC technology," *1st Asian and Pacific Conference on Synthetic Aperture Radar APSAR,* 2007.

[97] F. Casares-Miranda, et al., "Vertical microstrip transition for multilayer microwave circuits with decoupled passive and active layers," *IEEE Microw. Wireless Compon. Lett.,* vol. 16, no. 7, pp. 401–403, July 2006.

[98] A. M. Abbosh, "Ultra Wideband Vertical Microstrip-Microstrip Transition," *IET Microw. Antennas Propag.,* vol. 1, no. 5, pp. 968–972, Oct. 2007.

[99] M. Nedil, T. A. Denidni and A. Djaiz, "Ultra-wideband microstrip to CB-CPW transition applied to broadband filter," *Electron. Lett.,* vol. 43, no. 8, pp. 464–466, Apr. 2007.

[100] N.-B. Wang, Y.-C. Jiao, L. Zhang, Y. Song, and F.-S. Zhang, "A simple low-loss broadband 1-14 GHz microstrip-to-slotline transition," *Microwave Opt. Technol. Lett.,* vol. 51, no. 9, pp. 2236–2239, Sept. 2009.

[101] A. S. Theodorou and N. K. Uzunoglu, "Transition properties of a vertical conductor connecting two microstrip lines at different planes," *IEEE Trans. Microw. Theory Tech.,* vol. 42, no. 12, pp. 2277–2284, Dec. 1994.

[102] Chen, M. Tsai, and G. Alexopoulos, "Optimization of aperture transitions for multiport-microstrip circuits," *IEEE Trans. Microw. Theory Tech.,* vol. 44, no. 12, pp. 2457–2465, Dec. 1996.

[103] L. Zhu and K. Wu, "Ultrabroad-band vertical transition for multilayer integrated circuits," *IEEE Microwave Guide Wave Lett.,* vol. 9, no. 11, pp. 453–455, Nov. 1999.

[104] E. Li, J. Cheng, and C. Lai, "Designs for broadband microstrip vertical transitions using cavity couplers," *IEEE Trans. Microw. Theory Tech.,* vol. 54, no. 1, pp. 464–472, Jan. 2006.

[105] R. Mongia, I. Bahl, and P. Bhartia, RF and Microwave coupled-line circuits, Artech House, Norwood, MA, second ed., 2007.

[106] T. Tanaka, K. Tsunoda, and M. Aikawa, "Slot-coupled directional couplers between double-sided substrate microstrip lines and their applications," *IEEE Trans. Microw. Theory Tech.,* vol. 36, no.12, pp. 1752–1757, Dec. 1988.

[107] A. Abbosh, and M. Bialkowski, "Design of Compact Directional Couplers for UWB Applications," *IEEE Trans. Microw. Theory Tech.,* vol. 55, no.2, pp. 189–194, Feb. 2007.

[108] A. M. Abbosh, "Broadband quadrature coupler with slotted ground plane," *Microwave Opt. Technol. Lett.,* vol. 50, no. 2, pp. 328–331, Feb. 2008.

[109] M. Nedil and T. A. Denidni, "Analysis and design of an ultra wideband directional coupler," *Progress In Electromagnetics Research (PIER) B,* vol. 1, pp. 291–305, 2008.

[110] F. Zhang, "Miniaturized and harmonics-rejected slow-wave branch-line coupler based on microstrip electromagnetic bandgap element," *Microwave Opt. Technol. Lett.,* vol. 51, no. 4, pp. 1080–1084, Apr. 2009.

[111] W. Hilberg, "From approximations to exact relations for characteristic impedances," *IEEE Trans. Microw. Theory Tech.,* vol. 17, no.5, pp. 259–265, May 1969.

[112] M. F. Wong, V. F. Hanna, O. Picon, and H. Baudrand, "Analysis and design of slot-coupled directional couplers between double-sided substrate microstrip lines," *IEEE Trans. Microw. Theory Tech.,* vol. 39, no. 12, pp. 2123–2129, Dec. 1991.

[113] B. Schiffman, "A new class of broadband microwave 90-degree phase shifters," *IRE Trans. Microw. Theory Tech.,* vol. 6, no. 4, pp. 232–237, Apr. 1958.

[114] B. Schiffman, "Multisection microwave phase-shift network," *IEEE Trans. Microw. Theory Tech.,* vol. 14, no. 4, pp. 209–209, Apr. 1966.

[115] S. Y. Zheng, S. H. Yeung, W. S. Chan, K. F. Man and S. H. Leung, "Improved broadband dumb-bell-shaped phase shifter using multi-section stubs," *Electron. Lett.,* vol. 44, no. 7, pp. 478–480, Mar. 2008.

[116] Y. Guo, Z. Zhang, and L. Ong, "Improved wideband Schiffman phase shifter," *IEEE Trans. Microw. Theory Tech.,* vol. 54, no. 3, pp. 1196–1200, Mar. 2006.

[117] V. Meschanov, I. Metelnikova, V. Tupikin, and G. Chumaevskaya, "A new structure of microwave ultrawide-band differential phase shifter," *IEEE Trans. Microw. Theory Tech.,* vol. 42, no. 5, pp. 762–765, May 1994.

[118] Corona, A. and M. J. Lancaster, "A high-temperature superconducting Butler matrix," *IEEE Trans. on Applied Superconductivity,* vol. 13, no. 4, pp. 3867–3872 Dec. 2003.

[119] HFSS, v10, Ansoft Corporation Software, Pittsburgh, PA, USA.

[120] CST Microwave Studio, Ver. 2010 Computer Simulation Technology, Framingham, MA, USA.

[121] M. Clements and T. Weiland, "Discrete electromagnetism with the Finite Integration Technique", *Progress In Electromagnetics Research,* vol. 32, pp. 65–87, 2001.

[122] Constantine A. Balanis, "Antenna Theory Analysis and Design", 2005, by John Wiley & Sons, INC.

[123] J. Liang, "Antenna Study and Design for Ultra Wideband Communication Applications," PhD Thesis, July 2006.

[124] Q. Rao, T. A. Denidni, A. R. Sebak, and R. H. Johnston, "On improving impedance matching of a CPW fed low permittivity dielectric resonator antenna," *Progress In Electromagnetics Research,* vol. 53, pp. 21–29, 2005.

[125] M. Lapierre, Y. M. M. Antar, A. Ittipiboon, and A. Petosa, "Ultra Wideband Monopole/Dielectric Resonator Antenna," *IEEE Microwave and Wireless Components Lett.,* vol. 15, no. 1, pp. 7–9, Jan. 2005.

[126] A. A. Kishk, "Experimental study of the broadband embedded dielectric resonator antennas excited by a narrow slot," *IEEE Antennas Wireless Propag. Lett.,* vol. 4, pp. 79–81, 2005.

[127] T.-H. Chang and J.-F. Kiang, "Broadband dielectric resonator antenna with an off-set well," *IEEE Antennas Wireless Propag. Lett.,* vol. 6, pp. 564–567, 2007.

[128] R. Chair, A.A. Kishk, and K.-F. Lee, "Wideband stair-shaped dielectric resonator antennas," *IET Microw., Antennas Propag.,* vol. 1, no. 2, pp. 299–305, Apr. 2007.

[129] X. L. Liang and T. A. Denidni, "H-shaped dielectric resonator antenna for wide-band applications," *IEEE Antennas Wireless Propag. Lett.,* vol. 7, pp. 163–166, 2008.

[130] Liang, X. L., T. A. Denidni, and L. N. Zhang, "Wideband L- shaped dielectric resonator antenna with a conformal inverted- trapezoidal patch feed," *IEEE Trans. Antennas Propag.,* vol. 57, no. 1, pp. 271–274, Jan. 2009.

[131] K. S. Ryu and A. A. Kishk, "Ultrawideband Dielectric Resonator Antenna with Broadside Patterns Mounted on a Vertical Ground Plane Edge," *IEEE Trans. Antennas Propag.,* vol. 58, no. 4, pp. 1047–1053, Apr. 2010.

[132] O. Ahmed, A. R. Sebak, and T. A. Denidni, "A Novel Compact UWB Printed Monopole Loaded with Dielectric Resonator Antenna", *IET Electronics Letters,* vol. 47, no.1, Jan. 2011.

[133] O. Ahmed, A. R. Sebak, and T. A. Denidni, "Size Reduction and Bandwidth Enhancement of a UWB Hybrid Dielectric Resonator Antenna for Short-Range Wireless Communications", *Progress in Electromagnetics Research Letters PIER L,* vol. 19, pp. 19-30, 2010.

[134] M. Nedil, T. A. Denidni, A. Djaiz, and A. M. Habib, “A new ultra-wideband beamforming for wireless communications in underground mines", *Progress in Electromagnetics Research PIER M,* vol. 4, pp. 1-21, 2008.

[135] M. Traii, M. Nedil, A. Gharsallah, and T. A. Denidni, “A novel wideband Butler matrix using multi-layer technology", *Microwave Opt. Technol. Lett.,* vol. 51, no. 3, pp. 659–663, Mar. 2009.

[136] O. Ahmed, A. R. Sebak, “A Novel Printed Monopole Antenna for Future Ultrawideband Communication Systems", *Microwave Opt. Technol. Lett.,* vol. 53, no. 8, pp. 1837–1841, Aug. 2011.

[137] O. Ahmed, A. R. Sebak, “Numerical and Experimental Investigation of a Novel Ultrawideband Butterfly Shaped Printed Monopole Antenna with Bandstop Function", *Progress In Electromagnetics Research PIER C,* vol. 18, pp. 111-121, 2011.

[138] A. Elboushi, O. Ahmed, A. R. Sebak, “Study of Elliptical Slot UWB Antennas with A 5.0-6.0GHz Band-Notch Capability", *Progress In Electromagnetics Research PIER C,* vol. 16, pp. 207-222, 2010.

[139] O. Ahmed and A.-R. Sebak, “Planar Ultrawideband Antenna Array for Short-Range Wireless Communications", *Microwave and Optical Technology Letters,* vol. 52, no. 5, pp. 1061 – 1066, Mar. 2010.

[140] O. Ahmed and A.-R. Sebak, “Experimental Investigation of New Ultra Wide band In-Phase and Quadrature-Phase Power Splitters", *J. of Electromagn. Waves and Appl.,* vol. 23, pp. 2261–2270, 2009.

[141] O. Ahmed and A.-R. Sebak, "A Novel Maple-Leaf Shaped UWB Antenna with a 5.0-6.0 GHz Band-Notch Characteristic", *Progress In Electromagnetics Research PIER C,* vol. 11, pp. 39-49, 2009.

[142] O. M. Haraz and A.-R. Sebak, "A Novel Circularly Polarized Dielectric Resonator Antenna for UWB Applications", *IEEE International Symposium on Antennas and Propagation and CNC/USNC/URSI Radio Science Meeting (AP-S/URSI),* Toronto, Ontario, Canada July 11-17, 2010.

[143] O. M. Haraz, A. Elboushi, and A.-R. Sebak, "Band Rejection Capabilities of UWB Elliptical Slot Antenna with Half Circular and Crescent Ring Shaped Radiators", *IEEE International Symposium on Antennas and Propagation and CNC/USNC/URSI Radio Science Meeting (AP-S/URSI),* Toronto, Ontario, Canada July 11-17, 2010.

[144] O. M. Haraz, A. Elboushi, and A.-R. Sebak, "Analysis and Design of UWB Elliptical Slot Antennas", *the 14th International Symposium on Antenna Technology and Applied Electromagnetics [ANTEM] and the American Electromagnetics Conference [AMEREM],* Ottawa, Canada, July 5 – 9, 2010.

[145] O. Ahmed and A.-R. Sebak, "A Modified Wilkinson Power Divider / Combiner for Ultrawideband Communications", *IEEE International Symposium on Antennas and Propagation and USNC/URSI National Radio Science Meeting (AP-S/URSI),* North Charleston, USA, 2009.

[146] O. Ahmed, A. A. Abumazwed and A.R. Sebak, "A Trapezoidal Printed Monopole Antenna with Bell-Shaped Cut for Ultra Wideband Applications with 5.0-6.0GHz

Band Rejection", *the third European Conference on Antennas and Propagation* (EuCAP 2009).

[147] O. Ahmed and A.-R. Sebak, "A Compact UWB Butterfly Shaped Planar Monopole Antenna with Bandstop Characteristic", *13th International Symposium on Antenna Technology and Applied Electromagnetics and the Canadian Radio Sciences Meeting (ANTEM/URSI),* 2009.

[148] O. Ahmed and A.-R. Sebak, "Study a Compact Printed Monopole Antenna with Two Notches and an Offset Circular Slot for UWB Communications", *IEEE International Symposium on Antennas and Propagation and USNC/URSI National Radio Science Meeting (AP-S/URSI),* San Diego, USA, 2008.

[149] J. P. A. Bastos and N. Sadowski, *Electromagnetic Modeling by Finite Element Methods*, New York: Marcel Dekker, Inc. 2003.

[150] W. C. Gibson, *The Method of Moments in Electromagnetics*, Chapman & Hall/CRC, Taylor & Francis Group 2008,

[151] A. Taflove and S. C. Hagness, *Computational Electrodynamics: The Finite-Difference Time-Domain Method*, Third Edition, Artech House, 2005.

[152] D. Swason, *Microwave Circuit Modeling using Electromagnetic Field Simulation*, ARTECH, 2003.

[153] X. R. Yan, S. S. Zhong, and G. Y. Wang, "Compact Printed Monopole Antenna with 24:1 Impedance Bandwidth," *Microwave Opt. Tech. Lett.* 49 (11), 2883–2886 (2007).

[154] X.-R. Yan, S.-S. Zhong, and X.-L. Liang, Compact printed semi-elliptical monopole antenna for super-wideband applications, *Microwave Opt Technol Lett* 49 (2007), 2061–2063.

[155] Z.N. Low, J.H. Cheong, and C.L. Law, Low-cost PCB antenna for UWB applications, *IEEE Antennas Wireless Propag Lett* 4 (2005), 237–239.

[156] Choi,S. H.,J. K. Park,S. K. Kim,and J. Y. Park,"A new ultrawideband antenna for UWB applications," *Microwave Opt. Tech. Lett.,*V ol. 40, No. 5,399–401, Mar. 2004.

[157] K. S. Yngvesson, D. H. Schaubert, T. L. Korzeniowski, E. L. Kollberg, T. Thungren, and J. F. Johansson, "Endfire tapered slot antennas on dielectric substrates," *IEEE Trans. Antennas Propag*, Vol. 33, No. 12, 1392–1400, Dec. 1985.

Appendix A

Analysis of Modified UWB Wilkinson Power Dividers

Figure A.1 shows the schematic diagram of the proposed power divider for UWB operation. It simply consists of modified two-section Wilkinson power divider with removing the resistor of the second section R_2. The first section consists of transmission lines with characteristic impedance of Z_1 and electrical length of θ_1. To enhance the bandwidth, the first transmission lines are extended (Z_1, θ_1') and one open-circuit (OC) stub with (Z_S, θ_S) has been added to each branch. The second section consists of transmission lines with characteristic impedance and electrical length of (Z_2, θ_2) at the end of first section. By adjusting the length and width of the stubs, the bandwidth can be increased.

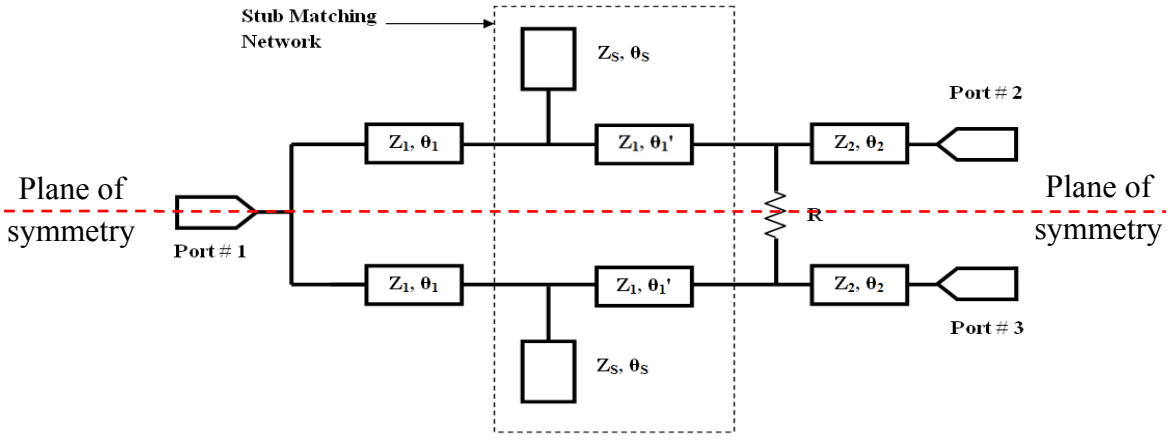

Figure A.1 Schematic of the proposed UWB in-phase power divider/combiner

The proposed power divider for UWB applications is symmetric in structure, so it can be analyzed by the even–odd decomposition method [88]. The purpose of the present analysis is to determine the divider basic or initial parameters for UWB frequency operation such as $Z_1, Z_2, Z_S, \theta_1, \theta_1', \theta_2$ and θ_S. The impedance of the input and output ports are chosen to be 50Ω. To prevent signal transmission between the two output ports for good isolation between them, a single lumped resistor R is attached between the two output ports. The OC stubs are represented by their equivalent input admittance $Y_S = jB_S$:

$$Y_S = jB_S = j\frac{tan\theta_S}{Z_S} \tag{A.1}$$

The equivalent half circuits of the divider in the even- and odd-modes are shown in Figure A.2 and Figure A.3, respectively. Assuming that the proposed power divider is matched at all ports, hence the equivalent half circuits should be matched at all ports as well as the complete circuit [89]:

$$S_{11}^e = S_{22}^e = S_{22}^o = 0 \tag{A.2}$$

where S is the scattering parameter of the divider and the superscripts e, o denote the even- and the odd-mode half circuits, respectively. The reflection coefficients can be obtained by analyzing the even- and the odd-mode half circuits in the following sections.

A.1 Even-mode Analysis

In case of an even-mode, there is no current flow through the plane of symmetry, which means the middle of the power divider is open circuit (OC) case. Therefore, the resistor R can be omitted and the impedance at port # 1 is doubled to be $2Z_o$. Using transmission line theory [89], the even-mode input admittance at port # 1 (Y_{in1}^e) is:

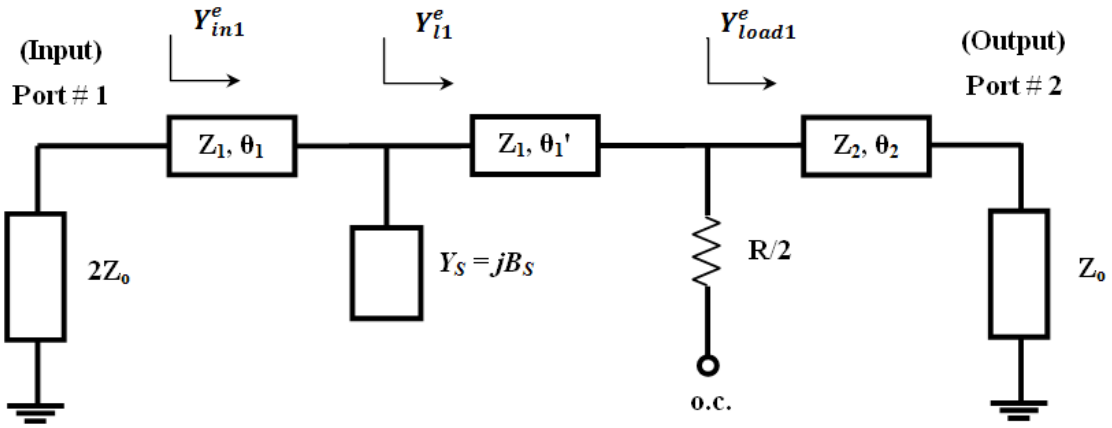

Figure A.2 Circuit of the power divider for the even-mode analysis

$$Y^e_{in1} = \frac{1}{Z_1}\frac{Y^e_{l1} + j(1/Z_1)\,tan\theta_1}{1/Z_1 + jY^e_{l1}\,tan\theta_1} \tag{A.3}$$

$$Y^e_{l1} = jB_S + \frac{1}{Z_1}\frac{Y^e_{load1} + j(1/Z_1)\,tan\theta_1^{'}}{1/Z_1 + jY^e_{load1}\,tan\theta_1^{'}} \tag{A.4}$$

$$Y^e_{load1} = \frac{1}{Z_2}\frac{1/Z_o + j(1/Z_2)\,tan\theta_2}{1/Z_2 + j(1/Z_o)\,tan\theta_2} \tag{A.5}$$

The even-mode input admittance at port # 2 (Y^e_{in2}) can be calculated from:

$$Y^e_{in2} = \frac{1}{Z_2}\frac{Y^e_{l2} + j(1/Z_2)\,tan\theta_2}{1/Z_2 + jY^e_{l2}\,tan\theta_2} \tag{A.6}$$

$$Y^e_{l2} = \frac{1}{Z_1}\frac{Y^e_{load2} + j(1/Z_1)\,tan\theta_1^{'}}{1/Z_1 + jY^e_{load2}\,tan\theta_1^{'}} \tag{A.7}$$

$$Y^e_{load2} = jB_S + \frac{1}{Z_1}\frac{1/2Z_o + j(1/Z_1)\,tan\theta_1}{1/Z_1 + j(1/2Z_o)\,tan\theta_1} \tag{A.8}$$

Then the even-mode scattering parameter at port # 1 (S^e_{11}) and port # 2 (S^e_{22}) can be calculated using:

$$S^e_{11} = \frac{(1/2Z_o - Y^e_{in1})}{(1/2Z_o + Y^e_{in1})};\; S^e_{22} = \frac{(1/Z_o - Y^e_{in2})}{(1/Z_o + Y^e_{in2})} \tag{A.9}$$

A.2 Odd-mode Analysis

In case of an odd-mode, there is a voltage null along the plane of symmetry which means the middle of the divider is short circuit (SC) case. Therefore, the resistor R will be grounded and the impedance at port # 1 is to be zero. The odd-mode input admittance at port # 2 (Y_{in2}^{o}) can be calculated as follows:

$$Y_{in2}^{o} = \frac{1}{Z_2}\frac{Y_{l2}^{o} + j(1/Z_2)\,tan\theta_2}{1/Z_2 + jY_{l2}^{o}\,tan\theta_2} \tag{A.10}$$

$$Y_{l2}^{o} = \frac{2}{R} + \frac{1}{Z_1}\frac{Y_{load2}^{o} + j(1/Z_1)\,tan\theta_1^{'}}{1/Z_1 + jY_{load2}^{o}\,tan\theta_1^{'}} \tag{A.11}$$

$$Y_{load2}^{o} = jB_S - j\frac{1}{Z_1\,tan\theta_1} \tag{A.12}$$

Then the odd-mode scattering parameter at port # 2 (S_{22}^{o}) can be calculated from:

$$S_{22}^{o} = \frac{(1/Z_o - Y_{in2}^{o})}{(1/Z_o + Y_{in2}^{o})} \tag{A.13}$$

By applying the condition in Eq. (A.2) to the scattering parameter expressions in Eq. (A.3) through Eq. (A.5), the solution of the divider can be determined.

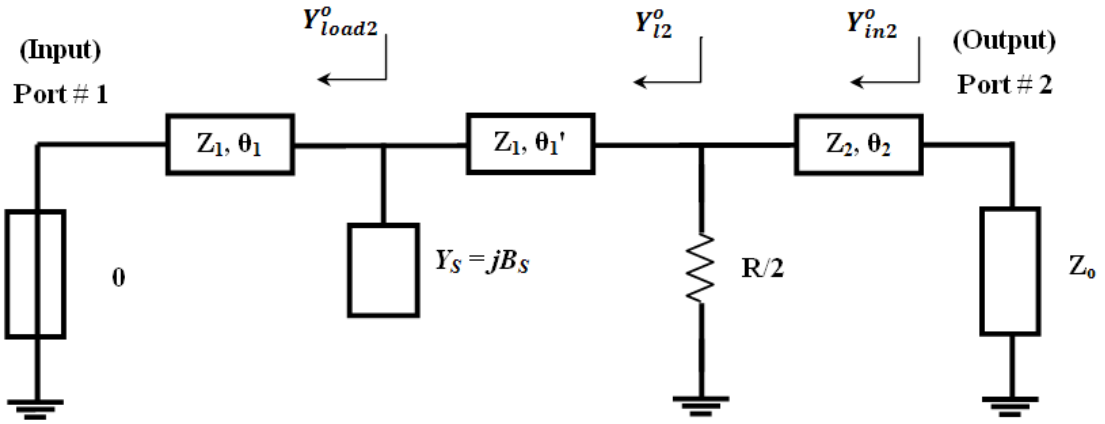

Figure A.3 Circuit of the power divider for the odd-mode analysis

Using arbitrary values for $Z_1, Z_2, Z_S, \theta_1, \theta_1', \theta_2$ and θ_S makes the solution is very complicated. We can simplify our model by removing the two additional transmission lines at the end of each branch (Z_2, θ_2) this will lead to $R = 2Z_o$ and:

$$Z_1^2 tan\theta_1 tan\theta_1^{'} - 2Z_o^2 = 0 \tag{A.14}$$

$$tan\theta_1 tan\theta_1^{'} + B_S Z_1 tan\theta_1 - 1 = 0 \tag{A.15}$$

and by solving the above two equations, the relationship between divider parameters can be formulated as:

$$Z_1 = \sqrt{2} Z_o / \sqrt{tan\theta_1 tan\theta_1^{'}} \tag{A.16}$$

$$B_s = \left(1 - tan\theta_1 tan\theta_1^{'}\right)/(Z_1 tan\theta_1) \tag{A.17}$$

$$Z_s = \left(Z_1 tan\theta_1 tan(\theta_s)\right)/\left(1 - tan\theta_1 tan\theta_1^{'}\right) \tag{A.18}$$

The initial value of θ_1 can be calculated according to the operating bandwidth from [91]:

$$\theta_1 = 90° \left[1 - \frac{1}{\sqrt{2}} \left(\frac{f_U/f_L - 1}{f_U/f_L + 1}\right)\right] \tag{A.19}$$

where f_U/f_L is the desired bandwidth ratio.

From the above equations, according to the desired bandwidth ratio, the initial values for the divider parameters $\theta_1, Z_1,$ and B_s can be determined. Then, the length of the extended line is chosen arbitrarily to be different than that of the main line, i.e. $\theta_1' \neq \theta_1$ to obtain more design flexibility and hence the bandwidth can be enhanced. Also, two additional transmission lines are installed at the end of each branch and by adjusting them; the frequency response can be improved. With the aid of CAD tools, we can determine the other parameters by using full-wave analysis of the whole structure.

Appendix B

Analysis of Two-Layer Vertical Microstrip Transition

First, we consider that the transition is a 4-port coupler with two open circuit (OC) ports as shown in Figure B.1. Assuming that a_i is the input signal to the ith port while b_i is the output signal from the ith port and C is the coupling between the top and bottom microstrip-coupled patches. The output signals at the input (port # 1) and output (port # 2) can be calculated as [112]:

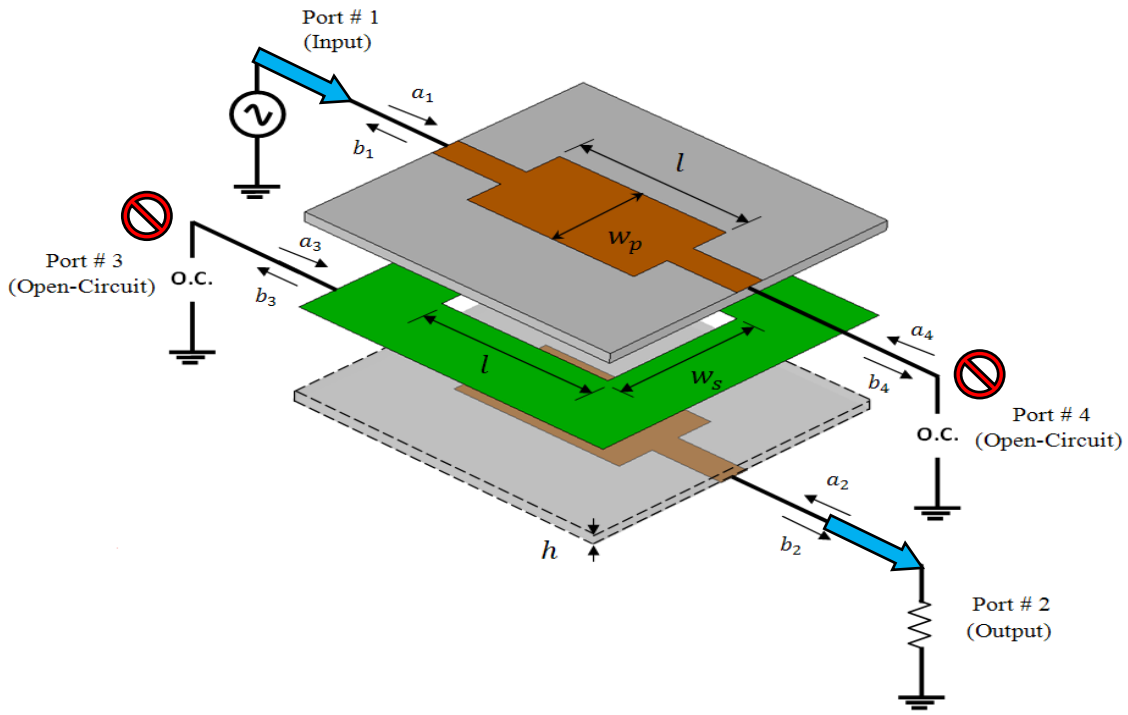

Figure B.1 The arbitrary microstrip vertical transition as a four-port coupler.

$$b_1 = \frac{jC\sin\theta \cdot a_3 + \sqrt{1-C^2} \cdot a_4}{\sqrt{1-C^2}\cos\theta + j\sin\theta} \tag{B.1}$$

$$b_2 = \frac{\sqrt{1-C^2} \cdot a_3 + jC\sin\theta \cdot a_4}{\sqrt{1-C^2}\cos\theta + j\sin\theta} \tag{B.2}$$

The reflection coefficient at OC-terminated port # 3 and port # 4 is equal to unity. If we assume that the output port # 2 is perfectly matched, so the incident (or reflected) signals at port # 3 and port # 4 are calculated from:

$$b_3 = a_3 = \frac{jC\sin\theta \cdot a_1}{\sqrt{1-C^2}\cos\theta + j\sin\theta} \tag{B.3}$$

$$b_4 = a_4 = \frac{\sqrt{1-C^2} \cdot a_1}{\sqrt{1-C^2}\cos\theta + j\sin\theta} \tag{B.4}$$

where the phase $\theta = \beta_{ef} l$ with l is the length of the coupling structure and β_{ef} is the effective phase constant and it is related to the even- and odd-mode phase constants β_e and β_o from:

$$\beta_{ef} = \frac{\beta_e + \beta_o}{2} = \frac{2\pi\sqrt{\varepsilon_r}}{\lambda} \tag{B.5}$$

The return loss of the input port # 1 (S_{11}) and the insertion loss from the input port # 1 to the output port # 2 (S_{21}) can be expressed as:

$$S_{11} = \frac{b_1}{a_1} = \frac{1 - C^2(1 + \sin^2(\theta))}{\left[\sqrt{1-C^2}\cos\theta + j\sin\theta\right]^2} \tag{B.6}$$

$$S_{21} = \frac{b_2}{a_1} = \frac{j2C\sqrt{1-C^2}\sin\theta}{\left[\sqrt{1-C^2}\cos\theta + j\sin\theta\right]^2} \tag{B.7}$$

The coupling C can be expressed in terms of the even- and odd-mode characteristic impedances Z_{0e} and Z_{0o}, respectively and vice-versa from:

$$C = \frac{Z_{0e} - Z_{0o}}{Z_{0e} + Z_{0o}} \tag{B.8}$$

$$\mathrm{Z_{0e}} = \mathrm{Z_0}\sqrt{\frac{1+C}{1-C}} \tag{B.9}$$

$$\mathrm{Z_{0o}} = \mathrm{Z_0}\sqrt{\frac{1-C}{1+C}} \tag{B.10}$$

where Z_0 = 50Ω is the characteristic impedance of the microstrip ports of the assumed coupler and $\mathrm{Z_{0e}Z_{0o}} = \mathrm{Z_0^2}$.

The relationship between the even- and odd-mode characteristic impedances and the transition dimensions can be calculated from:

$$Z_{0e} = \frac{60\pi K(k_1)}{\sqrt{\varepsilon_r}K'(k_1)} \tag{B.11}$$

$$Z_{0o} = \frac{60\pi K'(k_2)}{\sqrt{\varepsilon_r}K(k_2)} \tag{B.12}$$

where $K'(k) = K(k') = K\left(\sqrt{1-k^2}\right);\ k' = \sqrt{1-k^2}$

In the above expression, $K(k)$ denotes the first kind elliptical integral. The parameters k_1 and k_2 are related to coupling structure dimensions. An approximate expression for $K(k)/K'(k)$ is [112]:

$$\frac{K(k)}{K'(k)} = \frac{K(k)}{K(k')} = \frac{2}{\pi} ln\left(2\sqrt{\frac{1+k}{1-k}}\right), 0.5 \le k^2 \le 1 \tag{B.13}$$

$$= \frac{\pi}{2ln\left(2\sqrt{\frac{1+\sqrt{1-k^2}}{1-\sqrt{1-k^2}}}\right)}, 0 \leq k^2 \leq 0.5$$

k_1 and k_2 which can be calculated using the even-odd mode analysis for the broadside-coupled structures [107] are:

$$k_1 = \sqrt{\frac{\sinh^2(\pi^2 w_s/(4h))}{\sinh^2(\pi^2 w_s/(4h)) + \cosh^2(\pi^2 w_p/(4h))}} \quad \text{(B. 14)}$$

$$k_2 = \tanh(\pi^2 w_p/(4h)) \quad \text{(B. 15)}$$

where h is the substrate thickness, w_p and w_s are the widths of the coupled microstrip patches (at the top and bottom layers) and the coupling slot (at the middle layer).

The length of the microstrip/slot coupling structure $l = l_p = l_s$ can be calculated from [107] as a function of the effective wavelength λ_c at the center frequency of operation f = 6.85 GHz and the transition dimensions w_p and w_s from:

$$l = \frac{\lambda_c}{4}\left[1 - \left(\frac{\pi(w_p + w_s)}{4\lambda_c}\right)^2\right]^{-1} \quad \text{(B. 16)}$$

Perfect coupling means that C = 1 where the even-mode characteristic impedance Z_{0e} goes to infinity and the odd-mode characteristic impedance Z_{0o} is zero. The case for no coupling means that C = 0 where $Z_{0e} = Z_{0o} = Z_0$. The desired coupling value can be determined by the desired operating bandwidth for the proposed transition. The effect of varying the operating frequency on both transition insertion loss S_{21} and return loss S_{11} for different coupling values are demonstrated in Figure B.2 and Figure B.3, respectively. The curves show the relationship among insertion and return losses at different coupling

values, i.e. C = 0.5, 0.6, 0.7, 0.8 and 0.9. It can been noticed that to design a transition for UWB operation, the optimum coupling value C should be ranging from 0.7 to 0.8 where the corresponding frequency will be ranging from 3 GHz to 11 GHz to cover the whole UWB frequency spectrum.

To design a UWB vertical transition, it is important to make sure that it covers the whole UWB range with acceptable performance. We should select a suitable coupling value C to achieve the desired UWB bandwidth. Then the even- and odd-mode characteristic impedances can be determined from Eq. (B.9) and Eq. (B.10). The dimensions parameters of the transition patches and the coupling slot can be determined from Eq. (B.11) through Eq. (B.16). The width of the microstrip transmission lines at the top and bottom layers is chosen to give 50Ω impedance using the standard microstrip design equations.

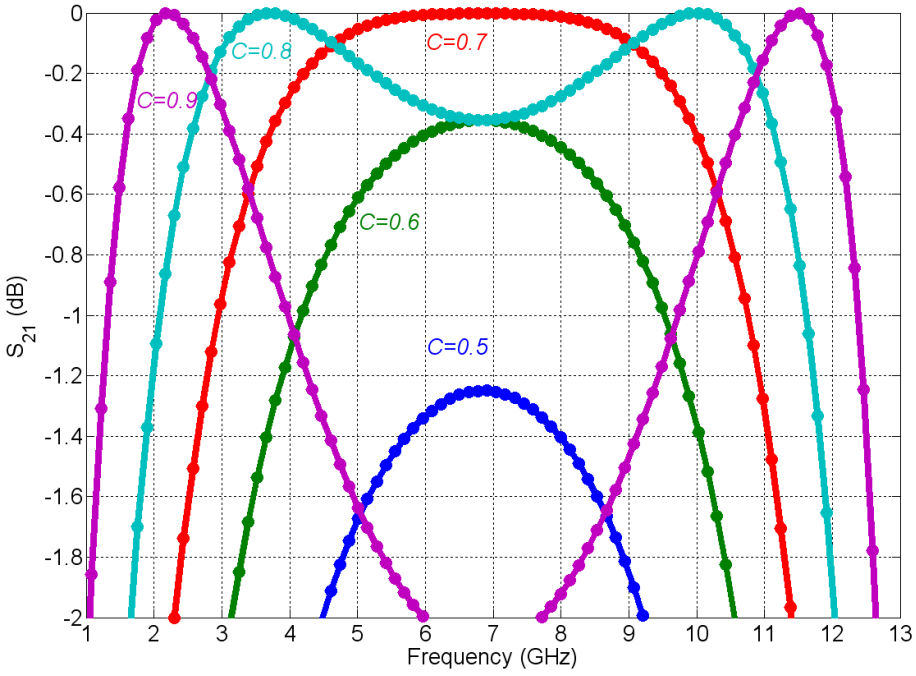

Figure B.2 Transmission coefficients versus frequency for different coupling values.

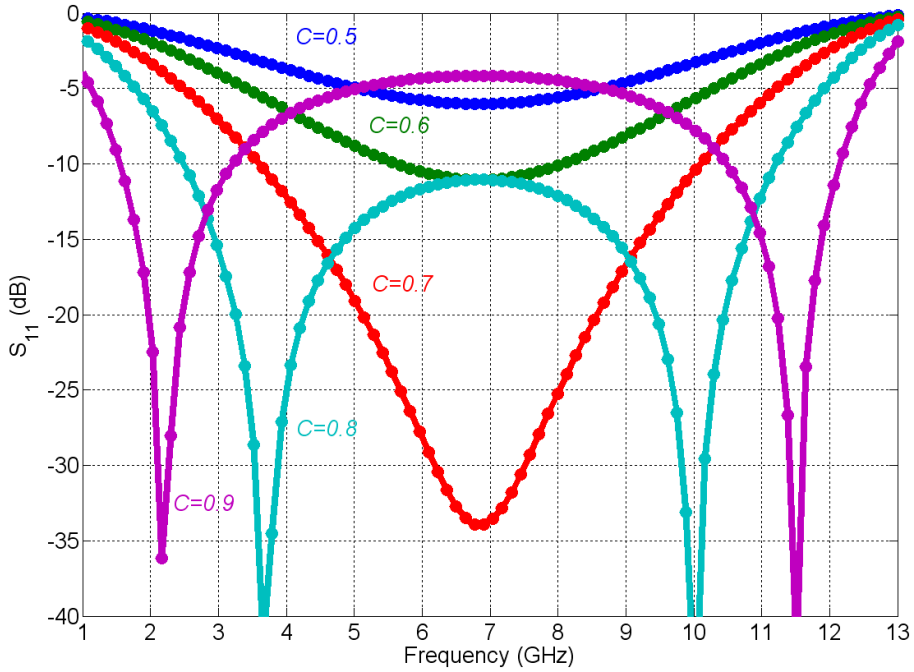

Figure B.3 Reflection coefficients versus frequency for different coupling values.